Improvement of the coherence Characteristics of Laser Diode Arrays Using Photorefractive Phase Conjugation

Løbel, Martin Bo Hjort

Publication date:
1998

Document Version
Publisher's PDF, also known as Version of record

Risø–R–1038(EN)

Improvement of the Coherence Characteristics of Laser Diode Arrays Using Photorefractive Phase Conjugation

Martin Bo Hjort Løbel

Risø National Laboratory, Roskilde, Denmark
May 1998

Abstract This thesis deals with new techniques for improvement of the coherence properties of high-power laser diode arrays. A new configuration where a laser diode array is coupled to an external phase conjugate cavity is presented. The phase conjugator is a self-pumped photorefractive barium titanate crystal. The external cavity includes a frequency selective element and a spatial filter. Experimentally it is verified that the frequency selective element (an etalon or a diffraction grating), the spatial filter, and the phase conjugator cause the laser diode array to oscillate in one single spatial mode at one longitudinal mode. Therefore, the radiation becomes almost diffraction limited and the coherence length is improved significantly.

It is found that the material frequency dispersion in the barium titanate crystal plays a crucial role in the self-induced frequency scanning process that takes place when a multimode laser is coupled to such a conjugator. It is shown that a new concept - counterbalanced dispersion - that is based on dispersion in prisms or diffraction gratings can suppress the self-induced frequency scanning.

Furthermore, a theoretical model of the dynamic, complex grating structure in the barium titanate crystal is presented. From this model it is predicted that the material dispersion causes the reflectivity of the phase conjugator to become asymmetric with respect to the wavelength. The asymmetry leads to the scanning phenomenon and, consequently, we conclude that dispersion is the origin of the frequency scanning process. Moreover, it is found that the grating structure in the crystal is much more frequency selective than previously assumed. The wavelength selectivity depends on the coherence length of the laser beam that induces the dynamic gratings. This dependency leads to the *self-narrowing* effect and through this effect the coherence length of a multimode laser can be increased significantly when the laser is coupled to a photorefractive conjugator.

The most important new results of the present Ph.D. thesis are described in chapters 7-10.

Front page figure: numerical simulation of a self-pumped phase conjugator formed in a barium titanate crystal. The beam enters from the left-hand side. The c-axis points downwards. The simulations in the present work are used to determine the characteristic wavelength response of the complex grating structure when the conjugator is coupled to a multimode laser.

This thesis is submitted in partial fulfilment of the requirements for the degree of Doctor of Philosophy in Physics at the Technical University of Denmark.

ISBN 87-550-2373-8
ISBN 87-550-2409-2 (internet)
ISSN 0106-2840

Information Service Department · Risø · 1998

Contents

List of Figures

List of Tables

List of Symbols

α ..... field absorption coefficient [m^{-1}]
α_p ..... intensity absorption coefficient [m^{-1}]
A_p ..... field amplitude [V/m]
β ..... angle between grating vector and c-axis [rad]
β_c ..... antiguiding parameter [-]
β_{ba} ..... propagation constant in laser cavity for array mode [m^{-1}]
β_t ..... rate of thermal generation of carriers [s^{-1}]
c ..... velocity of light [m/s]
C ..... feedback parameter [-]
d_1, d_2, d_3, d_4 ..... distance between gratings [m]
$\delta\lambda$ ..... fraction of a longitudinal mode spacing [m]
Δf_{FP} ..... longitudinal mode spacing [Hz]

$\Delta f_{m,m+1}$ ..... spatial mode spacing [Hz]
$\Delta\lambda_{fwhm}$ ..... spectral bandwidth [m]
$\Delta\lambda_{fsr}^{etalon}$ ..... free spectral range of etalon [m]
$\Delta\lambda_{fwhm}^{etalon}$ ..... spectral bandwidth of etalon [m]
$\Delta\lambda_{FP}$ ..... longitudinal mode spacing [m]
$\Delta\lambda_p$ ..... side band spacing of detuning curve [m]
$\Delta\lambda_{m,m+1}$ ..... spatial mode spacing [m]
$\Delta\lambda_s$ ..... wavelength selectivity (FWHM) [m]
$\Delta\lambda_w$ ..... spectral linewidth of writing laser beam (FWHM) [m]
Δg ..... change in gain [m^{-1}]
Δn ..... (modulation) change in refractive index [-]
$\Delta\widetilde{n}$ ..... change in complex refractive index [-]
Δt ..... time step [s]
Δx ..... size of sampling [m]
$\Delta\omega$ ..... spectral linewidth [rad/s]
$\partial n_0/\partial\lambda$ ..... dispersion coefficient [m^{-1}]
e ..... numerical electronic charge [C]
E, E_o, E_w, E_c, E_r, E_0 ..... complex field amplitude [V/m]
E_g ..... bandgap energy [J]
E_k ..... k'th element of electric field vector [V/m]
E_s ..... electric space charge field [V/m]
$\widetilde{\mathbf{E}}_s$ ..... normalized electric space charge field [-]
E_q ..... characteristic saturation field [V/m]
ε_0 ..... vacuum permittivity [F/m]
$\overleftrightarrow{\epsilon}$ ..... low frequency (or static) dielectric tensor [F/m]
ϵ_{eff} ..... effective low frequency (or static) dielectric tensor [F/m]
ϵ_a ..... element of low frequency (or static) dielectric tensor [F/m]
ϵ_c ..... element of low frequency (or static) dielectric tensor [F/m]
$\overleftrightarrow{\varepsilon}_r$ ..... relative dielectric permittivity tensor [F/m]
$\overleftrightarrow{\varepsilon}$ ..... dielectric permittivity tensor [F/m]
F ..... feedback coefficient [-]
F_{eff} ..... effective feedback coefficient [-]
g ..... gain [m^{-1}]
γ ..... coherence degree [-]
γ_0 ..... coupling constant [m^{-1}]
γ_r ..... recombination constant [s^{-1}]
H^p ..... phase conjugate fidelity (simulation) [-]
H_T ..... transmittance of grating [-]
H_R ..... reflectance of grating [-]
i ..... imaginary unit
i_{th} ..... threshold current [A]
I , I_0, I_1, I_2 ..... intensity [W/m^2]
I_d ..... equivalent dark intensity [W/m^2]
I_{in} ..... peak intensity of injection lobe [W/m^2]
I_{max} ..... maximum intensity in interference pattern [W/m^2]
I_{min} ..... minimum intensity in interference pattern [W/m^2]
I_{out} ..... peak intensity of output lobe [W/m^2]
J ..... current density [A/m^2]
J_{pv} ..... photovoltaic current [A/m^2]
k_0, k_o, k_w, k_a, k_b ..... wave vectors [m^{-1}]
k ..... wave vector in crystal [m^{-1}]
k_d ..... Debye wave vector [m^{-1}]
$\overline{K}$ ..... grating wave vector [m^{-1}]
$\overline{K}_g$ ..... grating wave vector [m^{-1}]

$\widehat{K}_g$ ..... unit vector along grating wave vector [m^{-1}]
k_B ..... Boltzmann constant [JK^{-1}]
κ ..... feedback rate [s^{-1}]
l_c ..... width of crystal [m]
L_1, L_2, L_3, L_4 ..... thickness of grating [m]
l_z ..... length of crystal [m]
l_{loop} ..... length of internal beam loop in crystal [m]
L_c ..... coherence length [m]
L_{ext} ..... length of external-cavity [m]
L ..... length of solitary laser cavity [m]
λ ..... free space wavelength [m]
λ_{-1} ..... free space wavelength of side mode [m]
λ_{+1} ..... free space wavelength of side mode [m]
λ_0 ..... center wavelength [m]
Λ ..... grating period [m]
m ..... index for array mode [-]
μ ..... mobility of carriers [$m^2/(Vs)$]
μ_0 ..... vacuum permeability [Vs/(Am)]
n, n_a, n_c ..... average, ordinary and extraordinary refractive index [-]
n_e ..... number density of carriers [m^{-3}]
n_0 ..... refractive index at center wavelength [-]
n_{array} ..... refractive index of laser cavity for array mode [-]
N ..... number of stripes/elements in laser diode array [-]
N_A ..... concentration of acceptors [m^{-3}]
N_D ..... concentration of donors [m^{-3}]
N_D^+ ..... number density of ionized donors [m^{-3}]
η ..... diffraction efficiency [-]
$\overleftrightarrow{\eta}$ ..... impermeability tensor [m/F]
η_0 ..... impedance of vacuum [Ω]
P ..... photons in lasing mode [-]
p ..... index for longitudinal modes [-]
ρ ..... charge concentration [m^{-3}]
ϕ ..... slant angle of grating [rad]
σ_s ..... spontaneous emission rate [s^{-1}]
$\overleftrightarrow{\mathrm{r}}$,$\mathrm{r}_{ijk}$ ..... electro-optic tensor [m/V]
r_{eff} ..... effective electro-optic coefficient [m/V]
r ..... focal length of lens [m]
R_{end}, R_{out}, R_{ext} ..... reflection coefficient (intensity) [-]
R_{pc} ..... phase conjugate reflectivity (intensity) [-]
R^p ..... reflectivity (simulation) [-]
s ..... photoexitation cross section[m^2J^{-1}]
t ..... time [s]
t_c ..... arbitrary (time) constant [s]
T_C ..... Curie temperature [K]
T ..... absolute temperature [K]
T ..... transmittance of hologram [-]
τ_{ext} ..... external-cavity round-trip time [s]
τ_L ..... round-trip time in solitary laser cavity [s]
τ_{di} ..... dielectric time constant times intensity [sm^2/W]
w_0 ..... beam width (simulation) [m]
φ_{ext} ..... phase shift in external-cavity [rad]
φ_{pcm} ..... constant phase shift at phase conjugate mirror [rad]
θ ..... radiation angle [rad]
θ ..... angle of incidence for grating [rad]

θ_i ..... angle of incidence [rad]
θ_0 ..... Bragg angle [rad]
θ_r ..... angle of refraction [rad]
θ_m ..... radiation angle for lobes of array mode m [rad]
θ_{diff} ..... diffraction limit (FWHM) [rad]
θ_{fwhm} ..... width of one radiation lobe (FWHM) [rad]
θ_{twm} ..... half-angle between two beams [rad]
Φ_0 ..... near field profile of array mode in the transverse direction
Φ_m ..... near field profile of perturbed array mode m in the lateral direction
Φ_m^{array} ..... near field profile of array mode m
Ψ_m ..... near field profile of unperturbed array mode m in the lateral direction
x ..... molar fraction [-]
x ..... power of intensity proportionality [-]
x_0 ..... half-width of gain medium of laser diode array or broad-area laser [m]
x_{off} ..... position offset [m]
ω_0 ..... angular center frequency [rad/s]

Abbreviations and indices

CW ..... Continuous Wave
PCM ..... Phase Conjugate Mirror
FSPCF ..... Frequency Selective Phase Conjugate Feedback
FWHM ..... Full Width at Half-Maximum
$i, j, k, l,$ ..... tensor indices representing x, y and z or a, b and c
$\widehat{x}$ ..... x-axis of laser diode array
$\widehat{y}$ ..... y-axis of laser diode array
$\widehat{z}$ ..... z-axis of laser diode array
$\widehat{z}_c$ ..... longitudinal axis (c-axis) of crystal
$\widehat{x}_c$ ..... transverse axis of crystal
$*$ ..... complex conjugation

Preface

The present thesis describes the work carried out in the Optics and Fluid Dynamics Department (OFD), Risø National Laboratory, Denmark, during the period from February 1995 to May 1998. Within this period I was on parental leave for four months due to which my Ph.D. study was equivalently prolonged.

The work was supervised by

> Dr. Paul M. Petersen, Senior Scientist in OFD, Risø Nat. Lab;
>
> Dr. Per M. Johansen, Senior Scientist and Head of Research Programme in OFD, Risø Nat. Lab;
>
> Prof. Preben Buchhave, Professor in the Physics Department, Technical University of Denmark.

The project was financed partly by the Research Academy of Denmark (grant # 95-0058-SAM) and partly by Risø National Laboratory.

With all my sincere gratitude and appreciation I wish to thank my main thesis advisor, Dr. Paul Michael Petersen, for his encouragement throughout this Ph.D. work, for all helpful and fruitful discussions and for making these three years a very enjoyable and worthwhile experience. I also wish to extend thanks to Dr. Per M. Johansen and Prof. Preben Buchhave for helpful and enlightening discussions. I further acknowledge the fruitful interaction and assistance from colleagues and staff in the Optics and Fluid Dynamics Department.

In the period from September 1995 to March 1996 I had the great pleasure of visiting the Physics Department at University of Southern California (USC), Los Angeles, USA. In this connection I would like to thank Prof. Jack Feinberg - the inventor of the Cat conjugator - at USC for helpful discussions and for providing the photorefractive crystals as well as the laboratory facilities for experimental measurements. I am also very grateful for the help from Ph.D. Student San-Ching De La Cruz at USC who assisted me with the use of much of the laboratory equipment and with whom I had many productive discussions. Special thanks go to Dr. Stuart MacCormack; through his own experimental experience with the improvement of laser diode arrays using photorefractive techniques, he contributed significantly to my knowledge about the subject. This contribution and our many discussions are highly appreciated and gave me a good background for the work to follow.

Last, but not least, I would like to express my sincere gratitude to my parents, Bente and Per, for their lifelong support, and to my dearest Annette for her patience and support during the whole period, in particular duing my six months' stay in Los Angeles.

It is when things do not work we start to learn -
Achievements come through hard work, not through luck !

To my dearest Annette, my son Lucas, and my parents -

Martin Bo Hjort Løbel, May 1998, Risø National Laboratory

Dansk resumé

Dansk titel: "Forbedring af kohærensegenskaberne af højeffektslaserdiode-arrays ved brug af fotorefraktiv fasekonjugation".

I denne afhandling introduceres et nyt lasersystem hvor et højeffektslaserdiode-array kobles til en ekstern kavitet med en fotorefraktiv fasekonjugator. Fasekonjugatoren er en selvpumpet bariumtitanatkrystal. Den eksterne kavitet i lasersystemet indeholder desuden et frekvensselektivt element og et rumligt filter. Det vises eksperimentelt at et laserdiode-array ved denne konfiguration kan tvinges til at oscillere i kun én rumlig- og én longitudinal mode hvorved kohærensegenskaberne forbedres betydeligt. Udgangsstrålen fra lasersystemet bliver næsten diffraktionsbegrænset.

Det fastslås, at materialedispersionen i bariumtitanatkrystallen har en afgørende betydning for det selvinducerede frekvensskift som kan forekomme når en laser kobles til en selvpumpet fasekonjugator. Det demonstreres endvidere, at frekvensskiftet kan undertrykkes ved brug af dispersion fra prismer eller fra et gitter. Herved opnås et stabiliseret udgangssignal fra lasersystemet.

Ved brug af en numerisk model undersøges de dynamiske gitre der opbygges i bariumtitanatkrystallen. Det fastslås, at detuningskurven for den samlede gitterstruktur er asymmetrisk og det konkluderes, at denne asymmetri er den fysiske årsag til det selvinducerede frekvensskift. Det vises, at asymmetrien hidrører fra materialedispersionen i krystallen. Ydermere måles det at gitterstrukturen er meget mere bølgelængdeselektiv end hidtidigt antaget. Bølgelængdeselektiviteten afhænger af kohærenslængden af laserstrålen der inducerer gitterstrukturen. Der redegøres for hvorledes bølgelængdeselektivitetens afhængighed af kohærenslængden kan medføre at kohærenslængden af en laser kan forøges når den kobles til en selvpumpet fasekonjugator.

1 Introduction

The first laser ever to be successfully operated was the flash-pumped ruby laser demonstrated by T. H. Maiman back in 1960 [1]. Since then, there has been intensive and ongoing research around the world to develop new lasers with various wavelengths, narrow line widths, better spatial radiation properties, etc. Lasers based on semiconductors were for the first time reported in 1962 [2] and the progress in the performance of such lasers has since then been tremendous. Over time, semiconductor lasers have proven to be very useful and cost effective due to a number of different factors such as, e.g., small size, easiness of mass production, functional reliability, and electrical pumping. This is especially the case for applications that require low optical power on the order of milliwatts: e.g. optical communications, bar code scanners and a large variety of sensors. These low-power devices in general operate on a single fundamental spatial mode; they are referred to as fundamental-mode lasers and have a diffraction limited radiation pattern with good directionality and focusability. Such factors are important for applications that require focusing to a small spot size, launching light into waveguides or maintaining a well collimated beam over a long distance. Moreover, most of these low-power lasers operate on a single longitudinal mode, and the radiation from the lasers therefore has a long coherence length which makes them suitable for applications such as interferometric sensors, holography, and fiber communication. A semiconductor laser that operates in only one spatial mode and one longitudinal mode simultaneously is generally referred to as a single-mode diode laser.

Today single-mode diode lasers are capable of delivering up to approximately 200 milliwatt of optical power; this limit arises because severe damage will occur to the output facet of the laser if the intensity density becomes too large. However, many applications such as material processing, penetration of flesh in surgical operations, and pumping of solid state lasers demands much higher power of the order of watts. To increase the optical power from a semiconductor device one can either increase the cross section of the gain region (referred to as broad-area laser or laser diode array), or place a number of lasers next to each other (referred to as a laser diode bar). One can also do both. Unfortunately, both of these two approaches result in high-power devices that operate in several spatial and longitudinal modes simultaneously, or the radiation being partly incoherent due to no coupling between the individual laser elements, which leads to an output radiation that is many times the diffraction limit and has a very short coherence length of the order of a few hundred micrometers. This fact limits the usefulness of the high-power devices since it especially destroys the focusability of the output beam, which is essential in many applications.

Over the last 15 years there has been intensive research into the development of high-power monolithic coherent sources. This has proven to be a particularly challenging task. In the past many complex designs have been investigated in order to achieve better mode discrimination and the desired diffraction limited radiation. The basis for obtaining a coherent source is to establish some phase relation across the entire emitting region. Thus, several designs of so-called phase-locked arrays such as gain tailored arrays [3], Y-coupled arrays [4], diffraction coupled arrays [4] and leaky coupled arrays [5] have been proposed and tested. All these designs have had only partial success. As a result, virtually all the high-power laser arrays commercially available at present emit their radiation into two broad far-field lobes, in directions which are symmetric around the normal of the output facet, instead of the desired single diffraction-limited lobe.

Alternative products such as the master oscillator power amplifier (MOPA)[6], which can deliver high-power with good coherence properties, are commercially

available but are relatively expensive due to the much more complicated chip design as compared with the very simple design of traditional laser array. Moreover, they are very sensitive to feedback.[7]

In general, one may say that so far high-power monolithic sources either have a very complex design which makes them expensive but coherent (e.g. MOPA), or are simple in design and do not yield good coherence properties. There is therefore an interest in techniques for external improvement of the coherence properties of laser arrays and laser bars if the techniques are simple, stable, and effective. This circumstance has been the motivation for the work performed in connection with the present Ph.D. thesis.

1.1 External-Cavity Controlled Devices

In parallel with the research on monolithic coherent sources there have been investigations in the area of external-cavity controlled devices. These investigations have resulted in several techniques for the enhancement of the coherence properties of especially laser diode arrays (and broad-area laser diodes). The reported techniques for laser diode arrays can be divided into five groups:

1. Injection locking with a master laser.
2. External feedback using a diffraction grating.
3. External feedback using a mirror.
4. Coupled cavity scheme.
5. Phase conjugate feedback (phase conjugate laser).

Each of these techniques will be discussed in Chapter 5. Phase conjugate feedback is the technique that is used in connection with the present Ph.D. thesis and will be discussed in detail. The expression *phase conjugate laser* refers to a laser exposed to phase conjugate feedback, or a laser that has a resonator with a phase conjugate mirror included. Table 1 gives an overview of the reported techniques for enhancement of the coherence properties of the laser diode arrays. The table shows the characteristics of the radiation (spectral and spatial) from a laser diode array at which the enhancement technique has been applied. In the table the section in which the technique is discussed is also shown. Moreover, in the last row of the table (Frequency selective phase conjugate feedback) the results obtained in connection with this Ph.D. work are summarized.

Injection locking provides both a single-mode spectrum and an almost diffraction limited far-field pattern. However, injection locking is a complex and expensive technique since it requires a single-mode injection laser, feedback isolation optics as well as fine control of the temperatures of the injection laser and the laser diode array. An external cavity scheme where a laser diode array is used as an amplifier in a ring configuration has been demonstrated and yields both a single-mode spectrum and a nearly diffraction limited far-field pattern. However, the conversion efficiency of the energy provided by the laser diode array to the single-mode performance was very low.

To summarize, one can therefore say that the previous work on external configurations (excluding injection locking) indicates either that it is possible to force a laser array to operate in a single longitudinal mode (single-mode spectrum) and a have a non-diffraction limited far-field, or that the array can be forced to operate in an almost diffraction limited single-lobe far-field, but in that case it has a multimode spectrum. There seems to be a trade-off. As it will be shown in the present Ph.D. thesis, it is actually possible to avoid this trade-off using frequency selective phase conjugate feedback generated in a photorefractive barium titanate crystal,

Technique	Spectrum	Far-field pattern	Section
Injection locking	Single-mode	Diffraction limited	Sec. 5.3
External grating cavity	Single-mode	Broad (not enhanced)	Sec. 5.1
External grating cavity and spatial filter	Multimode	Diffraction limited	Sec. 5.5
External mirror cavity	Multimode	Diffraction limited	Secs. 5.3.1, 5.5
External cavity (ring config.)	Single-mode	Diffraction limited	Sec. 5.3.1
Coupled cavity (mirror)	Single-mode	Broad (not enhanced)	Sec. 5.1
Phase conjugate feedback	Multimode	Diffraction limited	Sec. 1.2
Frequency selective phase conjugate feedback	Single-mode	Diffraction limited	Chaps. 9, 10

Table 1. Overview of reported techniques for improvement of the coherence properties of laser diode arrays. The frequency selective phase conjugate feedback technique has been developed during the present Ph.D. work. The term 'diffraction limited' is to be understood as 'nearly' diffraction limited.

and as a result a laser diode array can be forced to operate in a single longitudinal mode and has a nearly diffraction limited far-field pattern. In the following section a review of the development of phase conjugate laser diode arrays up to now is given.

1.2 Previous Work on Phase Conjugate Arrays

In this section a review of previous work on phase conjugate laser diode arrays using a photorefractive medium is given.

The concept of phase locking two separate self-oscillating lasers to each other by means of four-wave mixing in a photorefractive medium was reported and demonstrated by Sternklar and colleagues back in the mid eighties.[8] The two incoherent beams were both directed to interact in a $BaTiO_3$ crystal where they formed a four-wave mixing geometry. This configuration was originally named the double phase conjugate mirror [9], but the term mutually pumped phase conjugator is often used as well. Later on, coherent coupling of two laser diodes were demonstrated and configurations for coupling multiple diodes were proposed.[10] The first demonstration of a laser diode array with phase conjugate feedback was reported in 1987.[11] In that experiment it was the intention to lock two arrays to each other using a mutually pumped phase conjugator. It was observed that the highest phase conjugate reflectivity (10%) was obtained if only a part of the far-field from the array was directed towards the conjugator. Moreover, a considerable change in the far-field pattern was noted but it was still far from the diffraction limit. Only a small enhancement of the spectral quality was observed. The wavelength selectivity of the phase conjugate feedback was increased by using a semi-linear phase conjugate geometry where one mirror was a diffraction grating, and a laser diode array was reported to operate in a single longitudinal mode with a line width of less than 0.02 nm.[12] This configuration, however, did not lead to any significant enhancement of the far-field pattern. In 1990, phase conjugation was used to achieve mode locking (generation of periodic train of short pulses) of a laser diode array.[13] In that configuration a diffraction grating was placed between the laser array and the phase conjugator that made it possible to tune the wavelength of the output over a wavelength range of several nanometers. In the following years, MacCormack et al. demonstrated an almost diffraction limited output from a laser array using a self-pumped phase conjugator.[14] Later, MacCormack and Feinberg realized the importance of incorporating a spatial filter in

the external cavity to limit the number of spatial modes that can subsequently interact with the phase conjugator. They also increased the interaction strength in the $BaTiO_3$ crystal using a new orientation of the laser array with respect to the optical axis of the crystal. Using this new orientation and a spatial filter they operated a one watt laser array in a nearly diffraction limited single-lobe.[15] The spectrum, however, was not enhanced by this configuration. They also successfully demonstrated injection locking of a laser array using a single-mode laser and a double phase conjugate mirror that resulted in an almost diffraction limited single-mode output.[16] Furthermore, in 1994 they demonstrated single-lobe operation of a one centimeter wide laser diode bar, which consisted of twelve laser arrays.[17] The spectrum was also enhanced significantly and was predominantly a single mode.

1.3 Scope of Thesis

The main purpose of this thesis is to develop a new technique using phase conjugation in a photorefractive barium titanate crystal for the improvement of the coherence properties of the radiation from laser diode arrays. The thesis is composed as follows:

In chapter 2 an introduction to the double heterostructure laser is given. This structure is used in most commercial high-power laser arrays. The physical origin of self-induced filamentation in the active region of the heterostructure, which leads to broadening of the far-field pattern, is explained. A description of the differences and similarities between broad-area lasers, laser diode arrays and laser bars is given. The emission characteristics of a typical laser diode array, with emphasis on the spatial modes and the far-field behavior, are given. Moreover, the spectral characteristics, the polarization state and the astigmatism of the emission are discussed.

In chapter 3 the physical properties of the barium titanate crystal are described, with emphasis on the physical mechanisms responsible for the photorefractive effect. The properties of rhodium doped barium titanate crystals for photorefractive applications at near infrared wavelengths are discussed. The band transport model is shortly outlined; it is used with the numerical simulations presented in chapter 7.

Chapter 4 starts with a short introduction to four-wave mixing. The four-wave mixing concept is described with its analogy to holography. A description of the scheme for mutually pumped phase conjugation is given. This is followed by a description of two different self-pumped phase conjugators, with emphasis on the Cat configuration in which the illumination undergoes internal reflections upon the crystal surfaces. Aspects about the requirements for the spatial coherence properties of the illumination are discussed; this discussion is based on experimental observations. Moreover, the formation of transmission gratings, reflection gratings, and 2k-gratings is discussed.

In chapter 5 a general description of diode lasers exposed to optical feedback is given. The differences between conventional feedback (from, e.g., a mirror) and phase conjugate feedback are discussed. The technique of injection locking of a laser diode array by injecting a beam from a single-mode laser is outlined. This is followed by an introduction to the concept of self-injection locking using both conventional and phase conjugate feedback. In addition, a description of mode discrimination in an external cavity using spectral and spatial filtering is given. At the end of the chapter experimental results on self-injection locking of a laser diode array with conventional feedback from a mirror or a diffraction grating are presented.

In chapter 6 we present experimental observations of the behavior of a laser

diode array exposed to optical feedback generated by a self-pumped phase conjugator. The observed phenomenon is known as self-induced frequency scanning. Through experiments it is established that the frequency scanning has its origin in the photorefractive effect. It is observed that the frequency material dispersion of the barium titanate crystal plays an important role in the scanning mechanism. Furthermore, it is experimentally observed that the frequency scanning can be suppressed by counterbalanced dispersion from prisms or a diffraction grating placed in front of the crystal. The results indicate that the material frequency dispersion of the crystal may be the origin of the scanning process.

In chapter 7 the physical origin of the self-induced frequency scanning is verified to be the frequency material dispersion of the barium titanate crystal. This verification is based on numerical simulations of beam propagation in the crystal. In the simulations the band transport model is solved.

In chapter 8 measurements of the detuning curve of a Cat conjugator is presented. The measurements show that the shape of the detuning curve depends strongly on the coherence length of the incident beam. The findings will explain the observed line width of 0.02 nm obtained from a multimode laser diode array coupled to a Cat conjugator (chapters 9 and 10). The forced reduction of the line width has influence on the spatial distribution and the strength of the gratings that eventually will form in the conjugator crystal. This phenomenon of the coupled system is here referred to as *the self-narrowing effect*. A simple theoretical analysis of the detuning curve of the Cat conjugator is presented.

In chapter 9 the first reported experimental observations of a phase conjugate laser diode array forced to operate in a single longitudinal mode with a nearly diffraction limited far-field pattern are presented. The concept of this technique is referred to as frequency selective phase conjugate feedback. The self-induced frequency scanning is suppressed by inserting a Fabry-Perot etalon in the external cavity. A detailed presentation of the characteristics and performance of the system is given. There is emphasis on the line width, the far-field pattern, and the stability of the radiation (intensity noise and wavelength jitter).

In chapter 10 the implementation of another scheme for frequency selective phase conjugate feedback is presented. In this scheme the etalon has been replaced with a diffraction grating. The implementation of the grating scheme is the first reported experimental observations of a laser diode array forced to have a nearly diffraction limited far-field pattern and forced to operate in a single longitudinal mode that is widely tunable. A detailed presentation of the characteristics and the performance of the system is given. Emphasis is put on the line width, the far-field pattern, the stability of the radiation (intensity noise and wavelength jitter), and the tunability of the wavelength.

In Appendix A, specifications of many of the important components used in connection with the experimental work have been listed. Other appendices are referred to in the text.

The most important results of the work presented in this thesis are described in Chapters 7 - 10. Essential parts of the work have been published in four papers. Moreover, one other paper has been submitted. A list of the five papers and conference presentations can be found in Appendix B.

2 High-Power Semiconductor Lasers

The majority of high-power semiconductor laser devices are based on GaAs and GaAlAs. Conventional high-power lasers - such as the laser diode array - are based on the well-known double heterostructure. In the following sections this structure and the structures of typical high-power devices are presented and the characteristic optical properties are discussed. If the reader is familiar with the structure of laser diode arrays and the properties of such devices, this chapter can be skipped.

2.1 Double Heterostructure Laser

Figure 1 shows a typical heterostructure GaAlAs diode laser. The active layer is $Ga_{1-x}Al_xAs$. The active layer has a thickness of approximately 0.2 μm and is sandwiched between two cladding layers of another semiconductor material. The active layer is often referred to as the *junction*. The *lateral* direction, the *transverse* direction and the *longitudinal* direction are along the x-axis, the y-axis, and z-axis, respectively, as shown in Fig. 1. This x-y-z coordinate system will be included in following figures that contain laser configurations, in order to indicate the exact orientation of the laser device with respect to the other components in the configurations. The laser cavity is formed between two cleaved surfaces of the semiconductor material. These two surfaces act as partial transmitting mirrors and provide the optical feedback which is necessary for the operation of all types of lasers. The cleaved surfaces are referred to as *facets* and have a reflection coefficient of approximately 30%. However, a coating is often applied to the facets; a high reflection coating (R > 99%) for one facet and an anti-reflection coating to the opposite facet (R = 4 - 10%). The facet with high reflection is referred to as the *end* facet, and the one with the lowest reflection coefficient is referred to as the *output* facet. In the active region, as indicated in Fig. 1, there is a large concentration of electrons in the conduction and holes in the valence band. These electrons and holes are confined to the *same* space and, as a result, an electron in the conduction band can decay to fill a hole in the valence band. This process, called *electron-hole* recombination, can lead to the emission of a photon (radiative recombination). If no photon is emitted, as for instance when the energy is transferred to lattice vibrations, the process is said to be a nonradiative recombination. The electron-hole recombination can also occur by simulated emission, where a photon causes an electron-hole recombination and the emission of an extra photon. This process is fundamental to the amplification process of spontaneous emission, which eventually leads to the lasing action.

2.2 Lateral Gain-Guiding

Laser structures are divided into two groups: (1) index-guided and (2) gain-guided, according to the guiding mechanism and confinement of the optical field in the lateral direction. In Fig. 1 there is no lateral confinement of the optical field such as a refractive index variation in the active layer along the x-axis, which is known from index-guided structures.[2] If such an index variation along the x-axis has a peak in the center of the device, the optical field is confined due to a waveguide effect. If the device is gain-guided, the lateral gain profile is controlled by the width of the metallization contact on top of the structure that provides the current for the laser device. A narrow contact leads to better confinement of the injected carriers and thereby also limits the region with gain. However, for gain-guided devices an effect known as *antiguiding* counteracts the gain induced confinement

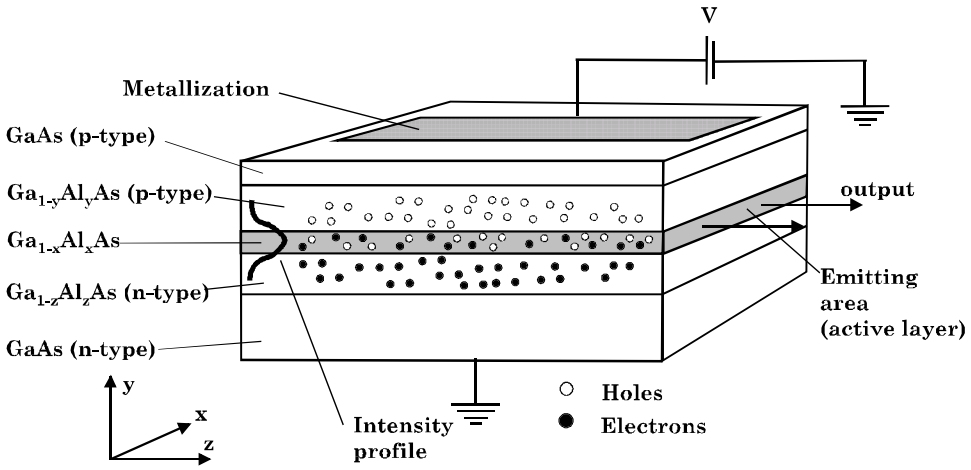

Figure 1. Schematic diagram of a typical double heterostructure GaAlAs laser. Electrons and holes are injected into the active $Ga_{1-x}Al_xAs$ layer from the n and p GaAlAs layers. The end surfaces, which are cleaved crystal faces, serve as feedback mirrors of the laser cavity.

of the optical field. The antiguiding leads to a broader field distribution in the lateral direction. To summarize, the laser structure shown in Fig. 1 is gain-guided in the plane parallel to the junction, and is index-guided in the plane perpendicular to the junction. The index guiding in the transverse direction is discussed in Sec. 2.3.

2.2.1 Lateral Antiguiding Effect

The refractive index of a semiconductor material depends on the concentration of free carriers. The antiguiding parameter (or the line width enhancement factor [2]) β_c, defined as the ratio of decrease in real refractive index (Δn) to increase in imaginary refractive index, can be expressed as [18]

$$\beta_c = -2k_0 \frac{\Delta n}{\Delta g}, \tag{1}$$

where k_0 is the free-space wave vector and Δn is the change in the real part of the refractive index when the gain has altered Δg due to a change in the carrier density. For gain-guided GaAlAs lasers the antiguiding parameter is estimated to $\beta_c \simeq$ 1.5-3.[19] Strictly speaking, β_c varies, for example, with the current but is often treated as a fixed parameter. A change in the carrier density in the center of the active layer leads to a change in the local complex refractive index given by

$$\Delta\widetilde{n} = \Delta n + i\Delta g/(2k_0), \tag{2}$$

where i is the imaginary unit. Since the parameter β_c is positive, an increase in carrier density (increase in gain), which is the case right under the metal contact, will reduce the refractive index at the same location. The optical field that oscillates in the laser cavity will as a consequence experience a lower index in the center of the device as compared with the index at the locations near the edge of the device. For this reason the optical field will experience defocusing and a broadening of the field distribution in the cavity in the lateral direction. For broad-area lasers (stripe-geometry lasers) the antiguiding effect has a substantial influence on the radiation and results in a far-field that has two lobes in the far-field instead of a single lobe.[20, 21]

2.3 Transverse Confinement and Amplification

The heterostructure shown in Fig. 1 is index-guided in the transverse direction. The heterostructure also leads to a confinement of the amplification to the active region. The mechanism for the index guiding and the confinement of the amplification are described in the following.

The molar fraction dependence of the bandgap energy, E_g, for $Ga_{1-x}Al_xAs$ is approximated by $(x < 0.37)$[22]

$$E_g = (1.424 + 1.247x) \text{ eV}. \tag{3}$$

In Fig. 1 the molar fraction x in $Ga_{1-x}Al_xAs$ and the molar fraction z in $Ga_{1-z}Al_zAs$ are both chosen to be less than y in $Ga_{1-y}Al_yAs$, which means that the active layer has a smaller bandgap than those of the surrounding layers. The refractive index of $Ga_{1-x}Al_xAs$ also depends on the molar fraction. This dependence can be expressed as [22]

$$n_{GaAs} - n_{Ga_{1-x}Al_xAs} \simeq 0.62x. \tag{4}$$

Since x and z are chosen to be less than y, the active layer also have the highest refractive index of all the layers.

Figure 2 is a schematic illustration of the simultaneous confinement of charge carriers and photons in the active region when the laser device is forward-biased by applying an external voltage. The schematic illustration is a cross section through the laser device along the y-axis. Figure 2(a) shows the bandgap along the y-axis. The active layer has a lower bandgap than those of the cladding layers. The concentrations of electrons and holes are illustrated by black circles and open circles, respectively. Before the external voltage was applied, an equilibrium was established through diffusion of electrons from the n side toward the p side, while the reverse occurs for holes; the diffusing electrons and holes recombined in the active region. The equilibrium originates from a built-in electric field across the two interfaces of the active region arising from the negatively charged acceptors on the p side and the positively charged donors on the n side. Due to the external voltage, this built-in field is reduced, making possible further diffusion of electrons and holes toward the center of the active region, as illustrated in Fig. 2(a). When an electron and a hole have the same position along the y-axis, it is possible that they can met in the x-z plane, where they recombine and a photon can be emitted. The electron-hole recombination process reduces the number of electrons and holes in the active region. The external voltage, however, constantly provides new electrons and holes by injecting electrons into the conduction band on the n side, and by injecting holes into the valence band on the p side. These new electrons and holes migrate toward the active region where they will recombine and again emit a photon. The voltage can be regarded as a pump of electrons and holes. As mentioned previously, the recombination process can be stimulated by a photon; a photon can thereby experience gain when it propagates in the active region. However, photons in the active region can also be absorbed through a reversed process that generates a electron-hole pair in which case the photons experience loss. When the external voltage exceeds a critical value, referred to as threshold, population inversion is achieved. In this condition the injection of electrons and holes is so large that the rate of photon emission exceeds that of absorption. Figure 2(b) shows the profile for the refractive index across the junction. The index is largest in the active region. As a result, the emitted photons are confined in the active region due to the waveguide effect formed by the layers. The confinement increases the simulated emission in the active layer. When the applied voltage is larger than threshold, the lasing condition occurs and the laser emits photons through the output facet. Figure 2(c) shows the profile of the laser field during lasing.

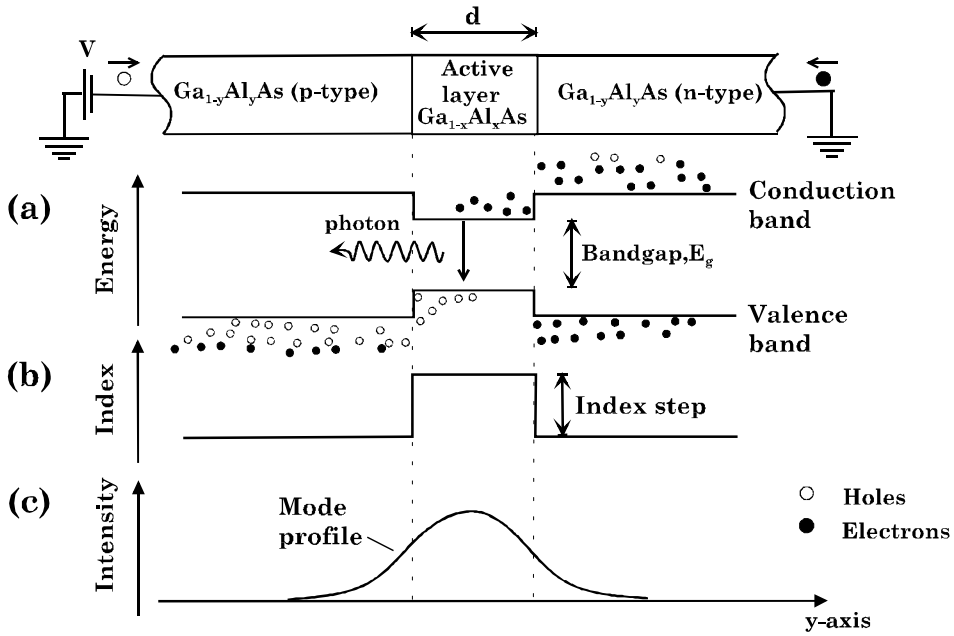

Figure 2. Schematic illustration of the simultaneous confinement of the charge carriers and the optical mode in the active region occurring in a double-heterostructure GaAlAs semiconductor laser. Forward biased; electrons are injected from the right and holes are injected from the left. (a) The bandgap is smallest in the active region. The n-type material has electrons in the conduction band, and the p-type material has holes (empty energy states for electrons) in the valence band. In the active region large concentrations of electrons in the conduction band and holes in the valence band are developed. (b) The refractice index is largest in the active region. This leads to confinement of the optical mode in a waveguide-like structure. (c) The intensity profile of the lasing mode (confined to the active layer where the gain is highest).

2.4 Structure of High-Power Semiconductor Lasers

Most commercial high-power semiconductor lasers are based on GaAlAs and the simple double heterostructure, which was discussed in Sec. 2.1. As mentioned earlier, effects such as severe catastrophic optical damage at the facet mirrors or local heating damage of the structure can occur if the power density becomes too large.[23, 24] To avoid fast degradation and achieve stable and reliable laser performance the intensity in the cavity must be limited. Therefore, fundamental-mode GaAlAs diode lasers, which typically have a cross section (x-y plane) of 1×3 μm^2, can deliver no more than approximately 200 milliwatt of optical power during CW operation.[23] The basic concept of high-power devices is that more energy can be extracted if the cross section is increased. The device structure for typical high-power GaAlAs diode lasers can be divided into three groups: (1) broad-area lasers, (2) laser diode arrays, and (3) laser diode bars.

2.4.1 Broad-Area Lasers

Figure 3 shows a schematic diagram of the epitaxial structure of a double heterostructure broad-area laser diode. The type of structure is also known as a broad-stripe laser or just stripe geometry. The width of the junction (along the x-axis) where photons can experience gain is increased by applying a wide metalliza-

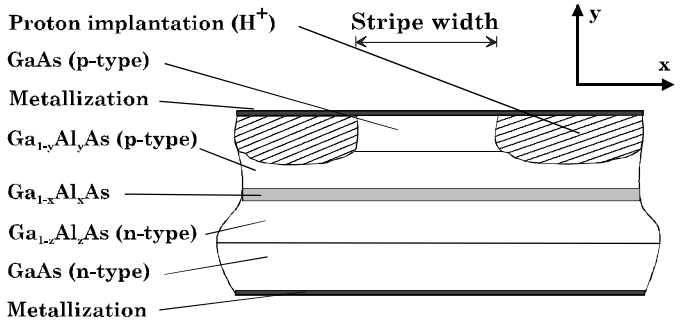

Figure 3. Cross section of the double heterostructure broad-area laser diode (stripe-geometry). This type of laser is often also referred to as broad-stripe laser. The laser is gain-guided; the migration of carriers towards the active layer predominantly takes place under the stripe.

tion contact, also known as a *stripe*, on top of the structure. The metal is applied on top of the entire structure but the effective width of the stripe is controlled by bombarding specific areas of the structure with protons (proton implantation) as shown in Fig. 3. As an alternative to proton implantation, the metallization can be applied on only a limited part of the structure in order to confine the injection of carriers.[25] In proton implanted areas the conductivity is low and the electrons and holes will predominantly migrate toward the active region near the center of structure.[25] The width of the stripe is normally in the range from 20 to 100 μm. Commercial broad-area lasers with a 50 μm wide junction can emit up til 1 watt of optical power during CW operation.

Broad-area lasers experience self-induced filamentation, which leads to the well known far-field pattern with the twin-lobe shape. Filamentation is caused by waveguiding due to a carrier-induced change in the refractive index (the antiguiding effect).[26] The self-induced filamentation causes the lateral intensity distribution of the broad-area laser to have a periodic variation. The period of this variation is on the order of 10 μm for a 100 μm wide broad-area laser, i.e. ten peaks along the junction.[27] The number of peaks and thereby also the period of the variation, for the oscillating mode depends, however, on parameters such as the drive current.[28] The cavity of the broad-area laser therefore support different spatial modes. These different modes are referred to as *filamentation solutions* or simply *broad-area modes.*[27]

2.4.2 Laser Diode Arrays

Figure 4 gives a schematic presentation of a gain-guided laser diode array. In contrary to the broad-area laser, the laser diode array has a periodic gain perturbation in the lateral direction; the schematic gain profile is shown in the lower part of the figure. This gain profile is used to avoid the self-induced filamentation and, thereby, to control the spatial modes of the laser by prescribing the lateral position of the filaments (intensity peaks of the spatial mode). For the laser diode array the gain perturbation has been introduced by applying a number of stripes next to each other. In-between the stripes, proton implantation enhances the separation of the current flow from each stripe. With the implementation of the multistripe structure, as compared with the structure of the broad-area laser, a more uniform intensity distribution is achieved whereby the risk of, e.g., catastrophic optical damage to the output facet is reduced. Typically the stripes are 5 - 10 μm wide with a spatial separation similar to the width of a stripe. The width of a laser

diode array is normally in the range from 100 to 500 μm. Commercial laser diode arrays with a 100 μm wide junction have approximately ten stripes and can emit 1-2 watts of optical power during CW operation. A 500 μm wide junction can typically emit 4 watts.

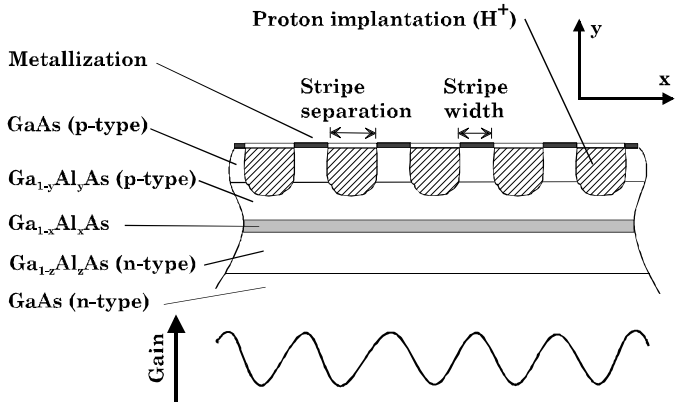

Figure 4. Schematic diagram of a gain-guided laser diode array. In the lower part of the figure the gain profile across the junction is shown.

Traditionally, the arrays have been regarded as a number of individual laser elements placed next to each other, which are coupled to the neighbor elements by evanescent coupling. Investigations, however - as will be explained in Sec. 2.5 - have shown that this coupling is too strong for such a model. Instead, the entire cross section much be considered as a single broad laser. This approach leads to different spatial modes (array modes) that the laser cavity can support.

2.4.3 Laser Diode Bars

Figure 5(a) shows a schematic diagram of the structure of a typical laser diode bar. A number of laser diode arrays or broad-area lasers are fabricated monolithically on the same chip placed next to each other. Figure 5(b) shows a typical laser bar; it contains ten laser diode arrays. The length of the bar is 1 cm and the output power is in the range of 10-20 watts for CW operation. The electrical to optical conversion efficiency for high-power lasers is approximately 50%,which means that a large amount of heat is dissipated in the material of the laser structure itself. In order to avoid thermal effects that will eventually cause failure, this heat must be removed. A laser diode bar is a configuration that allows efficient heat removal, since there is direct access to the surface of all the arrays of the laser bar. The widths of the individual arrays are typically 100 - 300 μm. The array separation along the bar may vary, i.e. a pair of arrays that can be placed close to each other is placed far from the next pair of arrays. In general, the array separation is on the order of the array width. The individual arrays can be regarded as incoherent sources. The radiation from a laser diode bar is therefore partly incoherent. The radiation pattern from a bar has a shape similar to the pattern from the individual arrays, i.e. the well known twin-lobe shape.

Often, the term array is used as a synonym for bar. Laser diode bars can also be stacked on top of each other. Such a configuration is referred to as a two-dimensional laser diode bar or two-dimensional stacked arrays. Due to thermal limitations such devices are often operated in a pulsed mode.

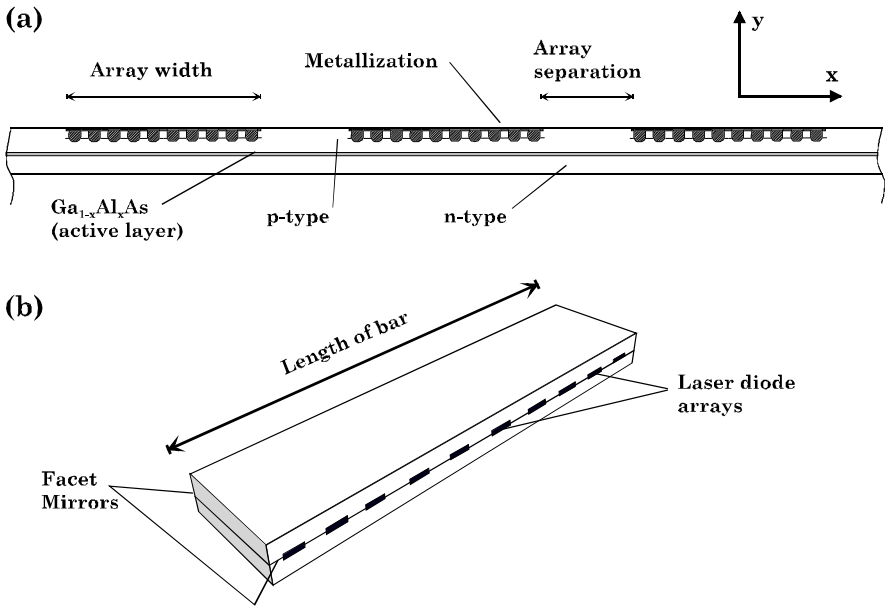

Figure 5. Laser diode bar. The bar in the figure consists of ten laser diode arrays or broad area lasers placed next to each other. (a) Cross section of laser bar, where three of the laser diode arrays are seen. (b) 3D view of the laser bar.

2.5 Emission Characteristics

Experimental investigations have over the years revealed that broad-area lasers essentially behave like laser diode arrays. Moreover, laser diode bars are typically based on a number of laser diode arrays. The emission characteristics of broad-area lasers, laser arrays and laser bars are therefore well described due to knowledge of the characteristics of a single laser diode array. In the following the spectral and spatial characteristics of a laser diode array will be discussed. Besides a presentation of some reported observations of the emission properties, a theoretical description will briefly be given for better understanding of the effects of spatial filtering in an external cavity used for mode discrimination (see Sec. 5.4).

2.5.1 Description of Transverse Modes

Laser diode arrays are index-guided in the plane perpendicular to the junction and gain-guided in the plane parallel to the junction. The waveguide structure perpendicular to the junction is designed in such a way that it can only support the fundamental mode; this is achieved using a thickness of the active layer, which is the core of the waveguide structure, of 0.1-0.2 μm. As a result, broad-area lasers, laser arrays and bars radiate in the transverse direction in a nearly Gaussian beam pattern. Such a pattern is diffraction limited and can in the transverse direction be reimaged to the dimension of the active layer. All the array modes, which will be introduced in the following section, have nearly the same Gaussian pattern in the transverse direction. In this context array mode is equivalent to spatial mode. The scalar electrical near-field of this almost Gaussian mode in the transverse direction (y-axis) is denoted $\Phi_0(y)$. The maximum radiation angle with respect to the normal of the output facet is typically 20° for a commercial laser array.

2.5.2 Description of Lateral Modes

Better understanding of the modal features of gain-guided laser arrays is of great interest, because it gives useful information about how to achieve single-lobe emission from such devices. There are mainly two descriptions of the lateral modes of laser diode arrays, the *supermode theory* and the *perturbed broad-area* model. The term array mode is used as synonym for lateral mode.

Supermode theory The supermode theory [29, 30] was the first theory that could explain some aspects of the array modal behavior. In this theory, the array modes are expressed in terms of linear combinations of individual modes from each waveguide corresponding to one laser element of the array. Each waveguide is coupled to its neighbors via evanescent coupling. By assuming that all N laser elements of an array support the same single spatial mode, it was shown that the coupling between N stripes gives rise to N lateral array modes, which originally was called supermodes (lateral modes).[30] The N modes are labelled with a mode number m ($m = 1 \cdots 10$ for N = 10). The fundamental mode ($m = 1$), where all the N elements are in-phase, has a single-lobe far-field pattern. All the other modes ($m > 1$) are referred to as *higher-order* modes. The supermode theory predicts that all higher-order modes are associated with a characteristic twin-lobe far-field. The existence of such multiple lateral modes has been confirmed experimentally.[31] Later experimental investigations[32, 33] have, however, revealed the existence of mode orders superior to N, i.e. $m >$ N for an N stripe laser, that cannot be explained by the supermode theory. For gain-guided laser diode arrays the perturbed broad-area model has proven to be superior to the supermode theory in describing the modal behavior. However, for index-guided arrays, where the coupling between the laser elements is small, the supermode theory may be applied.[34]

The perturbed broad-area model The original work [35] of the perturbed broad-area model included the periodic gain and index gratings formed by the current stripes (and the temperature variation across the junction). The model showed excellent agreement with experiments. The model is closely related to a similar model that has been reported.[32, 36] Later, the model was extended [37] and it was shown that the gain of the array medium also leads to a broadening of the far-field lobes. Below the original work is outlined.

For a gain-guided array, the stripes induce two perturbations in the effective index profile: (1) a periodic modulation of the gain, and (2) a periodic modulation of the real refractive index due to the carrier induced index change through the antiguiding effect. The coupling relation between (1) and (2) is given by Eq. 1. These effects are accounted for by introducing a sinusoidal perturbation in the local complex index ($\Delta\widetilde{n}$). Using Eqs. 1 and 2 the following expression for the change in the local complex index is obtained for an N stripe laser array

$$\Delta\widetilde{n}\,(x) = (-1)^N \frac{\Delta g}{2k_0}\,(\beta_c + i)\cos\left(\frac{\pi N x}{x_0}\right). \tag{5}$$

The factor $(-1)^N$ is necessary to obtain minimum gain at the center of the array for even values of stripes and maximum gain for odd values. Equation 5 is a gain and index grating with the grating vector parallel to the x-axis. The presence of such a grating has been experimentally verified by investigations of a traveling-wave amplifier.[38] An additional perturbation arising from the temperature variation across the junction can be added to Eq. 5; however, here this part is skipped. The scalar electrical near-field of a perturbed array mode is denoted $\Phi_m\,(x)$ where m is the mode index. In order to obtain the array modes the wave equation must be solved after the index change $\Delta\widetilde{n}\,(x)$ has been included. The presentation of this

solution, however, is beyond the scope of the present thesis but can be found in Refs. [35, 37]. Instead, some important results of the analysis are presented.

Far-Field Pattern from an Array Some of the characteristics of the far-field pattern of an array can be illustrated with the solution for the *unperturbed* problem. This problem is modeled similar to an eigenvalue problem of an infinite square-well potential. Inside the well, a uniform refractive index and gain is assumed. i.e. $\Delta\widetilde{n}\,(x) = 0$.[37] The solution to the unperturbed problem is referred to as the *unperturbed array modes*. The scalar electrical near-field distribution of the unperturbed array modes are denoted $\Psi_m\,(x)$ - where m is the mode index - and is given by [35]

$$\Psi_m\,(x) = \frac{1}{\sqrt{x_0}} \sin\left(\frac{m\pi x}{2x_0} + \frac{m\pi}{2}\right) rect\left(\frac{x}{x_0}\right), \tag{6}$$

where x_0 is the half-width of the laser array and the function $rect\,(x/x_0)$ has the value unity for $|x| < x_0$ and zero everywhere else. The far-field of the unperturbed array modes may be obtained as the Fourier transform of the near-field given by Eq. 6, and is found to be [37]

$$\begin{aligned} FT\left\{\Psi_m\,(x)\right\} \;=\; & \frac{\sqrt{x_0}}{2\pi}\left[\exp\left(i\frac{(m-1)\,\pi}{2}\right) Sinc\left(\frac{m\pi}{2} - k_0 x_0\theta\right) + \right. \\ & \left. + \exp\left(i\frac{-(m-1)\,\pi}{2}\right) Sinc\left(\frac{m\pi}{2} + k_0 x_0\theta\right)\right], \end{aligned} \tag{7}$$

where θ is the radiation angle with respect to the normal of the output facet, i.e. the z-axis. Even though unperturbed array modes are not the correct solution to the perturbed problem, they still provide very good understanding of the radiation properties and the way the array modes are spatially separated in the far-field. Figure 6 shows the far-field pattern for three different array modes. The graphs are obtained as $\left|FT\left\{\Psi_m\,(x)\right\}\right|^2$, which is equivalent to the intensity, for a N = 10 stripe array that is 100 μm wide and is lasing at 800 nm. Figure 6(a) shows the fundamental array mode (m = 1). This mode has a single lobe and was originally referred to as the *in-phase* mode.[29] Figures 6(b) and (c) show the far-field pattern for m = 10 and m = 18, respectively. Both array modes are higher order and have the characteristic and rather well known *twin-lobe* shape. It is seen that the two lobes of an array mode are radiated symmetrically with respect to zero angle.

The radiation angles for the peak intensity of the two lobes are given by [37]

$$\theta_m = \pm\frac{m\pi}{2k_0 x_0} = \pm\frac{m\lambda}{4x_0}, \tag{8}$$

where m again is the mode index. The plus sign refers to the *positive* lobe and the minus sign refers to the *negative* lobe. As can be seen from this expression, and also from Figs. 6(b) and (c), the lobes of different array modes are radiated at different angles. This fact makes it possible to introduce array mode discrimination by spatial filtering in an external cavity (will be discussed in Sec. 5.4).

For comparison Fig. 7 shows a number of far-field patterns and near-field distributions corresponding to different array modes. The data have been obtained experimentally with a 10 stripe array (after Ref. [33]). As can be seen in the figure, the highest order modes radiate their lobes at the largest angles, as expected from Eq. 8. Furthermore, it is seen that near-field distribution has a number of peaks that correspond to the mode index number m.

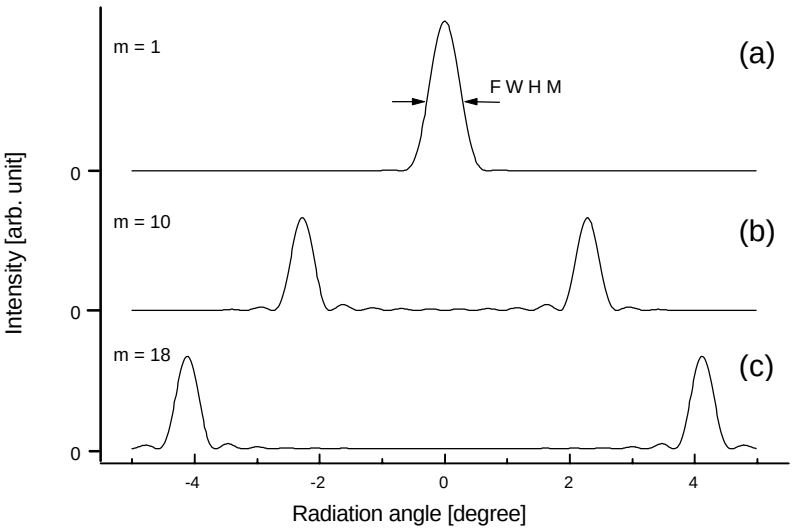

Figure 6. Theoretical far-field patterns (Eq. 7) from an N = 10 stripe laser diode array. The width of the array is 100 μm (x_0 = 50 μm). The wavelength is λ = 800 nm. (a) The fundamental mode, m = 1, which is single-lobed. The definition of diffraction-limited *is based on the FWHM of this single lobe as indicated by the arrows. (b) The mode with the highest gain, m = 10. (c) A higher order mode, m = 18.*

Definition of 'Diffraction-Limited' The full width at half-maximum (FWHM) of the fundamental array mode m = 1 (intensity profile), as shown in Fig. 6(a), is equal to [37]

$$\theta_{diff} = \frac{1.189\lambda}{2x_0}. \tag{9}$$

Traditionally, this has been the definition of the *diffraction limit* for a laser array or a broad-area laser. This definition will also be used in the present thesis. For a 100 μm wide array at 800 nm wavelength, the diffraction limit is θ_{diff} = 0.55°. If the radiation from the array is less than the limit given by Eq. 9, the radiation is said to be *diffraction-limited.*

Modal Gain of Array Modes The different array modes experience different gains. Figure 8 shows the modal gain for the first 20 array modes of a 10-stripe array. The array modes do have a slightly different oscillation frequencies. The oscillation frequency of a particular mode relative to the oscillation frequency for array mode $m = 1$ is referred to as a frequency shift. In Fig. 8 the corresponding frequency shift for the array modes have also been plotted. If the laser diode array is driven far above threshold, several array modes will be oscillating simultaneously. The total far-field observed from an array may therefore be more like a uniform energy distribution in the range $\theta \approx$ -3° to 3° since the different array modes radiate their lobes at different angles. The m = 10 array mode has the highest gain (as also reported in Ref. [36]). At threshold this array mode will dominate. The m < 10 array modes have a low gain and at a drive current above threshold, these modes are rarely present.

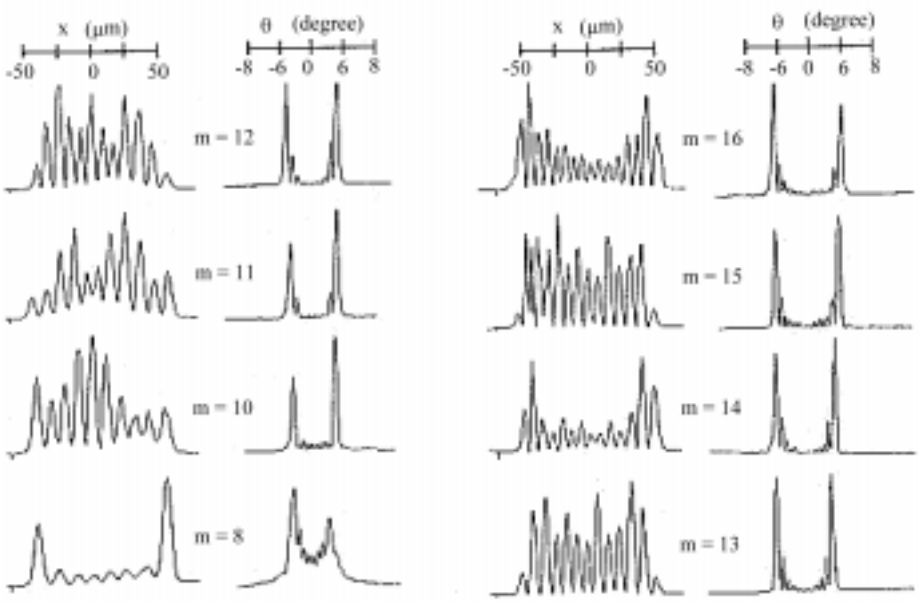

Figure 7. Far-field patterns and near-field distributions of different array modes. The data have been experimentally obtained. The array was a ten-stripe gain-guided array (model SDL-2422-H1). From Ref. [33].

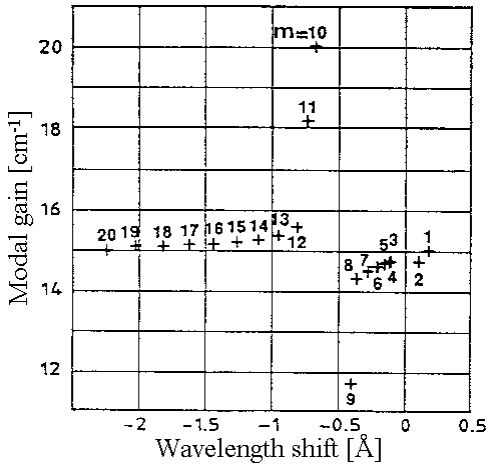

Figure 8. Plot of the modal gains of the first 20 array modes of a ten-stripe array. The gain has been plotted against the wavelength shift for each array mode. From Ref. [35].

2.5.3 High and Low Coherence Axes

Having established the characteristics of the spatial modes in the transverse and the lateral directions, the spatial modes of the laser array are fully described. To summarize, each spatial mode of the array, $\Phi_m^{array}(x,y)$, can be written as a multiplication of the transverse and the lateral dependence, i.e.

$$\Phi_m^{array}(x,y) = \Phi_m(x)\,\Phi_0(y)\,, \tag{10}$$

where the transverse dependence is taken from Sec. 2.5.1. As discussed above, there can be several array modes ($\Phi_m(x)$) oscillating simultaneously. As seen from Eq. 10, however, they all have the same transverse dependence since $\Phi_0(y)$ does not depend on the mode index m. As a consequence, the spatial coherence is much larger along the y-axis as compared with the x-axis. This leads to the definition of the *high* and the *low coherence axes* of an array, which are the y-axis and the x-axis, respectively. Previously, the term 'array mode' referred to $\Phi_m(x)$, but in the following it will be used as a reference to $\Phi_m^{array}(x,y)$. The high and the low coherence axes are often referred to as the *fast* and the *slow* axes, respectively, due to the difference between the maximum radiation angle (θ) observed along the two axes.

2.5.4 Astigmatism of the Array Emission

Owing to the different guiding mechanisms in the plane perpendicular to the junction (index-guided) and in the plane parallel to the junction (gain-guided), the emission has astigmatism. Along the y-axis the emission has its beam waist at the surface of the output facet, while along the x-axis its beam waist is located behind the output facet. For typical laser arrays the separation between the spatial positions of the two waists is 100-1000 μm (based on information from SDL Inc., San Jose, USA). This separation is known as longitudinal astigmatism.[39] A consequence of the astigmatism is that in order to reimage the junction or to collimate the radiation, an anamorphic system is needed. It cannot be done with a single conventional lens.

2.5.5 Spectral Properties of the Array Emission

Semiconductors tend to be homogeneously broadened. Nevertheless, spatial hole burning permits the simultaneous oscillation of many longitudinal modes. A laser diode array has no built-in mechanism for discrimination of longitudinal modes and, as a result, several longitudinal modes oscillate simultaneously. The bandwidth (FWHM) of a typical device is in the range 1-2 nm. As a consequence of this huge bandwidth, the coherence length is only a fraction of a millimeter. The longitudinal mode spacing $\Delta\lambda_{FP}$ is determined by the length of the Fabry Perot cavity of the array. The mode spacing is given by [40]

$$\Delta\lambda_{FP} = \frac{\lambda^2}{2n_{array}L}, \tag{11}$$

where λ is the lasing wavelength in vacuum, n_{array} is the background refractive index for the array and L is the length of the cavity. For GaAlAs the refractive index is $n_{array} \approx 3.6$, and for $\lambda = 800$ nm and $L = 0.80$ mm the mode spacing is $\Delta\lambda_{FP} = 0.11$ nm. For a bandwidth of 1-2 nm there is therefore 10 to 15 longitudinal modes that oscillate simultaneously. As is the case for, e.g., an argon ion laser - which supports the well known TEM spatial modes [41] - each longitudinal mode is a cluster of spatial modes. The cluster of resonances for each longitudinal mode originates from the different propagation constants associated with the different array modes. In other words: the different array modes all have a slightly different oscillation frequency. The wavelength shifts for the different array modes are given in Fig. 8. The spatial mode spacing $\Delta\lambda_{m,m+1}$, which is the difference between the resonant wavelength for two adjacent array modes m and $m+1$, is for typical arrays in the range 0.01-0.03 nm.[33, 40]

Figures 9(a) and (b) show a frequency-resolved near-field distribution and far-field pattern, respectively. In Fig. 9(a) one longitudinal mode is shown. This longitudinal mode is a cluster of array modes. The m = 10-17 array modes can be

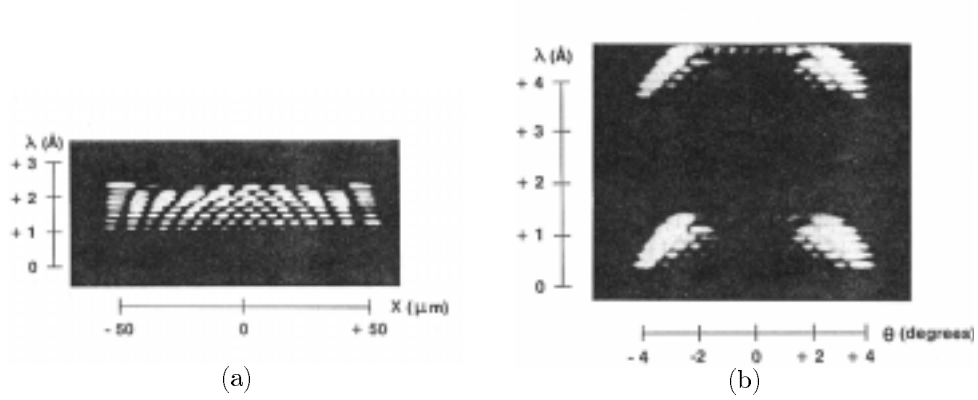

Figure 9. (a) Frequency resolved near-field of a longitudinal mode. The m = 10 - 17 array modes are oscillating. (b) Frequency resolved far-field of two consecutive longitudinal modes. Six array modes are clearly distinguishable in each mode. The angular separation between the two lobes of an array mode increases for higher mode number (smaller oscillating wavelength). From Ref. [33].

identified. The spatial mode spacing is $\Delta\lambda_{m,m+1} \approx 0.02$ nm. Figure 9(b) shows a frequency-resolved far-field pattern of two consecutive longitudinal modes. The longitudinal mode spacing is $\Delta\lambda_{FP} \approx 0.3$ nm. The angular separation between the two lobes of an array mode increases for higher mode number and the oscillating wavelength becomes shorter, which is in agreement with Figs. 6 and 8.

The line width of each array mode is typically 50-100 MHz but can be up to the GHz range depending on the power in the mode.[42]

2.5.6 Polarization State of the Array Emission

In the double heterostructure laser shown in Fig. 1, there is a waveguide confinement in the direction perpendicular to the junction, i.e. along the y-axis. As mentioned earlier, this slab-waveguide structure supports the fundamental mode only. However, there exist two fundamental modes, the TE and TM modes, that are distinguished on the basis of their polarization. For TE modes the electric field is polarized along the heterojunction plane, i.e. the polarization vector is along the x axis. For TM modes, it is the magnetic field that is polarized along the x-axis. It turns out, however, that the oscillation of the TM fundamental mode requires a thicker slab waveguide as compared with the TE mode, i.e. by choosing the correct thickness of the active layer the laser structure can be designed to support the TE fundamental mode only. As a result, most broad-area lasers, laser diode arrays and lasers diode bars are linearly polarized with the electrical field polarized along the junction, i.e. along the x-axis. The polarization ratio (x-axis compared with y-axis) of commercial broad-area lasers and laser diode arrays is typically in the range 20:1 to 30:1 or larger.

2.5.7 Emission Characteristics of Laser Diode Bars

In short, a laser diode bar has characteristics similar to the characteristics of a laser diode array, since a bar consists of separated laser diode arrays. However, both the spatial coherence and the coherence length are decreased substantially for a bar as compared with the coherence properties of an array. The reason for this is that the output of a laser bar is in general an incoherent summation of the partly coherent output of the arrays of the bar. The spectra associated with the individual arrays are slightly different owing to effects such as temperature

variation and, as a result, the summed spectrum is broader than the spectra of the individual arrays. A bandwidth on the order of 3 nm is typical. The coherence length, however, may be even shorter than expected from such a bandwidth due to the incoherent summation. The spatial coherence is also smaller as compared with the properties of a single array because of the incoherent summation. Moreover, there may be differences between the structure and size of the arrays due to manufacture processes which can lead to different modal behavior such as radiation angle for a given array mode.

3 Photorefractive Effect

The photorefractive effect has become the accepted term that is used to describe the light intensity dependent refractive index observed in many electro-optic materials. This effect was first discovered in $LiNbO_3$ at Bell Laboratories in a second harmonic generation experiment.[43] At that time the phenomenon was referred to as *optical damage* since it ruined the phase matching condition in the crystal of the pump beam and the generated second harmonic beam. The photorefractive effect has later been observed in many electro-optic materials such as $BaTiO_3$ [44, 45], $KNbO_3$ [46], $LiNbO_3$ [47], $LiTaO_3$ [43], $Sr_{1-x}Ba_xNb_2O_6$ (SBN) [48], $Bi_{12}SiO_{20}$ (BSO) [49], $Bi_{12}GeO_{20}$ (BGO) [50], CdS [51], GaAs [52], and InP [52, 53]. The photorefractive effect relies on the electro-optic effect that leads to a change in the refractive index as the illumination generates an internal electrical field.

Photorefractive crystals used as the nonlinear medium in conjunction with the generation of phase conjugation by four-wave mixing have the advantage - as compared with, e.g., stimulated Brillouin scattering - that they are sensitive even at low optical power in the milliwatt range. As a result, photorefractive crystals can be used with CW illumination from low-power sources such as semiconductor lasers. In connection with phase conjugation generated by a semiconductor laser, barium titanate ($BaTiO_3$) is often used because of its large electro-optic effect and due to the fact that through doping it can be made sensitive in the near-infrared wavelength range. This material will be described in the present chapter. If the reader is familiar with the photorefractive effect, this chapter can be skipped.

3.1 Physical Mechanisms

First we consider a simple model which is referred to as the *one center band transport model*. This model is useful for explaining many of the photorefractive phenomena observed in, for example, barium titanate. Figure 10 shows a schematic energy band diagram of the photorefractive medium. The medium contains certain types of impurities or imperfections and include donor atoms whose density is N_D (m^{-3}) and acceptor atoms N_A. The donor atoms have energy levels close to the center of the bandgap, as shown in Fig. 10(a). Since the energy of a valence electron in the acceptor atom state is lower than that of the donor, each acceptor atom has deprived a donor atom of an electron. As a result, the density of ionized donor impurities equals the density acceptor impurities in the absence of illumination. The donor atoms that have not been deprived of an electron ($= N_D - N_D^+$) are candidates for excitation and can generate free electrons by absorbing photons in the presence of illumination. By excitation an unionized donor is converted into the ionized state. At the same time the free carriers can be recaptured by an ionized donor. The excitation and recapturing processes are ongoing.

The free electrons (carriers) in the conduction band are free to move whereas the ionized donor atoms remain fixed in the crystal lattice. If the applied electromagnetic radiation throughout the medium is nonuniform, the generated carrier density will as a result become spatially varying. After the free carriers have been generated by nonuniform illumination, they can migrate due to drift and diffusion. As a result of the migration of the free carriers and due to the fact that the ionized donor atoms remain fixed in the crystal lattice, a spatially varying charge distribution is generated. This nonuniform charge distribution leads to the generation of an internal electrical space charge field. The space charge field also contributes to the drift effect during the migration of the free carriers. Finally, the generated space charge field results in a change in the refractive index because of the linear electro-optic properties of the photorefractive crystal.[54]

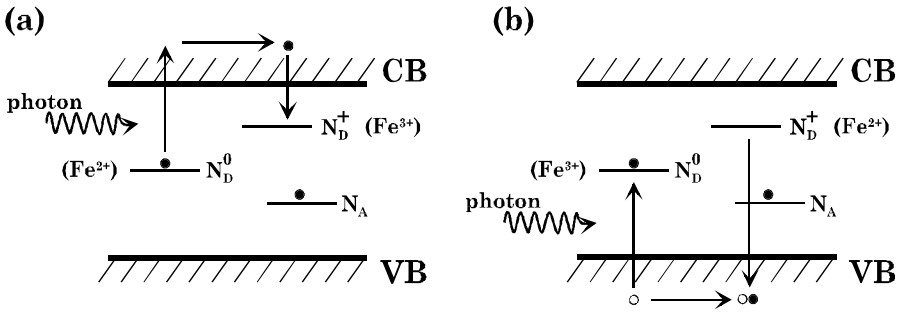

Figure 10. Model of light induced charge transport in a $BaTiO_3$ crystal. VB and CB are the valence band and conduction band, respectively. (a) the carrier is electrons. (b) the carrier is holes.

For undoped $BaTiO_3$ it is believed that the photoionization, as described in the preceding, involves the following process [55, 56]

$$Fe^{2+} + h\nu \rightarrow Fe^{3+} + e^-_{CB}, \tag{12}$$

where Fe^{2+} and Fe^{3+} are valence states of the iron atom, $h\nu$ is the energy of the interacting photon and e^-_{CB} represents an electron in the conduction band. Since the energy state of N^0_D is in the middle of the bandgap, however, electrons can also be excited from the valence band and up to N^0_D, as shown in Fig. 10(b). This can be regarded as holes that are excited into the valence band where they are free to move. The hole excitation process is for the given case described by [55]

$$Fe^{3+} + h\nu \rightarrow Fe^{2+} + h^+_{VB}, \tag{13}$$

where h^+_{VB} represents a hole in the valence band. In $BaTiO_3$ the hole excitation process is often dominating which explains the relatively slow response time of $BaTiO_3$ (on the order of one second) since the migration speed for holes is slow compared with the migration speed of electrons.[55] The electron excitation process can become dominating by giving the crystal a reduction treatment (the crystal is placed in a reduced atmosphere pressure of oxygen).[57] If both types of excitation processes take place simultaneously, the induced change in the refractive index can be reduced due to hole-electron competition.[58, 59] In addition to the donors and acceptors, some secondary center may be present in the crystal.[60] Experiments have shown that these secondary centers can cause the photoconductivity to be proportional to I^x, where I is the intensity and x is an exponent. The exponent ranges from 0.5 to 1.0 (if the secondary centers are not present x equals 1.0).[61]

3.2 Barium Titanate - Properties

The particular advantage of $BaTiO_3$ for photorefractive applications is the very large value of the elements in the linear electro-optic tensor, which in turn leads to a large grating efficiency in two-wave mixing (amplification) and four-wave mixing (phase conjugation). A large grating efficiency in four-wave mixing reflectivity is particularly desirable in phase conjugate resonator applications.

$BaTiO_3$ has a Curie temperature around $T_c \simeq$ 120-130 °C.[63] Above this temperature it has a cubic structure with Ba^{2+} ions at the cube corners, O^{2-} ions at the face centers and a Ti^{4+} ion at the body center, as shown in Fig. 11(a). At room temperature $BaTiO_3$ transforms into a tetragonal ferroelectric phase with

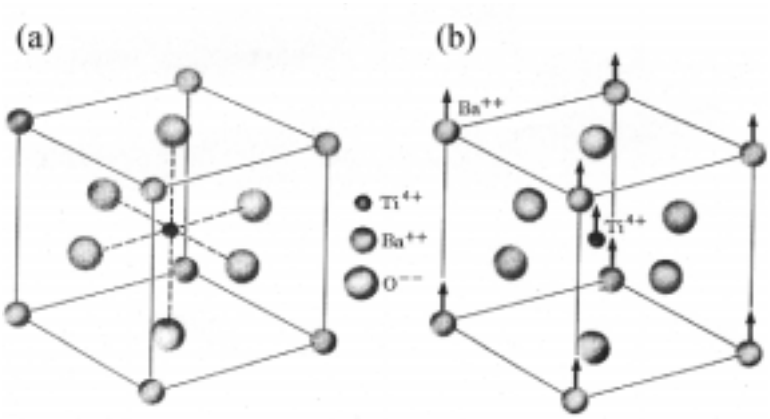

Figure 11. The crystal structure of barium titanate. (a) The structure is cubic, with Ba^{2+} ions at the cube corners, O^{2-} ions at the face centers, and a Ti^{4+} ion at the body center. (b) Below the Curie temperature the structure is slightly deformed, with Ba^{2+} and Ti^{4+} ions displaced relative to the O^{2-} ions, thereby developing a dipole moment. From Ref. [62].

a point group 4mm symmetry. The origin of the permanent dipole moment (ferroelectric phase) is owed to a shift of the Ba^{2+} ions and Ti^{4+} ions with respect to the O^{2-} ions, as shown in Fig. 11(b). This shift produces a spontaneous polarization (c-axis) in the direction of motion. The polar nature leads to a variety of properties, including the piezoelectric effect, the pyroelectric effect and the linear electro-optic effect. In the tetragonal phase the spontaneous polarization of each molecule may be oriented along any of the six pseudocubic directions of the crystal. This means that "as grown crystals" have domains in which the polarization may be different from each other.[64] A crystal, however, is made homogeneous by heating it to well above T_c and placing it in a DC electric field, a procedure known as poling.[63] The crystal is then cooled to room temperature. $BaTiO_3$ also has a phase transition at $T \simeq 6$ °C at which the structure becomes orthorhombic and the crystal loses its spontaneous polarization and photorefractive properties.[65] If the crystal passes through any of the transitions at 6 °C or 120 °C, it must be repoled before it can be used for wave mixing again. A $BaTiO_3$ can therefore be operated safely in the range of 12 °C to 110 °C. The lower limit is in general not a problem since experiments are often performed at room temperature. The high temperature limit may be a problem with high-power lasers since the absorption in the crystal can be large and may lead to significant heating. Another problem with operating a crystal at high temperature is the potential risk of cracking the crystal if the temperature drops too fast, e.g. if the high-power beams are suddenly turned off.

In summary, $BaTiO_3$ is optically uniaxial at room temperature. The optical axis is referred to the c-axis and indicates the direction of the spontaneous polarization. The two other axes are identical and are denoted a-axes. The refractive index depends on the polarization of the electromagnetic radiation. The refractive indices are $n_a = 2.41$ and $n_c = 2.36$ (at 633 nm wavelength) for radiation polarized along the crystallographic a-axis and c-axis, respectively.[66] The values, however, vary from crystal to crystal. A data sheet of the properties of $BaTiO_3$ can be found in Appendix C.

3.2.1 Rhodium Doped Barium Titanate

The energy level of the iron atoms - which are active in the photoionization process - in an undoped $BaTiO_3$ crystal is approximately 2.4 eV above the valence band. This means that the crystal has its highest photorefractive response in the green part of the visible spectrum. In order to extend the response range towards longer wavelengths a dopant that requires lower excitation energy is needed. In order to increase the sensitivity, $BaTiO_3$ has over time been investigated with may different dopants.[67] $BaTiO_3$ doped with cobalt has demonstrated increased response characteristics in the near-infrared range.[68] Another dopant that has received a vast amount of interest is rhodium. Rhodium incorporated into $BaTiO_3$ has a peak absorption at 640 nm but has a tail that extends into the near-infrared range.[69] This makes Rh:$BaTiO_3$ sensitive to illumination from AlGaAs laser diodes which have wavelengths around 750-880 nm.

Figure 12 shows the absorption coefficient as a function of the wavelength for three rhodium doped $BaTiO_3$ crystals that contain different concentrations. For comparison the absorption spectrum for an undoped crystal has also been plotted. For high rhodium concentrations the absorption extends beyond one μm. Several successful experiments using 1.064 μm have been reported.[70, 71]

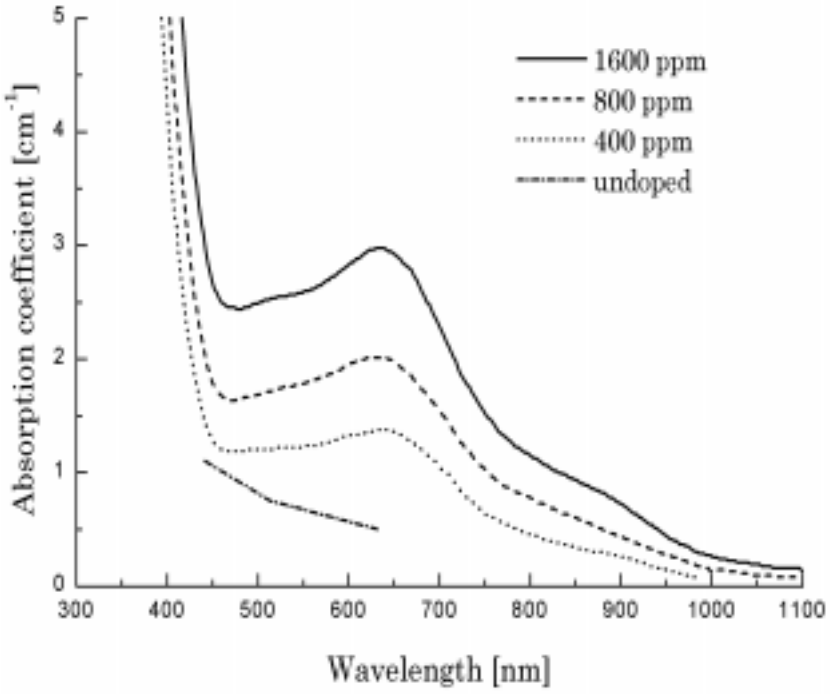

Figure 12. Optical absorption spectra of one undoped and three rhodium doped $BaTiO_3$ crystals. The light was polarized parallel to the c-axis. The numbers indicate the concentration of rhodium in the melts during growth. From Refs.[69, 55].

Valence state of rhodium Photo-EPR measurements have revealed that the photoconductivity may involve ionization of a hole according to the following

process

$$Rh^{4+} + h\nu \rightarrow Rh^{3+} + h^{+}_{VB}, \tag{14}$$

which has an ionization level of ~0.9-1.1 eV (1 μm) above the valence band maximum of $BaTiO_3$.[69, 72] The excitation of electrons into the conduction band would require at least 2 eV (the bandgap is 3.1 eV (400 nm) for $BaTiO_3$) and, therefore, the Rh^{3+}/Rh^{4+} electron ionization is probably not important during infrared illumination. However, at visible wavelengths, i.e. $h\nu > 2$ eV (620 nm), the process associated with electron photoconductivity may not be neglected. In Rh:$BaTiO_3$ a dopant Rh^{4+} ion is substituted for a Ti^{4+} ion in the center of the unit cell. Recent spectroscopic determinations of the levels involved at 1.06 μm illumination also identified the Rh^{4+}/Rh^{5+} valence states as in the following ionization process [73, 72, 74]

$$Rh^{5+} + h\nu \rightarrow Rh^{4+} + h^{+}_{VB}. \tag{15}$$

This process has an ionization level of 0.7 eV (~1.8 μm) above the valence band and may, indeed, be the origin of the photorefractive effect at long wavelength (> 1 μm).[73]

3.3 Band Transport Model

The dynamic charge distribution in many photorefractive media can be described by the well known one center band transport model.[75] More sophisticated models, which, e.g., take into account more centers, have been described in the literature.[76, 77] For rhodium doped crystals a three-charge-state model (Rh^{3+}, Rh^{4+}, Rh^{5+}) has been proposed [77] and experimentally verified.[74] However, it has been demonstrated that a rhodium doped $BaTiO_3$ crystal is well described by the one center band transport model as soon the incident intensity is large enough.[70] The one center model will therefore be presented in the following.

The one center model is based on the following four coupled differential equations [78]

$$\frac{\partial}{\partial t} N_D^+(\mathbf{r},t) = (\beta_t + sI(\mathbf{r},t)) \left(N_D - N_D^+(\mathbf{r},t)\right) - \gamma_r n_e(\mathbf{r},t) N_D^+(\mathbf{r},t), \tag{16}$$

$$\frac{\partial}{\partial t} n_e(\mathbf{r},t) = \frac{\partial}{\partial t} N_D^+(\mathbf{r},t) + \frac{1}{e} \overline{\nabla} \cdot \overline{J}(\mathbf{r},t), \tag{17}$$

$$\overline{J}(\mathbf{r},t) = e\mu n_e(\mathbf{r},t) \overline{\mathrm{E}}_s(\mathbf{r},t) + k_B T \mu \overline{\nabla} n_e(\mathbf{r},t) + \overline{J}_{pv}(\mathbf{r},t), \tag{18}$$

$$\overline{\nabla} \cdot \left(\overleftrightarrow{\epsilon} \cdot \overline{\mathrm{E}}_s(\mathbf{r},t) \right) = \rho(\mathbf{r}) = e \left(N_D^+(\mathbf{r},t) - N_A - n_e(\mathbf{r},t) \right), \tag{19}$$

where n_e is the carrier density, $\overline{\mathrm{E}}_s$ is the internal electric field created by the charge imbalance (and by the external electric field, if such is applied), N_D is the density of donors, N_D^+ is the density of ionized donors, N_A is the density of acceptors, e is the electron charge, s is the cross section of the photoionization, β_t is the rate of thermal generation of carriers, γ_r is the recombination constant, μ is the carrier mobility, k_B is Boltzmann's constant, T is the absolute temperature, $\overleftrightarrow{\epsilon}$ is the low frequency (static) dielectric tensor, t is the time, I is the intensity of the electromagnetic radiation and $\overline{J}_{pv}$ is the photovoltaic current. Furthermore, $\overline{\nabla}\cdot$ and $\overline{\nabla}$ are the divergence and gradient operators. In general, N_D^+, n_e and $\overline{\mathbf{E}}_s$, which are all functions of space and time, are the unknowns to be found for known illumination I. A numerical solution of the band transport model will be given in Chapter 7.

3.3.1 The linear electro-optic effect

The linear electro-optic (or Pockels) effect is present in $BaTiO_3$. This effect is the change in refractive index of the material caused by an applied electric field. The effect is referred to as linear since the index change is proportional to the magnitude of the applied electric field. The effect is local; the index change at one position is proportional to the electric field, i.e. the induced space charge field, at this same position.

In the following it will be determined how large an index change an induced space charge field will generate, and how electromagnetic radiation will respond to this change. The propagation of electromagnetic radiation in crystals can be described by the wave equation and the relative dielectric tensor $\overleftrightarrow{\varepsilon_r} \equiv (\overleftrightarrow{\eta})^{-1}$, where $\overleftrightarrow{\eta}$ is the impermeability tensor. The dielectric constant tensor is $\overleftrightarrow{\varepsilon} = \varepsilon_0 \overleftrightarrow{\varepsilon_r}$, where ε_0 is the vacuum permittivity. Often it is more convenient to describe the electro-optic effect as a change in the impermeability tensor rather than as a change in the dielectric tensor; thus [78]

$$\Delta \overleftrightarrow{\eta} \equiv \Delta \left(\frac{\overleftrightarrow{1}}{n^2} \right) = \Delta \left(\overleftrightarrow{\varepsilon_r} \right)^{-1} = \overleftrightarrow{\mathrm{r}} \cdot \overline{\mathrm{E}}, \tag{20}$$

where $\overline{\mathrm{E}}$ is the electric field present in the crystal (e.g. the space charge field), n is the refractive index associated with the polarization state of the electromagnetic wave and $\overleftrightarrow{\mathrm{r}}$ is the linear electro-optic tensor, which is of rank 3. Equation 20 can also be written in the following form

$$\Delta \eta_{ij} = \sum_k \mathrm{r}_{ijk} \mathrm{E}_k, \tag{21}$$

where $\Delta\eta_{ij}$ is the ij'th component of $\Delta \overleftrightarrow{\eta}$, r_{ijk} is the ijk'th component of $\overleftrightarrow{\mathrm{r}}$ and E_k is the k'th element of the electric vector field. It has been shown that an arbitrary electric field E(r) generates a refractive index change given by [79, 80]

$$\Delta n\,(\mathrm{r}) = -\frac{1}{2} n^3 r_{eff}\, \mathrm{E}\,(\mathrm{r})\,, \tag{22}$$

where r_{eff} is the effective electro-optic coefficient and n is the refractive index associated with the polarization state of the propagating radiation. The effective electro-optic coefficient r_{eff} is a function of the crystal orientation and the polarization state. A large index modulation in a $BaTiO_3$ crystal is achieved if the polarization of the incident beam is linearly polarized with the polarization in the c-k plane ($\overline{k}$ is the direction of propagation). This is known as extraordinary polarization and gives access to the large electro-optic coefficient r_{42} in the $BaTiO_3$ crystal. For the special case of two-wave mixing with extraordinary polarization and propagation in the a-c plane, the r_{eff} is given by the following expression [81, 82]

$$\begin{aligned} r_{eff} \;=\; & \frac{1}{2} \left[n_a^4 r_{13} \left(\cos\left(2\theta_{twm}\right) - \cos\left(2\beta\right) \right) + 4 n_a^2 n_c^2 r_{42} \sin^2\left(\beta\right) + \right. \\ & \left. n_c^4 r_{33} \left(\cos\left(2\beta\right) + \cos\left(2\theta_{twm}\right) \right) \right] \cos\left(\beta\right), \end{aligned}$$

where β is the angle between the c-axis and the grating vector $\overline{K}_g$, θ_{twm} is the half angle between the two interfering waves, and the elements of the linear electro-optic tensor are given in contracted notation (see Appendix C). For $\beta = 45^\circ$ and $\theta_{twm} = 12^\circ$ we obtain $r_{eff} = 3{\cdot}10^{-8}$ m/V (for parameters, see Appendix C). The magnitude of the space charge field in $BaTiO_3$ is on the order of 10 kV/m [78, 80], which according to Eq. 22 yields a maximum refractive index change on the order of $\Delta n \approx 2{\cdot}10^{-3}$.

3.3.2 The low frequency dielectric tensor

There are two different electric fields in the photorefractive medium: (1) the electric field corresponding to the electromagnetic radiation, and (2) the induced space charge field. The electric field of the illumination has an extremely high frequency (10^{15} Hz), while the electric space charge field varies with a very low frequency or may even be static. A given charge distribution will generate a space charge field according to the low frequency dielectric tensor, denoted $\overleftrightarrow{\epsilon}$. This tensor is often referred to as the *low frequency* or the *static* dielectric tensor to emphasize the difference from the high frequency dielectric tensor $\overleftrightarrow{\varepsilon}$. Consider a space charge field in the a-c plane, i.e. the grating vector $\overline{K}_g$ is also in the a-c plane. The effective dielectric constant ϵ_{eff} depends on the orientation of the grating vector $\overline{K}_g$ with respect to the c-axis and is thus given by [54]

$$\epsilon_{eff} = \widehat{K}_g \cdot \overleftrightarrow{\epsilon} \cdot \widehat{K}_g = \varepsilon_0(\epsilon_a \sin(\beta) + \epsilon_c \cos(\beta)), \tag{23}$$

where $\widehat{K}_g$ is a unit vector along $\overline{K}_g$, and ϵ_a and ϵ_c are the tensor elements corresponding to the dielectric constant along the a-axis and c-axis, respectively. The effective dielectric constant varies between the value of ϵ_c ($= 129 \cdot \varepsilon_0$ [65]) and the value of ϵ_a ($= 4380 \cdot \varepsilon_0$ [65]).

4 Optical Phase Conjugation

The concept of *phase conjugate light* was for the first time precisely described by the Russian Zel'dovich and his colleagues in the early seventies.[83] They discovered an interesting phenomenon (the distortion correction theorem) that occurred in their work with stimulated Brillouin scattering in a CS_2 filled waveguide. They placed a beam distorting element in front of the CS_2 waveguide and observed that, after returning back through the distorting element, the backscattered light had the same undistorted spatial beam profile as the original beam. The CS_2 filled waveguide was a phase conjugate mirror. Figures 13(a) and (b) show reflection of light in a conventional mirror and the concept of phase conjugate backreflection from a phase conjugate mirror (PCM), respectively. The conventional mirror will reflect the light in a direction which is opposite to the angle of incident, as seen in Fig. 13(a). Moreover, after reflection the beam maintains a distorted wavefront, which originates from passing through the distorting medium. For the phase conjugate mirror, however, the light is backreflected towards the light source. The reflected wavefront is identical to the wavefront of the incident beam, as indicated by the dashed lines in Fig. 13(b). Since the wavefronts are identical, the phenomenon of phase conjugation is often referred to as *'time' reversal*; the only difference between the incident and the reflected beams is that they propagate in opposite directions. The backreflected light is referred to as the *phase conjugate light*. As the phase conjugate beam passes the distorting medium on its way back to the light source, its wavefront will be corrected for phase distortions. As a result of the phase correction, the beam will return to its source and, by the time it reaches the source, it will have the same wavefront as when it was emitted from the light source. This phenomenon makes phase conjugation suitable for phase locking of, e.g., laser diode arrays. Phase correction in laser resonators, such as high-energy solid state lasers, is one of the applications of phase conjugate light generated by stimulated Brillouin backscattering that over the years has received a vast amount of attention.[84]

In 1977 four-wave mixing was proposed by Hellwarth as a technique for generation of phase-conjugate light.[85] In this technique two pump waves with the same frequency ω are injected from opposite directions through a medium with a third-order optical nonlinearity (Kerr effect). A third beam (probe) with frequency ω is also directed towards the medium and, as a result of the nonlinear interaction, the phase conjugate beam (signal) corresponding to this beam is generated. Almost at the same time back in 1977 Yariv and Pepper also proposed the four-wave mixing configuration and introduced an analysis of phase conjugate light by coupled-mode theory, which has been the basis for a great deal of the work in the years to follow.[86]

Photorefractive media such as $B_{12}SiO_{20}$ (BSO), $BaTiO_3$ and $Sr_{1-x}Ba_xNb_2O_6$ have Kerr-like behavior (in the sense that an interference pattern can generate a refractive grating) and are suitable for the generation of phase conjugate light. The first demonstration of phase conjugate light from a photorefractive medium generated by four-wave mixing was in 1979 where a BSO crystal was used.[87] Phase conjugate light generation via a self-excitation arrangement with a $BaTiO_3$ crystal was reported in 1982.[88] This scheme did not require two external pump beams for the four-wave mixing process but was self-pumped, i.e. the pump energy for the process was provided by the probe beam itself. The idea was extended by Feinberg who demonstrated self-pumped four-wave mixing in $BaTiO_3$ using total internal reflection upon the crystal surfaces; the proof of the generation of a true phase-conjugate beam with this configuration was done with an image of Feinberg's cat, and the configuration has ever since been referred to as the *Cat*

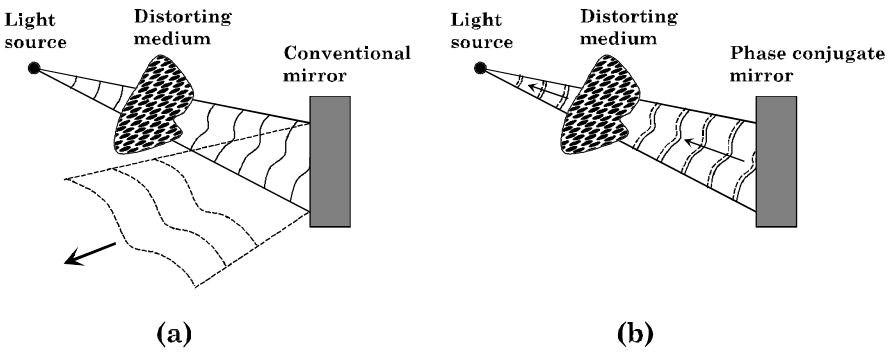

Figure 13. (a) Reflection of light in a conventional mirror. The solid lines indicate the wavefront before incidence. The dashed lins indicate wavefront after reflection.(b) Reflection of light by a phase conjugate mirror. The phase conjugate beam propagates directly back to the light source.

configuration.[81]

The concept of phase conjugation and its generation by four-wave mixing in photorefractive media are described in more details in Sec. 4.2.

4.1 Phase Conjugation - Analogy to Holography

Phase conjugate light can be generated by four-wave mixing in a nonlinear medium that yield an refractive index change due to illumination. A photorefractive barium titanate crystal is such a medium. In this section the basic concept of the generation of phase conjugation by four-wave mixing is described.

There is a fundamental relationship between conventional holography and the four-wave phase conjugation process. To demonstrate this analogy, consider the conventional holographic procedure illustrated in Figs. 14(a) and (b). Holography is divided into a recording step, as shown in Fig. 14(a), and a reconstruction step, as shown in Fig. 14(b). In the recording step an object beam E_o and a reference beam E_w (write wave) simultaneously illuminate a hologram plate, and the interference pattern is recorded. The transmittance (T) of the hologram can simply be described by

$$T \propto |E_o + E_w|^2 = |E_o|^2 + |E_w|^2 + E_o E_w^* + E_o^* E_w, \tag{24}$$

where the field amplitudes - $E_o(x,y)$ and $E_w(x,y)$- are taken in the plane coincident with the hologram ($z = 0$). In the reconstruction step the hologram is illuminated by a single reference beam (read wave) impinging from the right in a direction opposite to that of E_w, as shown in Fig. 14(b), that $E_r = E_w^*$. The reconstructed field E_c (image) - which is generated by diffraction in the hologram - to left of the thin hologram is given by

$$\begin{aligned} E_c &= TE_r \propto \left(|E_o|^2 + |E_w|^2 + E_o E_w^* + E_o^* E_w\right) E_w^* = \\ &\left(|E_o|^2 + |E_w|^2\right) E_w^* + \left(E_w^*\right)^2 E_o + |E_w|^2 E_o^*. \end{aligned} \tag{25}$$

The first term on the right-hand side of Eq. 25 is a directly transmitted part of E_r ($= E_w^*$) and is of no interest in this discussion. For a thin hologram the second term corresponds to the first-order diffraction of the E_r ($= E_w^*$) in the holography grating written by E_o and E_w. The propagation direction of this diffraction is towards the left but not opposite to E_o. If the hologram was thick the phase

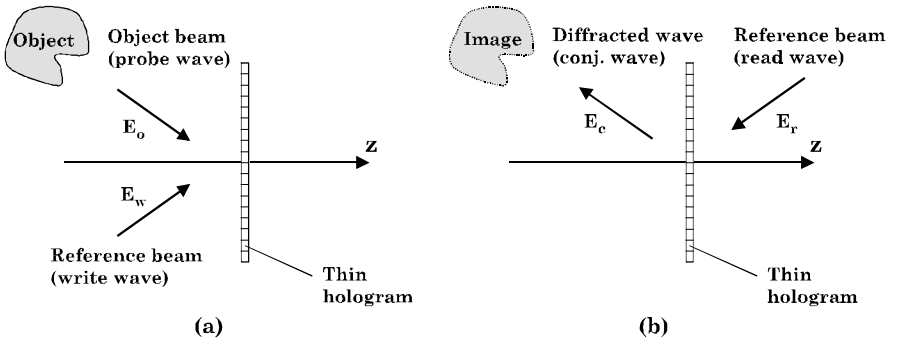

Figure 14. Object recording and reconstruction in holography. The reference waves E_w and E_r counterpropagate. (a) Recording step. (b) Reconstruction step.

factor $\exp[-i\,(2k_w - k_o)\cdot\mathbf{r}]$ of the second term, where i is the imaginary unit, $\mathbf{r}$ is the spatial coordinate, and k_w and k_o are the wave vectors of the writing wave and the read wave, respectively, would lead to no radiation, since radiation for thick holograms requires phase matching, i.e. $2k_w - k_o = 0$. The third term, however, is the one of interest here

$$E_c \propto |E_w|^2 E_o^* = |E_w E_r|\, E_o^*, \tag{26}$$

which shows that E_c is proportional to E_o^* and, thus, at $z < 0$ E_c corresponds to the phase conjugate replica of the original object field E_o. The conjugate wave E_c propagates in the opposite direction of E_o, since $\exp[ik_o\cdot\mathbf{r}]^* = \exp[-ik_o\cdot\mathbf{r}]$.

4.2 Four-Wave Mixing

In four-wave mixing, it is not necessary to interrupt the holographic process to develop the hologram (if the recording medium, e.g., is a photographic film), thereafter to replace it in position in the setup and, finally, to reconstruct the image of the object by illuminating it by the read wave. All of these steps occur simultaneously. The basic configuration of four-wave mixing is obtained if Figs. 14(a) and 14(b) are superimposed. The resulting figure is shown in Fig. 15(a). The gratings are produced by interference of the write beam and the probe beam. The phase conjugate beam is generated as diffraction of the read wave in this grating. The dashed arrow shown in the figure indicates the direction of the transfer of energy from the read wave to the phase conjugate wave. In this configuration the energy transfer is *through* the medium and the gratings are referred to as *transmission* gratings. The region where the interaction between the waves takes place and the gratings are formed is referred to as the *interaction* region.

Since both pump waves, i.e. one write wave and one read wave, are present at all time, another set of gratings in interaction region is also generated (shown in Fig. 15(b)). The gratings are produced by interference of the write wave and the probe wave. Note that the write wave in Fig. 15(b) was the read wave in Fig. 15(a). The energy is not transferred through the medium, as was the case for the transmission gratings, but the energy is backreflected in the direction of the phase conjugate beam and the gratings are therefore referred to as *reflection* gratings. Both types of grating are present simultaneously, but the diffraction efficiency of the two sets of gratings may vary. If the wavelengths of the probe beam and the two pump beams are the same, the process is known as degenerate four-wave mixing. If the probe beam has a slightly different wavelength than the one of the pump beams, the process is called non-degenerate four-wave mixing.

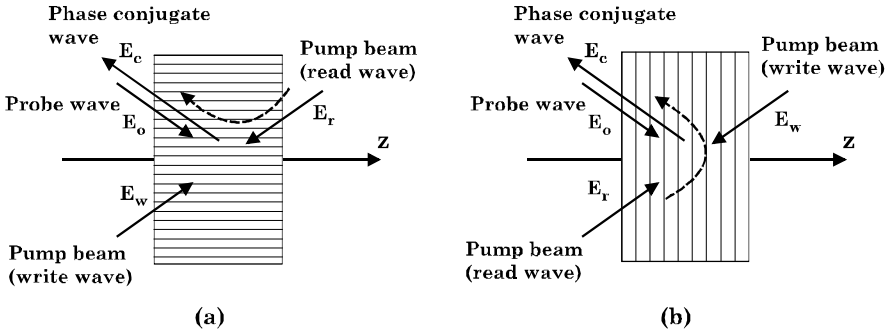

Figure 15. Four-wave mixing configuration. The dashed arrows show the direction of energy transfer to the phase conjugate wave. (a) Phase conjugate signal generated by diffraction in transmission *gratings. (b) Phase conjugate signal generated by diffraction in* reflection *gratings.*

4.3 Formation of 2k-Gratings

In many practical configurations for generation of phase conjugation, a special type of gratings, referred to as *2k-gratings*, can be excited. These gratings are reflection gratings like the ones shown in Fig. 15(b). They develop when the probe wave and the write wave counterpropagate exactly, i.e. k_o = -k_w. In that case a reflection grating with a grating wave vector of $K_g = k_o - k_w = 2k_o$ is produced. Moreover, the probe wave also reconstructs the hologram, i.e. the energy to the phase conjugate wave originates from the probe wave itself. In other words: the phase conjugate of a probe beam can be generated by counterpropagating a pump beam with respect to the probe beam. The only requirement for the pump beam is - just as it is for conventional four-wave mixing - that it must be the conjugate of the other pump beam, i.e. in this special case it must be the conjugate of the probe beam. This condition is fulfilled for the four-wave mixing configuration shown in Figs. 15(a) and (b). As can be seen in the figures, the probe beam and its phase conjugate replica counterpropagate in the nonlinear medium, which means that 2k-gratings will always be produced when a four-wave mixing geometry is used for the generation of phase conjugation. The diffraction efficiency of the 2k-gratings, however, depends on parameters such as the coherence lengths of the probe beam and the pump beams. This issue will be discussed in more details in Chapter 8.

Phase conjugation can be generated by diffraction in 2k-gratings only. This is the case for stimulated Brillouin scattering. The same applies to a photorefractive crystal: when a laser beam passes through the crystal, photon scattering occurs due to diffraction upon imperfections, defects, etc, and under the appropriate conditions the backward scattered light can become amplified. Such a amplification eventually leads to the generation of 2k-gratings and the phase conjugate replica of the incident beam is produced. This have been demonstrated in barium titanate.[89]

4.4 Polarization State of Phase Conjugate Light

So far, the discussion of the polarization state of the fields has been left out. In many situations, however, there may also exist undesirable phase shifts due to, e.g., an anisotropic distortion medium that can lead to polarization distortions. True phase conjugation, i.e. the phase conjugate beam is the complex conjugate of the incident beam, not only inverts the wave fronts of a given field, but also its polarization state. For example, the phase conjugate mirror must reflect a right-

hand circularly polarized wave into a right-hand circularly polarized wave, and vice versa. Recall that a conventional mirror reflects an incoming right-hand circularly polarized wave into a left-hand circularly polarized wave. Phase conjugation generated in, e.g., photorefractive crystals or by a stimulated Brillouin backscattering process does not in general conjugate the polarization state. The realization of polarization conjugation places constraints upon the polarization states of the beams and the orientation of the nonlinear medium.[90] Polarization-preserving phase conjugation can be obtained with a scheme where the incident light is decomposed into two orthogonally polarized components, which are then conjugated separately and, finally, the phase conjugate beam is generated by summation of the two conjugated components.[78] One configuration for which true phase conjugation can always be achieved is if the incident beam is linearly polarized, i.e. the phase conjugate beam also becomes linealy polarized. As discussed in Sec. 3.3.1, the most efficient generation of phase conjugation in photorefractive barium titanate does indeed require linearly polarized light and, thus, attention to polarization distortion of the phase conjugate light can be left out in the following.

4.5 Mutually Pumped Phase Conjugation

In self-pumped phase conjugators, a single incident laser beam is responsible for the oscillation and the subsequent generation of the phase conjugate wave. However, before this class of conjugators is discussed (see Sec. 4.6), another class of phase conjugators in which two incident laser beams mutually pump the photorefractive medium and produce phase conjugation will be introduced. This configuration is known as the double phase conjugate mirror or the mutually pumped phase conjugator. [8] A schematic illustration of the physical arrangement is shown in Fig. 16(a). Two beams illuminate a barium titanate crystal from opposite sides with wave vectors k_a and k_b, respectively. These beams are referred to as pump beams. With regard to phase locking of lasers, this is of most interest if the two waves originate from two completely isolated sources, such as it is shown in the figure. Both beams scatter in all possible directions due to imperfections or impurities in the crystal. The scattered light interferes with its corresponding pump beam and generates gratings. For certain directions this scattered light is amplified due to a phenomenon known as *fanning*, which is unique to photorefractive media. This amplification enhances the process of the grating formation. Fanning is particularly strong in crystals such as barium titanate, strontium barium niobate and lithium niobate. The origin of fanning is amplification of scattered light by energy coupling (two-wave mixing) between the scattered light and the beam from which the light scatters from.[78] Examples of the nature of fanning in barium titanate can be found in Sec. 7.2.6. At the same time the pump beams and the scattered light also erase gratings that were generated only few moments ago, etc. In the long run all the gratings will be erased with the exception of the one that is generated by k_a and its scattered wave $k_a^{'}$, and by k_b and its scattered wave $k_b^{'}$, as shown by the vector diagram in the lower part of Fig. 16(a). Only the grating that is mutual or shared will remain. An analysis of the mutually pumped phase conjugator reveals that by means of diffraction this shared grating - or more correct the shared grating structure - converts the beam from laser a into the phase conjugate of the beam emitted by laser b. At the same time the grating structure converts the beam from laser b into the phase conjugate of the beam from laser a. In other words: the photons from laser a are diffracted by the grating structure into the phase conjugate beam of laser b, and vice versa. The result is the simultaneousgeneration of two phase conjugate beams. Furthermore, if no optical isolators are placed in front of the lasers, the diffracted photon from beam a and beam b will enter the cavity of lasers a and b, respectively. Thereby

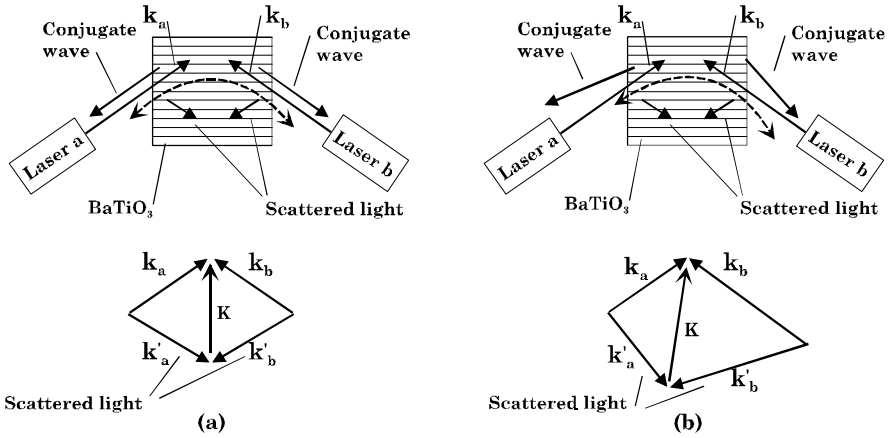

Figure 16. Mutually pumped phase conjugator. (a) $|k_a| = |k_b|$. (b) $|k_a| \neq |k_b|$.

the two lasers are phase locked to each other since they eventually share the same photons, and beams a and b become coherent. The conjugation process can be described by four-wave mixing.[91]

The conversion process is true phase conjugation if the wavelengths of the two lasers are identical, i.e. when $|k_a| = |k_b|$. However, the conversion process works even when this is not the situation, i.e. when $|k_a| \neq |k_b|$. This situation is shown in Fig. 16(b). The directions of propagation of the beams from laser a and laser b are the same as for the situation shown in Fig. 16(b). However, as a consequence of $|k_a| \neq |k_b|$, the orientation of the shared grating, K, is changed with the result that the diffracted beams k'_a and k'_b do not counterpropagate with respect to k_a and k_b, respectively. This can be seen from the vector diagram in the lower part of Fig. 16(b). If the difference between the wavelengths is sufficiently large, the diffracted photons originating from laser a will not enter laser b, and vice versa, and phase locking between the two lasers cannot be established. Experiments have shown that the wavelength difference must be less than a fraction of a nanometer in order to obtain phase locking.[16]

4.5.1 Requirements for the coherence properties

In general, there are no constraints on the coherence properties of the interacting beams. Since the two beams can originate from two different sources, there are no requirements to the mutual coherence. Neither is there any prerequisite for the coherence length of the beams. However, since the operation of the mutually pumped conjugator to some extent relies on fanning, there may be some requirements for the spatial coherence of the beams. This issue will be discussed in Sec. 4.6.4.

4.6 Self-Pumped Phase Conjugation

In self-pumped phase conjugation the energy of the two pump beams originates from the probe beam itself. Especially for photorefractive media numerous self-pumped configurations exist.[92, 93] These configurations, however, can all be regarded as active devices that return a phase conjugate replica of a beam that is sent into the device. From a practical point of view self-pumped phase conjugators are very attractive since they do not require any external pump source.

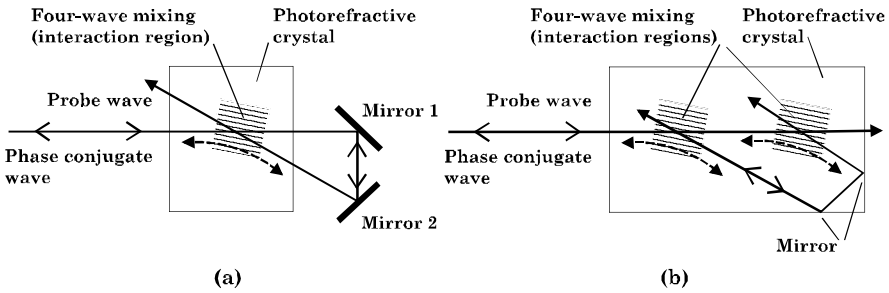

Figure 17. Schematic diagram of two self-pumped phase conjugators. The dashed arrows indicate an important direction of energy transfer for the operation of the conjugator. (a) Ring configuration: the beam is directed back to the crystal by two external mirrors. (b) In this configuration the external mirrors are replaced by total internal reflection upon the surfaces of the crystal. This configuration is known as the Cat conjugator.

4.6.1 Ring Phase Conjugator

One of the most simple self-pumped configuration is the *ring* configuration.[94] A schematic presentation of the ring configuration is given in Fig. 17(a). A fraction of the incident probe beam is transmitted through the photorefractive crystal. This fraction is redirected back into the crystal by two external mirrors and can then interfere with itself. In order for the ring configuration to start, however, there must be bidirectional propagation in the external cavity, as indicated by the arrows in the figure. The propagation in direction from mirror 2 to mirror 1 originates from scattered photons in the photorefractive crystal in the direction of mirror 2.

This scattered light is amplified due to the mechanism of fanning. The operation of all self-pumped configurations based on photorefractive media requires a sufficiently large amount of scattered light and the fanning amplification makes the operation of self-pumped conjugators possible. In Fig. 17(a) the interaction region with the four-wave mixing process is shown. The dashed arrow indicates an important direction for the energy transfer in order for the conjugator to operate.

The phase conjugate reflectivity is here defined as the ratio of the power carried by the phase conjugate beam (P_{pc}) to the power carried by the incident beam (P_{in}), i.e. $R_{pc} = P_{pc}/P_{in}$. For all self-pumped configurations the phase conjugate reflectivity is always less than unity.

Besides photorefractive media, the ring configuration has also been demontrated in a semiconductor material (InP:Fe).[95]

4.6.2 Cat Phase Conjugator

A much more compact phase conjugator is the Cat conjugator [81], which is shown in Fig. 17(b). The external mirrors have been replaced with internal reflections upon the surface of the crystal. The principle of operation of the Cat conjugator can be explained by the presence of two interaction regions inside the crystal, as shown in Fig. 17(b).[96] These two interaction regions - in which four-wave mixing takes place - are coupled with an internal beam that undergoes reflections off the crystal surfaces. The beam that reflects off the surfaces is referred to as the *internal* beam, and the path it makes is referred to as the *internal loop*. Other investigations have revealed that the four-wave mixing may not be limited to these two regions but, instead, takes place in a region that is smeared out covering a

much larger area including the area with the internal loop.[97] In addition to $BaTiO_3$, the Cat configuration has been demonstrated with SBN [98], KNSBN [99], $KNbO_3$ [100] and KTN [101].

4.6.3 Requirements for the Spectral Coherence

In connection with the operation of a Cat conjugator with the illumination from a source with limited coherence, it is of great importance to know whether the build-up of the grating structure in the crystal requires some minimum coherence. This issue with regard to the spectral coherence will be discussed below.

One could argue that the operation of the Cat conjugator requires a minimum coherence length of the incident beam since this beam must be coherent with the internal beam - which has traveled a longer way in the crystal - in order to be able to interfere and, subsequently, to produce gratings in the two interaction regions. However, the two interaction regions can be regarded as two mutually pumped phase conjugators [9], that are connected with the internal beam. If this is the case, the internal beam and the incident beam do not have to be mutually coherent in order to develop the four-wave mixing process in the two interaction regions (as explained for the mutually pumped phase conjugator). The operation of a Cat geometry in a barium titanate crystal has been demonstrated with a laser source that had a coherence length of approximately 20 μm.[102] This demonstration clearly shows that there may not be a prerequisite for coherence length in order for the Cat conjugator to operate, since 20 μm is many times less than the typical length of the internal loop of a Cat geometry, which is on the order of millimeters. The issue about the influence of the coherence length on the operation and characteristics of a Cat conjugator will be discussed in more details in Chapter 8.

4.6.4 Requirements for the Spatial Coherence

In the following we investigate whether the Cat conjugator requires a minimum of spatial coherence in order to operate. Experimental results will be presented.

Since the operation of the self-pumped Cat configuration necessitates a sufficiently large amount of fanning, there are some requirements for the spatial coherence of the beam. If the spatial coherence is high, there will a large amount of fanning and the Cat conjugator can build up the required grating structure. If the spatial coherence is low, however, the fanning will be low and may be insufficient for the build-up of the nexessary grating structure. The influence of the spatial coherence on the amount of fanning can be understood as follows. Consider light scattered from a strong pump beam inside a photorefractive crystal: for a spatially coherent pump beam the scattered light couples across the entire width of the pump beam; however, for a spatially incoherent pump beam the scattered light becomes incoherent with the strong pump beam itself even after only a short distance of propagation across the pump beam, and there is very little coupling.

As a laser diode array has a low and a high coherence axis (see Sec. 2.5.2), this issue is of great importance when an array is coupled to a Cat conjugator. The fanning can be increased by aligning the high coherence axis in such a way that it is in the a-c plane of the barium titanate crystal. Moreover, the polarization of the light must also be in the a-c plane of the crystal (see Sec. 3.3.1). This can be accomplished by the configuration that is schematically shown in Fig. 18. The polarization is rotated by a half-wave plate whereby both the high coherence axis and the polarization are in the a-c plane of the crystal.

Figures 19(a) and (b) show images of the beam production of a laser beam in a Cat conjugator in a barium titanate crystal. In Fig. 19(a) the beam is from a single-mode laser (see Appendix A for specifications) and in Fig. 19(b) the beam

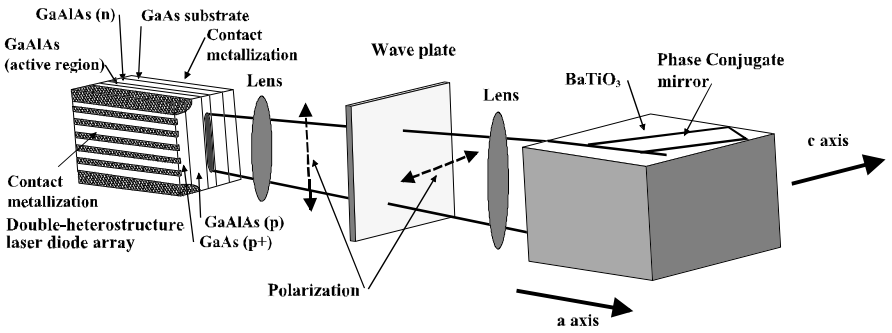

Figure 18. Laser diode array coupled to a self-pumped Cat conjugator formed in a barium titanate crystal. The high coherence axis of the array is aligned with the a-c plane of the crystal. A half-wave plate rotates the polarization. One lens collimates the output of the array and another lens focuses the beam into the crystal.

is from a laser diode array (array I) with the configuration shown in Fig. 18 (for details about the experimental setup, see Sec. 6.1 and Appendix A). In both images the internal reflections are clearly seen in the lower right corner. As can be seen in the figures, the beam width for the case with the laser diode array is much larger than that of the single-mode laser.

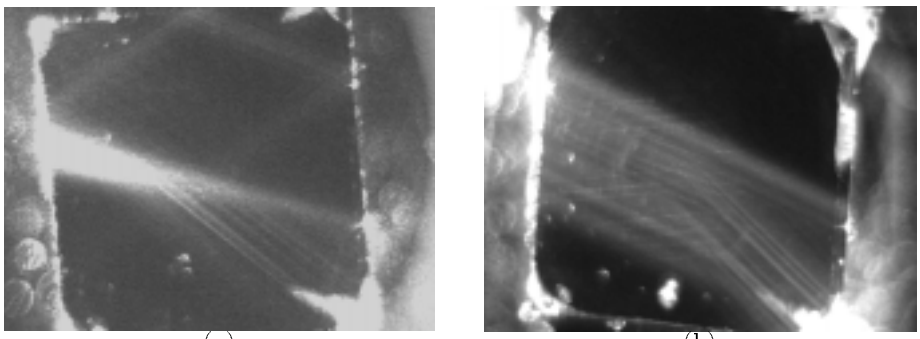

(a) (b)

Figure 19. Image of the beam production in a 45° cut rhodium doped barium titanate crystal (Blue II, see App. C). The c-axis points downwards. The beam enters midway along the left-hand surface of the crystal. (a) The beam is from a 100 mW single-mode laser diode @ 816 nm. The angle of incidence is 52°, the incident power is 35 mW and $R_{pc} \approx 40\%$. (b) The beam is from a 500 mW laser diode array @ 811 nm (array I - see App. A). The angle of incidence is 54°, the incident power is approx. 200 mW and $R_{pc} \approx 10\%$. The recording has been taken from the measurements presented in Sec. 6.1.

From the experiments with the laser diode array it was established that even when the high coherence axis is aligned in the a-c plane, the operation of the Cat conjugator with an array required a minimum beam width. Figure 20 shows the phase conjugate reflectivity of the Cat conjugator when it was illuminated with the radiation from an array as a function of the beam width inside the crystal. The experimental setup is shown in Fig. 18. It is seen that if the horizontal beam width is less than approximately 1 mm, no reflectivity could be obtained, i.e. the grating structure in the Cat conjugator could not build up. Moreover, if the beam width becomes too large (approx. 2 mm), it would not fit into the crystal and the conjugator could not build up either. The highest reflectivity was obtained with a beam width of 1.5 mm. The reduction in the reflectivity as the width is increased

towards 2 mm is probably due to scattering at the crystal edges that erases the grating structure.

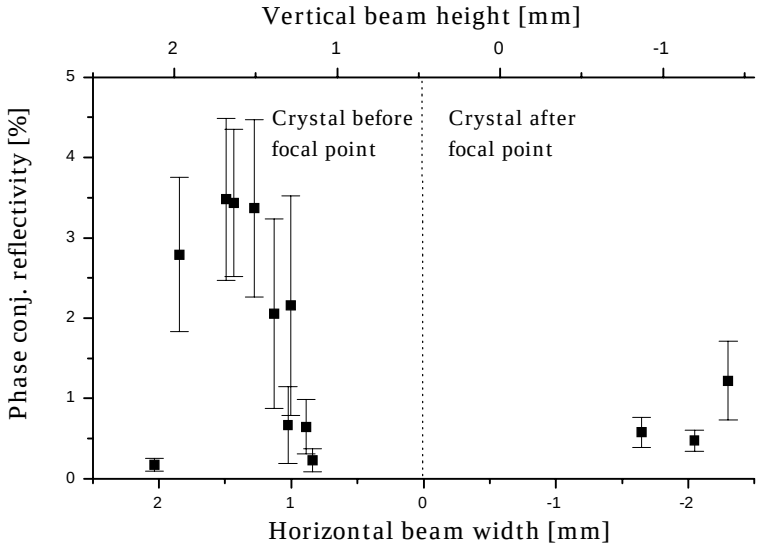

Figure 20. The phase conjugate reflectivity from a Cat conjugator in a 45° cut $BaTiO_3$ crystal (Blue II) as a function of the horizontal (i.e. in the a-c plane) beam width (full width at $1/e^2$) measured inside the crystal. The crystal is illuminated with 120 mW from a laser diode array (array I). The angle of incidence is 54°. The setup is shown in Fig. 18. The focusing lens had a focal length of 100 mm. The different beam widths are obtained by translating the crystal towards the focusing lens. The top axis shows the corresponding vertical beam height.

5 Behavior of Lasers Exposed to Optical Feedback

In this chapter some fundamental properties of lasers exposed to conventional and phase conjugate optical feedback are reviewed. Moreover, properties of injection locked laser arrays are discussed, the concept of off-axis self-injection locking is introduced, and experimental results are presented. On the next page a description of the structure of this chapter is given.

The term optical feedback refers to the process where a fraction of the output energy returns to the active region of the laser structure by means of reflection, diffraction, scattering, etc. Figure 21 shows a schematic diagram of the laser system considered here. The external reflector, which for example can be a conventional mirror, a diffraction grating, a phase conjugate mirror, the end of an optical fiber, or any surface, returns a fraction of the laser radiation to the active region of the laser structure. This optical feedback then influences the field and carrier distribution in the laser causing it to change behavior.

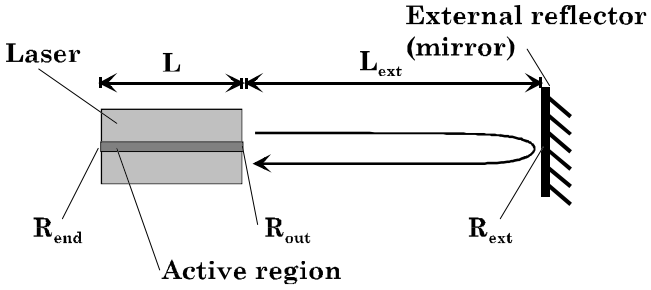

Figure 21. Schematic diagram of the external cavity laser. The external reflector returns a fraction of the emitted laser power to the active region of the laser (optical feedback). The parameters R_{end}, R_{out}, and R_{ext} are the intensity reflectivity of the end facet, the output facet, and the external reflector, respectively.

For the case of laser diode arrays (and broad-area lasers) it is necessary to distinguish between two different external cavity configurations. The two configurations are referred to as:

- The *on-axis* external cavity
- The *off-axis* external cavity

In the on-axis configuration all the far-field radiation is collected and directed towards the external reflector that returns a fraction of the incident energy. In the off-axis configuration, however, only a part of the twin-lobe far-field (for example only the positive lobe) is directed towards the external reflector that returns a fraction of the energy contained in that lobe. The behavior of the laser system is completely different for the two configurations. The on-axis configuration may be regarded as a coupled cavity scheme since the coupling between the laser and the external reflector becomes much stronger as compared with the off-axis feedback scheme. Note that a fundamental-mode laser (single spatial mode), which may have numerous longitudinal modes, can only be operated in the on-axis configuration since a split up of its far-field will not change the behavior of the laser substantially. When a laser diode array is operated in the on-axis configuration,

the far-field pattern cannot be narrowed down and become almost diffraction limited. However, the spectral properties may be improved significantly.

In Fig. 21 the intensity reflectivity of the end facet, the output facet, and the external reflector is labeled R_{end}, R_{out}, and R_{ext}, respectively. The distance between the laser and the external reflector is denoted L_{ext}. There is one parameter which is often used to characterize the strength of the feedback. This is the *feedback coefficient*, which indicates how strong the feedback is (intensity), and is given by [42]

$$F = (1 - R_{out})^2 \frac{R_{ext}}{R_{out}}, \tag{27}$$

which is independent of the external-cavity round-trip time τ_{ext} $(= 2L_{ext}/c)$.

The structure of this chapter is as follows: in Sec. 5.1 the characteristics of the on-axis configuration with conventional feedback are discussed. The discussion includes previous work on laser diode arrays, external cavity modes, as weel as a phenomenological classification of different feedback regimes and their characteristics. Section 5.2 introduces phase conjugate feedback and gives a description of the effect of the response time of phase conjugators, the unique characteristics of the phase delay in the external cavity, and a phenomenological classification of different feedback regimes and their characteristics. Moreover, the concept of coupling two incoherent laser sources through a Cat conjugator geometry is presented. In Sec. 5.3 we give an introduction to conventional injection locking, and the concept of off-axis self-injection locking. In Sec. 5.4 we describe how mode discrimination in an external cavity can be applied to laser diode arrays. Finally, in Sec. 5.5 we present experimental results of off-axis self-injection locking of a laser diode array using conventional feedback from a mirror and a diffraction grating.

5.1 On-Axis Configuration with Conventional Feedback

Fundamental studies have shown that the ultimate line width reduction of the modes that oscillate in a diode laser is proportional to {(power reflected back into the laser cavity)×(length of external cavity)^2}$^{-1}$.[103] This indicates that a significant line width reduction is possible if either a long cavity or a high feedback level is used. This is consistent with the expression for the fundamental line width of a single-mode diode laser which is given by [104]

$$\Delta\omega = \frac{\sigma_s}{2P}\left(1 + \beta_c^2\right), \tag{28}$$

where σ_s is the spontaneous emission rate into the lasing mode, P is the number of photons contained within the lasing mode, and β_c is the antiguiding parameter (or the factor for the carrier-induced index change) given by Eq. 1. The line width is reduced with a longer external cavity or with higher reflectivity of the external reflector, both of which give rise to an increase in the photon number in the lasing mode. The line width reduction proportionality stated above is valid only for low feedback levels ($< 0.1\%$). At higher feedback different instabilities that lead to broadening, increased intensity noise, etc. may occur (will be discussed in Sec. 5.1.4). This means that with a low feedback level it is possible to achieve a line width reduction of each of the oscillating modes of a multimode laser diode (such as a laser diode array), but the reduction does not enhance the coherence length of the laser diode. However, if the feedback reduces the number of oscillating modes, which causes the bandwidth of the spectrum to be narrowed down, the coherence length is increased. Only if the spectrum is reduced by the feedback to a single longitudinal mode, the line width reduction will lead to a longer coherence length.

Unfortunately, low feedback levels are often not sufficiently to force a multimode laser diode array to oscillate at one single mode. The line width reduction (or broadening) is therefore in general often only of interest for single-mode lasers and such lasers have over the time received a vast amount of attention since, e.g., low feedback reflections from optical fibers in connection with telecommunication can reduce the laser performance.[105, 106, 107] Moreover, feedback can also be used to acquire control over the oscillating wavelength; a widely tunable source (> 60 nm) using grating feedback and a fundamental-mode diode laser has been demonstrated.[108]

5.1.1 Previous Work with Laser Diode Arrays

By applying the feedback to all of the radiation, i.e. the on-axis configuration, the coherence length of a laser diode array has been improved significantly.[109] The feedback was generated by applying a reflection coating to the collimating objective that was placed in front of the array. The coating made the objective only partly transmitting and caused backreflection (10%) into the laser array. In another and similar scheme the multiple longitudinal mode output of a laser array has been converted into a single mode by external feedback from an etalon.[110] The etalon is placed close to the output facet of the array and a coupled cavity is formed. The far-field pattern is not enhanced in any way by the feedback.

A variation of conventional feedback from a mirror has been demonstrated using microlenses and diffractive coupling to induce mutual coherence among the laser elements of a laser array to produce a single-lobed far-field pattern.[111] There have been other demonstrations of this technique where the microlenses have been replaced with a spatial filter that is placed between the laser array and a mirror.[112]

Improvement can also be obtained using a diffraction grating as external reflector. The feedback to the laser array is generated with the grating mounted as in a standard Littrow configuration (the light is diffracted directly back towards the source).[113] The frequency selective feedback has a huge impact on the spectral quality and single-mode operation of a laser array has been demonstrated.[114, 115] Feedback from a diffraction grating that is monolithically integrated with the laser array has also been reported [116] and with such a design, significant improvement of especially the spectral properties was demonstrated.

5.1.2 Line width Narrowing and Broadening

The paper by Lang and Kobayashi published in 1980 [117] is generally considered to be the basic one that initiated the research on semiconductor laser dynamics. The relevant parameters in case of conventional external optical feedback are:

- Length of external cavity (delay time).
- Feedback power level, i.e. the ratio of the power reflected from the external reflector to the power reflected from the output facet of the diode laser (F).
- Feedback phase, determined by the number of optical wavelengths in the external cavity. The phase changes over 2π by varying the external cavity length over half a wavelength.

As light is emitted from the laser and propagates in the external cavity, it experiences an external phase shift that is given by $\varphi_{ext} = \omega_0 \tau_{ext} + \varphi_0^{ext}$, where ω_0 is the laser frequency. For the sake of generality, a constant phase shift φ_0^{ext} is allowed at the external reflector. The external-cavity phase shift plays a subtle role through the phase factor $\exp(-i\varphi_{ext})$ for the delayed field that is fed back

into the laser cavity. It turns out (see Ref. [118]) that the line width of a single-mode laser exposed to weak feedback ($R_{ext} \ll 1$) depends on the value of φ_{ext}. In other words: for an experimental setup both line width broadening and narrowing - as compared with the line width of the solitary laser with no feedback - can be observed by varying the length of the external cavity over half a wavelength. The mechanical tolerance of the coupled system for optimum performance is therefore extremely critical.

5.1.3 External Cavity Modes

The external reflector in Fig. 21 leads to the formation of an external cavity. The external cavity is often much larger than the cavity of the laser ($L_{ext} \gg L$) and has its own set of resonance frequencies. The resonance frequencies of the external cavity are fundamentally the same as the longitudinal modes of the solitary laser. These resonances are referred to as *external cavity modes*. However, the external cavity and the laser cavity are coupled and, consequentially, some of the external cavity modes will experience higher gains than others. For this reason, the oscillating external cavity modes are closely spaced at $c/2L_{ext}$ ($= \tau_{ext}^{-1}$), where c is the speed of light in free space, and essentially form an unresolved continuum centered around each of the longitudinal modes of the laser cavity.[119] Figure 22 illustrates the presence of external cavity modes with respect to the array modes and the longitudinal modes in the spectrum. This unresolved continuum - which for short external cavities can actually be resolved with a high-finesse spectrum analyzer - gives rise to an apparent line width of the array mode that is the width of the cluster.[120, 121] In other words: for a single-mode laser the oscillation of external cavity modes leads to a broadening of the laser line width with a reduction in coherence length as a result.[122]

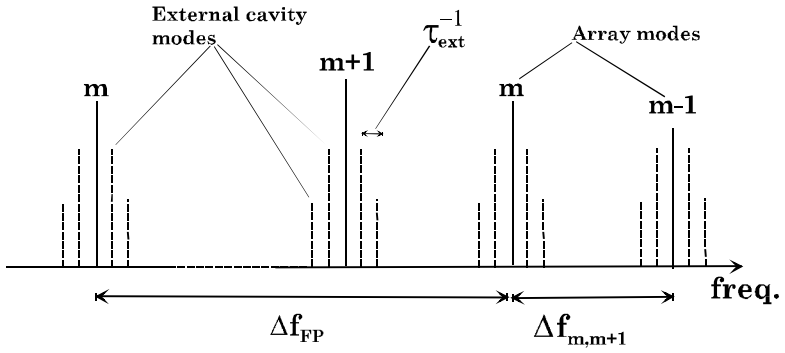

Figure 22. Spectrum of laser diode array exposed to optical feedback. The feedback leads to the presence of external cavity modes. These modes are clusters around all of the oscillating modes of the solitary laser array.

It has been shown that more than one external cavity mode is present in the external cavity if [123, 2]

$$C = \kappa\tau_{ext}\sqrt{1+\beta_c^2} > 1, \tag{29}$$

where κ is the feedback rate (i.e. how large an amount of energy is fed back into the laser cavity per unit time), which is given by [118, 106]

$$\kappa = \frac{1-R_{out}}{\tau_L}\sqrt{\frac{R_{ext}}{R_{out}}}, \tag{30}$$

where τ_L is the round-trip time of the field in the solitary laser cavity. As the feedback parameter C increases, potentially more external cavity can be oscillating. For fixed reflectivity, the number of modes can be decreased by reducing the length of the external cavity.

The presence of external cavity modes can be used for short pulse generation. This can be achieved by mode locking techniques.[41] Generation of short pulses has been demonstrated in numerous external cavity configurations using both an ordinary mirror [53, and references therein], and with a photorefractive phase conjugate mirror as external reflector [13, 124, 125].

5.1.4 Phenomenological Classification

For conventional on-axis feedback a hierarchical classification of different feedback regimes (labeled I, II, III, IV and V) in terms of the value of the effective feedback reflectivity and the external cavity length has been introduced.[126, 127] Each regime corresponds to a well-defined type of behavior of the laser system, which in short can be described as [42]

I For very weak feedback levels ($F < 10^{-6}$) considerable line width narrowing and improved frequency stability can be achieved, but broadening is also possible.[118]

II Depending on the value τ_{ext} the II regime will be reached around 10^{-6}, where the system shows noise-induced hopping between external cavity modes.

III The system can exhibit mode hopping and periodic power fluctuations, i.e. the spectrum of the temporally observed output power consists of a number of peaks which have been attributed to beating between external cavity modes.[122, 128] The spacing between two peaks corresponds to the inverse of the external round-trip time.[129] Additional longitudinal modes can appear, and the line width of each mode continues to broaden for increasing feedback level.[130]

IV The *coherence collapse* phenomenon has been observed for feedback levels of $F = 3{\cdot}10^{-5}$ to 10^{-1}. This phenomenon stems from strong nonlinear instabilities [131] and results in a significant reduction in the coherence length.[123, 132] An observation of the emitted laser power reveals randomly distributed sudden intensity drops. The recovery time after such a drop is typically equal to several τ_{ext}.[123]

V For high feedback levels ($F > 10^{-1}$) stable laser operation with line width narrowing effects can again be observed.[133] Usually the V feedback regime can only be reached by using an antireflection coating on the output facet.

Often regimes I and II are grouped as the *weak* feedback regime ($\ll$ 1% reflectivity), regimes III and IV are grouped as the *moderate* feedback regime (1-10% reflectivity), and regime V is classified as the *high* feedback regime ($>$ 10% reflectivity).[127]

5.2 Phase Conjugate Feedback

From the investigations on conventional feedback it is known that the noise characteristics of semiconductor lasers and the spectral line width are extremely sensitive to the optional feedback that occurs when a portion of the laser output is fed back into the laser cavity from an external reflecting surface. As discussed in the preceding section, this high sensitivity is due to - among other parameters - the external cavity phase shift. One of the properties of phase conjugate light is the

distortion correction theorem, which means that the external cavity phase shift is always constant regardless of the length of the external cavity, since the phase of the returned light is reversed during reflection. As a result, the behavior of lasers with feedback from a phase conjugate mirror (PCM) has received considerable attention. Such feedback is referred to as phase conjugate feedback (PCF) and differs considerably from the conventional feedback.

The nature of phase conjugation will cause the phase conjugate beam to propagate directly back towards the laser source and will enter the gain medium unless precautions such as using an optical isolator are taken. If no such precautions are taken the phase conjugate beam is optical feedback which couples the laser and the phase conjugator (e.g. a self-pumped photorefractive $BaTiO_3$ crystal). It has been observed that phase conjugate feedback generated by four-wave mixing in $BaTiO_3$ has a strong influence on the characteristics of the radiation from lasers, such as semiconductor lasers, gas lasers and dye lasers; PCF has been demonstrated to reduce the line width of a single-mode diode laser by a factor of ten[89], to achieve single-mode operation of a multimode low-power diode laser (line width less than 100 kHz)[134], to narrow down the spectrum of a visible low-power multimode laser diode[135], to stabilize active mode locking of a visible laser diode in an external cavity[124], to reduce the power fluctuations in a multimode argon ion laser[136], and to narrow the line width to less than 6 GHz in a multimode dye laser[137]. However, PCF has also been observed to cause strong degradation of the output radiation, such as frequency scanning (see Chapter 6) in a diode laser[138] and a dye laser[139], spatial mode fluctuation in a dye laser[140], and line width broadening in an index-guided diode laser[135].

5.2.1 Response Time of Phase Conjugators

Many theoretical investigations on the dynamics of lasers with PCF assume instantaneous response of the the PCM.[141, 142, 143, 144, 145, 146, 147, 148] In experiments this approximation may be fulfilled with a fast nonlinear medium (e.g. semiconductor material [149]) which is externally pumped in a four-wave mixing geometry. However, if the PCM response time is slower than the external round-trip time, the feedback rate (κ) becomes time dependent and changes the dynamic behavior of the laser diode. In other words: the effect of PCF on a semiconductor laser depends on the type of PCM. The approximation concerning instantaneous response time does not apply to a self-pumped PCM.[141] Nevertheless, a self-pumped photorefractive $BaTiO_3$ phase conjugator is still capable of phase conjugating the output from a laser diode that is coupled to the conjugator.[89] This observation leads to speculations about how that can be the case. One explanation may be: once the grating structure in the photorefractive crystal has built up and returned the phase conjugate beam, a steady state occurs. In this steady state, the emitted power and the mode structure from the laser in the cavity are constant over time, and even though the response time of the phase conjugator is orders of magnitude larger than τ_{ext}, small variations in the emitted field will to some extent (lower fidelity) be phase conjugated by the present grating structure in the crystal. Recently, a few theoretical investigations have included the response time of the PCM.[150, 151]

The slow response time may be favorable in some applications. It has,e.g., been observed that the PCF from a self-pumped $BaTiO_3$ conjugator reduces the frequency jitter of a single-mode laser.[89] In contrast to conventional feedback, this reduction is due to a slow response time of the photorefractive crystal which does not allow any jitter from the central lasing wavelength to have enough time to write a new set of holographic gratings. Basicly, only the central frequency is cou-

pled back into the laser cavity. Theoretical investigations have revealed that a finite response time - in contrast to an instantaneously responding mirror - does indeed increase the stability of the emission from a diode laser with PCF.[150, 151]

The phenomenon of coherence collapse induced by a moderate feedback level may never be observed with a self-pumped conjugator, since any coherence collapse will lead to erasure of the grating structure causing the reflectivity to decrease to a level below the level of coherence collapse.

5.2.2 Phase Delay in a Phase-Conjugate External Cavity

A self-pumped phase conjugator differs in a fundamental way from an externally pumped phase conjugator. Because it has no external pump beams with a given phase reference, it cannot keep track of absolute phase.[152] For example, a self-pumped Cat conjugator cannot eliminate the spatially uniform component of the phase shift caused by inserting a distorting medium in the path of the incident beam. The self-pumped Cat conjugator, however, can eliminate the high spatial frequencies of the phase disturbance generated by the distorting medium (the distortion correction theorem). This can be explained as follows. Similar to Eq. 26, it can be shown that the electrical field amplitude of the phase conjugate replica (E_c) of the incident beam (E_o) is proportional to [90]

$$E_c \propto E_1^{pump} E_2^{pump} E_o^*, \tag{31}$$

where E_i^{pump} ($i = 1,2$) are the two pump beams of the four-wave mixing geometry. Consider a uniform phase shift of $\exp(i\varphi)$ impressed on the electric amplitude E_o of the incident optical beam. For external pumping this phase shift is not impressed on the two pump beams and the resulting phase of the output beam is thus $\exp(i0) \cdot \exp(i0) \cdot \exp(i\varphi)^* = \exp(-i\varphi)$. However, for a self-pumped geometry the phase shift is also impressed on both pump beams and the resulting phase shift of the output beam is consequently $\exp(i\varphi) \cdot \exp(i\varphi) \cdot \exp(i\varphi)^* = \exp(i\varphi)$. This clearly shows that there is a difference between the self-pumped and the externally pumped geometry. A self-pumped conjugator retains phase delay.[153] It therefore follows that if a resonator is formed between a conventional mirror and a self-pumped conjugator, the longitudinal mode spacing will be $c/2L_{cavity}$. This is in contrast to theoretical investigations [90] that have shown that for a resonator formed between a phase conjugator mirror and a conventional mirror, the longitudinal mode spacing is $c/4L_{cavity}$, or half the longitudinal mode spacing of a resonator with conventional mirrors; however, that does only apply to externally pumped phase conjugators.

5.2.3 Line Width Narrowing

For weak feedback levels line width narrowing can be achieved with PCF. Due to the distortion correction theorem for an externally pumped conjugator, which means that the light is reversed during reflection, the external phase shift can be written as [146]

$$\varphi_{ext} = \omega_0 \tau_{ext} + \varphi_{pcm} + (-\omega_0 \tau_{ext}) = \varphi_{pcm} + 2m\pi,$$

where m is an integer and φ_{pcm} is an arbitrary phase shift associated with the reflection in the PCM. The major difference between phase conjugate feedback and conventional feedback is that for PCF φ_{ext} does not depend on τ_{ext}, i.e. the cavity length, whereas this is not the case for conventional feedback. As a result, the cavity length of the external cavity can be chosen arbitrarily, and the length adjustment for optimum performance is therefore not critical. Despite the fact

that a self-pumped conjugator retains phase delay, it turns out that in a coupled system the conjugator will adjust its phase φ_{pcm} so that $\varphi_{ext} = 2m\pi$, which means that this system is also independent of τ_{ext}.[153, 89]

The concept of line width narrowing using weak PCF has been verified experimentally with a self-pumped $BaTiO_3$ conjugator.[89] Line width narrowing of a single-mode laser diode has been demonstrated using phase conjugation generated by four-wave mixing in another semiconductor broad-area laser.[154, 155] In one experiment [154] the line width was reduced with a factor of two hundred, from 5 MHz to 25 kHz, by feeding back $6{\cdot}10^{-5}$ of the output power from the single-mode laser.

5.2.4 Phenomenological Classification

Similar to conventional feedback a hierarchical classification of different phase conjugate feedback regimes in terms of the value of the effective feedback can be introduced. Here three regimes are used: the weak, the moderate, and the high feedback regime.

- For week feedback ($F < 1{\cdot}10^{-2}$), line width narrowing effects and increased frequency stability for a single-mode laser can be achieved.[89, 155] The intensity and the frequency noise are reduced.[141]. PCF can lead to single-mode operation of a visible multimode laser diode.[89]
- In the moderate feedback regime ($F > 1{\cdot}10^{-2}$) strong instability can occur, which leads to a reduced coherence length (coherence collapse regime).[142] Moreover, strong intensity variations such as period-doubling can take place.[144, 147] For some types of phase conjugate mirrors the coherence collapse regime may not be encountered due the finite response time of the PCM, as discussed in Sec. 5.2.1.
- In the high feedback regime ($F > 1{\cdot}10^{-1}$), stability, i.e. reduced intensity noise, can again be achieved. PCF can lead to effects such as spatial mode suppression.[148] Depending on the laser design PCF may result in either an increasing or a reduced number of longitudinal modes that are lasing.[135, 156, 124] In some cases PCF can cause a multimode laser to oscillate in a single mode.[134] For some types of lasers PCF leads to reduced intensity noise [136], whereas in others it may induces strong mode fluctuation[140]. In the high feedback regime some types of self-pumped phase conjugators may lead to instability such as frequency scanning (see Chapter 6).[138, 140]

From this description of the three feedback regimes - which is based partly on numerous experimental observations, partly on theoretical investigations - no clear picture of the behavior of lasers with PCF is found. Only for weak feedback is an enhancement of the laser performance for certain observed. Based on the experimental data collected during this Ph.D. work, the phase conjugate reflectivity from a self-pumped $BaTiO_3$ conjugator is typically 2-15% (lowest for the off-axis configuration and highest for the on-axis configuration), corresponding to $F = 4{\cdot}10^{-2} - 3{\cdot}10^{0}$ for $R_{out} = 0.04$. This means that the laser behavior should be compared with the moderate and high feedback regimes. The coherence collapse phenomenon, however, has not been observed during this work. It was found that high stability can be obtained if - and only if - active mode discrimination in the external cavity is applied. Thereby mode hopping is avoided. The concept of discrimination is discussed in Sec. 5.4.

5.2.5 Phase Locking of Two Lasers

Even when the radiated beams from two laser source are highly coherent, i.e. the lasers have a long coherence lengths, they cannot form an interference pattern. The laser beams are said to be mutually incoherent. However, the two laser sources can be made mutually coherent by applying phase conjugate feedback to the laser sources from a mutually pumped phase conjugator, as described in Sec. 4.2. Figure 23 shows the basic concept of phase locking of two incoherent laser sources using a self-pumped Cat configuration as well as a mutually pumped phase conjugator in a $BaTiO_3$ crystal. Each of the beams from the individual sources forms its own self-pumped Cat geometry and establishes PCF. The beams also spatially overlap in the crystal and a mutually pumped geometry can in addition to the Cat geometries be formed. The grating structure of the mutually pumped conjugator causes the photons from one laser to be injected into the other laser, and vice versa. As discussed in Sec. 4.5, this injection will become stronger if the sources have exactly the same wavelength and, consequently, they will try to match their wavelengths. In order to achieve complete phase locking of the sources, i.e. only one frequency is oscillating in each laser, it must be ensured that only one spatial mode can oscillate for each laser (and preferably the same spatial mode), since different spatial modes have slightly different resonance frequencies. The concept of interaction of two laser beams in a Cat conjugator has been verified experimentally.[157] This technique has been applied to a laser bar, which is a number of arrays placed next to each other.[17]

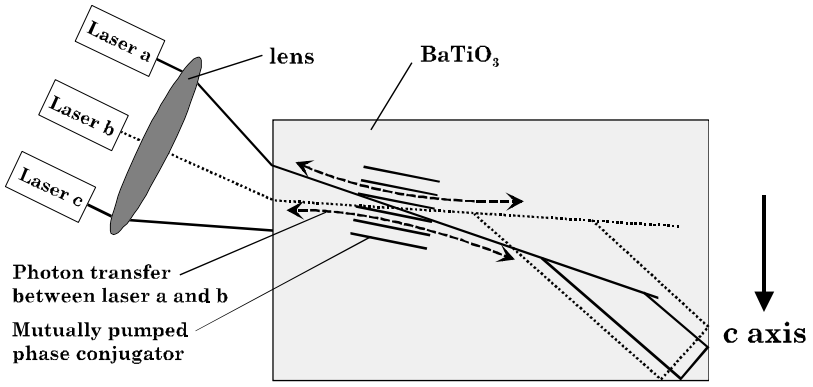

Figure 23. Basic concept of phase locking of several incoherent laser sources by phase conjugate feedback generated with a barium titanate crystal. Each laser source generates its own self-pumped Cat geometry and establishes phase conjugate feedback. In addition, the sources interfere and generate a mutually pumped grating structure that causes photon transfer between the sources and establishes phase locking. Only the beam paths corresponding to two sources are shown in the figure. The sources could, e.g., be laser diode arrays of a laser bar.

5.3 Injection Locking

Injection locking is the process of sending a low-power signal into a self-oscillating resonator (for example a laser diode array). The weak signal seeds the resonator and is capable of locking the subsequent oscillatory behavior of this resonator and, thereby, of controlling the spectral and spatial properties of the output of the resonator. Optical injection locking has proven to be a powerful tool in improving the performance of laser diode arrays, and the technique has been applied with

very good results.[158, 159, 160, 161, 162]

In an injection configuration the light of a *master* laser, which is typically a low-power single-mode laser, is coupled into a laser device, which is referred to as the *slave* laser. Even though the obtained results are impressive, the injection locking scheme requires - in addition to the master laser - an optical isolator to prevent optical feedback on the master laser from the slave laser. Moreover, for locking to occur two conditions must be satisfied: (1) the detuning between the frequency of the injected field and the resonance frequency of the slave laser must not be too large, while (2) the injected power should not be too small. Condition (1) requires that the lasing wavelength of the master and the slave lasers can be matched by temperature tuning the two laser cavities. Condition (2) calls for an efficient coupling of the low-power source into the cavity of the slave laser. The master-slave injection configuration is complex and not trivial to operate. A more simple configuration is the *self-injection* locking scheme where a fraction of the output power of the slave laser itself is used as replacement for the master laser. This scheme will be discussed in Sec. 5.3.1. Although self-injection is not free from difficulties, it takes advantage of fundamental properties of the master-slave injection locking scheme. In the following these properties will be discussed.

Fundamental aspects of the injection locking process for semiconductor lasers such as noise properties [163], locking range [164], static and dynamic behavior [165, 166], and chaos and instability [167, 168] have been investigated theoretically. Moreover, the dynamics of phase conjugate injection locking using a mutually pumped $BaTiO_3$ crystal (pumped by a master laser and a slave laser) has been investigated.[169] These investigations are in general based on the Lang-Kobayashi rate equations[117] or on the Fabry-Perot amplifier model[164] (the two models have been compared in Ref. [170]) and are most suitable to study the dynamic properties. In addition, no spatial effects are considered, and the injected signal is considered to be *on-axis*, i.e. the light is injected into the cavity of the slave laser along the axis of the radiation from the solitary slave laser. However, the injection locking of high-power broad-area lasers or laser diode arrays follows the completely different scheme, which is known as *off-axis injection*, and spatial effects must be taken into account in the theoretical analysis (such an analysis has so far not been reported).

Off-Axis Injection Locking Figure 24(a) shows schematically the off-axis injection locking configuration. The beam from a master laser is injected into the gain region of the slave laser - which can be either an array or a broad-area laser - at an angle of $+\theta$. The master beam is referred to as the *injection beam*. The output radiation from the slave laser array is referred to as the *output beam*. The output beam is radiated at an angle of $-\theta$ and contains a much larger amount of energy as compared with the injected energy. As a result of the subsequent experimental investigations of injection locked laser arrays, a number of new models have been developed to explain the observed injection behavior. Initially, the injection of a master signal into a free-running laser array was considered to increase the effective gain of specific array modes selectively, with the greatest gain increase for the modes that are most closely matched in frequency and field profile to those of the injected master laser beam.[171] This model, however, could not explain observations such as the scanning of the emission angle when the frequency of the injected light was changed.[162, 172] Later, the off-axis Fabry-Perot amplifier model was proposed, [161] a model that has shown good agreement with the experimental observations of the injection locking process in both broad-area lasers and laser diode arrays.

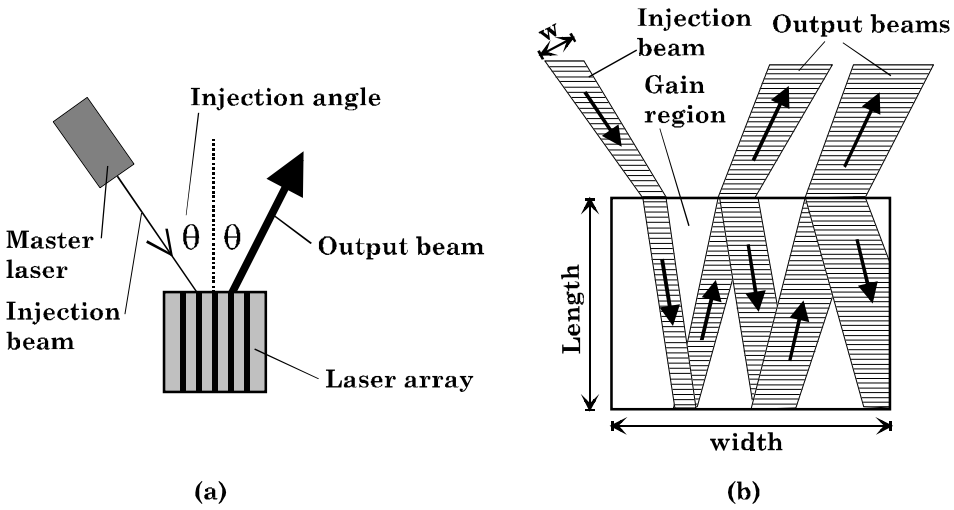

Figure 24. (a) Schematic diagram of the injection locking configuration. The beam from the master laser is injected into the laser array (slave laser) at an angle of $+\theta$. The output beam is radiated at an angle of $-\theta$. (b) Off-axis Fabry-Perot model for a broad-area laser. The length and the width of the gain region of the broad-area laser are shown.

Off-Axis Fabry-Perot Amplifier Model Figure 24(b) shows the proposed mechanism for the injection locking process. An injection beam with a width of w is injected into the gain region of the laser device. The injected beam is focused at one side of the junction. The waveguide structure of the laser device ensures that the injected signal is guided in the plane perpendicular to the junction (transverse direction), but is free to diverge in the plane parallel to the junction. Recall that the end facet has high reflectivity and that the output facet is partially reflecting. The injected beam propagates in the active region and is amplified. After reflection from the end facet the amplified beam is emitted as an output beam. However, a part of the beam is reflected at the output facet, reenters the gain region and is again amplified. Thereby, the injected beam makes a multipass propagation until the beam eventually propagates out of the laser gain region and is attenuated. If the width of the injection beam is small compared with the width of the junction, several output beams can arise (as shown in Fig. 24(b)). In the far-field these beams can interfere and form an interference pattern. This has been observed experimentally.[161] As a result of the wave-guiding effect in the transverse direction, the output beam in this plane is unaffected by the injection locking process and exhibits the same divergence as the free-running laser. This is not a problem since the emission is diffraction limited in the transverse direction. The proposed off-axis Fabry-Perot amplifier model does not include the lateral gain and the refractive index profile that are present within gain-guided laser diode arrays. However, experimental observations have shown that laser arrays and broad-area lasers exhibit near identical responses under injection locking conditions and thus support the case for considering the gain-guided array as a weakly perturbed gain-guided device (perturbed broad-area model, see Sec. 2.5.2) as opposed to a number of coupled oscillators (supermode theory, see Sec. 2.5.2).

The most relevant parameters in the case of optical injection are [173]:

1. The ratio of solitary slave laser power to injected power from the master laser.
2. Frequency detuning between the injected field and the solitary slave laser frequency.

For a given drive current of the slave laser, a minimum amount of energy must be injected in order to achieve complete locking.[158, 173] The frequency of the master laser must be matched precisely to a resonance of the slave laser (within GHz) to ensure efficient locking behavior.[162] Especially the latter is not trivial to obtain experimentally. This problem can, however, be overcome by using so-called off-axis self-injection locking, which will be described in the following section.

5.3.1 Off-Axis Self-Injection Locking

The off-axis self-injection locking scheme is very similar to the off-axis injection locking configuration shown in Fig. 24(a). The only difference is that the injection beam is a fraction of the energy from one of the two far-field lobes of the array which is subsequently fed back to the active region. This feedback is then amplified according to the broad-area model injection locking model. Figure 25(a) shows a schematic diagram of the off-axis self-injection locking configuration. The external reflector can, e.g., be a mirror. It may also be a phase conjugate mirror, in which case the configuration is referred to as *off-axis phase conjugate self-injection locking* (this technique will be presented in chapters 9 and 10). The external reflector returns a part of one far-field lobe to the laser array itself. As a result, bidirectional beam propagation arises in the external cavity between the array and the external reflector.

Previous Work with Arrays Off-axis self-injection locking with a conventional mirror has have been demonstrated and studied in details.[37, 174, 175] Generation of ultrashort pulses (ps) has also been presented using passive mode locking and off-axis self-injection.[176] Off-axis self-injection locking where a fraction of the output lobe is fed back to the laser array along the injection lobe has been reported.[177] The output loop is launched into the end of an optical fiber. The other end of the fiber provides the injection beam. The fiber contains an output coupler and an optical isolator to ensure propagation in only one direction of the fiber, and the system behaves like a ring oscillator where the laser is used as an amplifier. With this configuration a 40-element laser array has been enhanced to a diffraction limited far-field and a single-mode spectrum.[177] Unfortunately, only 20% of the total array energy was available at the output coupler.

Coupling of External Reflector and the Array Figure 25(b) shows an example of the far-field in the lateral direction (x-z plane) obtained from a configuration where the external reflector is a conventional mirror (see Sec. 5.5.1 for more details about the experimental configuration). The external mirror is placed and oriented in such a way that the array emission is fed back at an angle of $\theta \approx -2^\circ$. As a result of the self-injection locking process, the array emits a large amount of energy at an angle of $\theta \approx +2^\circ$. The far-field lobe at $\theta \approx -2^\circ$ is referred to as the *injection lobe* (or beam), and the lobe at $\theta \approx +2^\circ$ is referred to as the *output lobe* (or beam).

Due to the refractive index grating in the active region with the wave vector parallel to the x-axis (see Eq. 5 in Sec. 2.5.2), a part of the amplified injection beam (the output lobe) is diffracted and radiated towards the external reflector[38] and, consequently, the external reflector and the array become weakly coupled. As a result, the laser array is exposed to an effective feedback coefficient F_{eff}, which may be much smaller than F given by Eq. 27. The effective feedback coefficient may be estimated - even though this step is rather unjustified - by comparing the energy contained in the output lobe and the injection lobe. If the peak intensities of the injection and the output lobes are denoted I_{in} and I_{out}, respectively, the

effective feedback coefficient is given by

$$F_{eff} = \frac{I_{in}}{I_{out}} F = \frac{I_{in}}{I_{out}} (1 - R_{out})^2 \frac{R_{ext}}{R_{out}}, \tag{32}$$

where Eq. 27 has been used. Based on the far-field shown in Fig. 25(b), the effective feedback coefficient is $F_{eff} \simeq 0.1 \cdot F$. This means that the effective feedback level becomes a factor of ten smaller as compared with F. If a fraction of all of the far-field energy is fed back to the laser, the system becomes more strongly coupled and should be regarded as a system of coupled resonators. For that case $F_{eff} = F$, since $I_{in} = I_{out}$.

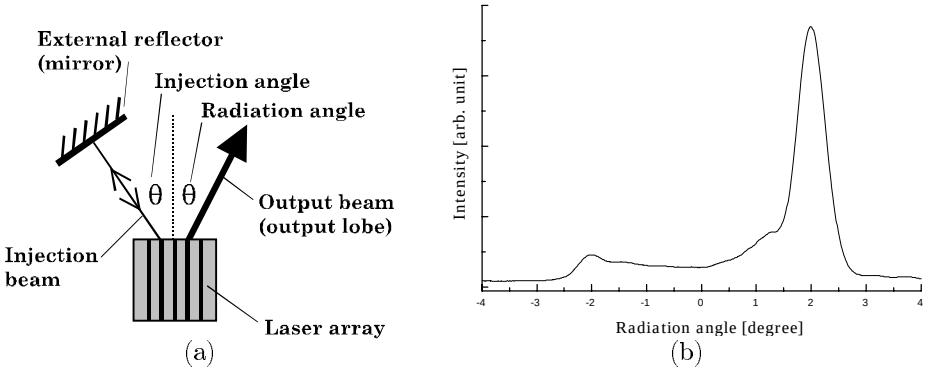

Figure 25. (a) Schematic diagram of off-axis self-injection locking. The external reflector returns a part of the array emission to the active region. (b) Far-field in the lateral direction from an off-axis self-injection locked laser array using a mirror as external reflector. It is the lobe at $\theta \approx -2^\circ$ that is the injection lobe. The output lobe is radiated at $\theta \approx +2^\circ$. The data have been obtained experimentally. See Sec. 5.5.1 for more details .

5.4 Discrimination of Array Modes in an External Cavity

In general, a high-power laser array oscillate in a number of spatial and longitudinal modes simultaneously. From numerous reported experiments with PCF it is known that the number of oscillating modes in a multimode laser can be reduced by coupling it with a phase conjugate mirror. However, it is also known (see Sec. 5.2.4) that different kinds of instability such as mode hopping can be caused by strong PCF. Since high PCF is necessary in order to suppress unwanted modes, which are oscillating when no feedback is applied to the laser, it is necessary to tailor the external cavity in some way. One way to achieve oscillation in a single mode is to have some sort of mode discrimination in the external cavity, i.e. high losses for all modes except one must be introduced. As a rule, mode discrimination can be achieved in two ways:

- filtering in the spectral domain (spectral filtering);
- filtering in the spatial domain (spatial filtering).

Figure 26(a) gives a schematic presentation of a part of the multimode spectrum of a laser array. Three clusters of array modes (spatial modes), which are oscillating, are shown in the figure. The different array modes are labeled with mode index m. Figure 26(b) shows the basic configuration of off-axis self-injection locking, where both spatial and spectral filtering is applied.

First, spatial filtering is considered. As discussed in Sec. 2.5.2, different array modes radiate their lobes at different angles (θ_m). A slit (with the edges parallel to the transverse direction) placed between the external reflector and the array increases the loss for some of the spatial modes. As shown in Fig. 26(b), the position of the slit controls which of the array modes that are selected. In this case it is array mode m. If the slit is suffiently narrow, both array mode $m-1$ and array mode $m+1$ (and array modes with even higher or lower mode indices) will not pass the spatial filter and reach the external reflector. In the spectral domain this spatial filtering can be illustrated by the dotted arrows shown in Fig. 26(a); the spatial filter selects array mode m from each of the array clusters around each of the longitudinal modes. Since several longitudinal modes oscillate, the spatial filtering will usually not lead to a narrowing of the array spectrum. However, the spatial filtering leads to the far-field pattern shown in Fig. 25(b).

Next, spectral filtering is considered. In general one can say that a spectral filter has a transmission that depends on the frequency of the beam. This could for example be an etalon, an interference filter, an absorption filter, or an interference filter in a photorefractive crystal[178]. In the spectral domain spectral filtering can be illustrated by a transmission function, as shown by the dashed line in the lower part of Fig. 26(a). The modes that have a wavelength outside the bandwidth of the spectral filter are subject to high loss, as compared with those modes which have a wavelength within the bandwidth. If the bandwidth is less than $\Delta\lambda_{FP}$ (longitudinal mode spacing), as shown in Fig. 26(a), one cluster of array modes (one longitudinal mode) can be selected. If spatial filtering is also applied, only one array mode m is selected from this cluster, and single-mode operation of the off-axis self-injection locked array can be achieved. If no spatial filtering is applied, single-mode operation can still be obtained. However, that requires that the bandwidth of the spectral filter is smaller than $\Delta\lambda_{m,m+1}$ (spatial mode spacing). The term *single-mode* is here used to specify that only one array mode at one longitudinal mode of the solitary laser array is oscillating. The external reflector may give rise to external cavity modes associated with the selected single mode.

In conclusion, one can say that if only spatial filtering is applied, single-mode operation (single array mode and single longitudinal mode) cannot be achieved. If very selective spectral filtering is applied, single-mode operation can be obtained. Moderate spectral and spatial filtering can be applied simultaneously and can lead to the selection of a single array mode and longitudinal mode.

5.5 Off-Axis Self-Injection Locking Using Conventional Feedback

In the following experimental observations of the behavior of a laser diode array with off-axis self-injection locking using conventional feedback are presented. The experiments have been performed during the present Ph.D. work.

In the locking process, mode discrimination is applied as discussed in Sec. 5.4. Two configurations are considered: (a) feedback from a mirror and (b) feedback from a diffraction grating. These experiments are performed in order to compare the conventional feedback with the phase conjugate feedback used in chapters 9 and 10.

The experimental setup is shown in Fig. 27. The laser diode array is a GaAlAs 10-stripe proton-implanted gain-guided laser array (Array I), with a 100 μm wide emitting junction. It is temperature controlled with a peltier element. The array has a threshold of 0.28 amp (= i_{th}) and a maximum output power of 0.5 watt at 0.9 amp (3.2·i_{th}). The center wavelength, λ_0, of the multimode spectrum at 25°C is 815 nm. The longitudinal mode spacing is $\Delta\lambda_{FP}$ = 0.11 nm. When the array

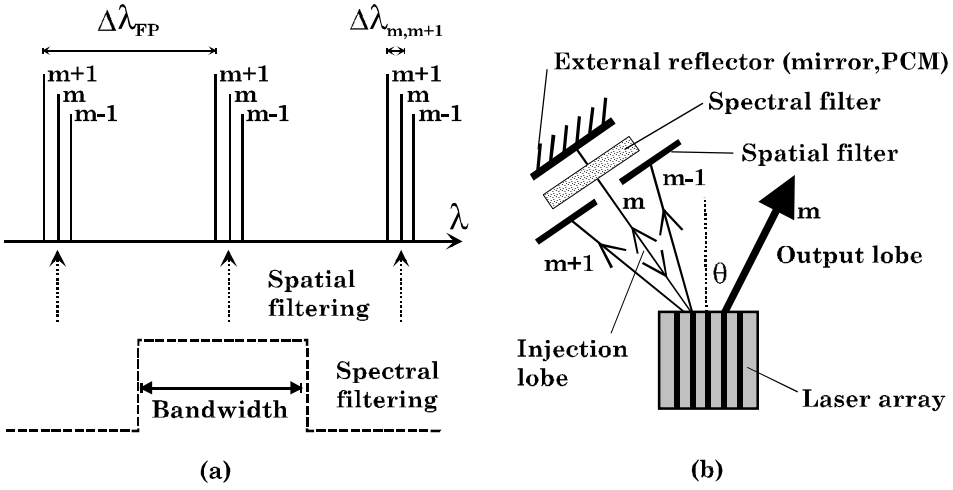

Figure 26. Illustration of the discrimination of array modes in an external cavity. (a) Spatial (dotted arrows) and spectral (dashed line - transmission function) filtering illustrated in the spectral domain. (b) Off-axis self-injection locking configuration for a laser array where spectral and spatial filtering is applied.

runs freely, a band of many spatial modes is oscillating at several longitudinal modes. At a drive current of $3 \cdot i_{th}$ the spectrum has a full width at half-maximum (FWHM) of 1.2 nm corresponding to approximately ten longitudinal modes. The output beam of the array is collimated with a lens (1) along the high coherence axis since collimation in this plane leads to the highest resolution for the diffraction in the grating. A second lens (2) generates a pseudo far-field at a distance of 400 mm from the array. This pseudo far-field is an image of the Fourier plane of the collimating lens (1). A half-wavelength wave plate is inserted in the beam path in order to rotate the polarization 90°. This rotation is of minor importance for the case of conventional feedback (the reflectivity of the grating depends only slightly on the polarization state). However, it has been included in order to draw better comparison with the experiments where phase conjugate self-injection locking is used. A 2° wedge is used as beamsplitter. The two reflections are used for beam diagnostics: one for monitoring the pseudo far-field generated with a lens; the other is directed to a spectrometer with a resolution of 0.02 nm. A coupling loss of approximately 20% occurs between the array and the collimating lens, and additionally 10% is lost at the beamsplitter, the wave plate and the lens (2). The external reflector is placed 610 mm from the laser array. Only one lobe is directed towards the external reflector. The other lobe is picked out by a mirror placed half way through the pseudo far-field, as shown in Fig. 27. Furthermore, a spatial filter is included in the external cavity allowing only a limited number of spatial modes to reach the external reflector, as described is Sec. 5.4. The spatial filter is formed by two razor blades mounted on translation stages, and by adjusting the position of them different array modes can be selected. In the experiments the size of the slit of the spatial filter corresponds to $\simeq 0.6°$ of the far-field and is centered at $\simeq 2°$. According to Fig. 6, this means that only one array will pass the filter. Note that the dashed box in Fig. 27 is rotated 90° around the z-axis.

5.5.1 Off-Axis Self-Injection Locking with a Mirror

First the case where the external reflector is an ordinary mirror is considered. Figure 28 shows the far-field of the laser array for the lateral direction. When the

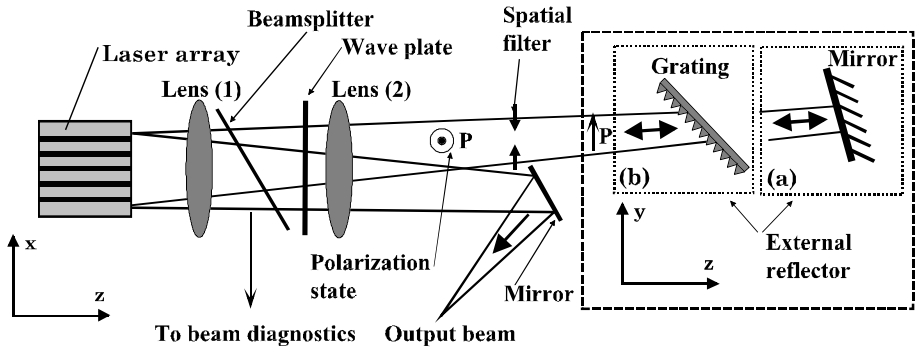

Figure 27. Off-axis self-injection locking of a laser diode array using conventional feedback. The external reflector is either a mirror (a) or a diffraction grating (b). The dashed box shall be rotated 90° around the z-axis of the laser diode array. Spatial filtering is applied using two razor blades in the external cavity.

array runs freely without any feedback, as seen in Fig. 28(a), the far-field consists of several spatial modes, and the characteristic twin-lobe far-field is smeared out to an almost uniform radiation pattern with an FWHM of approximately 4°. The drive current is $2 \cdot i_{th}$. However, when the off-axis feedback is applied, the array is forced to operate at one single spatial mode and the far-field changes to the well known asymmetric twin-lobe, as seen in Fig. 28(b), associated with injection locking. The FWHM of the output lobe is 0.64°, corresponding to only 1.15 times the diffraction limit (see Sec. 2.5.2). If the drive current is increased to $3 \cdot i_{th}$, several spatial modes emerge, and the output lobe broadens, as can be seen in Fig. 28(c).

The mode characteristics in the spectral domain are shown in Figs. 29(a) and (b) for a drive current of $2 \cdot i_{th}$. It is observed that the spectrum for the case where feedback is applied is unaffected by the spatial filtering and the feedback from the mirror. This is obvious since only spatial filtering is applied; the mirror provides no spectral filtering. Using the reflections from the beamsplitter, the effective reflectivity of the external cavity could be measured. The reflectivity ranged from 10% to 6% for an operating drive current of $2 \cdot i_{th}$ to $3 \cdot i_{th}$.

5.5.2 Off-Axis Self-Injection Locking with a Grating

In order to narrow down the spectrum, spectral filtering must be applied in addition to the spatial filtering. This can to some extent be achieved by using a diffraction grating instead of a mirror as external reflector. The experimental setup is shown in Fig. 27. The grating used is a ruled grating which has 1200 lines/mm. The grating is placed in a standard Littrow configuration in such a way that the first order diffraction is fed back towards the laser array.[113] Figures 30(a),(b), and (c) show the far-field pattern for the lateral direction when the laser array runs freely, when feedback is applied at a drive current of $2 \cdot i_{th}$, and when feedback is applied at a drive current of $3 \cdot i_{th}$, respectively. The obtained far-fields are very similar to the ones obtained when a mirror is used as external reflector. Since the spatial filtering is identical for these two cases, this was to be expected. For a drive current of $2 \cdot i_{th}$ the FWHM of the output lobe is only 0.68°, which corresponds to 1.23 times the diffraction limit. The reflectivity measured at the beamsplitter was 4.6% for a drive current of $2 \cdot i_{th}$. The grating also provides spectral filtering which leads to spectrum narrowing effects. Figures 31(a) and (b) show the lasing spectrum of the laser array when the feedback is applied and when it runs freely, respectively. The drive current is $2 \cdot i_{th}$. At this current three longitudinal modes

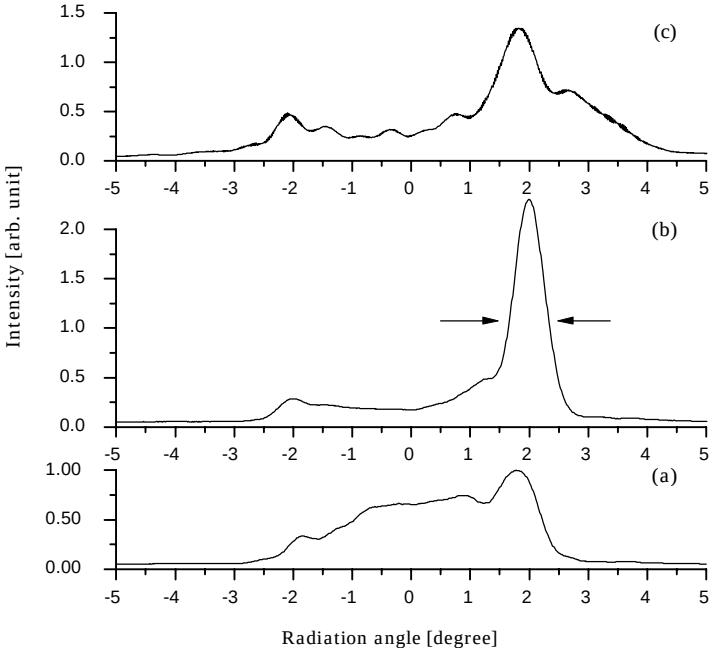

Figure 28. Far-field pattern from a laser diode array for the lateral direction when off-axis self-injection locking using a mirror and spatial filtering is applied. (a) Array runs freely, drive current 2·i_{th}. (b) Feedback is applied, drive current is 2·i_{th}. The FWHM of the output lobe is 0.64°. (c) Feedback is applied, drive current is 3·i_{th}.

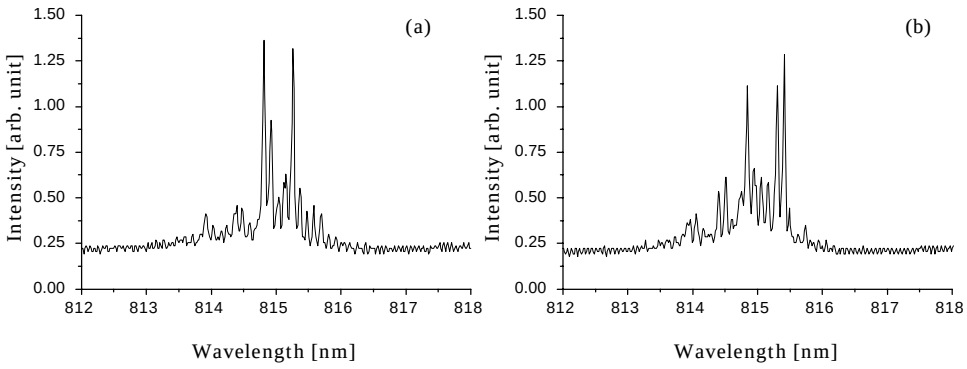

Figure 29. Spectra of a laser diode array when off-axis self-injection locking with a mirror and spatial filtering is applied. (a) Feedback is applied at a drive current of 2·i_{th}.(b) The array runs freely at 2·i_{th}.

are oscillating, and the bandwidth of the spectrum is $3{\cdot}\Delta\lambda_{FP} \simeq 0.3$ nm. For all drive currents a significant narrowing of the spectrum is observed. This is in sharp contrast to the case with the mirror where no narrowing effects are observed.

The center wavelength could be controlled by tilting the grating; the locked spectrum could be shifted over a range of approximately 5 nm around 815 nm. If the grating is tilted outside this range, the modes corresponding to the solitary laser (no feedback) will emerge. As explained in Sec. 5.3.1, the external cavity and the laser array are only weakly coupled. Therefore, the scanning range is

only a few nanometers. This short tuning range is in contrast to a large tuning range for systems that are more strongly coupled (achieved by using the on-axis configuration). For a laser array in such a system a tuning range of more than 30 nm has been reported.[115]

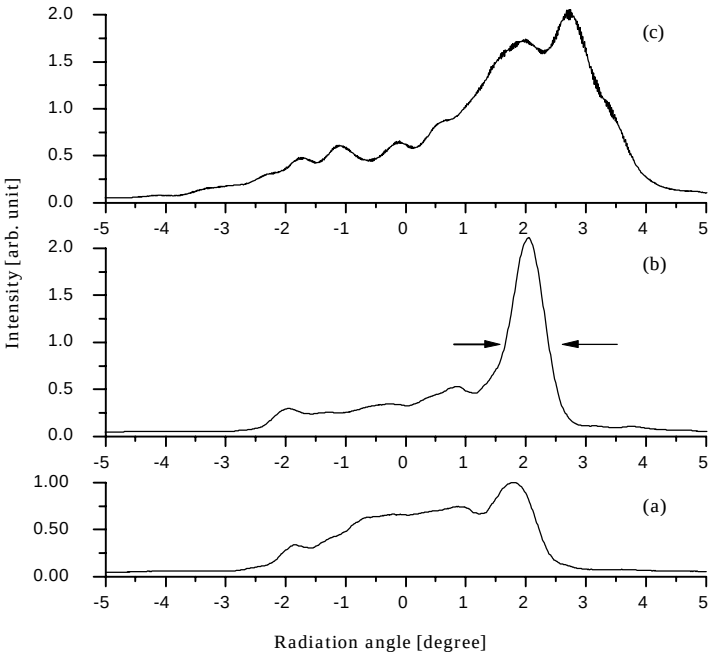

Figure 30. Far-field pattern from a laser diode array for the lateral direction when off-axis self-injection locking using a diffraction grating and spatial filtering is applied. (a) Array runs freely, drive current 2·i_{th}. (b) Feedback is applied, drive current is 2·i_{th}. The FWHM of the output lobe is 0.68°. (c) Feedback is applied, drive current is 3·i_{th}.

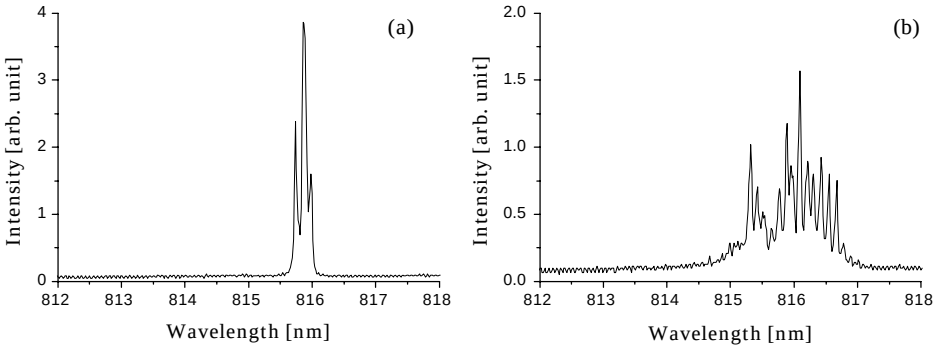

Figure 31. Spectra of a laser diode array when off-axis self-injection locking with a diffraction grating and spatial filtering is applied. (a) Feedback is applied at a drive current of 2·i_{th}.(b) The array runs freely at 2·i_{th}.

6 Self-Induced Frequency Scanning

In this chapter we report on the experimental observations of the behavior of a laser diode array coupled to a self-pumped Cat conjugator in an on-axis configuration. The purpose of these investigations is to understand the fundamental mechanisms of the coupled system. This understanding is crucial in the process of developing high-power laser diode arrays with improved coherence properties and high stability of the output radiation. The focus of the present chapter is on a phenomenon known as *self-induced frequency scanning* that can take place in such a coupled system.

The optical feedback from the self-pumped photorefractive phase conjugator can induce frequency scanning of the lasing wavelength of a multimode laser. The self-scanning effect has been observed with a GaAlAs laser diode coupled to a conjugator in a $BaTiO_3$ crystal[138], with an argon laser[179], with a dye laser[137, 140, 139], and with an AlGaInP laser diode.[180, 181] The wavelength sweep can be as much as 37 nm for a dye laser[140] and 10 nm for a diode laser [138]. The scanning phenomenon has mostly been observed[179, 137, 140, 139, 180, 181] with a phase conjugate mirror arranged in the Cat geometry, in which the beam undergoes total internal reflection in the $BaTiO_3$ crystal, but has also appeared[138] with the crystal in the ring geometry [156]. It has recently been observed that the frequency scanning does not take place when a low-power diode laser is coupled to a stimulated photorefractive backscattering phase conjugator.[181] The fact that the frequency scanning takes place with so many different types of lasers clearly indicates that the scanning is due to some characteristics of the self-pumped phase conjugate mirror (PCM). The exact mechanism and the physical origin of the frequency scanning process have not been established yet. However, in Chapter 7 numerical simulations will show that the material frequency dispersion of the $BaTiO_3$ is the physical origin of the scanning process.

The structure of this chapter is as follows: In Sec. 6.1 an introduction to the phenomenon frequency scanning is given. We report experimental observations of the coupled system. The observations include the dependence of the intensity inside the $BaTiO_3$ crystal on the frequency scanning (Sec. 6.2), and the dependence of the phase conjugate reflectivity of the conjugator on the frequency scanning (Sec. 6.3). These observations show that the frequency scanning has its origin in the photorefractive process. In Sec. 6.4 it is established that the orientation of the internal beam path inside the Cat conjugator changes during the frequency scanning, which suggests that the material frequency dispersion of the $BaTiO_3$ crystal plays an important role in the scanning mechanism. In Sec. 6.5 we present a technique for the suppression of the self-induced frequency scanning with the use of so-called counterbalanced dispersion. The suppression of the scanning increases the wavelength stability significantly. The successful suppression also verifies that the material frequency dispersion of the $BaTiO_3$ crystal is crucial for the scanning process. Finally, in Sec. 6.6 we describe the differences between the frequency scanning in the off-axis configuration as compared with the on-axis configuration. Section 6.7 summarizes the results.

6.1 Experimental Setup - On-Axis Configuration

The experimental setup is shown in Fig. 18. The laser diode array is a GaAlAs 10-stripe gain-guided device (array I - see Appendix A), with a 100 μm wide emitting junction. It is temperature controlled with a peltier element. The array has a threshold of 0.28 amp ($= i_{th}$) and a maximum output power of 0.5 watt at

0.9 amp ($3.2 \cdot i_{th}$). The center wavelength of the spectrum at 25° C is 815 nm. The rhodium doped $BaTiO_3$ crystal is Blue II, which is a 45°-cut crystal. The output beam is collimated with a lens that has a focal length of 4.5 mm. The collimated beam is focused into the crystal by means of an achromat lens with a focal length of 80 mm, which is placed 240 mm from the output facet of the laser array. All the output of the laser array is directed to the crystal in the on-axis configuration. The length of the external cavity is $L_{ext} = 363$ mm. The angle of incidence at the crystal is 54°. The center of the crystal is placed 121 mm after the plane of the lens that is used to focus the beam into the crystal. The spot size measured at the position corresponding to the center of the crystal is 2.12×0.61 mm^2. The reflection of the beamsplitter is directed to a spectrum analyzer in order to monitor the spectrum of the laser diode array.

A few seconds after the crystal has been illuminated, a Cat geometry will be formed in the crystal and the conjugator will start to direct light (optical feedback) back to the laser array. This feedback modifies the lasing spectrum. Figures 32(a-h) display how the lasing spectrum is influenced by the feedback as time elapses.

Figure 32(a) shows the lasing spectrum at time $t = 0$, right before the Cat geometry has been formed (the laser array runs freely). Figure 32(b) shows the spectrum at $t = 2$ s, where the spectrum starts to narrow down to fewer longitudinal modes due to the increased reflectivity of the Cat conjugator. When the spectrum has been narrowed down to a few longitudinal modes, as seen in Fig. 32(c), the spectrum starts to scan towards a longer wavelength, as seen in Fig. 32(d). The spectrum continues to scan towards a longer wavelength, as seen in Fig. 32(e); however, it eventually come to a maximum wavelength and the scanning stops. When the spectrum arrives at this maximum wavelength, the natural modes (freely running) of the laser array will start to emerge again, as seen in Fig. 32(f). The freely running modes will then tend to erase the photorefractive gratings in the $BaTiO_3$ crystal that will eventually reduce the reflectivity of the Cat conjugator. The reduced reflectivity can no longer maintain oscillation at the maximum wavelength, as seen in Fig. 32(g), and the suppression of the freely running modes comes to an end. The freely running modes grow in amplitude and reduce the reflectivity of the Cat conjugator to zero and, as a result, the spectrum becomes freely running (Fig. 32(h)). Figures 32(a-h) correspond to one scan cycle. After a few seconds the Cat geometry will be built up again and the scan cycle is repeated. The scanning can be characterized as the spectrum takes one 'step' at a time. This step corresponds to one longitudinal mode spacing ($\Delta\lambda_{FP}$); one longitudinal mode emerges in front of the scanning spectrum (longer wavelength) while another longitudinal mode behind the spectrum (shorter wavelength) decreases in amplitude and, eventually, stop to oscillate.

Figure 33(a) shows the center wavelength of the scanning spectrum as a function of time. In total eight scan cycles are shown. In Figs. 33(b) and (c) the corresponding reflectivity of the Cat conjugator and the total output power from the laser array, respectively, are shown. Only scanning towards a longer wavelength (red) is observed. The spectrum would, however, occasionally scan a fraction of a nanometer towards a shorter wavelength (blue) or make a stop for a short while before resuming the scanning towards the red. The maximum scan range observed is 8 nm. The angle of incidence, the position of the beam at the crystal surface, and the intensity all affect the scan rate (wavelength shift per unit time). The phase conjugate feedback causes the total output power of the laser array to vary with time. The variation is approximately ±5% of the average output power. As can be seen in Fig. 33(b), the length of one scan cycle varies over time.

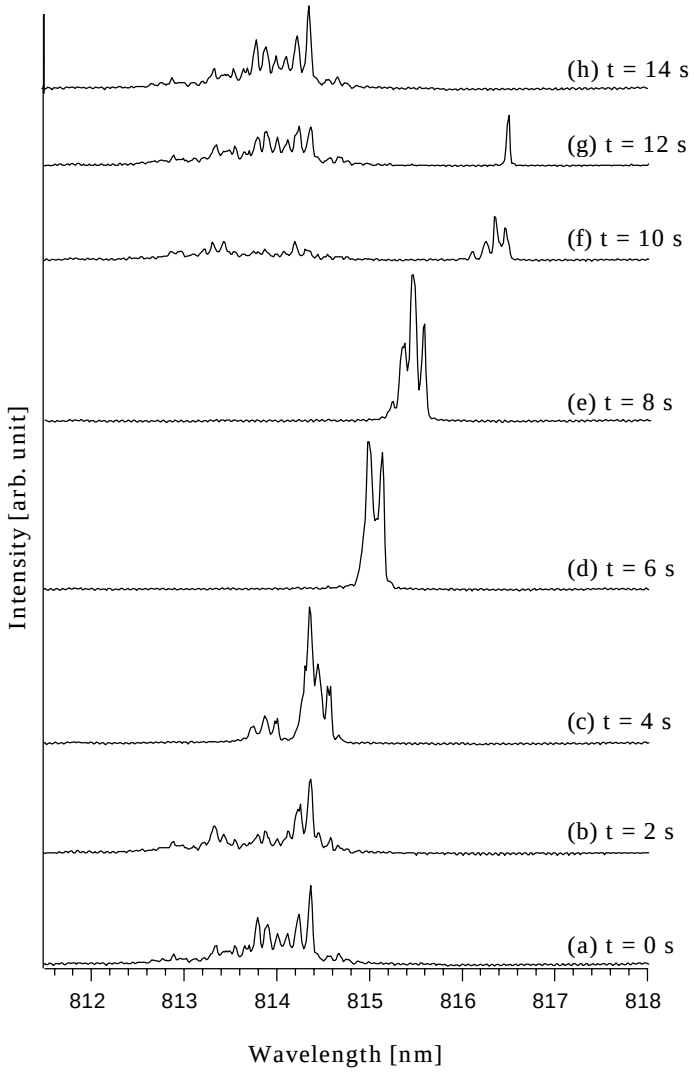

Figure 32. Typical spectrum of a laser diode array coupled to a self-pumped Cat conjugator in the on-axis configuration. The optical feedback causes the spectrum to narrow down to a few longitudinal modes and to scan towards longer wavelength. At a certain wavelength the scanning ceases and shortly after the reflectivity of the Cat conjugator is reduced to zero causing the laser array to become freely running. The Cat conjugator builds up again and the scanning process repeats itself.

6.2 The Dependence of Intensity on Scan Rate

The scan rate depends on the intensity of the incident beam inside the photorefractive crystal. Figure 34 shows the scan rate (wavelength shift per unit time) as a function of intensity at the crystal. The scan rate is determined by fitting a linear function to one cycle of the wavelength versus the time graph (Fig. 33(a)). The scan rate plotted in Fig. 34 has been calculated as an average of the scan rate determined for 20 to 40 scan cycles (the error bars are the standard deviation). In Fig. 34 the maximum phase reflectivity observed during all of the 20 to 40 scan cycles is also shown. The intensity at the crystal has been augmented by increasing the drive current of the laser diode array. The scan rate increases as the intensity at the crystal is augmented.

If the scanning process is due to the photorefractive process, the scan rate

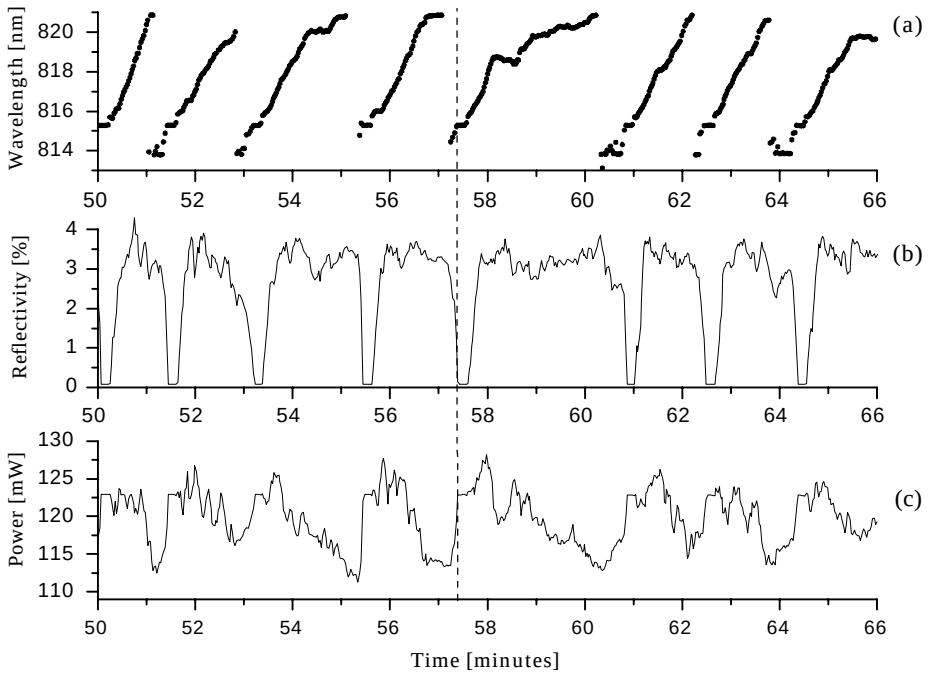

Figure 33. Laser diode array coupled to a self-pumped Cat conjugator in the on-axis configuration. The optical feedback causes the spectrum to scan towards longer wavelength. (a) The center wavelength of the spectrum as a function of time. (b) The reflectivity of the Cat conjugator as a function of time. (d) The output power of the laser diode array as a function of time.

will depend on the response time of the crystal, since it takes a certain amount of time for the grating structure to adjust as the wavelength changes during a scan cycle. The response time of the crystal is inversely proportional to the photoconductivity.[80] Investigations have shown that the photoconductivity in general does not scale linearly with the light intensity (I), but is proportional to I^x where x varies from crystal to crystal ($x \simeq 0.5 - 1.0$).[61, 60] The presence of secondary centers in the crystal leads to $x < 1$.[61] If the scan rate depends linearly on the response time of the crystal, one would expect the following relation

$$\text{scan rate} \propto I^x. \tag{33}$$

The solid line in Fig. 34 is the I^x fit to the scan rate versus the intensity. The fitting procedure yields $x = 1.1 \pm 0.06$ and, consequently, we assume $x = 1$. This number is in agreement with reported data that showed that in a rhodium doped $BaTiO_3$ crystal the response time is inversely proportional to the intensity (i.e. $x = 1$) for intensities higher than ~ 35 mW/mm^2.[70] Moreover, experimental investigations of rhodium doped $BaTiO_3$ have revealed that $x = 1$.[72] One should note that this demonstrates that our rhodium doped crystal may be described by the one center model. The fact that the proportionality given by Eq. 33 is fulfilled suggests that the scan rate does indeed have its origin in the photorefractive process.

From Fig. 34 it is seen that the maximum phase conjugate reflectivity is decreased as the intensity is increased. This means that the feedback coefficient (F) is also decreased with increasing intensity. The scan seems to be unaffected by the reduced reflectivity since the scan rate follows the I^x behavior regardless of the maximum phase conjugate reflectivity. In other words: the observation indicates

that the scan rate does not depend on the phase conjugate reflectivity. This will be discussed in the following section.

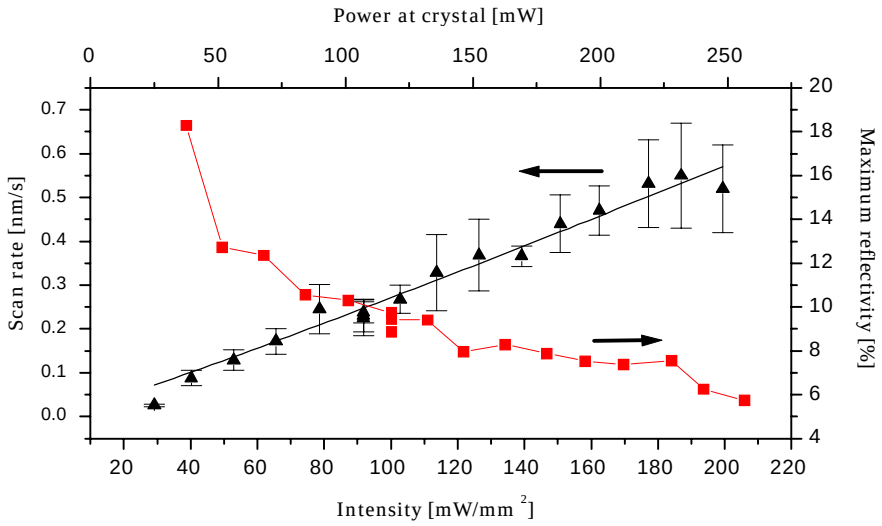

Figure 34. Scan rate and maximum phase conjugate reflectivity versus intensity at the crystal. The solid line is the I^x fit to the scan rate versus intensity. The fitting yields $x = 1.1 \pm 0.06$. The spot size is 2.12 × 0.61 mm^2.

6.3 The Dependence of Reflectivity on Scan Rate

It is of great interest to know whether the scan rate depends on the phase conjugate reflectivity. If the scan rate is independent of the reflectivity, the PCM is the source of the scanning process; for this situation the PCM behaves like a frequency dependent reflecting device (the reflectivity depends on the frequency) that seeds an amplifier (self-injection locking). However, if the scan rate depends on the reflectivity, the scanning process may instead arise due to a mechanism of the coupled cavities.

In order to investigate whether the scan rate depends on the phase conjugate reflectivity or not, a neutral density filter is placed in the external cavity. The neutral density filter has a transmission of 50%, which means that half of the power is absorbed by the filter. For a given drive current to the laser diode array the intensity at the crystal is reduced by half compared with the case where the neutral density filter is removed. Moreover, due to the neutral density filter, the phase conjugate feedback will also be halved by the time it enters the laser array. This means that if the reflectivity of the Cat conjugator is constant for all intensities, the feedback coefficient (F) will be reduced by a factor of $2^2 = 4$. For example, the laser array emits 100 mW and the phase conjugate reflectivity is 10%. This means that the 10 mW is returned to the laser array if the neutral filter is not included. However, if the neutral density filter is placed in the external cavity, only 50 mW will reach the crystal; if the phase conjugate reflectivity is still 10%, then 2.5 mW will eventually be returned to the laser array. This demonstrates that the feedback coefficient will be reduced by a factor of four.

Figure 35 shows the scan rate as a function of the intensity at the crystal when the neutral density filter is included in the external cavity. In the figure we also show the maximum phase conjugate reflectivity measure in front of the crystal, i.e.

the absorption in the neutral density filter has not been deducted. The solid line is the I^x fit to the scan rate as a function of the intensity. The fitting procedure yields $x = 0.98 \pm 0.16$. Similar to the case with no neutral density filter, this suggests that $x = 1$. Since the maximum phase conjugate reflectivity is in general lower than for the case where the neutral density filter is not included (Fig. 34), the feedback coefficient is at least reduced with a factor of four. The dotted line in Fig. 35 is the I^x fit ($x = 1.1 \pm 0.06$) taken from Fig. 34. The two fits (solid and dotted lines) are very similar, which shows that the scan rate does not depend on the feedback level but on the intensity, i.e. the response time of the crystal. In conclusion, it reveals that the self-induced frequency scanning is caused by the photorefractive process in the conjugator and not by a mechanism of the coupled cavities.

A very weak feedback level will not cause self-induced frequency scanning, but will at the most just modify the number of oscillating longitudinal modes. The observations here, however, suggest that the frequency scanning takes place when the phase conjugate reflectivity becomes sufficiently large. The exact threshold level for scanning to take place has not been established, but the data in Fig. 34 indicate that regular scan cycles occur when $R_{ext} > R_{out}$ ($R_{out} \simeq 0.04$ for array I). However, we have observed scanning for $R_{ext} \sim 0.01$.

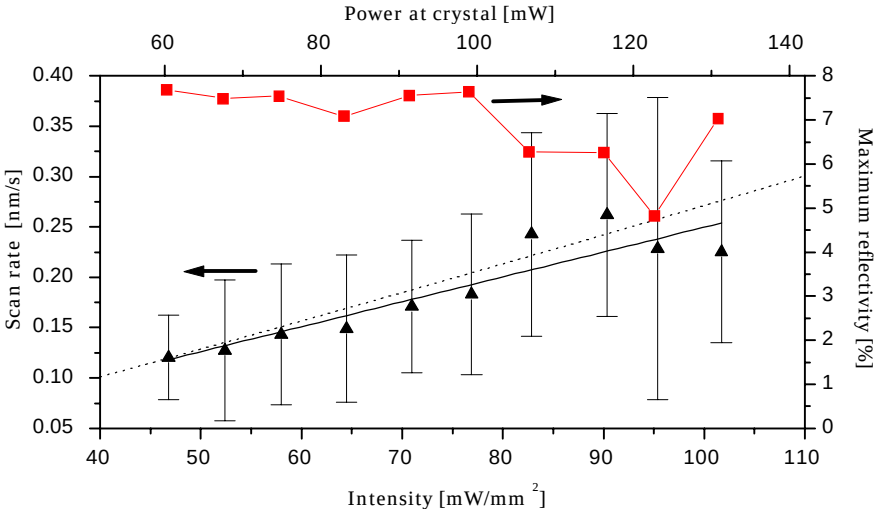

Figure 35. Scan rate and maximum phase conjugate reflectivity versus intensity at the crystal. A neutral density filter with a transmission of 0.5 has been placed in the external cavity in order to reduce the feedback level. The solid line is the I^x fit to the scan rate versus intensity. The fitting yields $x = 0.98 \pm 0.16$. The dotted line is the I^x fit taken from Fig. 34.

6.4 The Internal Beam Path during Scanning

Based on the dependence of the intensity on the scan rate and the fact that the scan rate is independent of the phase conjugate reflectivity, it has been established that the scanning process is closely related to the photorefractive process. During one scan cycle the wavelength changes several nanometers and the angle of refraction (θ_r) at the air crystal interface will therefore also change during a scan cycle. In order to get an understanding of the fundamental mechanisms of the conjugator, we want to investigate whether the beam path inside the crystal

changes during a scan cycle. If this is the case, the frequency material dispersion will play an important role in the scanning process. In this section we investigate the orientation of the internal loop during a scan cycle.

We have recorded the internal beam path in the crystal with a video camera placed above the crystal. Figure 19(b) shows an example of such a recorded image. However, for the measurements performed here the camera was positioned so that the full field of view only covered one quarter of the crystal corresponding to the internal loop in the lower right corner (see Fig. 19(b)). Over a period of 80 seconds an image was recorded every two seconds. During the 80 seconds, the laser system performed three scan cycles. The images were digitized and stored on a computer; the format of the images is 480×640 pixels. During a scan cycle the beam filaments will change, i.e. some will vanish and others will emerge as time elapses. However, as a whole the filaments are to some extent parallel, as can be seen in Fig. 19(b). The purpose of these recordings is to determine the orientation of the internal loop as a function of time. This is done in the following way. First we perform an edge detection process on the 40 digitized images. The edge detection algorithm is described in Ref. [182]. The detected edges in an image form to some extent straight lines. The orientation of one detected edge is determined by calculating the orientation of the best linear fit to the edge. Next, the orientation of the internal loop is calculated as the average of the orientation of all the detected edges. This is performed for all 40 images.

Figure 36 shows the orientation of the internal loop as a function of time. The orientation is given in degrees. The orientation angle is measured between the direction of the internal loop and the normal of the crystal surface where the beam enters the crystal.

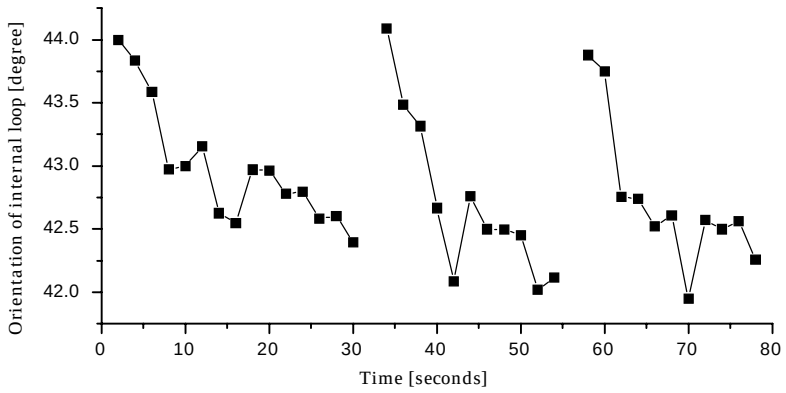

Figure 36. Orientation of the internal loop in a self-pumped Cat conjugator. The orientation is given as an angle. The angle is measured between the direction of the internal loop and the normal of the crystal surface where the beam enters the crystal. The full time period (0-80 s) corresponds to three scan cycles.

It is seen from the figure that the orientation of the internal loop changes as time passes. At time $t = 0$ the laser runs freely, and at $t \approx 30$ seconds the scanning spectrum has reached the maximum wavelength in the first scan cycle. The period $t = 0$-80 seconds should be compared with three scan cycles in Fig. 33. During the scan cycles, the orientation follows a regular cycle that is synchronized with the change in wavelength. As the wavelength becomes longer, the orientation angle

is decreased. This can be understood in terms of the dispersion of the crystal. The refractive index in the $BaTiO_3$ crystal is dependent on the optical frequency (dispersion) and, consequently, the angle of refraction (θ_r) at the air crystal interface is increased as the wavelength becomes longer. In order to maintain the same orientation of the grating vectors - which we may assume gives the highest beam coupling [183] - the orientation angle of the internal loop must subsequently also decrease. This is in agreement with the data shown in Fig. 36. The orientation angle changes by almost 2°. The angular dispersion at 813 nm is on the order of $\partial\theta_r/\partial\lambda = 2.8{\cdot}10^{-5}$ rad/nm (see Appendix D). If the wavelength during one scan cycle changes, e.g. 6 nm, the angular change is only $\Delta\theta_r \simeq 0.01°$. If the Cat conjugator tries to maintain the same orientation of the grating vectors, and compensates a change in θ_r by adjusting the orientation of the internal loop, this small change of $\Delta\theta_r \simeq 0.01°$ cannot explain the huge change in the orientation angle of almost 2°. However, in conclusion the orientation of the beam path in the crystal changes during self-induced frequency scanning. In Sec. 6.5 it will be shown that even though the effect of the dispersion is small, it turns out that the dispersion does play a crucial role in the mechanism of frequency scanning.

6.5 Suppression of Scanning Using Counterbalanced Dispersion

In this section we investigate a laser diode array coupled to a self-pumped phase conjugator based on a $BaTiO_3$ crystal arranged in the Cat geometry. We introduce a new concept: *counterbalanced dispersion*. We show that counterbalanced dispersion can be used to suppress the self-induced frequency scanning and to stabilize the output. The index of refraction of the $BaTiO_3$ crystal is dependent on the optical frequency (dispersion) and we investigate how the frequency scanning is altered by the angular dispersion of the different optical elements inserted into the experimental setup. Experimental data that demonstrate the concept are presented. It is verified that the scanning can be suppressed, and it is established that the material frequency dispersion of the $BaTiO_3$ crystal plays an important role in the frequency scanning process.

6.5.1 Counterbalanced Dispersion from Prisms

We examine the self-induced frequency scanning experimentally using the two setups presented in Figs. 37(a) and 37(b), and it is shown how the scanning behavior can be significantly changed by dispersive prisms placed in front of the $BaTiO_3$ crystal. For reasons given below we will name the setup in Fig. 37(a) the dispersion *enhancement* setup and the setup in Fig. 37(b) the dispersion *compensation* setup, respectively. The laser array is array I (see Appendix A) lasing at 811 nm (λ_0). The light is collimated with a lens (L1) and is sent through four 45° BK7 prisms and one 60° SF10 prism that are all oriented at minimum deviation to add angular dispersion to the system. After passing through the prisms the beam is focused by a lens (L2) and directed to the phase conjugate mirror which is made of a 0°-cut rhodium doped (800 ppm) $BaTiO_3$ crystal (Blue III). The crystal is placed after the focal point of lens L2 and is arranged in a self-pumped Cat configuration with an angle of incidence of $\theta_i = 60°$. The half-wave plate (WP) ensures that the incident beam at the crystal surface is extraordinarily polarized. The reflection from the beamsplitter (BS) is directed to a spectrometer so that the spectrum of the output of the laser array can be monitored.

The compensation setup is almost identical to the enhancement setup; the prisms, however, have been oriented differently with respect to the laser array

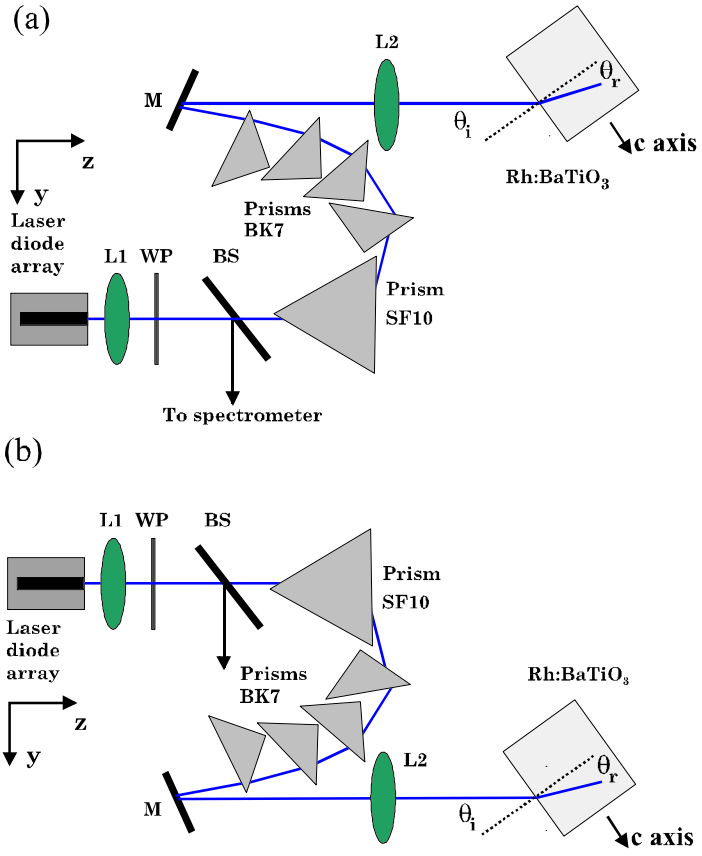

Figure 37. Experimental setups with prisms. The laser diode array is coupled to a phase conjugate mirror. L1: lens $f = 4.5$ mm, L2: achromat lens $f = 80$ mm, BS: beamsplitter, M: mirror, WP: half-wave plate; (a) dispersion enhancement setup, (b) dispersion compensation setup.

and the crystal. The dispersion of the prisms has different signs for the enhancement and the compensation setups. Using ray tracing with *Optica*^{TM} for Mathematica^{TM} the angular dispersion of the beam after refraction at the air crystal interface (θ_r in Fig. 37) is calculated by inserting accurate information about the experimental setup. If the dispersion of the prisms is ignored, the angular dispersion after refraction at the air crystal interface itself can be estimated to $d\theta_r/d\lambda = 3 \cdot 10^{-5}$ rad/nm (see Appendix D). The total angular dispersion of the prisms, the lenses and the refraction at the air crystal interface is calculated to $9 \cdot 10^{-5}$ rad/nm for the enhancement setup and to $-6 \cdot 10^{-5}$ rad/nm for the compensation setup, respectively. When the laser array has been switched on and the crystal is illuminated, dynamic gratings start to form in the crystal and, as a result, the reflectivity of the PCM is slowly increased. The phase conjugate feedback forces the spectrum of the laser array to narrow down from approximately ten longitudinal modes to a few modes and the center wavelength of the spectrum starts to shift towards a longer wavelength, as explained in Sec. 6.1. This behavior is identical for the enhancement and the compensation setups. Moreover, it also occurs if all the prisms are removed and, instead, the beam from the laser array is passed directly to the crystal (see Sec. 6.1), which means that the initial stage of the self-induced frequency scanning process is due to properties of the formed gratings in the crystal and has nothing to do with the prisms placed in front of the PCM. As the lasing wavelength of the output from the laser array

scans towards a longer wavelength, the angle of incidence (θ_i in Fig. 37), the angle of refraction (θ_r), and the position of the beam at the crystal surface change due to the dispersion of the prisms and the crystal. For the compensation setup the dispersion of the prisms is sufficiently large to cancel the angular dispersion of the air crystal interface. If dispersion is the origin and is responsible for the frequency scanning, then one may expect scanning for the enhancement setup and none, or at least reduced scanning - or even scanning towards a shorter wavelength - for the compensation setup.

Figure 38 shows the recorded center wavelength of the lasing spectrum from the laser array as a function of time. Figure 38(a) present data from the enhancement setup while Fig. 38(b) show data from the compensation setup. As is seen in Fig. 38(a), we do observe the well known self-induced frequency scanning cycles for the enhancement setup, as was to be expected. Due to the phase conjugate feedback, the spectrum scans away from the wavelength, λ_0, and the oscillating energy between the laser array and the crystal gradually decreases as the spectrum moves further away. After some time the spectrum has scanned several nanometers and the reduced feedback level can no longer suppress the oscillation of the natural modes of the freely running laser; the natural modes then emerge and erase whatever grating is left in the crystal. Consequently, the reflectivity of the PCM is reduced to zero, and the center wavelength jumps back to λ_0. The cycle is thereafter repeated. Only scanning towards the red was observed. The spectrum, however, would occasionally scan a fraction of a nanometer towards the blue or make a stop for a short time before resuming the scanning towards the red. The angle of incidence, the position of the beam at the crystal surface and the intensity all affect the scan rate. All these observations are identical to the ones reported in Sec. 6.1 where the array was coupled to the Cat conjugator without including the prisms in the setup. For the data shown in Figs. 38(a-b) the laser array was operated at two times the threshold current. The power of the incident beam at the crystal was 100 mW and the intensity was 250 mW/mm^2.

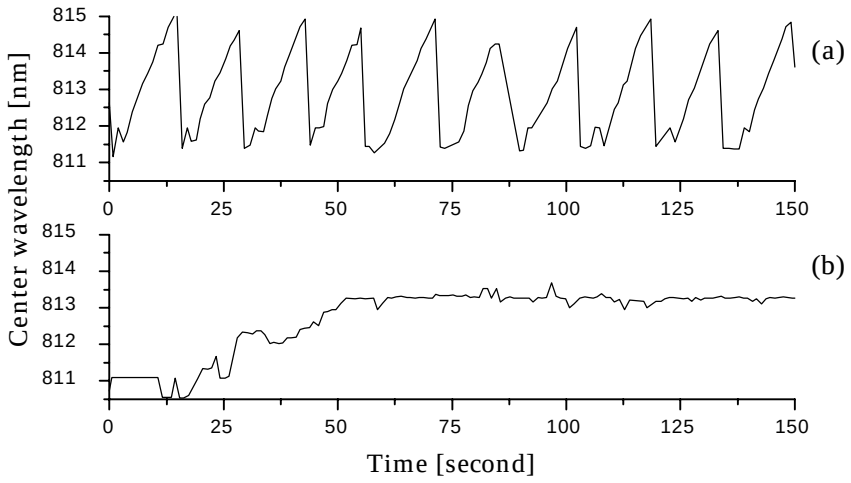

Figure 38. Laser diode array coupled to a phase conjugate mirror in the on-axis configuration. Prisms are included in the external cavity. Center wavelength of the optical spectrum versus time: (a) dispersion enhancement setup with prisms; (b) dispersion compensation setup with prisms.

Figure 38(b) displays the recorded center wavelength versus time for the com-

pensation setup. No regular scan cycles are observed but after the reflectivity of the PCM has been built up, the spectrum starts to scan until it reaches some equilibrium, where the effective round-trip gain of the cavity has become symmetric with respect to the center wavelength of the spectrum, i.e. the side modes of the spectrum have the same phase conjugate reflectivity (see Sec. 7.1 for a detailed description), and the output power and the spectrum become stable. The maximum phase conjugate reflectivity measured at the beamsplitter was 1.6% and 2.8% for the enhancement and the compensation setups, respectively. The higher phase conjugate reflectivity observed in the compensation configuration is due to the stabilization of the center wavelength that leads to a larger index modulation in the crystal.

Figure 38(b) clearly shows that for the compensation setup the dispersion of the prisms has suppressed the frequency scanning. We refer to this as *counterbalance dispersion* since the dispersion of the $BaTiO_3$ crystal is compensated by the prisms. In order to suppress the frequency scanning, a certain amount of counterbalance dispersion must at least be applied. With less dispersion applied, the scan cycles continue. If the four BK7 prisms were removed, the frequency scanning could not be suppressed.

6.5.2 Counterbalanced Dispersion from a Grating

In order to verify that the angular dispersion of the prisms is indeed responsible for the different types of behavior observed with the enhancement and the compensation setups, we replace the prisms with a diffraction grating. The experimental setups are shown in Figs. 39(a) and (b) and are also named the enhancement setup and the compensation setup, respectively. The only difference between the enhancement and the compensation setups is that the crystal has been turned upside down. The position of the beam at the crystal surface remains the same. This is equivalent to reversing the sign of the external angular dispersion of the grating. For the case with the prisms one can also change the enhancement setup to the compensation setup, and vice versa, by simply turning the crystal upside down as shown here. The dashed and solid lines in Figs. 39 correspond to a shorter (blue) and a longer (red) wavelength, respectively. It can be seen that by turning the crystal upside down and maintaining the position of the beam at the crystal surface, the angle of incidence is interchanged between the 'blue' and the 'red' wavelengths.

Figures 40(a) and (b) show the center wavelength of the spectrum versus time for the enhancement setup and the compensation setup, respectively. The laser array was operated at two times the threshold current and the incident beam intensity was 120 mW/mm^2. Again, it is observed that regular scan cycles take place with the enhancement setup and that the scanning is suppressed with the compensation setup due to the counterbalance dispersion of the grating. The build-up time for stabilization depends on many experimental parameters, such as angle of incidence and spatial position of the beam at the crystal surface. The initial scan rate is therefore not always higher for the compensation configuration than for the enhancement configuration, as can be seen in Fig. 38(b). The maximum phase conjugate reflectivity measured at the beamsplitter was 3.2% and 5.5% for the enhancement and the compensation setups, respectively.

In conclusion, the completely different kind of behavior observed for the compensation and the enhancement setups show that the material frequency dispersion of the crystal plays a vital role for the mechanism of the self-induced frequency scanning and can even be the very origin of the scanning effect.

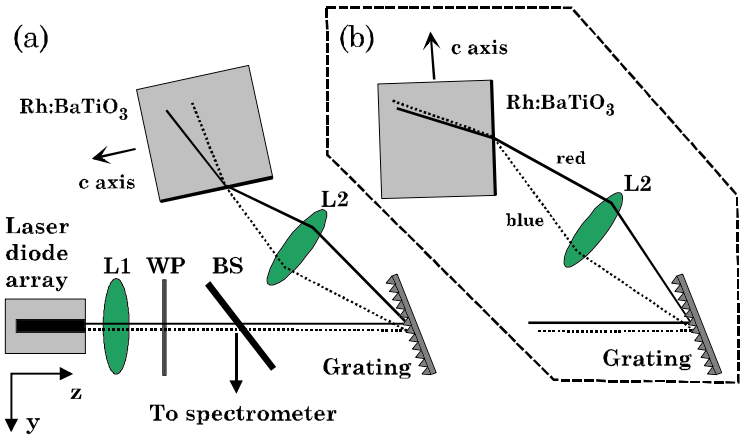

Figure 39. Experimental setups with grating. L1: lens f = 4.5 mm, L2: spherical lens f = 100 mm, WP: wave plate, BS: beamsplitter, grating: 1200 lines/mm, ruled with a blaze angle of 26.4 deg. (750 nm); (a) dispersion enhancement setup; (b) dispersion compensation setup (the $BaTiO_3$ crystal is turned upside down, but the position of the beam at the surface is maintained).

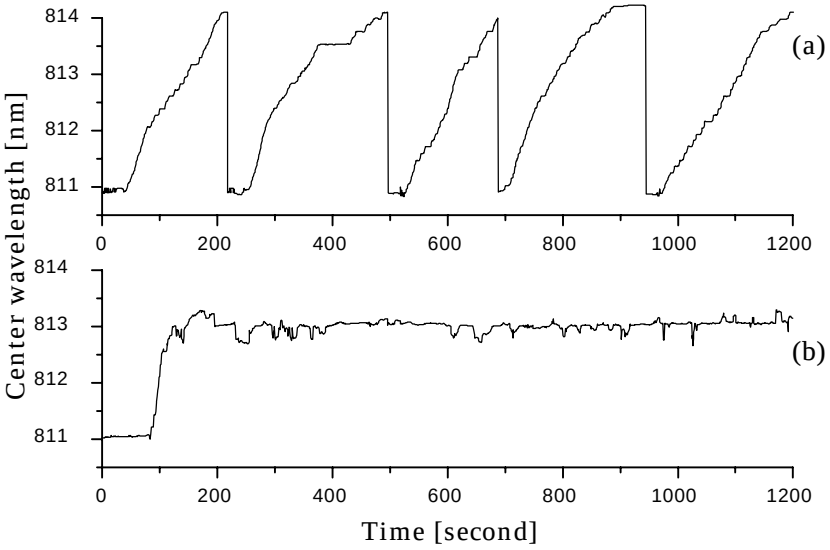

Figure 40. Laser diode array coupled to a phase conjugate mirror in the on-axis configuration. A diffraction grating is included in the external cavity. Center wavelength of the optical spectrum versus time: (a) dispersion enhancement setup with grating; (b) dispersion compensation setup with grating.

6.6 Frequency Scanning with Off-Axis Configuration

The self-induced frequency scanning cycle does only take place if both far-field lobes from the laser array are directed towards the Cat conjugator crystal (on-axis configuration). If only one lobe of the far-field is directed towards the Cat conjugator crystal (the off-axis configuration), the frequency scanning will take place, but the scan cycle will not repeat itself. Instead, the spectrum will come to

a rest at a certain wavelength where it will remain.[12, 15] For other types of lasers such as dye lasers or fundamental-mode diode lasers the off-axis configuration is of course not possible, and the scan cycle will in general be repeated for such coupled systems. The reason for the nonrepetitive behavior of the off-axis configuration may be attributed to the reduced coupling of the off-axis configuration as compared with the on-axis configuration (the reduced coupling is discussed in Sec. 5.3.1); the reduced coupling is not strong enough to shift the spectrum so much that the freely running modes will emerge and erase the grating structure in the crystal, which causes the scan cycle to repeat itself.

6.7 Summary

The scan rate is found to be proportional to the intensity inside the crystal. Furthermore, the scan rate does not depend on the feedback level but only on the intensity, i.e. the response time of the crystal. These observations reveal that the self-induced frequency scanning is due to the photorefractive process in the conjugator.

We have found that the orientation of the beam path in the crystal changes during self-induced frequency scanning. Moreover, we have shown that the self-induced frequency scanning of a laser diode array with external phase conjugate feedback from a self-pumped $BaTiO_3$ crystal arranged in the Cat configuration is significantly altered by the dispersion of prisms or a dispersive diffraction grating placed in the external cavity in front of the crystal. We have demonstrated that these prisms or the grating can even suppress the self-induced frequency scanning and stabilize the output power of the laser array. The experimental results show that the material frequency dispersion of the $BaTiO_3$ crystal is an important effect for the self-induced frequency scanning process.

7 Physical Origin of Frequency Scanning

In Chapter 6 it was shown that the optical feedback from a self-pumped photorefractive phase conjugator can cause self-induced frequency scanning of the lasing wavelength of a multimode laser. Moreover, it was demonstrated that the frequency scanning of a laser diode array could be suppressed and that it was possible to obtain a stable wavelength with the use of counterbalance dispersion from prisms or from a grating placed between the laser and the phase conjugate mirror (PCM), as shown in Sec. 6.5.

The fact that the frequency scanning takes place with so many different types of lasers clearly indicates that the scanning is due to some characteristics of the self-pumped conjugator. The exact mechanism and the origin of the frequency scanning process have not been established yet. Several explanations of the origin have been suggested: (1) mode competition in coupled cavities,[137] (2) accumulated Doppler shifts stemming from reflection of spontaneously moving gratings in the photorefractive crystal[140] and (3) asymmetric Bragg frequency selectivity of the photorefractive grating structure.[138] Here we rule out explanation (1) since frequency scanning has been observed in a single resonator formed between an ordinary mirror and a PCM.[140] The competition, however, has an effect on the scanning behavior; will be discussed later in this chapter. As pointed out in the literature[138], one can also rule out explanation (2) since the response time of the $BaTiO_3$ crystal is too low to explain the high scan rates that have been observed. The phase conjugate feedback forces the spectrum many nanometers away from the wavelength at which the gain medium has the highest gain and, as a result, the laser system does not seem to seek the wavelength that has the largest overall optical gain. Therefore, explanation number (3) seems very likely and in the present chapter we argue that the frequency scanning is indeed caused by asymmetric Bragg frequency selectivity of the complex grating structure formed in the crystal.

From the experiments with counterbalanced dispersion (Sec. 6.5) it is known that the material frequency dispersion of the $BaTiO_3$ crystal plays a crucial role in the frequency scanning process. The numerical results of this chapter confirm that the dispersion of the crystal is the origin of the asymmetric Bragg frequency selectivity which subsequently induces the scanning in frequency. However, from Sec. 6.4 we know that the orientation of the internal loop changes much more during a scan cycle than what can be explained by the angular dispersion (the air crystal interface) in the $BaTiO_3$ crystal. This tells us that there may be additional effects that cause the orientation of the internal loop to change during frequency scanning, but we still postulate that dispersion causes the frequency scanning process to initiate.

We investigate and analyze a multimode laser coupled to a PCM. The optical feedback is generated by self-pumped four-wave mixing in $BaTiO_3$ arranged in the Cat geometry. The analysis is based on a direct numerical approach that describes the propagation of light in photorefractive media. This approach is a powerful tool and has been used to analyze complex structures of light propagating in photorefractive media.[184, 185, 97, 186] The Cat geometry has been studied in details with this method.[97] Here we extend the method to study the shape of the detuning curve for the grating structure in the crystal and, thereby, also the characteristics of the conjugator as an external reflector.

We present numerical simulations that show that the complex grating structure formed in the crystal has asymmetric Bragg frequency selectivity that will

result in self-induced frequency scanning. The findings show that the asymmetric Bragg selectivity is due to the material frequency dispersion of the $BaTiO_3$ crystal. The results predict frequency scanning towards a longer wavelength, which are in general in agreement with reported experimental observations.

The structure of this chapter is as follows: In Sec. 7.1 the fundamental physics of the mechanisms of the self-induced frequency scanning are explained. Moreover, the basis and the approximations for the model are outlined. Section 7.2 presents the numerical approach and mathematical formulation of the model. In Sec. 7.3 the iterative process of the formation of the self-pumped grating structure is described. Finally, in Sec. 7.4 we give a presentation and discussion of the numerical results obtained. Section 7.5 summarizes the results.

7.1 Model of Frequency Scanning

In this section we present a model of the fundamental physical mechanisms behind the frequency scanning process. We explain how the scanning takes place and how the frequency material dispersion of the crystal leads to an asymmetric detuning curve.

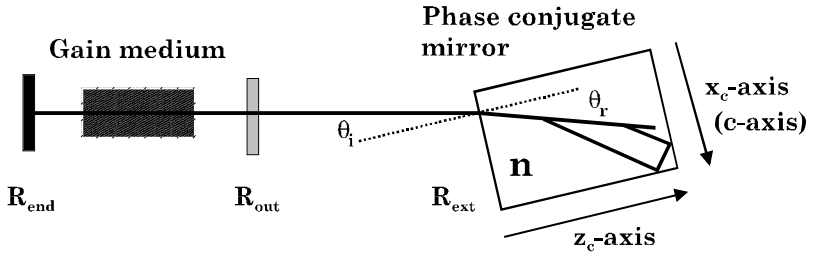

Figure 41. Schematic diagram of the laser cavity coupled to a self-pumped phase conjugator arranged in a Cat geometry. R_{end} and R_{out} are the frequency independent reflectivity of the end mirror and the output mirror, respectively. R_{ext} is the frequency dependent phase conjugate reflectivity of the conjugator. n is the refractive index in the $BaTiO_3$ crystal.

Figure 41 shows a schematic diagram of the coupled system that we want to investigate. The multimode laser has been simplified to a gain medium and two mirrors. The end mirror and the output mirror are assumed to have a frequency independent reflectivity of R_{end} and R_{out}, respectively. The output beam is directed to a $BaTiO_3$ crystal with an angle of incidence θ_i. Due to the refractive index of the crystal n the beam is refracted at the air crystal interface at an angle θ_r. The phase conjugate beam is generated by diffraction in a complex grating structure in the $BaTiO_3$ crystal. The PCM, however, acts on the laser like an external mirror with a wavelength dependent phase conjugate reflectivity R_{ext}. The shape of the reflectivity R_{ext} with respect to wavelength is equivalent to the detuning curve of the grating structure in the conjugator crystal. The question is: how can the center wavelength of the spectrum shift? Imagine that R_{ext} is asymmetric with respect to the center wavelength of the laser spectrum. The PCM can then cause the spectrum to shift in the following way: the phase conjugate feedback from the conjugator generally results in a more narrow bandwidth and at some moment in time, denoted t_0, the phase conjugate feedback reduces the multimode spectrum to, say, three modes, as shown in Fig. 42(a). The dashed line represents the envelope of the laser spectrum. The center mode has a wavelength of λ_0. The two side modes have wavelengths of $\lambda_{-1} = \lambda_0 - \Delta\lambda_{FP}$ and $\lambda_{+1} = \lambda_0 + \Delta\lambda_{FP}$, where $\Delta\lambda_{FP}$

is the longitudinal mode spacing of the solitary laser cavity. The center mode at λ_0 will experience the lowest loss upon reflection of the PCM corresponding to a reflectivity of $R(\lambda_0)_{ext}$. The two side modes experience a higher loss than the center mode. The side mode λ_{+1}, however, has a lower loss than λ_{-1}, i.e. R_{ext} is asymmetric and $R(\lambda_{-1})_{ext} < R(\lambda_{+1})_{ext}$. As time elapses, on the order of a few round trips in the external cavity ($t_c > \tau_{ext}$), the side mode λ_{+1} will increase in amplitude at the expense of the side mode λ_{-1}, as shown in Fig. 42(b). As a result, the center of the envelope of the spectrum is not λ_0 anymore, but has been shifted a small amount to $\lambda_0 + \delta\lambda$, where $\delta\lambda$ is much smaller than $\Delta\lambda_{FP}$. After this small shift the dynamic gratings in the photorefractive crystal will adjust for maximum Bragg reflection at $\lambda_0 + \delta\lambda$ (R_{ext} has its maximum for $\lambda_0 + \delta\lambda$). The cycle is then repeated and at some moment the center wavelength has been shifted by almost $\Delta\lambda_{FP}$ and a new side mode at $\lambda_0 + 2\Delta\lambda_{FP}$ will appear as the side mode at $\lambda_0 - \Delta\lambda_{FP}$ has been completely drained from energy.

7.1.1 Scan Rate

In our model the spectrum so to speak scans by taking one longitudinal 'step' at a time; this description of the scanning process is in agreement with our experimental observations of a highly resolved laser spectrum during the scanning (see Fig. 32 in Sec. 6.1). The time period of the spectrum to take one 'step' depends on the time constant for the grating formation in the crystal since the dynamic gratings need time to adjust to the shifted spectrum. For $BaTiO_3$ this time constant is on the order of one second and is orders of magnitude larger than the cavity round-trip time. This is the reason for the relatively slow scan rates that are observed (less than 0.6 nm/s; corresponding to a few longitudinal 'steps' per second).

7.1.2 The Effect of Dispersion

How does the dispersion of the crystal cause the detuning curve to become asymmetric? It can be explained as follows: imagine that the multimode laser beam with a spectrum corresponding to the one in Fig. 42(a) has written a grating structure in the crystal. If one sends a probe beam into the crystal (colinear with the writing beam), the detuning curve of the structure can be evaluated as the wavelength is tuned throughout the adjoining wavelengths of λ_0. Let us focus on one single grating in the structure. The angle of incidence at this particular grating inside the crystal is the Bragg angle when the probe wavelength is λ_0. Even when the probe wavelength is tuned away from λ_0, the angle of incidence will be fixed if no dispersion is present in the crystal. For this case the detuning curve of the particular grating will be symmetric with respect to λ_0. This will apply to all the gratings of the structure, and the effective detuning curve of the structure in the conjugator becomes symmetric, i.e. $R(\lambda_{-1})_{ext} = R(\lambda_{+1})_{ext}$. If dispersion is present, however, the angle of incidence of the particular grating will change when the angle of refraction θ_r is altered as the wavelength is tuned away from λ_0, and the diffracted energy off the grating will be asymmetric with respect to λ_0. This will hold true for all the gratings of the structure, and the effective detuning curve of the structure in the conjugator becomes asymmetric, i.e. $R(\lambda_{-1})_{ext} \neq R(\lambda_{+1})_{ext}$. If the angle of incidence at the crystal surface is 0°, the angle of refraction is constant ($= 0^\circ$) even though the presence of dispersion; the detuning curve is expected to be symmetric and frequency scanning should not occur. For a phase conjugator based on stimulated backscattering with an angle of incidence is 0°, it has been observed that self-induced frequency scanning indeed does not take place.[180] This observation supports that the dispersion leads to an asymmetric detuning curve.

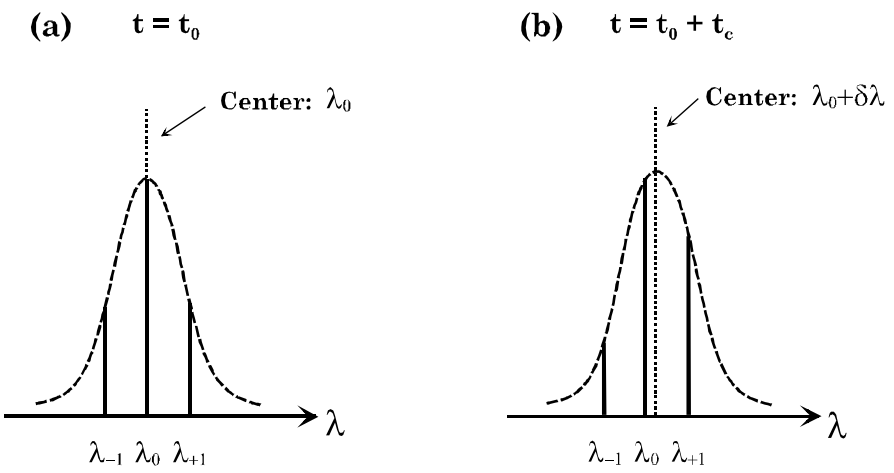

Figure 42. Schematic representation of the spectrum of the laser coupled to the conjugator during self-induced frequency scanning. (a) the three-mode spectrum at some moment in time $t = t_0$; (b) the three-mode spectrum at time $t = t_0+t_c$, where t_c is on the order of a few round trips in the external cavity. The center wavelength has been shifted slightly with respect to λ_0 due to asymmetric feedback (asymmetric detuning curve).

7.1.3 Mode Competition in the Cavities

In this simple description of the scanning mechanism the questions about competition in the coupled cavities and spatial mode competition in the gain medium have been left out. Such effects will influence the effective shape of the asymmetric detuning curve and have impact on the dynamic aspects of the scanning process. Experimental observations[137] have shown that the competition in the coupled cavities determines the scanning behavior of the system, i.e. whether the spectrum scans towards a longer (red) or a shorter (blue) wavelength. The effects of the coupled cavities may especially be important when investigating, e.g., dye lasers that have an output mirror (R_{out}) with a large reflectivity (> 0.9). For laser diodes, however, with $R_{out} \approx 0.04$ the system can as a better approximation be viewed as a single resonator, i.e. $R_{out} \equiv 0$, and the effects may be neglected; for this case the scanning behavior is fully described by determining the asymmetry of the feedback (the detuning curve). In other words: if the detuning curve of the phase conjugator is asymmetric, this asymmetry will certainly lead to frequency scanning in a single resonator formed between a mirror and a phase conjugate mirror.

7.1.4 Effect of Coherence Length

For self-induced frequency scanning there will always be more than one oscillating longitudinal mode, at least in the sense where the amplitude of one new mode builds up at the expense of the amplitude of an existing mode. The effective bandwidth is therefore in that case at least on the order of a mode spacing. It is often, however, observed that several longitudinal modes are present in the scanning spectrum (see, e.g., Fig. 32). Especially for laser diodes, the bandwidth can therefore be on the order of 0.1-0.5 nm. The coherence length of the incident beam can consequently be much smaller than the dimensions of the conjugator crystal. It has been observed that under such circumstances reflection gratings will be short and weak and will contribute only with a small amount to the phase

conjugate beam.[102] With an incident beam that has a short coherence length, the asymmetric detuning curve must therefore have its origin in the characteristics of the transmission gratings that are always present in a Cat conjugator with total internal reflection. For dye lasers coupled to a Cat conjugator the situation is different. The laser cavity is long and, as a result, the mode spacing is very short. In some experiments performed with a dye laser the coherence length was 20 cm.[140, 139] For that case reflection gratings may be present and have influence on the shape of the effective detuning curve of the grating structure. The presence of reflection gratings will be discussed in details in Chapter 8.

The model presented in the following section includes only transmission gratings and neglects all reflection gratings. This approximation is valid only if the coherence length of the incident beam is short compared with the dimension of the crystal (see Chapter 8). The outcome of the following analysis can therefore only be compared with the experiments with multimode laser diodes that have a short coherence length during scanning, as explained above.

7.2 Mathematical Formulation of the Model

In this analysis the $BaTiO_3$ crystal is illuminated with a spectrum that contains three longitudinal modes that propagate in the crystal. With the use of a beam propagation method the evolution of the modes is determined. Due to fanning the illumination will eventually form a self-pumped four-wave-mixing geometry based on total internal reflection. When the phase conjugate reflectivity has reached its steady state, a probe beam is sent into the crystal to evaluate the phase conjugate reflectivity at different wavelengths, especially at λ_{-1} and λ_{+1}, in order to obtain the detuning curve and confirm the hypothesis of an asymmetric shape of the detuning curve. It should be noted that the approach described in the following only takes into account transmission gratings. All reflection gratings have been neglected as discussed in Sec. 7.1.

7.2.1 The Band Transport Equation

The dynamic charge distribution in photorefractive media can be described by the well known band transport model, which was discussed in Sec. 3.3. The frequency scanning effect has been observed in both rhodium doped crystals (Chapter 6), in cobalt doped crystals [181], in chromium doped crystals (Chapter 8), and in undoped $BaTiO_3$ crystals [138]. Therefore, the scanning mechanism must be due to some fundamental aspects of the photorefractive effect. Moreover, as discussed in Sec. 6.2 rhodium doped crystals can be described by the one center model. Therefore, we can use the one center band transport model. The photovoltaic current is neglected since its contribution to the induced space charge field in barium titanate is small (a few percent only).[187] Equations 16-19 can be combined into one differential equation; in the diffusion dominated regime the normalized space charge field $\widetilde{\mathbf{E}}_s$ in a one-dimensional approach can be expressed by the following equation[97]

$$\begin{aligned} & \widetilde{\mathbf{E}}_s + \tau_{di}\frac{1}{I}\left(1+\frac{1}{k_d}\frac{\partial}{\partial x}\widetilde{\mathbf{E}}_s\right)\frac{\partial}{\partial t}\widetilde{\mathbf{E}}_s - \frac{1}{k_d^2}\frac{\partial^2}{\partial x^2}\widetilde{\mathbf{E}}_s\left(1+\frac{1}{k_d}\frac{\partial}{\partial x}\widetilde{\mathbf{E}}_s\right)^{-1} \\ = \; & -\frac{1}{I}\frac{1}{k_d}\frac{\partial}{\partial x}I, \end{aligned} \tag{34}$$

where

$$
\begin{aligned}
\widetilde{\mathbf{E}}_s &= \mathbf{E}_s/\mathbf{E}_q; \\
\mathbf{E}_q &= eN_A/\epsilon_{eff}k_d; \\
\tau_{di} &= (N_A\epsilon_{eff}\gamma_r)/(sN_D\mu e); \\
k_d &= (e^2N_A/k_BT\epsilon_{eff})^{\frac{1}{2}}.
\end{aligned}
$$

Here k_d is the characteristic Debye wave number, I is the intensity, and $\widetilde{\mathbf{E}}_s$ is the amplitude of the generated space charge field due to charge imbalance that has been normalized with the maximum value of the space charge field, $\mathbf{E}_q$, corresponding to a charge separation of $2\pi/k_d$. The normalized space charge field is dimensionless. The value τ_{di}/I^0 corresponds to the characteristic dielectric time constant[80], where I^0 is some characteristic intensity (e.g., at the center of the beam). Moreover, N_D is the density of donors, N_A is the density of acceptors, e is the electron charge, s is the photoexcitation constant, γ_r is the recombination constant, μ is the carrier mobility, k_B is Boltzmann's constant, T is the temperature, t is the time, and ϵ_{eff} is the effective low frequency (static) dielectric constant in the direction of the grating wave vector ($\overline{\mathrm{k}}_g$).

In deriving Eq. 34 it has been assumed, which is often the case[97], that $n_e \ll N_A \ll N_D$ and $\epsilon_{eff}\gamma_r/\mu e \gg 1$, where n_e is the electron density. The space charge field, which is a function of space and time, is the unknown to be found for known illumination I originating from the incident laser beam.

7.2.2 Wave Propagation in the Crystal

The problem is limited to two dimensions: one transverse direction ($\widehat{x}_c$) and one longitudinal direction ($\widehat{z}_c$). The orientation of the coordinate system for the crystal is shown in Fig. 41. The incident beam is extraordinarily polarized (TM) and has the electric field vector in the $\widehat{x}_c$-$\widehat{z}_c$-plane. The direction of the spontaneous polarization (c-axis) coincides with the direction of the positive $\widehat{x}_c$-axis. This configuration corresponds to a 0°-cut crystal. The longitudinal direction is the predominant direction of propagation of the incident beam, which means that we can assume that the intensity in space varies much more along the transverse direction than along the longitudinal direction. The beam propagation in a medium with small spatially varying perturbation of the refractive index, which is the case for an illuminated photorefractive crystal, is described by the Helmholtz wave equation

$$\nabla^2\overline{E} + k^2\overline{E} = 0, \tag{35}$$

where $\overline{E}$ is the complex amplitude of the electromagnetic field, k is the wave vector in the medium and ∇^2 is the Laplacian operator. It is assumed that the angle of propagation of all the beams with respect to the $\widehat{z}_c$-axis is small as compared with unity ($\theta_r \ll 1$) and that the field is taken in the form $\overline{E} = E_0(x,z)e^{ikz_c}$, where i is the complex imaginary unit. The generated space charge field, $\mathbf{E}_s$, modifies the crystal refractive index through the electro-optical effect. The refractive index is given by $n = n_0 + \triangle n(\mathbf{E}_s)$, where n_0 is the refractive index with no illumination which is taken to be a linear function of the wavelength

$$n_0(\lambda) = n_0(\lambda_0) + (\lambda - \lambda_0)\frac{\partial n_0}{\partial \lambda}, \tag{36}$$

where λ_0 is the wavelength around which the refractive index has been expanded. In practice the material dispersion coefficient $\partial n_0/\partial\lambda$ is negative corresponding to *normal* dispersion. The opposite case is here referred to as *anomalous* dispersion. The relation between the space charge field and the change in the refractive index

is given by Eq. 22, $\triangle n = -\frac{1}{2}n_0^3 r_{eff}\mathbf{E}_s$, where r_{eff} is the effective electro-optic coefficient. The coefficient r_{eff} depends on the direction of the grating vector $\overline{K_g}$, but is taken to be constant over the narrow range of propagation angles. Absorption has been neglected and the refractive index is taken to be a real value. With $k = k_0 n$, where $k_0 = 2\pi/\lambda$ is the wave vector in vacuum, the expressions for n and $\overline{E}$ are inserted into Eq. 35. With the use of the slowly varying envelope approximation the following equations that govern the propagation of the electromagnetic radiation inside the crystal are obtained[97]

$$\left(\frac{\partial}{\partial z_c} - \frac{i}{2k}\frac{\partial^2}{\partial x_c^2}\right) E_0^f(x_c, z_c) = 2i\gamma_0 \widetilde{\mathbf{E}}_s E_0^f(x_c, z_c), \tag{37}$$

$$\left(-\frac{\partial}{\partial z_c} - \frac{i}{2k}\frac{\partial^2}{\partial x_c^2}\right) E_0^b(x_c, z_c) = 2i\gamma_0 \widetilde{\mathbf{E}}_s E_0^b(x_c, z_c), \tag{38}$$

where $\gamma_0 = -\frac{1}{4}n_0^2 k_0 r_{eff}\mathbf{E}_q$ is the nonlinear coupling constant. The field envelope $E_0(x_c, z_c)$ has been labeled with a f (forward) for the field propagating along the $\widehat{z}_c$ axis and with a b (backward) for the field propagating in the opposite direction, respectively.

7.2.3 Spatial Profile of Input Beam

The spatial envelope of the beam that is launched into the crystal has a Gaussian shape and has a spectrum of three longitudinal modes with equal amplitude: one center mode at a wavelength of λ_0 and two side modes at λ_{-1} and λ_{+1}, respectively. In front of the entrance surface of the crystal the beam is sent through a lens with a focal length r. For a positive focal length the focal point is after the entrance surface of the crystal and for a negative focal length the beam diverges inside the crystal. In the crystal the beam is launched at a propagating angle θ_r with respect to the $\widehat{z}_c$-axis, as shown in Fig. 41. The field at the entrance of the crystal (inside the crystal) for each mode is taken to be [97]

$$\begin{aligned} E_0^{f,p}(x_c, z_c = 0) \quad = \quad & A_p \exp\left(-ik^p \tan(\theta_r^p) x_c - \left(2\frac{x_c - x_{off}}{w_0}\right)^2 + \right. \\ & \left. ik^p \frac{(x_c - x_0)^2}{2r}\right) + E_{noise}^p, \end{aligned} \tag{39}$$

where w_0 is the spot size and is the full width of the intensity profile measured at $1/e^2$, A_p is the amplitude, x_{off} is an offset along the $\widehat{x}_c$-axis, p is the mode index and E_{noise}^p is superimposed low-intensity broadband background radiation that is here referred to as noise.

7.2.4 Noise

The operation of all self-pumped phase-conjugation geometries are based on optical noise. The noise may be due to scattering caused by imperfections at the crystal surface or throughout the crystal volume. In the model the noise (E_{noise}^p) is superimposed on the illumination at the entrance surface of the crystal. The superimposed noise of the three modes are uncorrelated. The power spectrum of the noise has a Gaussian envelope with a full width at half-maximum of 30° centered around θ_r^p. The angle of 30° is similar to the value used in Ref. [97], but the value may be explained as follows: when a laser beam enters a crystal, the scattered light will predominantly propagate in the same direction as the laser, but will have a certain divergence.

The total power of the noise for each mode is 10^{-2} of that of its Gaussian kernel. The total intensity is given by

$$I(x_c, z_c) \equiv I_d + \sum_{\lambda_p} I_p \tag{40}$$

$$= I_d + \sum_{\lambda_p} \frac{n_0}{2\eta_0} \left(\left| E_0^{f,p}(x_c, z_c) \right|^2 + \left| E_0^{b,p}(x_c, z_c) \right|^2 \right), \tag{41}$$

where η_0 is the impedance of vacuum. Even with no illumination of the crystal, thermal generation of carriers will take place, which leads to dark conductivity. Therefore, an equivalent dark intensity I_d is added to Eq. 40. The dark intensity is taken to be constant within the crystal and is set to 10^{-3} of that of the peak intensity of the sum of the Gaussian kernels.[97]

7.2.5 Solver Algorithm

The problem can be significantly simplified by replacing the terms $(1+k_d^{-1}\frac{\partial}{\partial x_c}\widetilde{\mathbf{E}}_s)$ in Eq. 34 with unity. This step is equivalent to assuming that $\left|k_d^{-1}\frac{\partial}{\partial x_c}\widetilde{\mathbf{E}}_s\right| \ll 1$, a criterion that is fulfilled when the modulation of the intensity is small and the fringe spacing is larger than the Debye fringe spacing. For the grating structures presented in Sec. 7.4 the term $\left|k_d^{-1}\frac{\partial}{\partial x_c}\widetilde{\mathbf{E}}_s\right|$ is found to be less than 0.25 within the entire crystal and has a few spikes of up to 0.5. Furthermore, a direct comparison of the results obtained with and without the nonlinear terms for a self-formed four-wave mixing geometry has been reported.[184] The conclusion of that study was that the replacement of the nonlinear terms with unity had no significant influence. These facts justify the simplification performed here.

In order to solve the problem Eqs. 34, 37, and 38 must be solved simultaneously. The $\widehat{x}_c$-$\widehat{z}_c$-plane, which has a size of $\mathrm{l}_x \times \mathrm{l}_z$, is divided into a grid of 3000×1000 points with equal spacing along each dimension. Equation 34 depends only on the x_c-coordinate, and the space charge field, $\widetilde{\mathbf{E}}_s(x_c, z_c)$, can be determined along the $\widehat{x}_c$-axis (for fixed z_c) independently for each slide at z_c. For a known intensity distribution $I(x_c)$ (for given z_c) Eq. 34 can be solved with the following time averaged finite-difference scheme

$$\begin{aligned} &\frac{\widetilde{\mathbf{E}}_{s,v}^{u+1} + \widetilde{\mathbf{E}}_{s,v}^{u}}{2} + \tau \frac{1}{I_v^u} \frac{\widetilde{\mathbf{E}}_{s,v}^{u+1} - \widetilde{\mathbf{E}}_{s,v}^{u}}{\Delta t} \\ &-\frac{1}{2k_d^2} \left(\frac{\widetilde{\mathbf{E}}_{s,v+1}^{u+1} - 2\widetilde{\mathbf{E}}_{s,v}^{u+1} + \widetilde{\mathbf{E}}_{s,v-1}^{u+1}}{\Delta x^2} + \frac{\widetilde{\mathbf{E}}_{s,v+1}^{u} - 2\widetilde{\mathbf{E}}_{s,v}^{u} + \widetilde{\mathbf{E}}_{s,v-1}^{u}}{\Delta x^2} \right) \\ = \; &-\frac{1}{I_v^{u+1}} \frac{1}{k_d} \frac{I_{v+1}^{u+1} - I_{v-1}^{u+1}}{2\Delta x}, \end{aligned} \tag{42}$$

where v is the index along the transverse direction and u is the time index. The constant Δx is the sampling period along the $\widehat{x}_c$-axis and Δt is the time step. In this study the use of time averaging in the finite-difference scheme was found important since it enhanced the stability and the convergency of the solution. The replacement of the nonlinear terms $(1 + k_d^{-1}\frac{\partial}{\partial x_c}\widetilde{\mathbf{E}}_s)$ with unity, as discussed above, has the immense benefit that the final system of equations (Eq. 42) becomes tridiagonal and can be solved very fast numerically with a ready-to-use algorithm.[188]

According to Eqs. 37 and 38 $E_0(x_c, z_c)$ depends on both the x_c- and z_c-coordinate and can be solved with a finite-difference Crank-Nicholson type scheme. In this

thesis a wide-angle propagation method based on a generalized Douglas finite-difference scheme is applied.[189]

7.2.6 Fanning

Fanning is necessary for the build-up of the grating structure of the Cat geometry. As discussed in Sec. 4.5, the origin of fanning is amplification of scattered light by energy coupling (two-wave mixing) between the scattered beam (noise) and the incident beam itself. Figure 43 shows a numerically generated example of the fanning phenomenon. The figure displays the total intensity distribution throughout the crystal. The beam is launched into the crystal from the left-hand side and propagates towards the right-hand side. The initial propagation angle is θ_r = -2°. All other parameters are given in Table 2. The crystal surface at $z_c = \mathrm{l}_z$ is here taken to be transparent. It is observed that the superimposed noise causes the beam to split up into a fan of light. The noise is amplified by a two-wave mixing process and, as a result, the launched beam is almost drained from energy by the time it reaches the crystal surface at $z_c = \mathrm{l}_z$. The numerical results have been obtained by solving Eqs. 37 and 42.

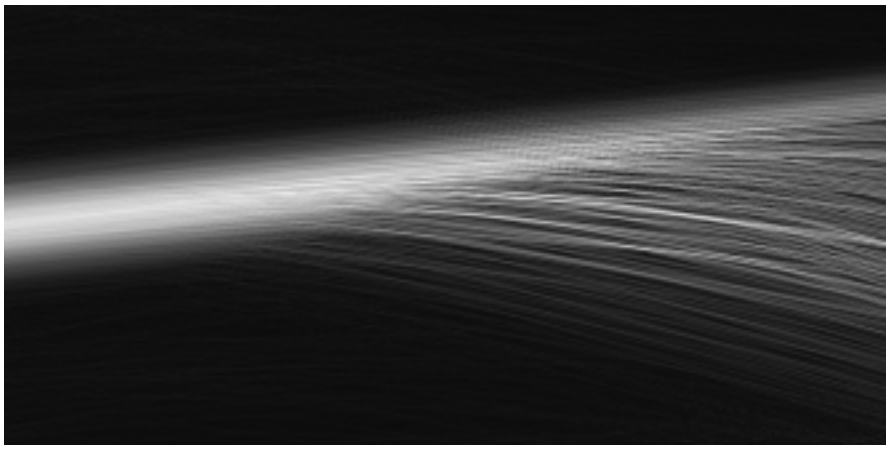

Figure 43. Example of fanning. Image of the total intensity distribution throughout the crystal. A single beam is sent through the crystal with no reflection at the end face of the crystal. The crystal is 0.25 mm wide and 1.0 mm long. The entrance surface is to the left. The c-axis points downwards.

7.3 The Formation of Gratings in the Cat Geometry

As the fields corresponding to the three modes propagate in the crystal, the side walls of the crystal, $x_c = 0$ and $x_c = \mathrm{l}_x$, are taken to be ideally reflecting. The forward propagating field $E_0^f(x_c, z_c = l_z)$ incident at the back of the crystal face at $z_c = \mathrm{l}_z$ is decomposed into Fourier harmonics. Due to the fanning a fraction of the beam propagates at angles different from the angle at which the beam was launched into the crystal (θ_r). Those incident at angles larger than 12° ($= \theta_{TIR}$) undergo total internal reflection; the rest are totally transmitted. The reflected field is transformed back into the space domain and becomes the backward propagating field $E_0^b(x_c, z_c = l_z)$. The procedure for the simulations is as follows: the three longitudinal modes are launched into the crystal one at a time. The field

corresponding to each mode propagates forward to the end of the crystal where a part of it undergoes total internal reflection. The reflected part of the field then propagates backward to the entrance surface of the crystal. In order to increase the formation of the grating structure for the backward propagation, broadband noise is added to the reflected part of the field. The power spectrum of the noise has a Broadband Gaussian envelope with a full width at half-maximum of 100° centered around the $\widehat{z}_c$-axis. The total power of the noise is $5{\cdot}10^{-3}$ of that of its Gaussian kernel at $E_0^f(x_c, z_c = 0)$. After the backward propagation of the three modes, the total intensity distribution throughout the $\widehat{x}_c$-$\widehat{z}_c$-plane is calculated according to Eq. 40. The space charge field is thereafter determined by solving Eq. 42. When the space charge field has been determined, one time step is taken and the three modes are again launched into the crystal for which the refractive index $n(x_c, z_c)$ has been slightly modified due to the space charge field through the electro-optical effect, and so on. As time elapses, the gratings will become stronger and, eventually, a self-pumped Cat geometry will form.

The output field $E_0^{b,p}(x_c, z_c = 0)$ of the Cat geometry is characterized by the reflectivity R and the phase conjugate fidelity H, determined by the relations[97]

$$R^p = \frac{\int_0^{l_x} \left| E_0^{b,p}(z_c = 0) \right|^2 dx_c}{\int_0^{l_x} \left| E_0^{f,p}(z_c = 0) \right|^2 dx_c}; \tag{43}$$

$$H^p = \frac{\left| \int_0^{l_x} E_0^{b,p}(z_c = 0) E_0^{f,p}(z_c = 0) dx_c \right|^2}{\left(\int_0^{l_x} \left| E_0^{b,p}(z_c = 0) \right|^2 dx_c \right) \left(\int_0^{l_x} \left| E_0^{f,p}(z_c = 0) \right|^2 dx_c \right)}, \tag{44}$$

The reflectivity and fidelity, as defined here, are measures of how large a fraction of the launched energy that is returned back through the entrance surface (z_c= 0) and how large a fraction that is sent back towards the laser, respectively. The reflectivity and the fidelity can have a value between zero and unity.

7.4 Numerical Results and Discussion

To keep the computational CPU time at a reasonable level, the dimensions of the nonlinear crystal and the beam size have been made smaller than the typical size of a crystal used for experiments. The result of the small crystal and beam sizes is that the number of layers of the generated gratings is low and, consequently, the grating structure is not very wavelength selective. Based on the beam size used in the nurmerical analysis, the wavelength selectivity of the transmission gratings has decreased roughly ten times compared with experiments. In order to enhance the interference of the gratings formed by the three longitudinal modes, the mode spacing used with these simulations is accordingly increased by a factor of ten. The mode spacing of a laser diode is typically 0.1 nm. In these simulations the mode spacing is $\Delta\lambda_{FP} = 1$ nm. The initial propagation angle θ_r^p of the side modes is determined by the refractive index. The angles θ_r^p are calculated by setting the angle of incidence at the crystal to $\theta_i = 60°$ for all the longitudinal modes. θ_r^p is calculated based on the refractive index and by subtracting the constant angle offset $\sin^{-1}\left(\sin(60°)/n_0\left(\lambda_0\right)\right) - 2°$ so that $\theta_r^0 = 2°$ for the center mode λ_0. For all the simulations presented in this chapter the parameters are given in Table 2.

The reflectivity and fidelity of the three modes are increased to more than 0.90 at $t = 10$ s. Steady state, i.e. where the reflectivity and fidelity asymptotically approach a maximum value, is typically reached at $t = 20$-30 s. At steady state the reflectivity generally approaches 0.99 and the fidelity becomes more than 0.95 for all the longitudinal modes. Figure 44 displays an image of the total intensity

distribution throughout the crystal for $t = 50$ s for a typical simulation. It is observed that most of the energy of the main beam bends towards the corner and is retroflected due to total internal reflection.

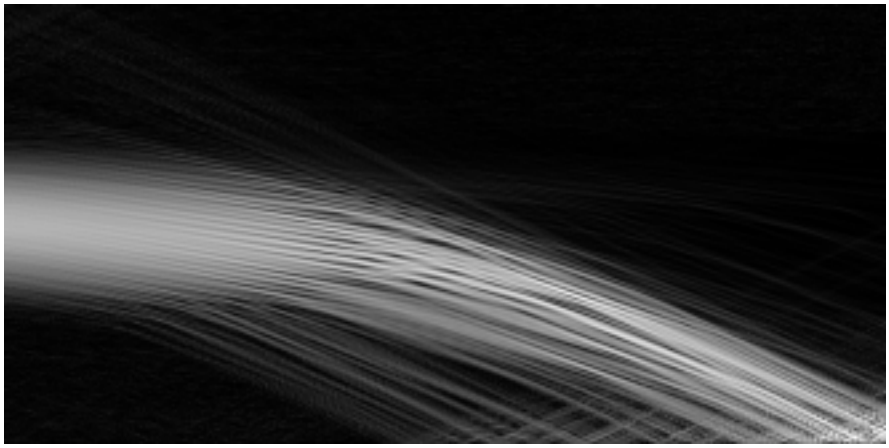

Figure 44. Image of the total intensity distribution throughout the crystal for a Cat geometry. The crystal is 0.25 mm wide and 1.0 mm long. The entrance surface is to the left. The c-axis points downwards.

Figure 45 displays the total intensity distribution $I(x_c, z_c = 0)$ at the entrance surface of the crystal for the simulation shown in Fig. 44. Both the launched input

Parameter	Value	Unit	Note	Reference
l_x	$2.5{\cdot}10^{-4}$	m		[97]
l_z	$1.0{\cdot}10^{-3}$	m		[97]
λ_0	814	nm		
$\Delta\lambda_{FP}$	1.00	nm		
n_0	2.40	-		[80]
w_0	$6{\cdot}10^{-5}$	m		
N_A	$2{\cdot}10^{22}$	m^{-3}		[190, 186]
N_D	$1{\cdot}10^{25}$	m^{-3}		[190]
ϵ_{eff}	$850{\cdot}\varepsilon_0$	F/m	a	[54]
ε_0	$8.85{\cdot}10^{-12}$	F/m		
r_{eff}	$8.10{\cdot}10^{-9}$	m/V		[185, 97]
I_p	$80{\cdot}10^{3}$	W/m^2	b	
$\gamma_0 l_z$	9.35	-		[185, 97]
s	$1{\cdot}10^{-6}$	m^2/J		[190]
μ	$5{\cdot}10^{-5}$	m^2/Vs		[80]
γ_r	$5{\cdot}10^{-14}$	m^3/s		[190, 191]
τ_{di}/I_p	1.1	s		
Δt	$1{\cdot}10^{-1}$	s		
x_{off}	$1.25{\cdot}10^{-4}$	m		
$\lvert\triangle n\rvert_{max}$	$5.8{\cdot}10^{-3}$	-		
θ_r^0	2.0	degree	c	[185]
r	$\pm 2.4{\cdot}10^{-3}, \infty$	m		

Table 2. Parameters used in all the numerical simulations. a: Corresponds to 25° between grating vector and c-axis, see Eq. 23. b: Peak intensity for one mode. c: Initial propagation angle for the center mode.

beam containing all the three modes and the phase conjugate beam (all three modes) have been plotted in the graph. It is seen that the profiles of the input beam and the phase conjugate beam are almost identical (H = 0.96). Only in the range from 0 to 0.025 mm of the distributions is there a slight mismatch which is caused by energy that has been retroflected due to total internal reflection at the corner but has escaped the gratings, as can be seen in the upper left corner of Fig. 44.

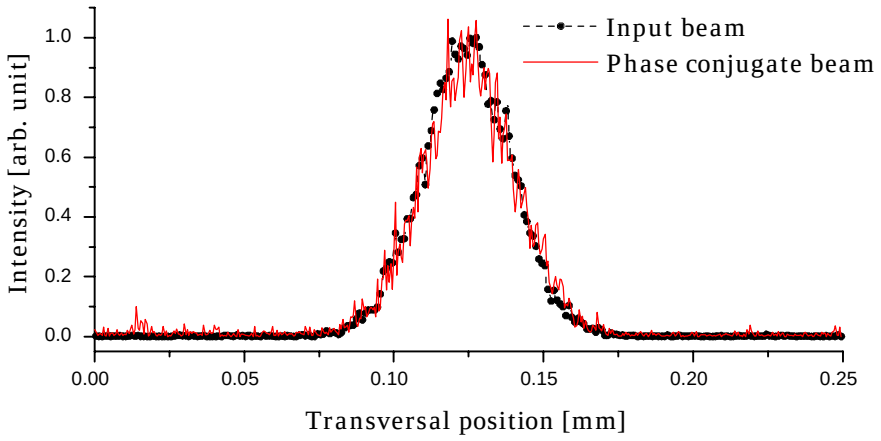

Figure 45. Cross section of total intensity at the entrance surface (z_c = 0). Both the input beam (solid dots) and the phase conjugate beam (solid line) are shown. The profiles are a summation of the intensity profiles corresponding to the three longitudinal modes.

7.4.1 Detuning Curve of the Grating Structure

When steady state has been reached, the characteristics of the grating structure of the Cat conjugator generated by the three modes can be evaluated by launching a probe beam with a wavelength λ into the crystal. The probe is propagated forward and backward through the crystal and, finally, the reflectivity and fidelity given by Eqs. 43 and 44, respectively, are calculated. By probing at several wavelengths the detuning curve can be obtained. Figure 46(a) shows a typical reflectivity detuning curve. The simulation parameters are given in the figure caption. The maximum reflectivity is 0.97 and is found at $\lambda = \lambda_0$, as was to be expected. The huge range of 100 nm on the abscissa is due to the very low wavelength selectivity of the grating structure, as discussed previously. As the wavelength is detuned with respect to λ_0, the amount of reflected energy is of course decreasing.

In Fig. 46(b) the fidelity detuning curve is shown. The maximum fidelity is found at $\lambda = \lambda_0$, as was to be expected. The shape has a few local minimums, which also is observed for a single transmission grating.[192] The wavelength selectivity, defined as the fidelity at full width at half-maximum, is found to be as large as 16 nm. Due to the nature of the phase conjugate beam (the distortion correction theorem) as it propagates back towards the laser through lenses, etc., a larger fidelity means that more energy will eventually be directed back into the gain medium of the laser. By comparing the wings of the detuning curve in Fig. 46(b) it is clearly seen that the curve is asymmetric with respect to the center wavelength (λ_0) of the spectrum that originally wrote the grating structure. For the scanning

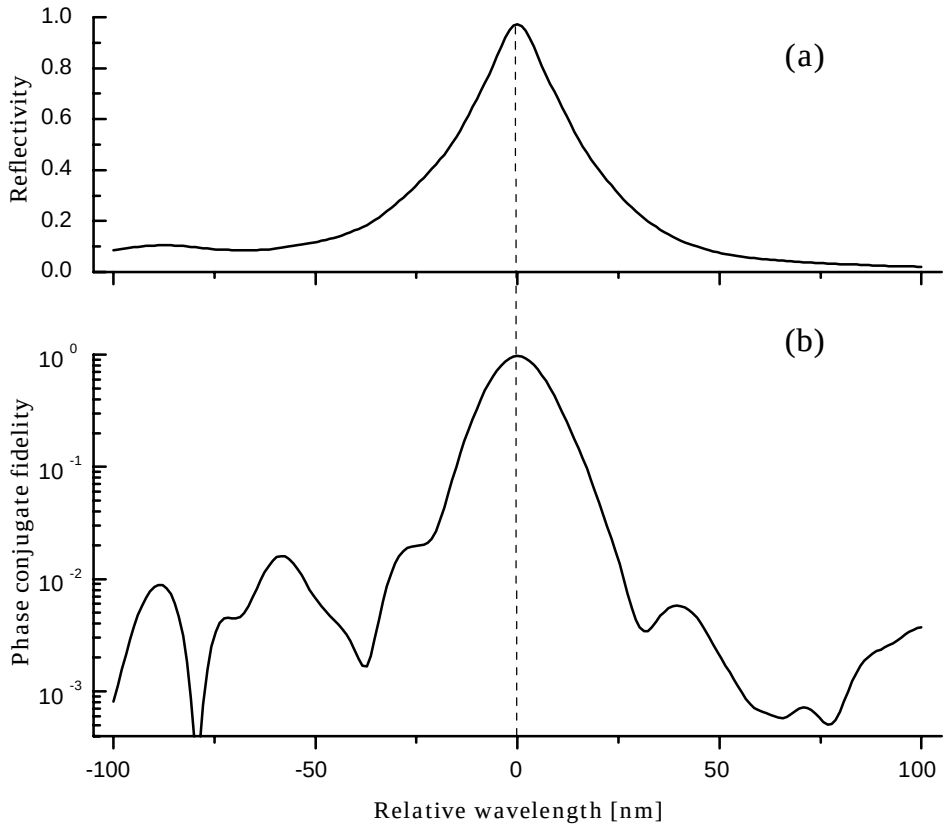

Figure 46. Detuning curves. The dispersion coefficient is -1.6·10^5 and the focal length r is -2.40 mm. The other parameters are given in Tabel 1. (a) the reflectivity R as a function of the relative detuned wavelength ($\lambda - \lambda_0$); (b) the phase conjugate fidelity H as a function of the relative detuned wavelength.

behavior the shapes of the wings are of minor importance if of any at all. It is only the shape of the detuning curve in the wavelength range corresponding to the spectrum of the laser that is important. The spectrum of the three modes used here spans over only 2 nm which is much less than the wavelength selectivity of the grating structure. The scanning behavior can therefore be evaluated by comparing the fidelity of the wavelengths corresponding to the two side modes λ_{-1} and λ_{+1}. A larger fidelity consequently means a larger reflection coefficient R_{ext} for the side mode considered. Moreover, the detuning curve in Fig. 46(b) has a convex shape with no local minimums in the range from λ_{-1} to λ_{+1}, and the scanning behavior is therefore fully described by comparing the fidelity evaluated at λ_{-1} and λ_{+1}, since one can imagine the dynamically generated detuning curve sliding along the wavelength axis as the spectrum scans by taking one longitudinal 'step' at a time, as described in Sec. 7.1.

7.4.2 The Influence of Material Dispersion

The influence of the material frequency dispersion of the crystal can now be investigated by calculating the detuning curve for different settings of the material dispersion. Different settings of the dispersion will result in a slight change in the shape of the detuning curve. Figure 47 displays the ratio between the fidelity at λ_{+1} and λ_{-1}, respectively, as a function of the material dispersion coefficient $\partial n_0/\partial\lambda$.

For a fixed dispersion coefficient, this phase conjugate fidelity ratio H^{+1}/H^{-1} changes slightly for each evaluation between the time steps in the 'steady state' range (i.e. for t > 30 s). In other words: the fidelity ratio fluctuates as time elapses. The fluctuations may be caused by limited numerical precision. In order to compensate for the fluctuations the fidelity ratio has been averaged in the 'steady state' range from t = 40 s to t = 50 s where H^{+1} and H^{-1} have been evaluated every 0.1 s (one time step). It is the averaged fidelity ratio that is shown in Fig. 47.

A fidelity ratio larger than one means that the fidelity at λ_{+1} is larger than at λ_{-1} and that the self-induced frequency scanning can be expected to be towards a longer wavelength. For $BaTiO_3$ the material dispersion $\partial n_0/\partial\lambda$ is approximately -1.6·10^5 m^{-1} at 814 nm wavelength (see Appendix D). To get a qualitative description of the tendencies the range of the dispersion axis in Fig. 47 has been expanded to twenty times this value. The dispersion at 500 nm, however, at which frequency scanning has also been observed, is five times as large as at 800 nm (see Appendix D), so the maximum dispersion used in these simulations is within a reasonable range. $BaTiO_3$ has normal dispersion but in order to have more general validity the anomalous dispersion has also been included in Fig. 47.

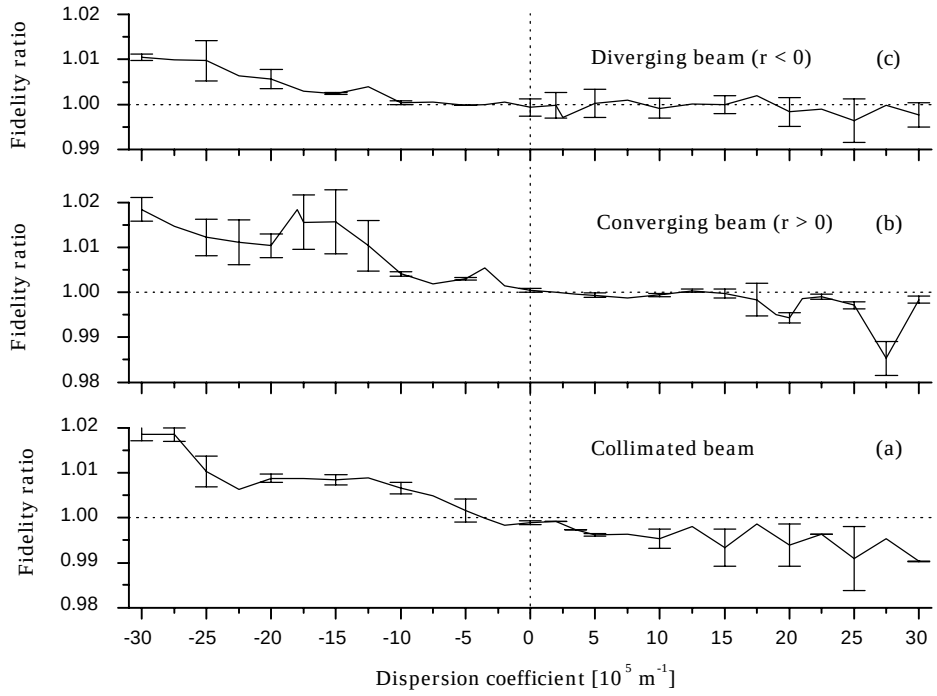

Figure 47. Ratio of the phase conjugate fidelity (H^{+1}/H^{-1}) evaluated at the wavelengths corresponding to the two side modes λ_{+1} and λ_{-1} as a function of the dispersion coefficient.

Three curves are shown in Fig. 47: one for a collimated beam (r = ∞), one for a diverging beam (r = -2.40 mm) and one for a converging beam (r = 2.40 mm). The probe beam has the same size and divergence as the beam that originally wrote the grating structure. No noise is added to the probe beam. The simulations are performed with two completely different sets of superimposed noise (E^p_{noise}, p = 1, 2 and 3, in Eq. 39). The two sets of noise are uncorrelated but contain the same total power. The obtained Cat geometries with the two sets of noise are similar,

but do not produce beam filaments at the same spatial positions (see Fig. 44). However, even through the complex grating structures are slightly different for the two sets of noise, they produce very similar detuning curves (from a physical point of view this would be expected). The fidelity ratio plotted in Fig. 47 is therefore an average of the fidelity ratio H^{+1}/H^{-1} obtained for each of the two sets of noise. The difference in H^{+1}/H^{-1} for the two sets of noise determines the magnitude of the error bars of the three curves.

Without regard to the focusing conditions, the first observation is that the fidelity ratio becomes larger as the amplitude of the normal dispersion is increased. If the beam is non-collimated and the dispersion is normal, the frequency scanning can be expected to be towards a longer wavelength. For the collimated beam, scanning towards a shorter wavelength may be expected in the range from 0 to -5·10^5 m^{-1}. The divergence and convergence angles, however, used in these simulations are roughly 0.7° and it is difficult to achieve better collimation in experiments since the beam is often focused with a lens in front of the crystal. The results of the simulations are therefore in good agreement with the experiments presented in Chapter 6 and the reported observations [138, 180, 181] with a laser diode coupled to a Cat conjugator for which scanning towards a longer wavelength is always observed. For the collimated beam the tendency is reversed, i.e. wether the scanning is towards a longer or a shorter wavelength, as the sign of the dispersion is altered; for anomalous dispersion the scanning is expected to be towards a shorter wavelength. This reversibility, i.e. scanning towards a longer wavelength for normal dispersion, and scanning towards a shorter wavelength for anomaleous dispersion, clearly manifests the influence of the material dispersion of the crystal on the scanning process. The scanning behavior is not as markedly reversed for the converging beam when the sign of the dispersion is changed as it was the case with the collimated beam. However, the tendency is the same: scanning towards a longer wavelength for normal dispersion, and scanning towards a shorter wavelength for anomaleous dispersion. Another important observation is that the fidelity ratio approaches unity if no dispersion of the refractive index of the crystal is present. This is regardless of the focusing conditions. In other words: we have shown that the presence of dispersion in the crystal leads to an asymmetric detuning curve and, consequently, we conclude that dispersion is the origin of the self-induced frequency scanning.

7.5 Summary

We have analyzed the complex grating structure formed in a self-pumped photorefractive barium titanate phase conjugator arranged in a Cat geometry. The framework for the analysis is a two-dimensional numerical model based on the photorefractive band transport equations. The model takes into account transmission gratings generated by three longitudinal modes from a laser. We have shown that the material frequency dispersion of the conjugator crystal leads to an asymmetric detuning curve with respect to the center wavelength of the spectrum of the laser that induces the grating structure. This asymmetry causes self-induced frequency scanning. For normal dispersion (negative dispersion) the results of the simulations predict self-induced frequency scanning towards a longer wavelength regardless of the focusing conditions of the incident beam. The scanning towards a longer wavelength is in agreement with previously reported experiments[138, 180, 181] where a diode laser is coupled to a Cat conjugator. The findings show that the material dispersion of the $BaTiO_3$ crystal is the origin of the self-induced scanning process.

8 Wavelength Selectivity of the Conjugator Grating Structure

The present chapter is devoted to a study of the Cat conjugator formed in a photorefractive $BaTiO_3$ crystal. In the process of suppressing the multimode operation of a laser diode by coupling it to a phase conjugate mirror (PCM), it is important to know the exact detuning curve (backreflection versus the wavelength of the incident beam) and the wavelength selectivity in order to get a better perception of the interaction in the coupled cavity.

Although the Cat conjugator is a very useful device, only little work with emphasis on the detuning curve of the complex grating structure has been published.[102] On the other hand, much work on the detuning curve of a single grating can be found in the literature.[193, 194, and references therein] The influence of partially coherent beams on the generation of a phase conjugation signal has only been investigated for a mutually pumped phase conjugator.[195, 196, 197] Theoretical investigations of the general case of contradirectional two-wave mixing with partially coherent beams have, however, recently been reported [198, 199], but the results have not been used in connection with an analysis of a Cat conjugator.

In this chapter measurements of the detuning curve of a Cat conjugator are presented. The measurements show that the shape of the detuning curve depends strongly on the coherence length of the incident beam. The findings explain the observed line width of 0.02 nm obtained from a multimode laser diode array coupled to a Cat conjugator (see Chapters 9 and 10). The forced reduction of the line width has influence on the spatial distribution and the strength of the gratings that eventually are formed in the conjugator crystal. This phenomenon of the coupled system is here referred to as *the self-narrowing effect*. A simple theoretical analysis of the detuning curve of the Cat conjugator is presented. The analysis is based on assigning a diffraction function to each of the gratings formed in the crystal and calculating the backreflected signal as a summation of several contributions. The analysis is simple and shows good agreement with the experimental results.

8.1 Detuning Curve

It is well known that a Cat conjugator can form transmission gratings and produce the phase conjugate replica of an incident beam even when the incident beam has a coherence length that is much shorter than the dimensions of the crystal (see Sec. 4.6). Two contradirectional laser beams in the crystal with the same wavelength λ ($= k/2\pi$) form a reflection grating with a grating wave vector $K_g = 2k = 2\pi/\Lambda$, where k is the wave vector of the laser beams and Λ is the fringe spacing of the grating. Such reflection gratings are known as 2k-gratings (see Sec. 4.3). In the Cat conjugator contradirectional beam propagation occurs and form 2k-gratings. 2k-gratings can play a significant role in the conjugation process. In addition to transmission gratings, it is known that the 2k-gratings contribute to the generation of the phase conjugate replica of the incident beam.[102, 200] The length of the 2k-gratings can become longer as the coherence length of the incident beam is increased. One will therefore expect the wavelength selectivity or the amount of reflected energy to depend on the coherence length of the incident beam that writes the grating structure, since the length of the 2k-gratings in general cannot be any longer than the coherence length of the incident beam itself.[198] On the other hand, it has been shown that the length of a 2k-grating can be significantly longer than the coherence length of two interacting beams if they have a large intensity

ratio.[198] For the Cat conjugator, however, the contradirectional propagating beams are of similar intensities and, therefore, in our experiments the maximum length of the 2k-gratings is given by the coherence length of the incident beam. Consequently, our hypothesis is that the grating structure - and through that the detuning curve and the wavelength selectivity - depends on the line width of the incident beam. The incident beam is in the following also referred to as the writing beam.

8.1.1 Experiments with a Single-Mode Laser

In order to measure the detuning curve of the grating structure formed in the Cat conjugator and to investigate the hypothesis mentioned above, the experiment shown in Fig. 48 has been designed. The output from a single-mode laser diode (SM) is collimated with a lens (L1) and sent through an optical faraday isolator (ISO) with an isolation of more than 35 dB to avoid mode hopping caused by feedback. The output polarizer of the faraday isolator is orientated so that the beam at the crystal is extraordinarily polarized. With a spherical lens (L2) and a cylindrical lens (L3) a spot size of 1 mm is generated at the surface of a chromium-doped $BaTiO_3$ crystal (CROW). The crystal measures $5.8 \times 5.2 \times 2.9$ mm^3, with the c-axis along the longest dimension. The angle of incidence is 60° and the position of the beam at the crystal surface is 1.5 mm from the nearest corner. When the laser diode is operated in continuous-wave, the line width is less than $3 \cdot 10^{-5}$ nm (15 MHz), which corresponds to a coherence length of several meters. Inbetween the isolator and the crystal two beamsplitters (BS1 and BS2) are placed. One detector (D1) measures the phase conjugate reflectivity and another (D2) measures the output power of the diode laser. A third beamsplitter (BS3) picks out a beam that is directed to a spectrum analyzer (SPEC) with a resolution of 0.02 nm so that the wavelength of the laser diode can be monitored. A waveform function generator (FUNC) is connected to the power supply (SUP) so that the amplitude of the drive current of the diode can be modulated. The temperature of the junction of the laser diode is controlled with a peltier element. By adjusting the temperature the single-mode wavelength, λ, can be controlled. The wavelength is 798 nm at 25°C.

The temperature of the junction is set to 26.5°C ($\lambda = \lambda_0$) and the crystal is operated in the Cat geometry and is illuminated with 9.1 mW. The phase conjugate reflectivity is in the range 30 to 40% (not corrected for Fresnel reflections). When steady state has been reached, the beam path is blocked. The dark conductivity of the crystal is relatively low and the formed gratings therefore degrade slowly. After several minutes of blocking of the beam path, the crystal is illuminated again and the phase conjugate reflectivity will instantaneously be almost as large as prior to the blocking. Before the beam path is unblocked, however, the wave plate (WP) is rotated to reduce the transmitted power through the isolator; the power at the crystal is set to 100 μW. This low power is necessary to avoid erasure of the gratings in the crystal. Moreover, the temperature of the laser diode junction is reduced to 24.0°C and, consequently, the lasing wavelength λ is reduced a fraction of a nanometer with respect to λ_0. The beam path is then unblocked and the detuning curve is recorded by measuring the backreflected power from the crystal by detector D1 as the temperature of the junction is slowly increased to 29.0°C. During the change of the junction temperature, the lasing wavelength λ, the phase conjugate reflectivity and the output power of the diode are all monitored and recorded. One scan cycle of the temperature (24°C $\rightarrow$ 29°C) takes approximately 30 seconds. Afterwards, the measurements are repeated with the temperature slowly decreased (29°C $\rightarrow$ 24°C). The obtained detuning curves are identical; in fact several scans can be performed with only little degradation of

the grating structure.

Figure 49(a) shows the measured phase conjugate reflectivity as a function of the relative wavelength $(\lambda - \lambda_0)$. It is seen that the detuning curve has a central peak with a maximum for $\lambda = \lambda_0$. This wavelength gives the best Bragg match and thereby also the highest reflectivity since it originally wrote the gratings of the Cat conjugator. The shape of the detuning curve is a Sinc-like function on top of a reflectivity floor, a floor that is not background reflections from lenses, etc. The reflectivity does not become zero at any wavelength within the observed detuning range. The spacing between the maxima of two adjacent sidebands, which is denoted $\Delta\lambda_p$ (see Fig. 49(a)), is constant throughout the left and the right wings of the detuning curve and is measured to be 0.024 nm. The wavelength selectivity, $\Delta\lambda_s$, is here defined as the full width at half-maximum of the central peak of the detuning curve. The wavelength selectivity is measured to be 0.026 nm.

In the next experiment the drive current of the laser diode is modulated. The lasing wavelength of the diode varies linearly with the current. The line width of the writing laser beam - denoted $\Delta\lambda_w$ (FWHM) - can be increased artificially by rapidly modulating the current with a triangular waveform at 10 kHz. The response time of the crystal is on the order of one second and the crystal averages the resultant frequency sweep to give the writing beam a spectrally flat and rectangularly shaped frequency spectrum with a center wavelength of λ_0. The measurement procedure is as follows: the current is modulated at 10 kHz and a Cat geometry starts to be formed in the crystal. When the phase conjugate reflectivity has stabilized, the beam path is blocked and the modulation is turned off reducing the line width of the probe beam to $3{\cdot}10^{-5}$ nm (15 MHz). The power of the probe beam is then lowered to 100 μW and the temperature is reduced to 24.0° C. The detuning curve of the grating structure of the Cat conjugator can subsequently be measured as the temperature is slowly increased as before.

Figure 49(b) shows the recorded detuning curve for a writing line width $\Delta\lambda_w$ = 0.03 nm. The coherence length is given by $\lambda_0^2/\Delta\lambda_w$ corresponding to 9 mm inside the crystal. Due to the lower coherence length, the wavelength selectivity has increased to 0.045 nm. In comparison with Fig. 49(a) the amplitudes of the sidebands have decreased. Another very important observation is that the sideband

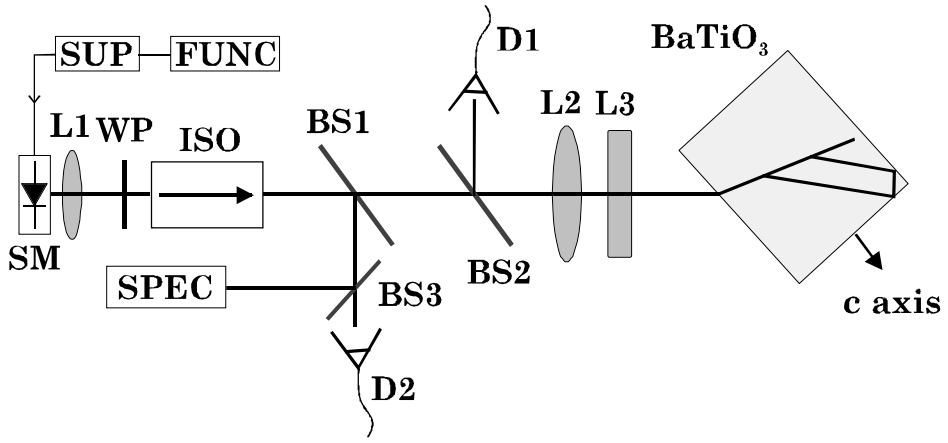

Figure 48. Experimental setup. A single-mode laser diode is directed towards a $BaTiO_3$ crystal. SM: single-mode laser diode, L1: lens f = 5 mm, L2: lens f = 150 mm, L3: cylindrical lens f = 100 mm, BS1-3: beamsplitters, ISO: optical isolator (35 dB), D1: detector, D2: detector, SUP: power supply, FUNC: function generator, WP: $\lambda/2$ wave plate.

spacing $\Delta\lambda_p$ is the same as in Fig. 49(a); the recorded signal in Fig. 49(b) is more noisy but the average sideband spacing is measured to be 0.024 nm.

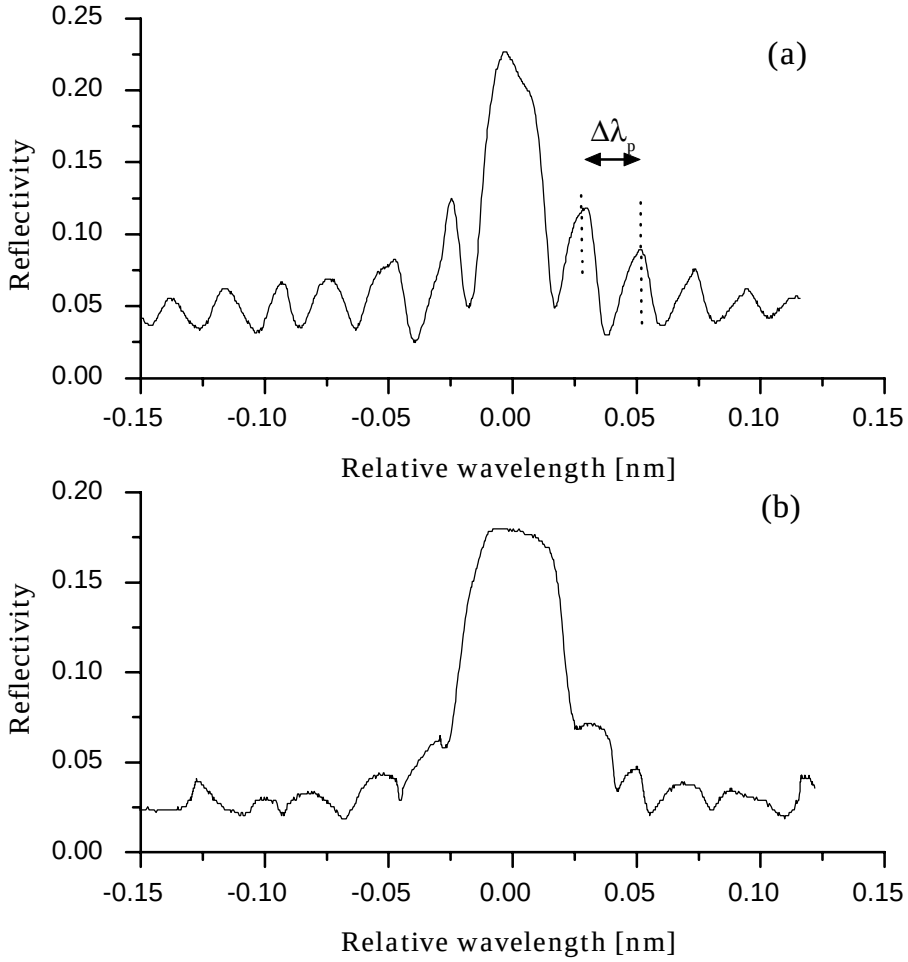

Figure 49. Measured detuning curve (the reflected energy as a function of relative wavelength of the probe beam) of a Cat conjugator: (a) the line width of the writing beam is $3{\cdot}10^{-5}$ nm (15 MHz), (b) the line width of the writing beam is 0.03 nm (FWHM).

Using this technique it is possible to generate an artificial line width of up to 0.04 nm and to measure the corresponding detuning curve from which the wavelength selectivity can be derived. The measured wavelength selectivities for other writing line widths in the range up to 0.04 nm will be presented in Sec. 8.1.3.

8.1.2 Experiment with a Multimode Laser

The phase conjugate feedback from the Cat conjugator can narrow the multimode spectrum of a laser diode. In the following the detuning curve of the Cat conjugator when the crystal is illuminated with a broad spectrum is investigated.

The experimental setup is shown in Fig. 50. The output from a laser diode array (array II) is collimated with a lens (L1) and is directed towards the crystal. The angle of incidence is 60°. The $\lambda/2$ wave plate (WP1) ensures that the output beam is extraordinarily polarized. The incident power at the crystal is 250 mW. Three

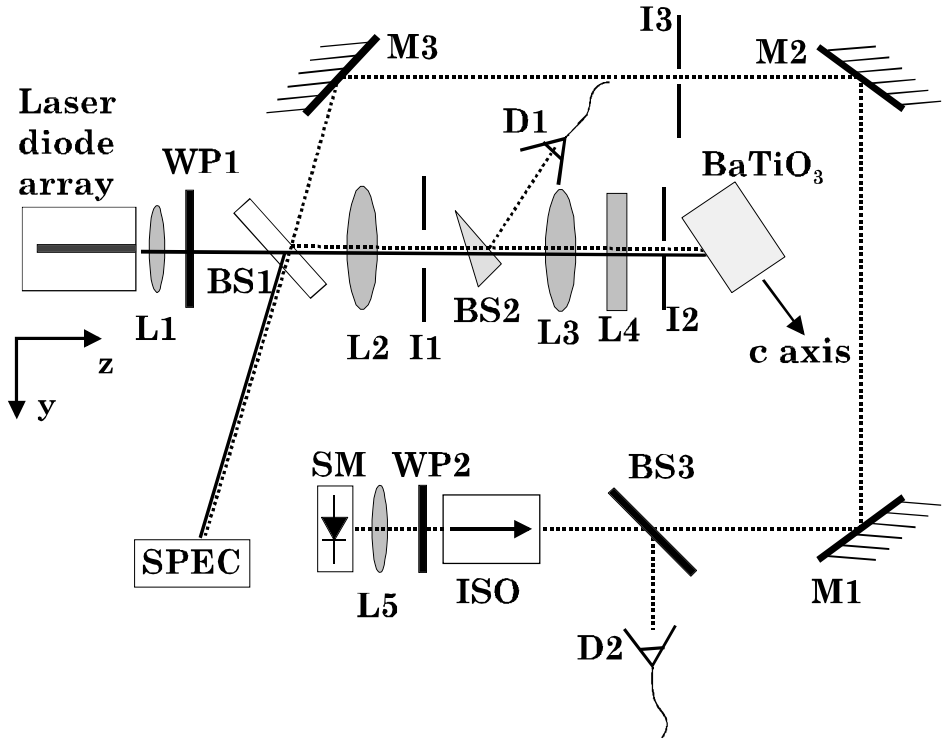

Figure 50. Experimental setup. A multimode laser diode array is coupled to a self-pumped phase conjugator in a $BaTiO_3$ crystal. SM: SDL-5412-H1 single-mode diode, L1: lens f = 5 mm, L2: lens f = 300 mm, L3: lens f = 200 mm, L4: cylindrical lens f = 100 mm, L5: lens f = 7 mm, BS1-3: beamsplitters, ISO: optical isolator (35 dB), D1: detector, D2: detector, WP1-2: $\lambda/2$ wave plate, SPEC: spectrum analyzer, M1-3: mirrors, I1-3: irises.

lenses (L2-4) generate a spot size that measures 0.5×1 mm (x-axis × y-axis) at the crystal surface. The cavity length is 2×550 mm. A beamsplitter (BS1) picks out a part of the beam and directs it to a spectrum analyzer (SPEC). A second beamsplitter (BS2) and a detector (D1) are used to measure the phase conjugate reflectivity of the crystal. As a probe beam, the single-mode laser (Sec. 8.1.1) is sent colinearly with the beam from the laser diode array into the crystal. When the crystal has been illuminated by the light from the laser diode array and the phase conjugate beam has been returned by the crystal, the probe beam is aligned colinearly by the use of three mirrors (M1-3) and three irises (I1-3). The spot size of the circular probe beam is 1 mm measured at the crystal surface. The initial center wavelength of the spectrum of the laser diode array is temperature tuned to be 1-2 nm below the wavelength of the probe beam. The feedback causes the spectrum of the laser diode array to narrow down from approximately ten longitudinal modes (the initial line width is 1 nm) to two to three modes and self-induced frequency scanning takes place. The maximum phase conjugate reflectivity of the crystal is approximately 10%. The experimental procedure is as follows: the crystal is illuminated by the light from the laser diode array and a Cat geometry is formed in the crystal. The phase conjugate feedback causes the spectrum to narrow down and it starts to scan towards a longer wavelength. When the scanning spectrum comes close to the wavelength of the probe beam, the beam path is blocked. The probe beam is then turned on and the wavelength of the probe beam (λ) is temperature tuned across a wavelength range. The detectors D1 and D2 measure the reflected

signal from the crystal and the power of the probe beam, respectively. The power of the probe beam is 50 μW at the front face of the crystal. The probe beam experiences a reflectivity of 2-3%. This should be compared with the maximum reflectivity of 10% of the laser diode array. The effective line width of the writing laser diode array is estimated to correspond to one longitudinal mode spacing (0.1 nm) since at most two modes are present at any single moment during the frequency scanning and writing process.

Figure 51 shows the detuning curve versus the relative wavelength $(\lambda - \lambda_0)$, where λ_0 is the center wavelength of the scanning spectrum of the laser diode array just before the beam path is blocked. Again, the detuning curve has a central peak at $\lambda = \lambda_0$ on top of a reflectivity floor. The wavelength selectivity is measured to be 0.07 nm. The sideband spacing is measured to be 0.022 nm. In comparison with Fig. 49(a) the amplitude of the sidebands has decreased and, contrary to Fig. 49(a) the amplitude of the sidebands is almost constant throughout the observed detuning range.

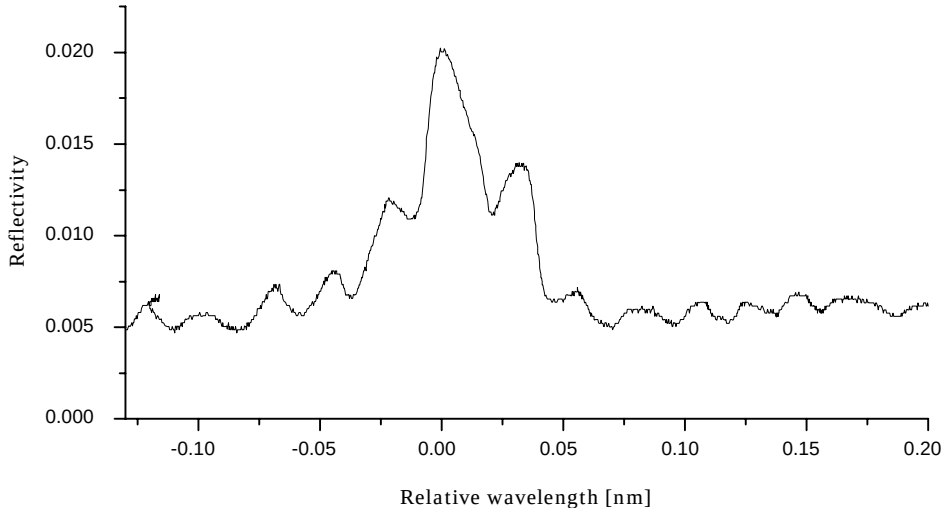

Figure 51. Measured detuning curve (reflected energy as a function of relative wavelength of the probe beam) of a Cat conjugator: the gratings of the conjugator have been formed by a multimode laser diode array. The effective line width of the multimode laser diode array is 0.1 nm.

8.1.3 Discussion of Results

In Fig. 52 the wavelength selectivity from the measurements with the single-mode laser and the multimode laser array is shown. The wavelength selectivity $\Delta\lambda_s$ has been plotted as a function of the writing line width $\Delta\lambda_w$ (bottom axis) and the coherence length inside the crystal (top axis) of the writing beam. The coherence length has been calculated as $\lambda_0^2/(\Delta\lambda_w n)$, where $n = 2.4$ is the refractive index of the crystal. Investigations of the wavelength selectivity of a Cat conjugator with $\Delta\lambda_w = 1.5$ nm have been reported.[102] The reported wavelength selectivity is also plotted in Fig. 52. It is well known that the size of the interaction regions is restricted by the width of the beam inside the crystal. The size of the beam accordingly sets limitations on the maximum number of layers of the transmission gratings and, consequently, on the wavelength selectivity of these as well. The data presented in Fig. 52, have, however, all been measured with a beam width of 1

mm.

The wavelength selectivity increases as the writing line width increases (a narrow central peak of the detuning curve corresponds to a small wavelength selectivity). For a line width in the range of 10^{-5} nm to 10^{-2} nm the wavelength selectivity is an slowly increasing function. At a line width of 0.02 nm, however, the wavelength selectivity abruptly increases and becomes a faster increasing function (as compared with the range of 10^{-5} nm to 10^{-2} nm). As can be seen in Fig. 52 (the vertical dashed line), a line width of 0.02 nm corresponds to a coherence length of approximately 10 mm. The reason for the abrupt increase of the wavelength selectivity at this line width is that the coherence length has become comparable with the path length of the internal loop (l_{loop}) of the Cat conjugator, which is approximately 11 mm for the experiments presented here. As the coherence length of the writing beam becomes larger than l_{loop}, the wavelength selectivity of the gratings reaches a minimum of 0.026 nm; a larger coherence length does not decrease the wavelength selectivity significantly. This can be explained as follows: as the coherence length becomes larger than l_{loop}, the 2k-gratings, which are caused by the contradirectionally propagating beams in the crystal, have already reached their maximum lengths due to the dimensions of the crystal and the length of the loop and, consequently, the wavelength selectivity cannot decrease any further. As the coherence length becomes shorter than l_{loop}, the lengths of the 2k-gratings are accordingly also reduced leading to correspondingly larger wavelength selectivity as seen in Fig. 52. For a very short coherence length the strength of the 2k-gratings are insignificant to affect the phase conjugate signal, and the detuning curve is mainly determined by the characteristics of the transmission gratings, which always exist. For the experiment in Ref. [102] the coherence length of the writing beam was 20 μm (inside the crystal) and the 2k-gratings contributed with less than 3% to the phase conjugate signal.

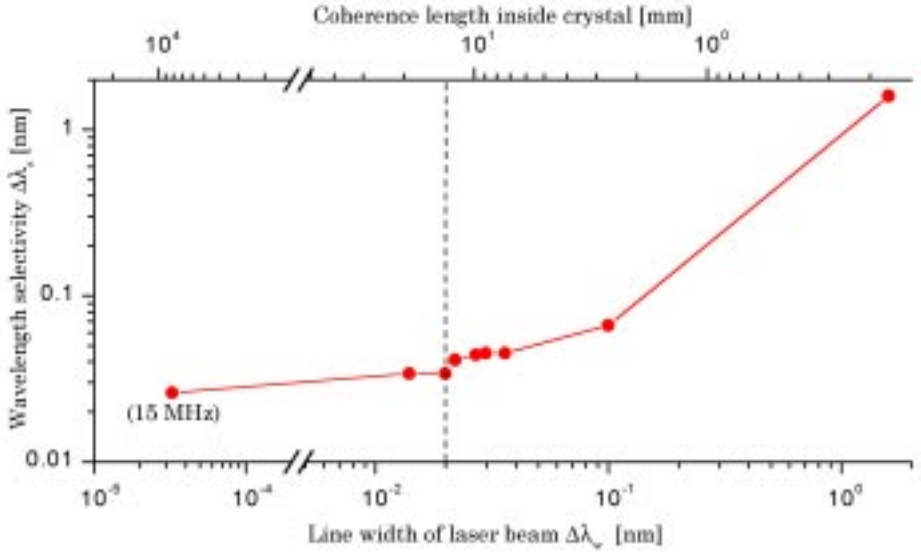

Figure 52. Wavelength selectivity (FWHM of detuning curve) of the gratings formed in a Cat conjugator as a function of the line width (bottom axis) and the coherence length inside the crystal (top axis) of the writing beam. The data point for $\Delta\lambda_w = 1.5$ nm is from Ref. [102].

8.2 Analysis of the Detuning Curve

In this section a simple model of the complex grating structure will be presented in order to explain the shapes of the measured detuning curves shown in Figs. 49(a-b) and 51.

One of the first models of the mechanism of the self-pumped Cat conjugator suggested the existence of four-wave mixing processes in two coupled interaction regions connected by light undergoing total internal reflection at the crystal surfaces.[96] This model has been widely accepted even though there have been other explanations such as only one interaction region[201], multiple interaction regions[202] and stimulated photorefractive backscattering[203]. Detailed experimental investigations of the internal beam production in barium titanate crystals have revealed a large variety of internal beam paths that cannot be described by one model only.[204, 205] The exact beam path depends on the crystal and the experimental settings. The observed beam paths for the experiments presented here reveal that the beam undergoes total internal reflection in agreement with the two interaction region model. One may argue, though, that the very low wavelength selectivity (0.026 nm) observed in Fig. 49(a) is due to one single 2k-grating that is formed just after the entrance surface of the crystal and that the loop is only essential for providing backscattered seed. If this was true, however, the detuning curve would have the well-known shape of a single 2k-grating.[192] The detuning curve corresponding to a single 2k-grating with a wavelength selectivity of 0.026 nm has a much lower reflectivity (almost zero) at the wings of the curve than what we experimentally observe from the Sinc-like function shown in Fig. 49(a). Moreover, if one compares the measurements in Figs. 49(a), 49(b) and 51, it is observed that all the detuning curves have the same constant spacing between two adjacent sidebands. These three curves have a sideband spacing of approximately $\Delta\lambda_p \approx 0.024$ nm. In this section we show that the sidebands can be regarded as a modulation of the wings of the detuning curve. If this modulation is due to a detuning curve corresponding to a single 2k-grating, then one should expect the sideband spacing (the period of the modulation) to vary for the three measurements since the coherence length of the writing beam used for the three experiments varies and, consequently, gratings with different lengths will be expected to form in the crystal (for a single 2k-grating the sideband spacing depends on the length of the grating). Since the sideband spacing is constant, however, it is much more likely that the modulation of the wings of the detuning curve is caused by interference of light diffracted in different gratings in the crystal. If the light travels the geometric path to and from the corner, as in the traditionally described loop operation of the total-internal-reflection Cat conjugator, it will experience an intensity absorption of $\exp(-\alpha_p l_{loop})$, where α_p is the intensity absorption coefficient. For the crystal (CROW) used for the experiments here, the absorption at 800 nm wavelength is 1.01 cm^{-1}, which means that less than 25% of the incident light can be backreflected towards the laser if the Fresnel reflection (loss) is taken into account. The amount of power that remains after circulation to and from the corner is insufficient to account for the observed maximum reflectivity of more than 40%. This fact indicates that additional 2k-gratings must be formed just after the entrance surface of the crystal and that they will contribute to the phase conjugate signal. Moreover, investigation have revealed the presence of such 2k-gratings.[200]

8.2.1 Model of Cat Conjugator

Based on the observations discussed in the preceding section, the model in Fig. 53 is proposed to explain the observed detuning curves shown in Figs. 49(a-b) and Fig. 51. In this model of the grating structure in the Cat conjugator, the

phase conjugate signal is generated by diffraction in four gratings. There is a transmission grating in each of the two interaction regions (labeled T1 and T2). Furthermore, we assume that two 2k-gratings are formed (R3 and R4); one just after the entrance surface of the crystal, the other is formed in the internal loop reflected off the corner. The length of the reflection grating R4 may extend beyond the distance between the two internal reflections.

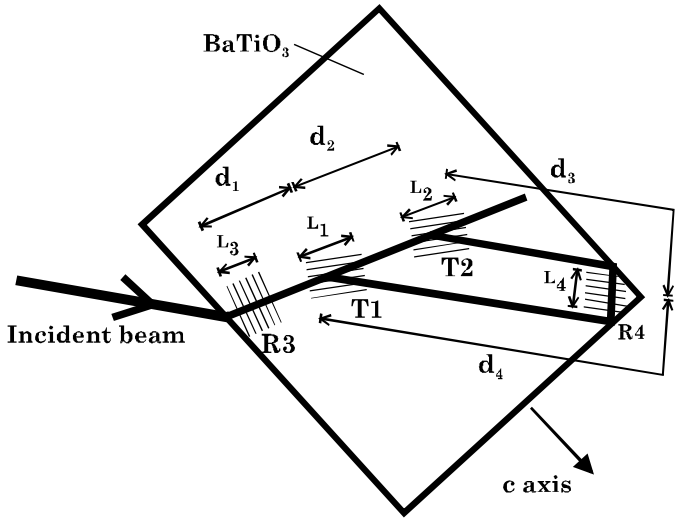

Figure 53. Model of the grating structure in the self-pumped Cat conjugator. The phase conjugate signal is a combination of signals originating from two transmission gratings (T1 and T2) and two reflection gratings (R3 and R4).

In Fig. 53 the labels of the lengths of the gratings (L_1-L_4) and the lengths of the beam paths of the Cat geometry (d_1-d_4) are also shown. The modulation of the wings of the detuning curves can be explained as interference of light that is diffracted back by R3 and light that has traveled all the way around the loop and then is backreflected towards the laser. If this is the case, the optical path length difference $2{\cdot}d_1{+}d_2{+}d_3{+}d_4$ ($= l_{loop}$) should be $(\lambda^{-1} - (\lambda + \Delta\lambda_p)^{-1})^{-1}$, where λ is the wavelength of the incident beam. For $\lambda = 800$ nm and $\Delta\lambda_p = 0.024$ nm the optical path length difference is 26.7 mm. In free space this corresponds to 11 mm which seems to agree very well with the physical dimensions of the crystal. In the model all the gratings have a spatial sinuous modulation (Δn) of the refractive index (n). Based on the coupled mode theory the complex diffraction amplitude for the transmission and the reflection gratings for a p-polarized beam with unit amplitude of the incident beam are given by[192]

$$H_T = -i\sqrt{\frac{c_r}{c_s}}\exp\left(\xi - \alpha L/c_r\right)\left(1 - \xi^2/\nu^2\right)^{-\frac{1}{2}}\sin\left(\sqrt{\nu^2 - \xi^2}\right), \tag{45}$$

$$H_R = \sqrt{\frac{c_r}{c_s}}\sinh\left(i\nu\cosh\left(a\right)\right) / \cosh\left(a + i\nu\cosh\left(a\right)\right), \tag{46}$$

respectively, where

$$\begin{aligned} \nu &= k_c L\left(c_r c_s\right)^{-\frac{1}{2}}; \\ \xi &= \frac{1}{2}L\left(\frac{\alpha}{c_r} - \frac{\alpha}{c_s} - i\frac{\vartheta}{c_s}\right); \\ a &= \sinh^{-1}\left(-i\xi/\nu\right); \end{aligned}$$

$$
\begin{aligned}
c_r &= \cos(\theta);\\
c_S &= \cos(\theta) - \frac{K_g}{k}\cos(\phi);\\
k &= 2\pi n/\lambda;\\
\vartheta &= K_g\cos(\phi-\theta) - \frac{K_g^2}{4\pi n}\lambda;\\
k_c &= -\frac{\pi\Delta n}{\lambda}\cos(2(\theta_0-\phi));\\
K_g &= \frac{2\pi}{\Lambda}.
\end{aligned}
$$

The grating parameters are: θ is the angle of incidence, θ_0 is the Bragg angle, ϕ is the slant angle, K_g is the grating wave vector, Λ is the fringe spacing of the grating, L is the thickness of the grating, λ is the wavelength in vacuum, n is the refractive index of the crystal, k is the wave vector in the medium, α is the field absorption coefficient, k_c is the coupling constant, ϑ is the dephasing factor, ξ is the mismatch factor, ν is the coupling factor and i is the imaginary unit. The diffraction efficiency, η, for a grating is given by

$$\eta = \frac{|c_s|}{c_r} HH^*,$$

where asterisk denotes a complex conjugate. The total phase conjugate signal from the Cat conjugator is a combination of five contributors (S_j): (1) diffraction in R3, (2) diffraction in T1, propagation around the loop and diffraction in T2, (3) diffraction in T2, propagation around the loop and diffraction in T1, (4) diffraction in T1, propagation along half of the loop, diffraction in R4 and diffraction in T1 and (5) diffraction in T2, propagation along half of the loop, diffraction in R4 and diffraction in T2. The contributors (2) and (3) are identical and so are (4) and (5). The five contributors are given by

$$S_1 = H_{R3}; \tag{47}$$

$$S_2 = S_3 = H_{T1}H_{T2}\exp(-(ik+\alpha)(2d_1+d_2+d_3+d_4));$$

$$S_4 = S_5 = H_{T1}H_{R4}H_{T1}\exp(-2(ik+\alpha)(d_1+d_4-L_4/2)). \tag{48}$$

Neglecting multiple reflections between the four gratings and setting the reference plan to be the front edge of R3, the total phase conjugate signal can be written as

$$\eta_{pc} \propto \left| S_1 e^{i\varphi_1} + (S_2+S_3)e^{i\varphi_2}(1-\eta_{R3})\sqrt{(1-\eta_{R4})} + \right. \tag{49}$$

$$\left. (S_4+S_5)e^{i\varphi_4}(1-\eta_{R3}) \right|^2. \tag{50}$$

The factor η_{R3} is the diffraction efficiency for the reflection grating R3 and the term $(1-\eta_{R3})^{\frac{1}{2}}$ is the transmission function of the field through R3. The factor η_{R4} is the diffraction efficiency in R4. The phase shifts of the transmitted fields through the gratings have been neglected. The phases φ_j (j=1,2,4) are constants and ensure that all the signals add up in phase for zero detuning ($\lambda = \lambda_0$).

8.2.2 Results of Analysis

It is now possible to calculate the detuning curve $\eta_{pc}(\lambda)$. When it is fitted to the measurements, the free parameters are the lengths (L_j, j = 1···4) and the

modulation index (Δn_j, j = $1\cdots4$) of all the gratings. The angle between the beams at T1 and T2 is taken to be 25°. The lengths d_1 and d_2 are set to 0.75 mm and 0.5 mm, respectively. The path l_{loop} = $2d_1+d_2+d_3+d_4$ is set to 11.4 mm to reproduce the sideband spacing of 0.024 nm. For a writing beam with low coherence the R4 grating will form where the optical path lengths of the two different ways around the internal loop are identical; that establishes the restriction $d_4 = d_2+d_3$. Figure 54(a) displays the calculated detuning curve (Eq. 49) (solid line) for the case where the coherence length of the writing beam is much larger than l_{loop}. The parameters are shown in the figure caption. On top of the calculated detuning curve the measured detuning curve from Fig. 49(a) has been plotted (dashed line with solid circles). There is very good agreement between theory and experiment. The grating R4 is assigned a length of 11.4 mm corresponding to the full internal path length. This can be interpreted in the following way: when the coherence length becomes very large, the contradirectional beams everywhere inside the crystal will form 2k-gratings. Figure 54(b) shows the amplitude of the five contributors to the phase conjugate signal. The signal from R3 gives rise to the phase conjugate reflectivity floor (dashed line), the long R4 grating results in the very small wavelength selectivity (solid line). Moreover, the presence of R4 causes the signals S_2 and S_3 to become band-stop filtered (dotted line). The filtered versions of S_2 and S_3 give occasion to the modulation of the wings of the detuning curve.

As the coherence length of the writing beam decreases the length of the 2k-gratings must decrease as well. Figure 54(c) shows the calculated detuning curve that shall be compared with the measurement with the multimode laser diode array. On top of the calculated detuning curve the measured detuning curve from Fig. 51 has been plotted (dashed line with solid circles). The length of R4 is set to be equal to the coherence length of the writing beam, which is approximately 4 mm. The calculated detuning curve is to some extent in agreement with the measured detuning curve. The wavelength selectivity and the shape of the central peak are similar. The sideband spacing obtained from the proposed theory is in good agreement with the experimental result. Again the modulation of the wings is due to interference of light diffracted in R3 and light that has traveled around the loop. The shape of the central loop is mainly due to the presence of the reflection grating R4.

8.2.3 Validity of Model

As the coherence length of the writing beam becomes much smaller than l_{loop}, more 2k-gratings will emerge around the internal loop [102] and the model presented here will not give an accurate description of the detuning curve, but should be extended to include additional 2k-gratings. For a very short coherence length (< 20 μm), however, all the 2k-gratings will contribute much less than the transmission gratings T1 and T2.[102] In this case the 2k-gratings may be neglected and the detuning curve is determined by the characteristics of the transmission gratings only. This means that the proposed model (Eq. 49) is only valid for a laser source with a coherence length $\gtrsim l_{loop}$, but may be used to explain the shape of a detuning curve corresponding to a coherence length that is even shorter.

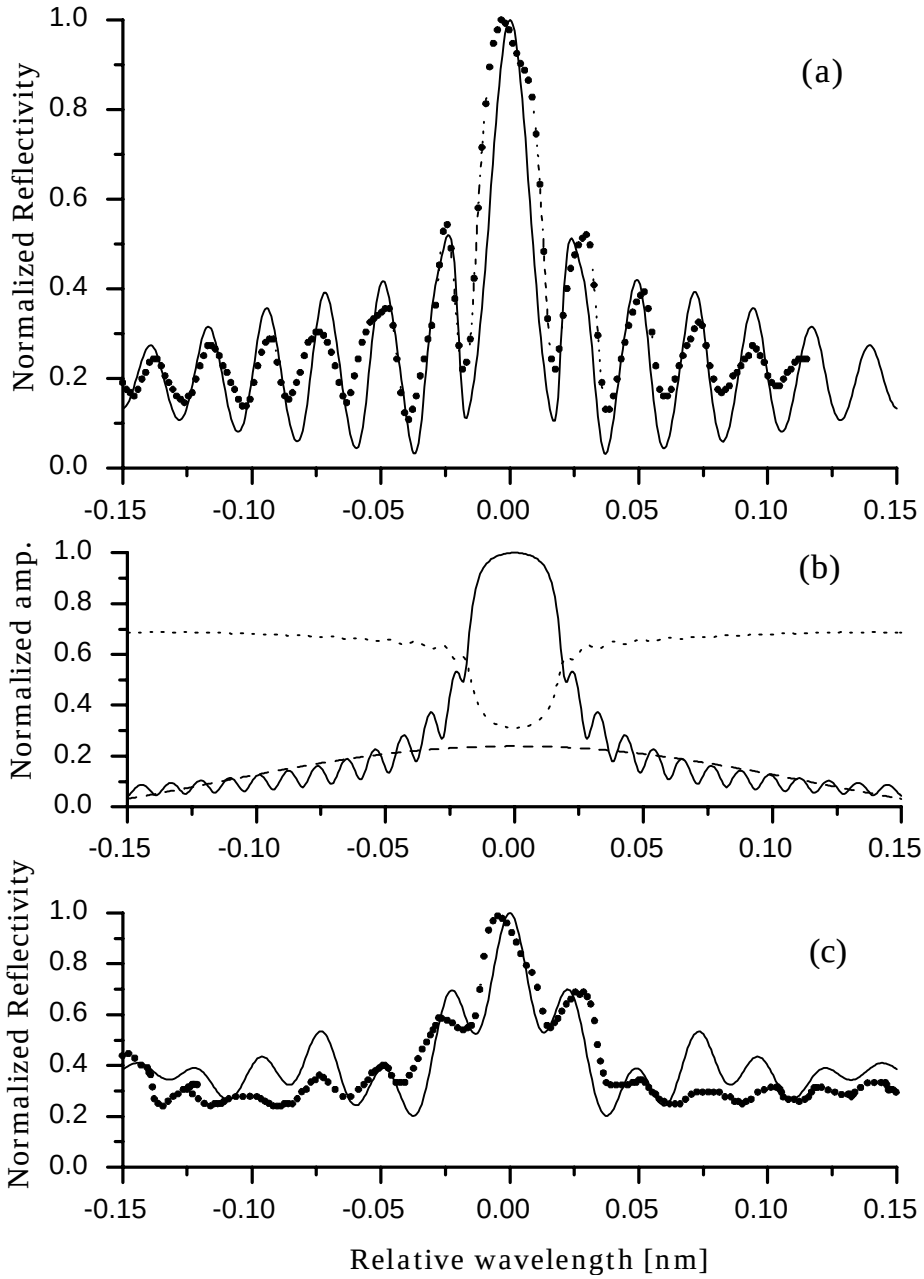

Figure 54. (a) Calculated detuning curve (solid line) of the Cat conjugator for a writing beam with a coherence length much larger than the dimensions of the crystal. Parameter used: α = 0.51 cm^{-1}, λ = 800 nm, n = 2.4, T1: L_1 = 1 mm, $\Delta n_1 = 2{\cdot}10^{-4}$, ϕ_1 = 56.4°, Λ = 0.77 μm, θ_0 = -21.2°; T2: same as T1; R3: L_3 = 0.75 mm, $\Delta n_3 = 1{\cdot}10^{-4}$, ϕ_3 = 0, Λ = 0.17 μm, θ_0 = 0; R4: L_4 = 11.4 mm, $\Delta n_4 = 1{\cdot}10^{-4}$, ϕ_4 = 0, Λ = 0.17 μm, θ_0 = 0. The dashed line with solid circles is the measured detuning curve taken from Fig. 49(a); (b) the five contributors of the total detuning curve shown in (a). Dashed line is $|S_1|$, dotted line is $|S_2 + S_3|$ and solid line is $|S_4 + S_5|$; (c) calculated detuning curve for a writing beam with a coherence length of 4 mm. Parameters used: T1: L_1 = 1 mm, $\Delta n_1 = 1.25{\cdot}10^{-4}$, T2: same as T1, R3: L_3 = 0.75 mm, $\Delta n_3 = 0.25{\cdot}10^{-4}$, R4: L_4 = 4 mm, $\Delta n_4 = 4{\cdot}10^{-5}$. All other parameters are the same as for (a). The dashed line with solid circles is the measured detuning curve taken from Fig. 51.

8.3 The Self-Narrowing Effect

The model in Fig. 53 reveals that as the coherence length of the writing laser beam becomes larger than l_{loop}, 2k-gratings must be formed in the internal loop of the Cat configuration in order to explain the very small wavelength selectivity that we observe experimentally. The 2k-gratings that can be formed in the relatively long loop are probably essential for the achievement of a very narrow bandwidth when a laser diode is self-injection locked with phase conjugate feedback, since transmission gratings formed in the limited interaction regions (typical dimensions are less than 1.5 mm) do not result in a small wavelength selectivity (> 0.5 nm). From the results presented in Fig. 52, it is known that for a coherence length of several meters the wavelength selectivity of the grating structure does not become smaller than 0.026 nm. This fact can explain the observed line width of 0.02 nm from a multimode laser diode array coupled to a Cat conjugator (see Chapters 9 and 10); as the multimode spectrum of the laser diode is narrowed down due to the feedback from the conjugator, the coherence length becomes larger and 2k-gratings with more layers and a larger index modulation are formed in the crystal. The new 2k-gratings are more wavelength selective and the phase conjugate feedback becomes even more frequency selective. Consequently, the coherence length of the laser diode is increased even further. The lower limit is, however, a wavelength selectivity of 0.026 nm due to the size of the crystal. This phenomenon is referred to as *the self-narrowing effect*.

One may expect an even smaller wavelength selectivity if one uses a phase conjugate feedback geometry which allows a larger interaction length with contradirectional propagating beams that are the phase conjugate of each other, so that the formation of 2k-gratings is stimulated. Such a geometry could, e.g., be a larger crystal or the use of an additional crystal placed in front of the Cat conjugator and orientated in such a way that only 2k-gratings can be formed (e.g. propagation along the c-axis of a 0°-cut crystal).

8.4 Summary

In conclusion, the detuning curve (backreflection versus wavelength of the incident beam) and the wavelength selectivity of the complex grating structure formed in a self-pumped photorefractive barium titanate phase conjugator arranged in a Cat geometry have been measured. The results show that as the coherence length of the incident writing beam is decreased, the wavelength selectivity of the grating structure of the Cat conjugator becomes larger (less selective). For a coherence length that is much larger than the dimensions of the conjugator crystal, a wavelength selectivity (full width at half-maximum of the detuning curve) as small as 0.026 nm can be achieved. This lower limit depends on the size of the beam path in the crystal. A simple model of the grating structure, which is capable of reproducing the measured detuning curves, has been presented. The model reveals that a long 2k-grating must be formed in the internal loop of the Cat conjugator in order to explain the small wavelength selectivity observed experimentally. Moreover, the shape of the detuning curve depends on the coherence length and is determined by the interference between light that is diffracted in a 2k-grating and light that travels one round trip in the internal loop. The results explain how the optical feedback generated by the dynamic gratings in the phase conjugator can increase the coherence length of a multimode laser.

9 Phase Conjugate Self-Injection Locking Using an Etalon

In this chapter we demonstrate a new and extremely powerful technique that forces a laser diode array, operated at a drive current far above threshold, to oscillate in a single spatial and a single longitudinal mode. The coherence length of the phase locked output is proven to be increased significantly. The laser array is coupled to an external photorefractive phase conjugate mirror (PCM). To discriminate the longitudinal modes a Fabry-Perot etalon is included in the external cavity. Thereby only a limited number of modes are subsequently allowed to interact with the adaptive PCM. The etalon is the key component in this new frequency selective phase conjugate feedback (FSPCF) system. It eliminates frequency scanning and stabilizes the output. When operated with the FSPCF system, all the radiated energy from the freely running array is present in one single mode. In the off-axis configuration the far-field becomes almost diffraction limited.

9.1 Experimental Setup

The principle of operation is shown in Fig. 55. The laser diode array is a GaAlAs ten-stripe gain-guided device (array I), with a 100 μm wide emitting junction. It is temperature controlled by a peltier element. The array has a threshold of 0.28 amp (= i_{th}) and a maximum output power of 0.5 watt at 0.9 amp ($3.2 \cdot i_{th}$). The center wavelength of the spectrum at 25°C is 815 nm.

The output beam of the array is collimated with a lens (L1) that has an effective focal length of 4.5 mm and a numerical aperture of 0.55. A spherical singlet with a focal length of 76.2 mm is used to generate a pseudo far-field (image of Fourier plane of lens L1) at a distance of 475 mm from the array; at the plane of the pseudo far-field approximately 1 mm corresponds to 1°. In the plane of the pseudo far-field spatial filtering is applied. The spatial filter consists of two parallel razor blades mounted on two translation stages, and only radiation in-between the razor blades is allowed to pass the filter. A cylindrical lens with a focal length of 150 mm is used to collimate the beam in the transverse direction of the array. A spherical singlet with a focal length of 150 mm is used to focus the light and generates a 2 mm beam spot size at the face of the phase conjugator made up of a rhodium doped $BaTiO_3$ crystal. The crystal is arranged in the self-pumped Cat configuration. Both a 45°- and a 0°-cut crystal (Blue II and Blue III) have been used in the experiments with no significant differences in the obtained performance of the system. However, the build-up of the Cat geometry seems easier for the 0°-cut crystal (Blue III). All lenses have a broadband anti-reflection coating (R < 1%) in order to minimize the loss of the external cavity. A coupling loss of approximately 20% occurred between the array and lens L1, and an additional 10% is lost due to the beamsplitter, the wave plate, and the lenses (L2 and L3). The external cavity has a length of $2 \cdot 775$ mm. To obtain the largest photorefractive response the high coherence axis, the polarization, and the c-axis of the crystal must lie in the same plane, a requirement that can be accomplished if we rotate the beam polarization 90° while keeping the coherence axis fixed. This is done by rotating the array 90° around its optical axis and inserting a half-wavelength wave plate in the path in-between the array and the PCM, as discussed in Sec. 4.6.4. In-between the array and the PCM a solid etalon is placed. The etalon is a spectral filter and allows only certain resonance frequencies to pass and subsequently to interact with the adaptive PCM. Lens L3 is included to ensure the highest collimation upon passing the etalon and, thereby, to increase the transmission of the resonance frequencies. Two different etalons are

tested with the setup. The first one (etalon I) has a thickness of 300 μm with a finesse of approximately 17. The free spectral range ($\Delta\lambda_{fsr}^{etalon}$) is 0.75 nm at 814 nm (or 350 GHz). The FWHM bandwidth of the etalon (= $\Delta\lambda_{fwhm}^{etalon}$) is 0.04 nm at 814 nm (or 20 GHz). The second etalon (etalon II) has a free spectral range of 225 GHz and a finesse of 2.6. The FWHM bandwidth is 0.19 nm at 814 nm (or 86 GHz). It is etalon I that is used in the configuration unless otherwise stated.

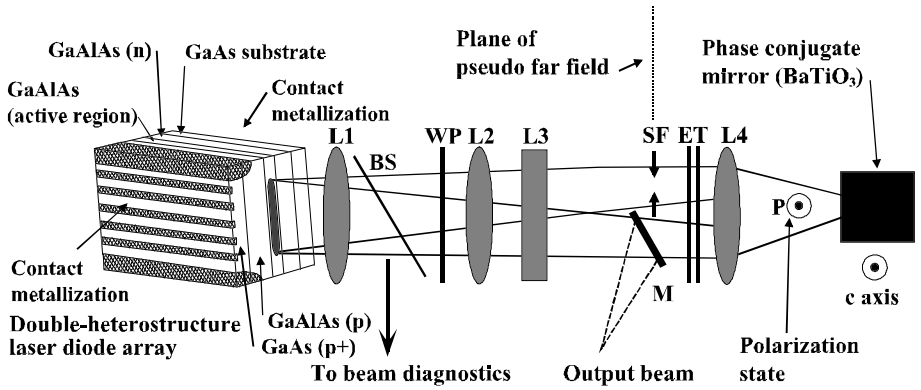

Figure 55. Experimental setup. A GaAlAs laser diode array is coupled to a phase conjugate mirror. L1: NA. = 0.55, f = 4.5 mm, L2: lens f = 76.2 mm, L3: cylindrical lens f = 150 mm, L4: lens f = 150 mm, BS: beamsplitter (2° wedge), WP: $\lambda/2$ wave plate (zero-order), ET: Fabry-Perot etalon, SF: spatial filter (two razor blades mounted on translation stages), M: removable mirror.

We consider two different feedback configurations: (i) the off-axis (or the single-lobe) and (ii) on-axis (or the twin-lobe). In the off-axis configuration a removable mirror (M) is inserted halfway through the beam line, at the position of the generated pseudo far-field, and it couples out one half of the radiated far-field pattern. The reflected beam is the output beam of the system. In the on-axis configuration the mirror and the spatial filter (SF) are removed and all the energy of the array is directed towards the PCM. The on-axis (twin-lobe) configuration (Sec. 5.1) may be regarded as a system of coupled resonators, whereas the off-axis configuration is the off-axis self-injection locking configuration (Sec. 5.3.1).

9.2 Characteristics of the On-Axis Configuration

First we consider the on-axis (twin-lobe) configuration. The etalon is a frequency filter and will only pass a limited number of frequencies that can subsequently interact with the phase conjugator.

9.2.1 Spectral Characteristics

When the crystal is illuminated, the reflectivity of the phase conjugator increases and the spectrum is narrowed down significantly. Figures 56(a) and (b) display the spectrum of the laser array when it is phase locked due to the frequency selective phase conjugate feedback (FSPCF) and when it runs freely, respectively. The drive current is two times the threshold current ($2 \cdot i_{th}$), and at this level it could take several minutes before the phase conjugator had built up and locking would be established. In Fig. 56(a) it is seen that the cooperative interaction among the PCM, the etalon and the array forces the spectrum to narrow down substantially. The bandwidth is measured to be reduced from a full width at half-maximum

(FWHM) of 0.7 nm to less than 0.02 nm (resolution limited). The etalon used (etalon I) has a bandwidth of $\Delta\lambda_{fwhm}^{etalon} = 0.04$ nm. The mode spacing between two adjacent array modes is on the order of $\Delta\lambda_{m,m+1} \simeq 0.02$ nm [33, 40], and even the closest spaced array modes therefore have sufficiently different transmission losses in the etalon. Consequently, a single array mode (single-mode operation) can be selected if the maximum transmission of the etalon is tuned to a frequency that matches an array mode with high gain. The tuning can be achieved by tilting the etalon with respect to the optical axis.

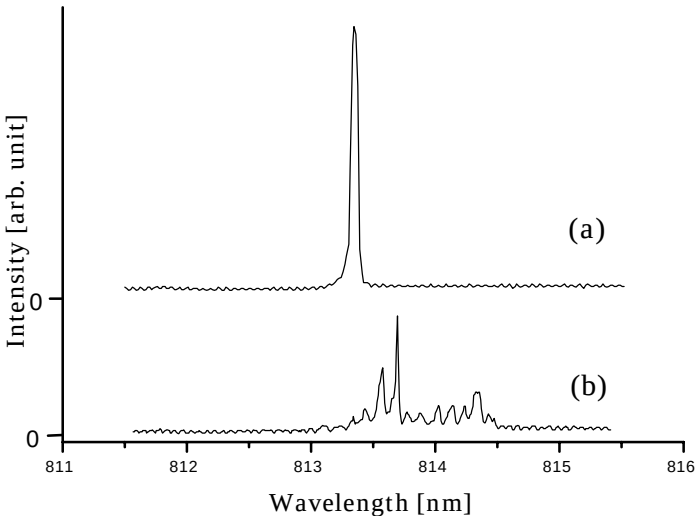

Figure 56. Spectrum from laser diode array. (a) Laser array is exposed to frequency selective phase conjugate feedback at a drive current of 2·i_{th} (on-axis configuration with etalon I). (b) Laser array runs freely with no feedback at a drive current of 2·i_{th}.

The Influence of the Etalon Bandwidth The on-axis configuration has also been tested with the low finesse etalon (etalon II). If etalon I is replaced with etalon II, more array modes will oscillate. The bandwidth of etalon II is 0.19 nm and only different longitudinal modes (consisting of several array modes) have different transmission losses; hence, a cluster of array modes around one longitudinal mode are lasing. At a drive current of 2·i_{th} the crystal provides a feedback of up to 10% measured at the beamsplitter. With etalon II the bandwidth of the spectrum is reduced to 0.15 nm. It should be noted that in the on-axis configuration where no spatial filtering is applied the bandwidth is determined by the bandwidth of the etalon, since the laser diode array and the phase conjugate mirror (which can only reflect light that can pass the etalon) form a coupled resonator.

Despite the modest increase in the coherence length ($\sim$ eight times), the configuration with etalon II is extremely stable with respect to the center wavelength of the phase locked spectrum that is determined by the peak transmission of the etalon. Under normal conditions the spectrum of the freely running laser diode array will shift 0.3 nm/°C. However, when the feedback is applied, the temperature of the laser diode array can be forced to change (using the peltier element) over a range of 15° C in less than one minute and the center wavelength is unaffected. This means that the laser array can in practice be operated without the active

temperature control if the FSPCF system is applied. If $\Delta\lambda_{fwhm}^{etalon}$ is comparable with $\Delta\lambda_{m,m+1}$, this is not the case. Then a temperature change leads to oscillation of other modes that match another transmission window of the etalon that is shifted $\Delta\lambda_{fsr}^{etalon}$ in wavelength.

9.2.2 Far-Field Characteristics

Figure 57(a) shows the far-field of the array in the on-axis feedback configuration using etalon I. When the array runs freely, as seen in Fig. 57(b), the far-field consists of several spatial modes and the radiation is almost uniform within θ = -2° to +2°. However, when the array operates in one single spatial mode, the far-field changes to the well known twin-lobe, as seen in Fig. 57(a). Compare this figure with Fig. 7 on page 28. The peaks are centered around $\theta \pm 2.3°$, which according to Eq. 8, corresponds to the $m = 10$ mode that for a ten-stripe array has the highest gain and is predicted to be centered at $\theta_{m=10} = \pm 2.33°$ (see Eq. 8). Only spectral filtering is applied in the on-axis configuration. Since the bandwidth of etalon I is comparable with $\Delta\lambda_{m,m+1}$ (the spectral filtering is very selective), single-mode operation can still be achieved using the phase conjugate frequency selective feedback. However, at a drive current of $3{\cdot}i_{th}$, the frequency selective phase conjugate feedback is not strong enough and single-mode operation cannot be optained. As a result, nearby array modes start to emerge and the bandwidth is increased to 0.1 nm and, consequently, the far-field lobes also broaden.

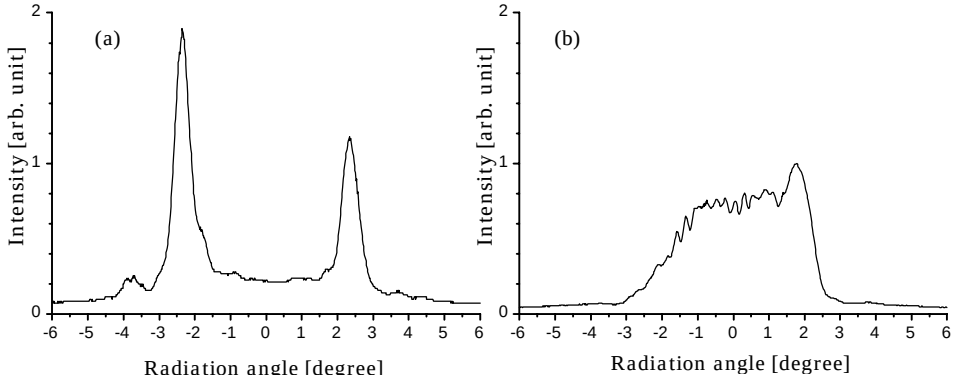

Figure 57. Far-field pattern of the laser diode array in the lateral direction. (a) Laser array is exposed to frequency selective phase conjugate feedback at a drive current of $2{\cdot}i_{th}$ (the on-axis configuration with etalon I). (b) Laser array runs freely with no feedback at a drive current of $2{\cdot}i_{th}$.

9.2.3 Intensity Noise of the Array Output

The phase conjugate reflectivity of the PCM ranges from 15% at low drive current ($2{\cdot}i_{th}$) down to 8% at higher drive current ($3{\cdot}i_{th}$). The feedback level measured at the beamsplitter (BS) ranges from 4-8% at low drive current to 1.5-2% at higher drive current. The amount of power that is fed back into the array is 4 mW and is independent of the drive current in the range of $2{\cdot}i_{th}$ to $3{\cdot}i_{th}$ (total radiated power is 200 mW and 440 mW at $2{\cdot}i_{th}$ and $3{\cdot}i_{th}$, respectively). This corresponds to an external reflectivity R_{ext} = 0.9-2%. Using Eq. 27 and $R_{out} = 0.04$ the feedback coefficient can be determined to a maximum of $F = 0.46$. According to Sec. 5.2.4 this is in the high feedback regime. The frequency scanning instability

has been avoided by using the etalon. However, there may be external cavity modes present that according to Sec. 5.2.4 can lead to increased noise through mode beating in the detection process. Using Eq. 29 yields $C \simeq 300$ ($F = 0.46$, $\beta_c = 2$, $L_{ext} = 550$ mm, $L = 0.8$ mm). Therefore, the feedback is sufficiently strong to generate external cavity modes. In order to verify the presence of the external cavity modes, the reflection at the beamsplitter is directed to a fast silicon detector with a bandwidth of 1 GHz. The measured electrical spectra are shown in Fig. 58. Both the spectrum corresponding to the case where the laser array runs freely (lower curve), and the spectrum where it is exposed to the FSPCF are shown (upper curve). The power incident on the detector has been adjusted so that the DC output is the same for the two measurements. It is clearly seen that the FSPCF leads to an increase in intensity noise. Moreover, several characteristic peaks are identified in the spectrum. The peaks are spaced with 258 MHz and originate from the beating between different external cavity modes in the optical to electrical detection process. For example, the second peak at 516 MHz is caused by beating between two external cavity modes that have an oscillation frequency that differ with 516 MHz corresponding to $2{\cdot}\tau_{ext}^{-1}$.

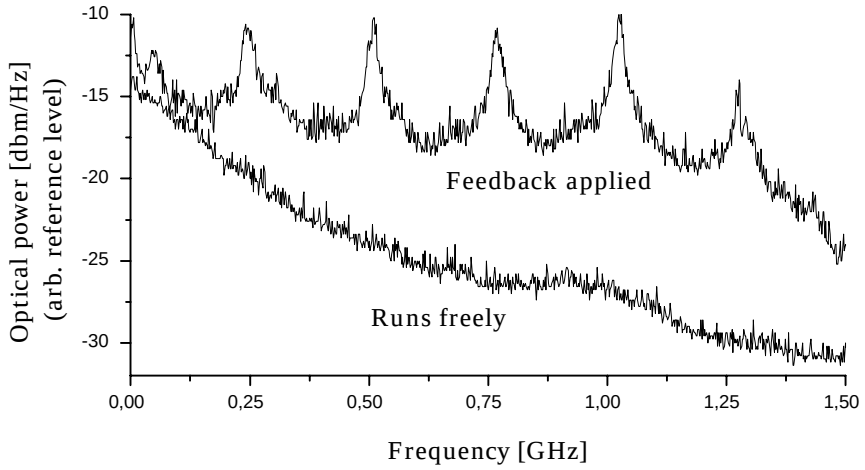

Figure 58. Electrical spectrum for detected output from laser diode array in the on-axis configuration. The spectra corresponding to both the freely running array (lower curve) and the case when the FSPCF is applied (upper curve) are shown. The external cavity is $L_{ext} = 0.55$ m. The drive current is $2{\cdot}i_{th}$.

External Cavity Mode Spacing According to Sec. 5.1.3, the frequency difference of 258 MHz predicts an external cavity length of $L_{ext} = 0.58$ m (free space). The external cavity was measured to be $L_{ext} = 0.55$ m (physical length) which is in agreement with the peak spacing if the reflective indices of the lenses in the external cavity are included. The presence of external cavity modes has hereby been established. The external cavity mode spacing is $c/2L_{ext}$ as is the case with a conventional cavity. Theoretical investigations [90, 206] have shown that for a cavity with a phase conjugator as one cavity mirror, the external cavity mode spacing is $c/4L_{ext}$, or half the longitudinal mode spacing of a cavity with conventional mirrors. However, as discussed in Sec. 5.2.2, this is only valid for externally pumped conjugators and does not apply to the self-pumped geometry that is used here. As a result, the external cavity mode spacing is $c/2L_{ext}$ as for conventional cavity.[153] It has experimentally been verified that if the length of the external

cavity is increased by a factor of two, the peak spacing is decreased by a factor of two.

9.3 Spatial Characteristics - Off-Axis Configuration

In the off-axis (single-lobe) configuration the far-field pattern is narrowed down significantly. Feeding back only one of the two lobes is somewhat similar to the previously reported self-injection locking techniques where a photorefractive PCM is used.[11, 15] The highest degree of brightness of the output of the system is obtained with the spatial filter and the etalon, and when only one single lobe is fed back to the laser diode array. From an experimental and practical point of view, this configuration is attractive since a large fraction of the radiated energy can be extracted from the laser system.

As the reflectivity of the PCM is built up, the output far-field lobe grows at the expense of the injection lobe. However, to achieve single-lobe operation it is often necessary to open the spatial filter slightly so that more energy will reach the PCM in order to start the self-pumped conjugator. After a few minutes the distance between the two razor blades can then be diminished again. Figure 59(a) shows the far-field of the laser array when it runs freely at a drive current of $2 \cdot i_{th}$. Figures 59(b) and (c) display the far-field for a drive current of $2 \cdot i_{th}$ and $3 \cdot i_{th}$, respectively, when the FSPCF is applied.

In the plane perpendicular to the junction the far-field is close to the diffraction limit and has a Gaussian shape that is unaffected of the number of oscillating array modes. It is the lobe at the negative angles (the injection lobe) that is fed back to the laser diode array. The peak of the output lobe is centered at $+2.3^\circ$ and $+2.2^\circ$ for $2 \cdot i_{th}$ and $3 \cdot i_{th}$, respectively. The most efficient performance of the system always takes place with an emission around 2.3° which corresponds to the $m = 10$ array mode. The edges of the two razor blades that form the spatial filter are positioned at θ = -1.9° and θ = -2.5°. The FWHM of the output beam (the positive angle) is measured to 0.75° ($2 \cdot i_{th}$) and 0.92° ($3 \cdot i_{th}$) corresponding to 1.4 and 1.7 times the diffraction limit, respectively. The total energy radiated from the laser diode array is increased by approximately 5% with the phase conjugate feedback compared with the freely running laser diode array.

The measured power of the output beam is 107 mW and 227 mW for a drive current of $2 \cdot i_{th}$ and $3 \cdot i_{th}$, respectively. When the laser diode array runs freely, the total power after the cylindrical lens (L3) is 147 mW and 320 mW for $2 \cdot i_{th}$ and $3 \cdot i_{th}$, respectively. At $2 \cdot i_{th}$ and $3 \cdot i_{th}$ and when the FSPCF is applied, the total radiated energy from the array (before lens L1) is 218 mW and 465 mW, respectively. This means that more than 70% of the available energy after lens L3 is contained in the output beam, and that 50% of the total radiated energy is contained in the output beam. However, as can be seen from the profile in Fig. 59(b), the output lobe (the positive lobe) contains more than 80% of the total radiated far-field energy. Based on this profile it is estimated that 80% of the radiated energy can be contained in the output beam provided losses at lenses, etc. are eliminated.

The amount of feedback measured at the beamsplitter is typically in the range of 0.4-1% (highest at lower current). The phase conjugate reflectivity of the PCM ranges from 12 to 15% for all drive currents. The amount of power that was fed back into the array is 0.5-1.4 mW (highest at lower current). At a drive current of $2 \cdot i_{th}$ the total radiated output power is 218 mW, which corresponds to an amplification of more than 21 dB (= 218 mW/1.4 mW) of the energy that is fed back into the array.

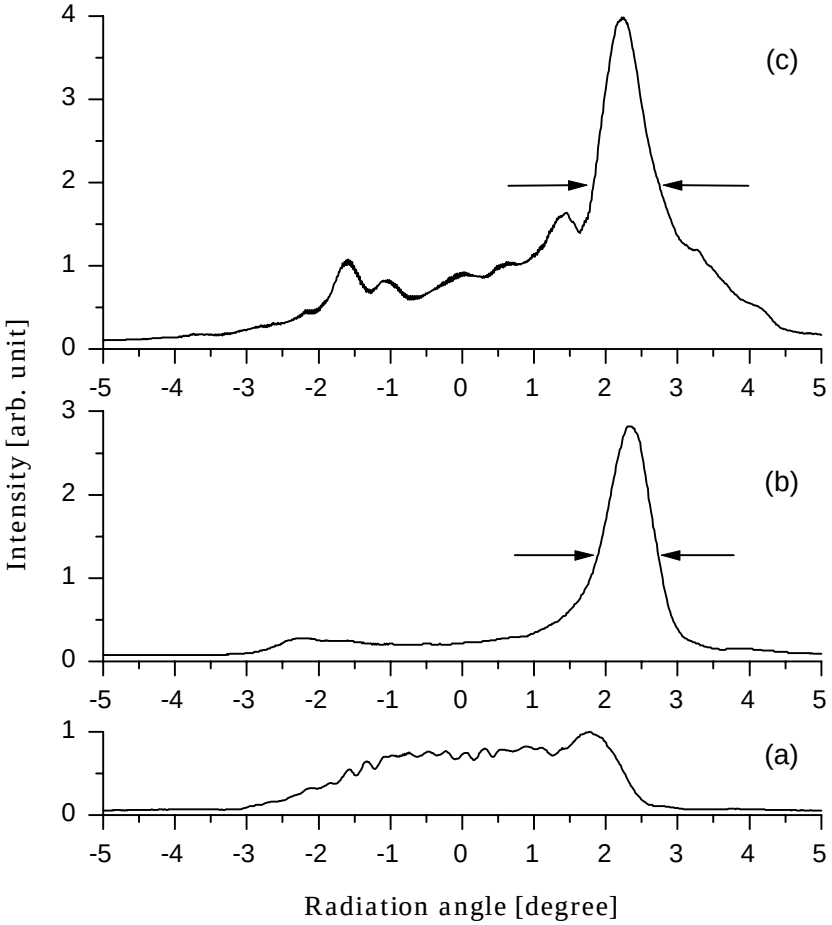

Figure 59. Far-field pattern of the laser diode array exposed to frequency selective phase conjugate feedback in an off-axis self-injection locking configuration using an etalon. (a) Laser array runs freely at a drive current of 2·i_{th}. (b) Feedback applied at 2·i_{th}. (c) Feedback applied at 3·i_{th}.

The far-field shown in Fig. 59(b) is also obtained if the etalon is removed from the external cavity. Despite the spatial filtering, however, the lack of spectral filtering leads to the oscillation of more longitudinal modes.

9.3.1 Focusability of the Output Beam

It was also tested how tight the output beam could be focused. The output beam has a size of $\sim 8 \times 1$ (mm)^2 (along the high and the low coherence axes of the laser array, respectively) measured at mirror M (see Fig. 55). The beam is collimated along the high coherence axis, but is slightly diverging along the low coherence axis. The output beam is expanded along the low coherence axis using two cylindrical lenses placed 0.70 m apart. The two lenses have a focal length of -60 mm and +800 mm, respectively. The output beam has a size of 10×10 mm^2 (= D×D) measured at the plane corresponding to last cylindrical lens, after which an achromat with a focal length of 40 mm (= f) is placed. This is a typical focal length used when, e.g., the output from diode arrays is used to pump solid state lasers. The measured spot size (full width at $1/e^2$) for the output beam is 11.7×11.8 (μm)^2. The measured spot is shown in Fig. 60.

The theoretically smallest spot size (full width at $1/e^2$) that can be achieved using a Gaussian beam is $4\lambda f/(\pi D)$, which gives 4.1 μm for $D = 10$ mm and $f = 40$ mm. Comparison with the 11.7 μm spot size indicates that the output beam is of a high quality yielding close to diffraction limited performance. Moreover, the measured output spot size can be compared with the smallest spot size that can be achieved with conventional lenses, prisms, etc. when attempts are made to focus the total radiation pattern of a freely running laser diode array. For the SDL-2432 laser diode array (the same as array I) the smallest nearly circular spot size reported [207] was 90×100 μm^2 (with a 40 mm focal length lens placed as the last lens in the configuration), which corresponds to an intensity that is more than fifty times smaller than the results presented here.

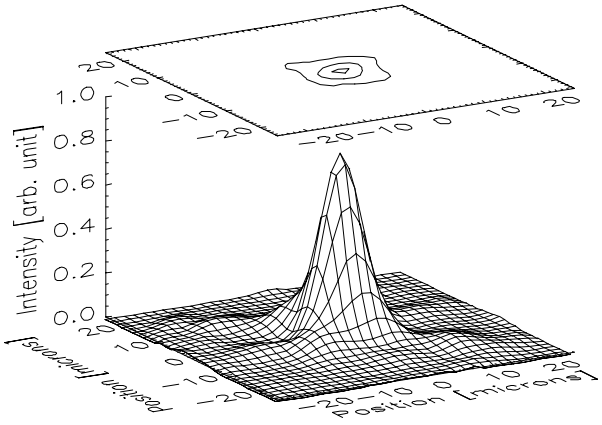

Figure 60. Minimum spot size of output beam focused by a lens with a 40 mm focal length. The drive current is 2·i_{th} and total power in the output beam is 107 mW. The three contour lines correspond to an amplitude of 0.135, 0.5, and 0.9.

9.4 Spectral Characteristics - Off-Axis Configuration

In this section the characteristics of the spectrum and the coherence length obtained with the off-axis configuration are presented and discussed.

9.4.1 Spectrum

Figures 61(a) and (b) display a frequency resolved near-field of the output facet of the laser diode array when it runs freely and when the FSPCF is applied, respectively, for a drive current of 2·i_{th}. The near-fields are obtained by imaging the near-field of the array (using the reflection from the beamsplitter) onto the input slit of a spectrum analyzer. The output slit of the spectrum analyzer is replaced with a two-dimensional photodetector array. The experimental setup is similar to the one presented in Ref. [33]. With the setup all longitudinal and spatial modes of the laser array can be resolved. In Figure 61(a) five clusters of array modes are identified (five longitudinal modes). Some of the array modes do not extend over the full width of the junction. When the phase conjugator is turned on, the spectrum of the output narrows down to a single array mode. The bandwidth is measured to be less than 0.02 nm (resolution limited). The right-

hand side of the near-field in Fig. 61(b) is brighter than the left-hand side due to the nonsymmetric radiation pattern that emerges with this self-injection locking scheme (compare with Fig. 24(b) on page 59). For a drive current of $3{\cdot}i_{th}$ the spectrum broadens slightly and a few adjacent array modes start to oscillate (as was also observed in Fig. 59(c)) The bandwidth is measured to be $\Delta\lambda_{fwhm} = 0.1$ nm.

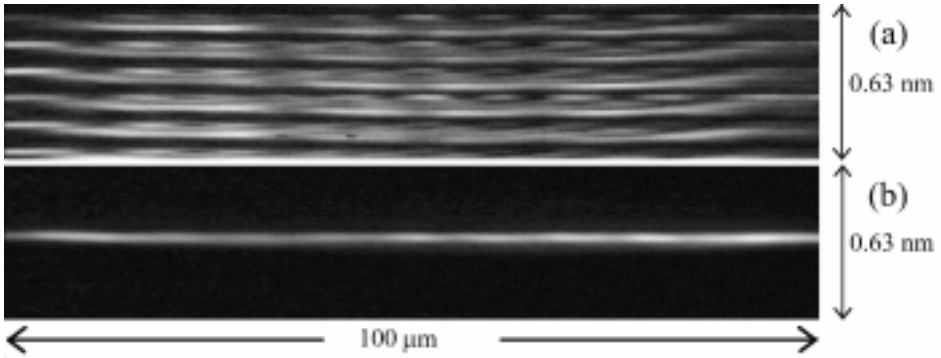

Figure 61. Spectrally resolved near-field of laser diode array exposed to off-axis phase conjugate feedback. Spectral (etalon I) and spatial filtering is applied in the external cavity. The drive current is $2{\cdot}i_{th}$. (a) Part of spectrum when laser array runs freely. Five clusters of array modes (five longitudinal modes) are indentified. (b) The feedback causes the spectrum to narrow down to one single array mode (single-mode operation). The bandwidth (FWHM) is less than 0.02 nm.

If the etalon with low finesse (etalon II) is used with the off-axis configuration, single-mode operation is still obtained at $2{\cdot}i_{th}$. This is due to the fact that for etalon II only one longitudinal mode (a cluster of array modes) can be selected. The spatial filtering then selects one array mode from this cluster and, as a result, single-mode operation can be obtained.

9.4.2 Coherence Length

The coherence length is measured by directing the output beam towards a standard Michelson interferometer that consists of two mirrors (one mounted on a translation stage) and a beamsplitter. The reference arm has a fixed length of 2×110 mm. The visibility of approximately five fringes of the interference pattern is recorded by a 25 mm wide photo array with 2048 pixels. Figure 62 displays the coherence degree versus the path difference of the two arms in the interferometer for different drive currents and when the FSPCF is not applied. The coherence degree is taken in the form $\gamma = ((I_{\max} - I_{\min})/(I_{\max} + I_{\min})) \times ((I_1 + I_2)/(2\sqrt{I_1 \cdot I_2}))$, where I_{max} and I_{min} are the maximum and the minimum intensity in the interference pattern; I_1 and I_2 are the intensity generated at the detector with the mirror in arms 2 and 1 covered, respectively. By comparing the path difference for the case where the array runs freely and the case where the FSPCF is applied, it is observed that the coherence length is increased by a factor of 70. At a drive current of $3{\cdot}i_{th}$ the coherence length is increased by a factor of 40. As can be seen in the figure, the FSPCF increases the coherence length to at least 25 mm. However, if the coherence length is defined as: $L_c = \lambda^2/\Delta\lambda_{fwhm}$ and λ is the lasing wavelength, the coherence length is calculated to be $L_c = 1$ mm when the laser diode array runs freely at a drive current of $2{\cdot}i_{th}$ (the bandwidth is ~ 0.7 nm when the array runs freely); the phase conjugate feedback increases the coherence length to

70 mm. At a drive current of $3 \cdot i_{th}$ the coherence length is increased by a factor of 40 to 22 mm.

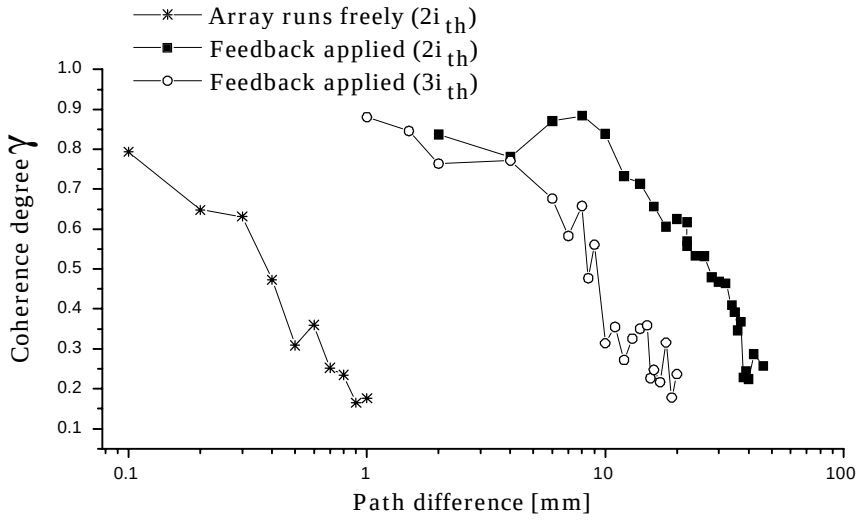

Figure 62. The coherence degree versus the path difference of the arms in a standard Michelson interferometer.

9.5 Stability and Noise Properties

Once the PCM is turned on and single-mode operation is obtained, the output becomes very stable with respect to wavelength and power. The key component in this new feedback system is the etalon. It significantly increases the stability of the center wavelength and the output power. The output characteristics are almost unaffected by even very strong mechanical vibrations that affect the optical components in the setup (such as taping on the components).

9.5.1 Stability of Center Wavelength

The stability of the center wavelength was measured with a spectrum analyzer with a resolution of 0.02 nm. The center wavelength was determined by fitting a Gaussian envelope to the response of the analyzer. Figure 63(a) shows the relative center wavelength as a function of time. The spectrum is a single array mode, and the variation of the center wavelength is very small. Over a period of six hours of operation the center wavelength was $\lambda_0 = 813.98 \pm 0.002$ nm (standard deviation). This variation is one order of magnitude less than the resolution of the analyzer. Therefore, we can conclude that the wavelength stability is less than $\pm$ 0.01 nm.

9.5.2 Stability of Output Power

The power contained in the output beam was also measured over a period of six hours of continuous operation. Figure 63(b) displays the output power as a function of time. During six hours of operation the measured power was $112.37 \pm$ 1.26 mW (standard deviation). The measured standard deviation of the detected power corresponds to less than 1.12%.

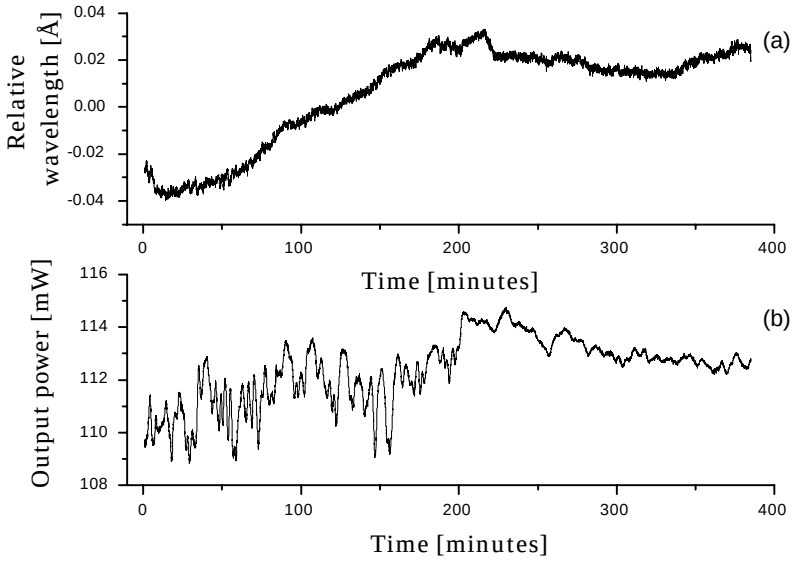

Figure 63. Off-axis frequency selective feedback (etalon configuration) is applied to the array at a drive current of 2·i_{th}. (a) Relative center wavelength of single mode spectrum versus time. (b) Power in output beam versus time.

9.5.3 Intensity Noise of Output

In order to characterize the intensity noise, the output beam is directed to a fast silicon detector with a bandwidth of 1 GHz. The measured electrical spectra are shown in Fig. 64. Both the spectra corresponding to the case where the laser array runs freely (lower curve), and where it is exposed to the FSPCF (upper curve) are shown. The power incident on the detector is adjusted so that the DC output is the same for the two measurements. It is clearly seen that the feedback leads to an increase in the intensity noise. Moreover, several characteristic peaks are identified in the spectrum. The peaks are spaced at 249 MHz. They originate from the beating between different external cavity modes in the optical to electrical detection process. The existence of the peaks establishes that external cavity modes are oscillating in the external cavity even in the off-axis configuration. This fact verifies that the phase conjugate mirror and the array are indeed coupled with each other. However, the strength of the coupling may be smaller than for the on-axis configuration, as discussed in Sec. 5.3.1. Figure 64 should be compared with the electrical spectrum for the on-axis configuration shown in Fig. 58. For the off-axis configuration the noise in the frequency range 0-1.5 GHz is approximately 10 dB larger than when the laser array runs freely. For the on-axis configuration, on the other hand, the feedback induced noise is larger in the higher frequency range than for the lower frequency range.

9.6 Summary of Results

With a phase conjugate mirror and an etalon, a novel technique (off-axis configuration) to enhance the spatial and the temporal coherence of laser diode arrays has been successfully demonstrated. For a drive current of 2·i_{th} single-mode operation is achieved. The spectral bandwidth is less than 0.02 nm, the coherence length is increased by a factor of 70 to at least 25 mm and the far-field is 1.4 times the diffraction limit. Even at maximum drive current the far-field is only

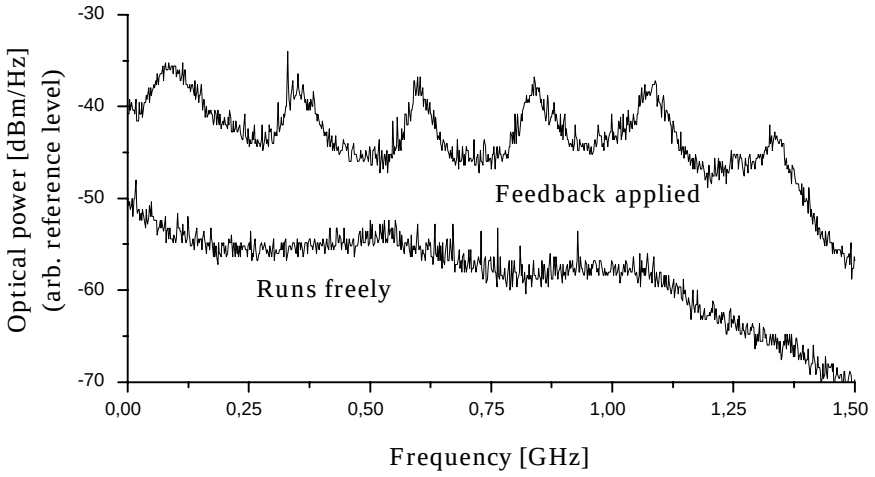

Figure 64. Electrical spectrum for detected output from laser diode array in the off-axis configuration. The spectra corresponding to both the freely running array (lower curve) and to the case when the FSPCF is applied (upper curve) are shown. The external cavity is L_{ext} = 0.55 m. The drive current is 2·i_{th}. The two curves have the same DC value.

1.7 times the diffraction limit, and the coherence length is increased by a factor of 40. In single-mode operation more than 50% of the radiated energy from the array is extracted in the experimental setup; however, a much larger fraction can be extracted with an optimized setup.

The existence of external cavity modes has been established for both the on-axis and the off-axis configurations. As discussed in Sec. 5.4, the term single-mode operation therefore refers to the modes in the freely running laser diode array.

Once the PCM has been turned on and single-mode operation has been obtained, the output becomes very stable with respect to wavelength and power. The measured standard deviations of the detected power and the center wavelength are 1.12% and 0.01 nm (resolution limited), respectively, during six hours of continuous operation at a drive current of two times the threshold current.

9.7 Phase-Conjugate Versus Conventional Feedback

The frequency selective phase-conjugate feedback scheme, which has been presented in this chapter, improves the coherence length of the laser diode array significantly in comparison with the modest improvement obtained using off-axis self-injection with conventional feedback (Sec. 5.5). The conventional feedback scheme, however, is also capable of forcing the laser array to emit an almost diffraction limited spatial radiation pattern. The phase-conjugate feedback is therefore only superior to the conventional feedback in the case where a light source with a long coherence length is needed. Therefore, if only a diffraction limited source is needed, conventional feedback may be applied instead of phase conjugate feedback. The conventional feedback scheme, however, may only be applied to broad-area lasers and laser diode arrays, and is not appropriate for laser diode bars. Conventional feedback may, consequently, only be used with laser devices with limited output power (< 4 watts), whereas phase-conjugate feedback can be used to increase the coherence length of laser diode bars with output power of up to tens of watts.

10 Phase Conjugate Self-Injection Locking Using a Grating

In this chapter we demonstrate how a laser diode array can be forced to oscillate in a single spatial and longitudinal mode simultaneously (single-mode operation). The laser diode array is driven with a drive current far above threshold and the wavelength is widely tunable.

Single longitudinal mode operation of a GaAlAs laser diode array operated with a drive current below threshold has been demonstrated by coupling it to an external cavity formed by a diffraction grating and a photorefractive phase conjugate mirror.[13] This system has proven to be widely tunable with respect to the frequency due to the presence of the diffractive grating. However, as discussed in Chapter 6, if operated far above threshold this system of coupled resonators is in general non stable due to nonlinear processes in the photorefractive phase conjugate mirror (PCM) and self-induced frequency scanning can take place. In order to have a stable system only one half of the far-field must be retroreflected back into the laser array so that it behaves like an injection locked amplifier (off-axis configuration).

In our off-axis configuration, we have included a spatial filter in the external cavity that allows only a limited number of spatial modes to interact with the adaptive PCM. Before the output beam from the array reaches the PCM, it is diffracted in a grating. The angular dispersion of the grating makes the feedback system much more frequency selective. The PCM and the grating form the frequency selective phase conjugate feedback (FSPCF) system and forces the laser array to oscillate in one single longitudinal mode. The interaction among the array, the dynamic gratings of the adaptive PCM, the spatial filter, and the diffractive grating enables a phase locking of the laser array and causes all the radiated energy to be transferred into only one single mode. The coherence length of the phase locked output is proven to be increased significantly. This technique allows a large fraction of the radiated energy to be extracted from the laser system with a single-lobe far-field pattern that is close to diffraction limited. The center frequency of the output of the array can be tuned more than 5 nm by tilting the grating.

10.1 Experimental Setup

The experimental setup is shown in Fig. 65. It is almost similar to the setup with the etalon in the external cavity (Chapter 9). In the grating configuration, however, the frequency selective element is a diffraction grating instead of an etalon. The laser diode array is array I (see Appendix A).

The output beam of the laser array is collimated with a lens (L1), and a second lens (L2) generates a pseudo far-field at a distance of 400 mm from the array. The collimated light is focused with a lens (L3) that generates a 2 mm spot at the face of the PCM made up of a 0°-cut rhodium doped (800 ppm) $BaTiO_3$ crystal (Blue III) in which a phase conjugation process takes place and returns the phase conjugate wavefront towards the array. The crystal is cut along its crystallographic axes and measures $5.11 \times 5.53 \times 5.33$ mm^3 (a-×a-×c-axis). The crystal is arranged in a self-pumped Cat configuration with an angle of incidence of 60°. The high coherence axis is in the a-c plane of the crystal in order to obtain the highest photorefractive response, as explained in Sec. 4.6. A 2° wedge is used as beamsplitter. The two reflections are used for beam diagnostics: one for monitoring the pseudo far-field generated with a lens; the second reflection is directed to a spectrometer

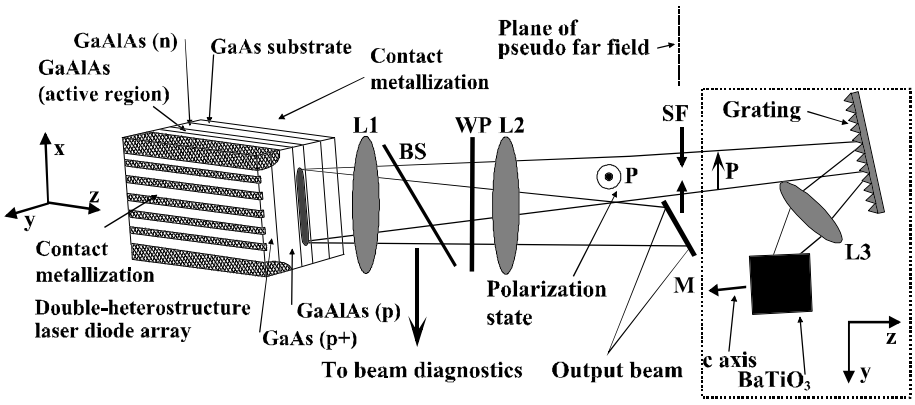

Figure 65. Experimental setup. A gain-guided GaAlAs laser diode array coupled to a phase conjugate mirror. L1: collimating lens, NA. = 0.55, f_1 = 4.5 mm, L2: Plano-convex cylindrical lens f_2 = 60 mm, L3: spherical singlet lens f_3 = 100 mm, BS: beamsplitter (2° wedge), WP: half-wave plate (zero-order) at 815 nm, Grating: 1200 l/mm ruled grating with Blaze angle of 26.4 deg. (750 nm), SF: spatial filter (two razor blades mounted on translation stages). P: indication of polarization (E-field). The components in the dotted box shall be rotated 90 degrees around the z-axis of the array.

with a resolution of 0.02 nm. A coupling loss of approximately 20% occurs between the array and the collimating lens (L1), and additionally 10% is lost at the beamsplitter, the wave plate, and the lenses. The external cavity has a length of 2 × 995 mm. As mentioned previously, the nature of the phase conjugate feedback mechanism of the $BaTiO_3$ crystal can cause self-induced frequency scanning of the array. To avoid this scanning and to obtain a much more stable configuration only one of the two far-field lobes is directed to the PCM; a mirror is placed at the position of the generated pseudo far-field to pick out one half of the radiated far-field pattern. The beam reflected off this mirror is the output beam of the system. The lobe that is directed to the PCM is diffracted in a 1200 lines/mm ruled grating before it enters the $BaTiO_3$ crystal. The angular orientation of the grating is controlled by a piezoelement. As discussed in Chapter 6, this grating adds angular dispersion to the system and has a strong influence on the dynamic behavior and the optical bandwidth of a multimode laser diode array when coupled to a self-pumped PCM. The interaction between the angular dispersion of the grating and the dynamic gratings formed in the $BaTiO_3$ crystal makes the external feedback system much more frequency selective. The different array modes are discriminated by a spatial filter placed in the plane of the generated pseudo far-field. The spatial filter (SF) is formed by two razor blades mounted on translation stages and by adjusting the position of them the number of spatial modes that can interact with the PCM can be controlled.

10.2 Spatial Characteristics

When the crystal is illuminated, the reflectivity of the PCM is built up and results in a significant narrowing of the spectrum. The far-field changes from a broad radiation pattern to the well-known pattern with two lobes. As time elapses, the phase conjugate reflectivity increases further and the intensity of the output lobe grows at the expense of the intensity of the lobe that is directed to the PCM. Often, however, it is necessary to open the spatial filter slightly so that more energy will reach the PCM in order to start the self-pumped conjugator; after typically

ten seconds the distance between the two razor blades can then be diminished again. The reflectivity of the PCM is normally 10-12% (not corrected for Fresnel reflections) in steady state. In this configuration the phase conjugate feedback often forces the phase locked spectrum to shift up to 1 nm towards a longer wavelength with respect to λ_0 (center wavelength of spectrum when it runs freely) before it reaches an equilibrium with stable output. At higher drive currents the shift can be as much as 2 nm. This shift is a part of the self-induced frequency scanning process (see Sec. 10.4 for a discussion).

Figure 66(a) displays the far-field of the array when it runs freely at a drive current of $2 \cdot i_{th}$. Figures 66(b) and (c) show the far-field of the array when the FSPCF is applied at drive currents of $2 \cdot i_{th}$ and $3 \cdot i_{th}$, respectively. The radiation angle is measured between the normal of the output facet of the array and the radiation direction in the plane of the junction (x-axis). It is the negative angle lobe that is directed to the PCM and then fed back to the array. The peaks of the output lobe are centered at $+2.0^\circ$ and $+2.1^\circ$ for $2 \cdot i_{th}$ and $3 \cdot i_{th}$, respectively. The most efficient performance of the system is always with the output lobe radiated at $2 - 2.1^\circ$. The edges of the two razor blades that form the spatial filter are positioned at -1.8° and -2.4° and allow only radiated energy in-between the razor blades to reach the PCM. With this setting only one array mode is transmitted through the filter (see Fig. 6). The FWHM of the output lobe (positive angle) is 0.84° ($2 \cdot i_{th}$) corresponding to 1.5 times the diffraction limit. As can be seen in Fig. 66(c), the main peak is still narrow as the drive current is increased to $3 \cdot i_{th}$; however, additional array modes start to oscillate and increase the bandwidth.

The total radiated energy from the array is increased by approximately 3% with the FSPCF applied as compared with the case where the array runs freely. With the configuration shown in Fig. 65 a large fraction of the radiated energy may be contained in the output beam which is nearly diffraction-limited provided that coupling losses and transmission loss at the lenses, etc. are eliminated. The power measured in the output beam is 110 mW and 220 mW for drive currents of $2 \cdot i_{th}$ and $3 \cdot i_{th}$, respectively. When the array runs freely, the total power just after the cylindrical lens (L2) is 150 mW and 320 mW for $2 \cdot i_{th}$ and $3 \cdot i_{th}$, respectively. At $2 \cdot i_{th}$ and $3 \cdot i_{th}$, and when the FSPCF is applied, the total radiated energy from the array (in front of L1) is 222 mW and 465 mW, respectively. This means that 70% of the available energy after the lens L2 is contained in the output beam, and that 50% of the total radiated energy (measured in front of lens L1) is contained in the output beam. However, similar to the discussion in Sec. 9.3, it is estimated that 80% of the radiated energy can be contained in the output beam provided losses at lenses, etc. are eliminated.

The amount of phase conjugate feedback measured at the beamsplitter is typically 0.4 to 0.7 % (highest at lower drive current). The amount of power that is fed back into the array is estimated to be 0.5-1.4 mW (highest at lower current). This corresponds to an external reflectivity R_{ext} = 0.1-0.6%. Using Eq. 27 and $R_{out} = 0.04$ the feedback coefficient can be determined to a maximum of $F = 0.14$. Using Eq. 29 yields $C \simeq 170$ ($F = 0.14$, $\beta_c = 2$, $L_{ext} = 550$ mm, $L = 0.8$ mm). This means that the feedback is strong enough to generate external cavity modes.

10.3 Spectral Characteristics

Figure 67 shows the optical spectra of the output beam of the array under different conditions. Figure 67(a) displays the spectrum when the array runs freely. At a drive current of $2 \cdot i_{th}$ several longitudinal modes are present and the FWHM bandwidth is 0.7 nm. Figures 67(b-e) show the spectra of the output beam at the same drive current when the FSPCF is applied, but for different tilts of the grating.

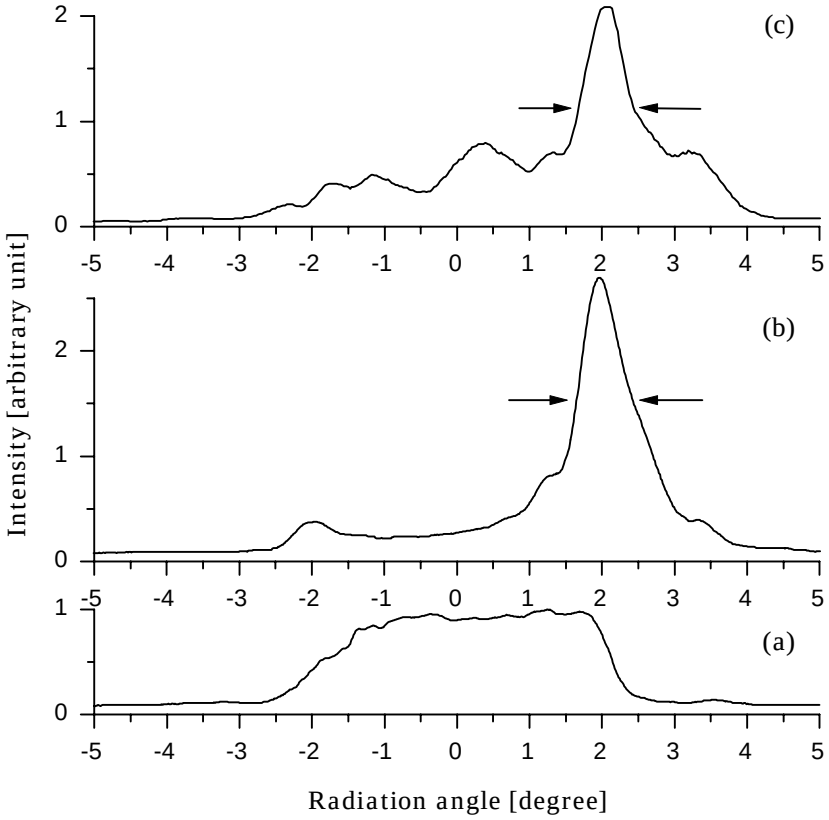

Figure 66. Measured far-field from array coupled to a grating and a PCM (measured in the plane of the junction - all curves on the same scale): (a) The array runs freely at a drive current of 2·i_{th}; (b) FSPCF applied at 2·i_{th}; (c) Same as (b) but drive current is 3·i_{th}.

Once the PCM is built up and the phase locking is established, the frequency can be tuned by tilting the grating. Between the recordings of Figures 67(b) and 67(e) the grating has been tilted 0.43°, which gives a sensitivity of the tunability of 12 nm/degree. A change in the tilt of the grating leads to a change in the angle of incidence at the air crystal interface, and also to a change of the position at the crystal surface at which the beam will enter. If the grating is tilted, the array will optimize the oscillating frequency for the best Bragg match to the existing gratings in the crystal and, thereby, again obtain high reflectivity from the PCM. By tilting the grating, the frequency is tuned by discrete steps corresponding to a longitudinal mode spacing of the array (0.11 nm); however, two longitudinal modes can oscillate simultaneously since the energy from one longitudinal mode is slowly transferred to the next mode as the grating is tilted. When the tilting of the grating stops, the adaptive PCM will adjust and optimize for the highest reflectivity and within seconds single-mode operation will again be obtained. For a fixed grating position the frequency can be tuned continuously over a range of 0.1 nm corresponding to one longitudinal mode spacing by changing the temperature of the junction of the array less than 1°C. By adjusting the grating and the temperature of the junction any wavelength within a 5 nm range can be achieved. The gain bandwidth of the GaAlAs array is huge, so the limited wavelength range may be explained as follows: the array and the PCM are only weakly coupled, and the PCM cannot suppress the oscillation of the natural modes of the array cavity

if the spectrum is forced too far away by tilting the grating. The tuning range of 5 nm is similar to the observed range for the off-axis self-injection locking scheme where conventional feedback from a diffraction grating is used (Sec. 5.5.2). This does indeed suggest that the limited tuning range has to do with the injection locking process and not the properties of the phase conjugator.

For a fixed grating tilt and for a drive current of $2 \cdot i_{th}$ the FWHM bandwidth of the single-mode spectrum is measured to be less than 0.03 nm. By recording the frequency resolved near-field pattern with a setup similar to the one in Ref. [33], it is verified that the array only operates on one array mode. This verifies true single-mode operation. As the drive current is increased to $3 \cdot i_{th}$, however, additional array modes start to oscillate and increase the bandwidth to 0.1 nm.

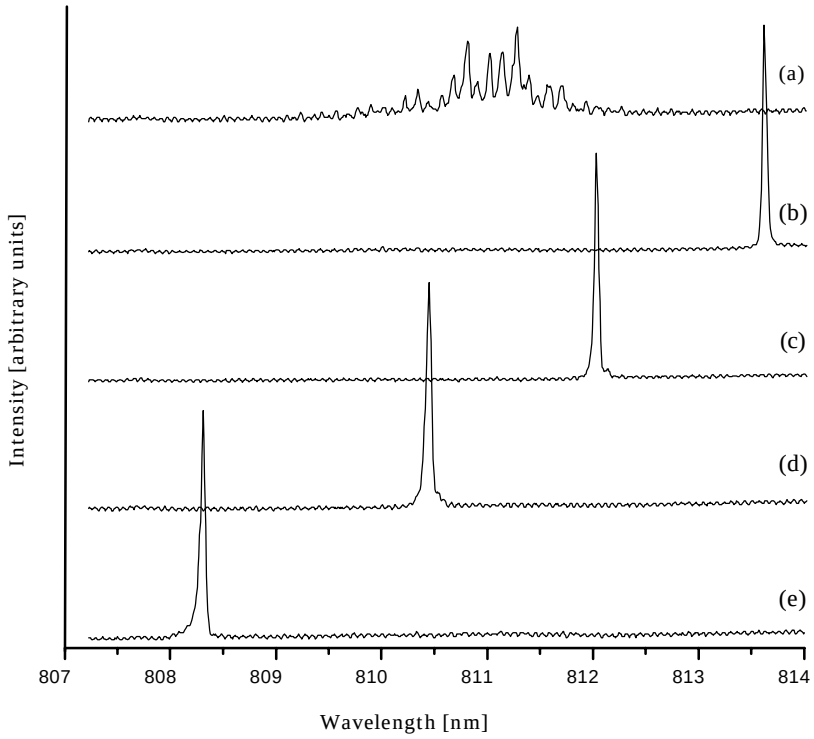

Figure 67. Laser diode array coupled with a grating and a PCM. Optical spectrum at a drive current of $2 \cdot i_{th}$: (a) The array runs freely; (b) The FSPCF is applied. The angle of incidence at the grating is 19.73 deg. Bandwidth (FWHM) of 0.03 nm; (c) Same as (b) but angle of incidence is 19.60 deg; (d) Same as (c) but angle of incidence is 19.47 deg; (e) Same as (d) but angle of incidence is 19.30 deg.

10.3.1 Continuous Tunability of the Center Frequency

The frequency can automatically be tuned by applying a sawtooth modulation voltage to the piezoelement. At a drive current of up to $2 \cdot i_{th}$ for the laser array, and a modulation frequency for the piezoelement of less than 0.2 Hz, the phase locked spectrum scans smoothly back and forth in a single mode that transfers its energy to the next longitudinal mode, as described previously. During the scanning the reflectivity of the PCM is decreased 10-20% as compared with the case where the grating is fixed. If the modulation frequency is higher than 0.5 Hz, the bandwidth of the phase locked spectrum will increase to more than 0.3 nm. For

modulation frequency in the range of 5-10 Hz, the bandwidth is the same as when the arrays runs freely. If the modulation frequency is larger than approximately 0.2 Hz, the reflectivity of the PCM will continuously fall to zero as time elapses. The response time for the $BaTiO_3$ crystal is on the order of one second and only for a very low modulation frequency (< 0.2 Hz) can the crystal respond to the changes of the incident beam and, thereby, maintain high phase conjugate reflectivity.

10.3.2 Coherence Length

The improved coherence of the output from the laser array is measured by a standard Michelson interferometer consisting of two mirrors (one mounted on a translation stage) and a beamsplitter. The reference arm has a fixed length of 2×110 mm. The visibility of approximately five fringes of the interference pattern is recorded by a 25 mm wide photodetector array with 2048 pixels. The coherence degree is taken in the form $\gamma = ((I_{\max} - I_{\min})/(I_{\max} + I_{\min})) \times ((I_1 + I_2)/(2\sqrt{I_1 \cdot I_2}))$, where I_{max} and I_{min} are the maximum and the minimum intensity in the interference pattern, respectively. I_1 is the intensity generated at the detector with the mirror in arm 2 covered and I_2 is the intensity with the mirror in arm 1 covered. Figure 68 displays the coherence degree versus the path difference of the two arms in the interferometer. By comparing the path difference for the case where the array runs freely and the case where feedback is applied, it is observed that the coherence length of the array with the phase conjugate feedback is increased by a factor of 45 to at least 16 mm for a drive current of $2\cdot i_{th}$. At a drive current of $3\cdot i_{th}$ the coherence length is increased by a factor of 28.

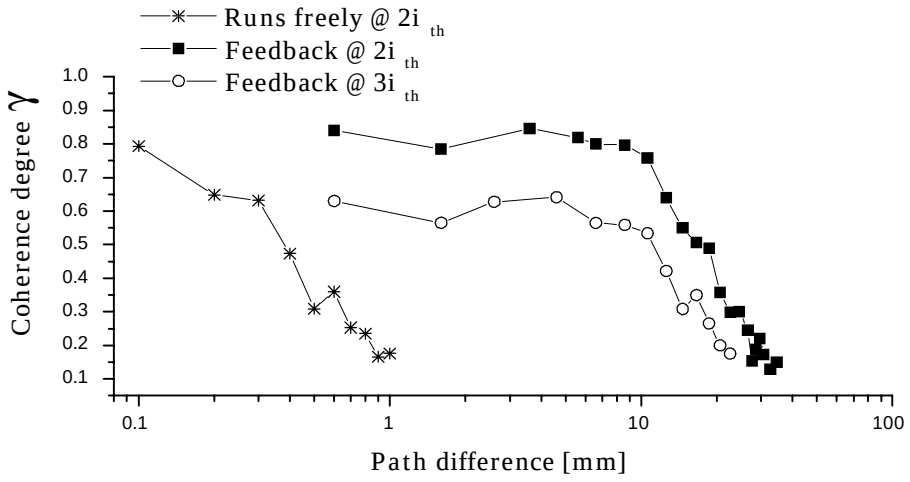

Figure 68. The coherence degree versus the path difference of the arms in a standard Michelson interferometer. Laser diode array coupled to a PCM and diffraction grating.

10.4 Physical Origin of the Single-Mode Operation

In the grating configuration the phase conjugate feedback often forces the phase locked spectrum to shift up to 1 nm towards a longer wavelength with respect to λ_0 (center wavelength of spectrum when it runs freely) before it reaches an equilibrium with a stable output. At higher drive currents the shift can be as

large as 2 nm. This shift is a part of the self-induced frequency scanning process. As previously described, the constant change of frequency (repeating cycles) is avoided by feeding back only one lobe of the far-field. The mechanisms of the weakly coupled system are not yet fully understood; however, we suggest that as the phase locked spectrum starts to shift, the system will reach an equilibrium due to the material frequency dispersion of the $BaTiO_3$ crystal. The fact that a very narrow spectrum and even single-mode operation can be obtained is due to the angular dispersion of the grating which disperses the beam inside the crystal and enhances this process. Moremore, the grating provides spectral filtering and discriminates the longitudinal modes. This leads to single-mode operation. If the grating is replaced with a conventional mirror, the configuration is similar to the one used in Ref. [15]. Even though an almost diffraction limited output beam was obtained using this configuration, the spectrum still had a bandwidth of more than 0.5 nm. This clearly demonstrates that the grating provides spectral filtering in the configuration used here. Furthermore, once the single-mode operation is almost established, the coherence length becomes longer (the self-narrowing effect), and the high wavelength selectivity of the grating structure in the phase conjugator causes the spectrum to become a single mode.

The fact that the grating provides high frequency selectivity, i.e. the phase conjugate reflectivity is smaller for the side modes as compared with the dominating mode, may be explained by two mechanisms. Firstly, for a change in wavelength the grating causes the diffraction angle to change and, as a result, the angle of incidence at the crystal will also change. This change can lead to reduced reflectivity because of the high wavelength selectivity of the grating structure in the conjugator. Secondly, the wavelengths are to some extent spatially separated inside the crystal due to the imaging properties of the lens used to focus the light into the crystal. For a change in wavelength, the incident beam will be shifted inside the crystal and will consequently propagate in parts of the crystal with less gratings causing the overall phase conjugate reflectivity to be reduced.

10.5 Stability of Output Beam

Once the PCM has been turned on and single-mode operation has been obtained, the output becomes very stable with respect to frequency and output power. The highest stability is achieved if the wavelength is shifted - by tilting the grating - 1-2 nm towards a longer wavelength with respect to λ_0 (the center wavelength of the multimode spectrum when the array runs freely).

10.5.1 Stability of Center Wavelength

The stability of the center wavelength is measured with a spectrum analyzer with a resolution of 0.02 nm. The center wavelength was determined by fitting a Gaussian envelope to the response of the analyzer. Figure 69(a) shows the center wavelength as a function of time. The drive current is $2 \cdot i_{th}$ and the spectrum is a single array mode. The variation of the center wavelength is very small, but at time $t \simeq 100$ minutes the center wavelength suddenly makes a shift of approximately 0.13 nm. This wavelength shift corresponds to one longitudinal mode spacing of the array cavity. If no such shifts take place, the wavelength is very stable. During five hours of continuous operation (t = 100 to 400 minutes) the center wavelength is $\lambda_0 = 812.51 \pm 0.004$ nm (standard deviation). This variation is one order of magnitude less than the resolution of the analyzer. We can conclude that the wavelength stability is less than $\pm$ 0.01 nm.

The sudden wavelength shift may be suppressed if a low finesse etalon is included in the external cavity. If the free spectral range is chosen to be, e.g., $\Delta\lambda_{fsr}^{etalon} =$

$1.5 \cdot \Delta\lambda_{FP}$, the wavelength shift will be less favorable for the system with regard to optimum feedback.

10.5.2 Stability of Output Power

The power in the output beam was also measured over a period of six hours of continuous operation. Figure 69(b) displays the output power as a function of time. For $t \simeq 100$ minutes, the power makes a sudden jump. This jump is associated with the shift in center wavelength seen in Fig. 69(a). Over a period of five hours ($t = 100$ to 400 minutes) of continuous operation the measured power was 120.19 ± 0.67 mW (standard deviation). The measured standard deviation of the detected power corresponds to less than 0.56%.

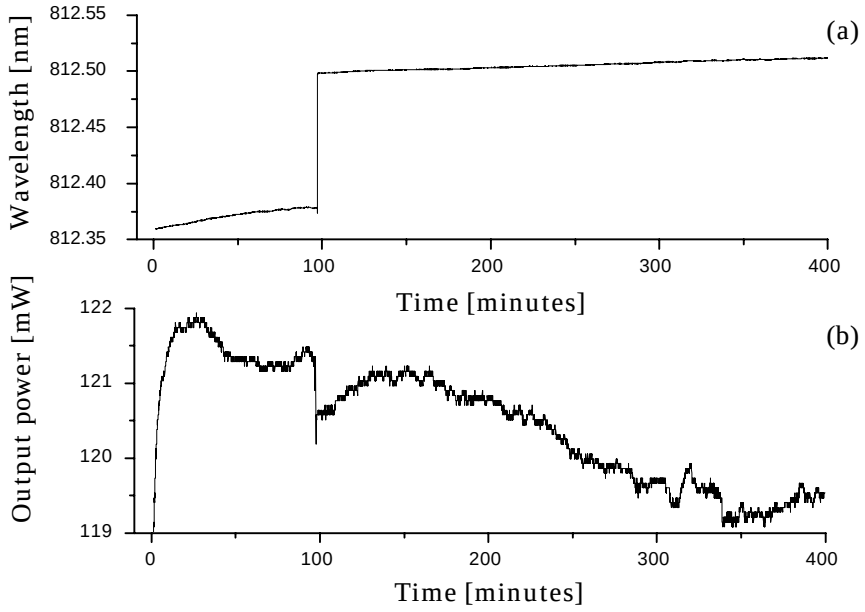

Figure 69. Off-axis frequency selective feedback (grating configuration) is applied to the array at a drive current of $2 \cdot i_{th}$. (a) The center wavelength of the single-mode spectrum versus time. (b) Power in the output beam versus time.

10.6 Summary of Results

A technique that make use of a phase conjugate mirror and a diffraction grating to enhance the spatial and temporal coherence of high-power laser diode arrays has been demonstrated. For a drive current of $2 \cdot i_{th}$ single-mode operation is achieved. The spectral bandwidth is reduced to less than 0.03 nm, the coherence length is increased by a factor of 45 to at least 16 mm, and the far-field is narrowed down to 1.5 times the diffraction limit. The frequency of the output can be tuned over a wavelength range of 5 nm by tilting the grating. Even at almost maximum drive current ($3 \cdot i_{th}$) the coherence length is still increased by a factor of 28. More than 50% of the radiated energy from the array is extracted in the experimental setup, but a much larger fraction can be extracted with an optimized setup. The output beam of the configuration is very stable with respect to the center frequency and the optical output power. During five hours of continuous operation the wavelength and the output power vary less than 0.01 nm and 0.56%, respectively.

11 Conclusion

In this thesis a new laser system consisting of a laser diode array with phase conjugate feedback has been presented. The conjugator is a self-pumped barium titanate crystal arranged in a Cat geometry. The work can be divided into the following main subjects: (1) improvement of the coherence characteristics of a laser diode array using photorefractive phase conjugate self-injection locking, and (2) a study of the characteristics of the phase conjugator. For the improvement of the laser diode array two configurations have been developed: (1a) the etalon configuration and (1b) the grating configuration. The investigations of the characteristics of the phase conjugator deal with (2a) the influence of the material frequency dispersion on the complex grating structure, and (2b) the wavelength selectivity of the complex grating structure in the crystal. In the following, a summary and a conclusion for each of these four subjects are given.

11.1 Etalon Configuration

With a phase conjugate mirror and an etalon, a novel technique using off-axis frequency selective phase conjugate self-injection locking to enhance the spatial and the temporal coherence of laser diode arrays has successfully been demonstrated. A fraction of the far-field radiation is directed to the self-pumped Cat conjugator. In the external cavity a Fabry-Perot etalon and a spatial filter are included. For a drive current (for the laser array) of two times the threshold current ($2 \cdot i_{th}$) one spatial array mode and one longitudinal mode are selected by spatial and spectral filtering (single-mode operation). The existence of multiple external cavity modes has been observed and the term single-mode operation therefore refers to the modes in the solitary laser array. The spectral bandwidth is less than 0.02 nm, the coherence length is increased by a factor of 70 to more than 25 mm, and the far-field is 1.4 times the diffraction limit. Even at almost maximum drive current ($3 \cdot i_{th}$) the far-field is only 1.7 times the diffraction limit and the coherence length is increased by a factor of 40. In single-mode operation more than 50% of the radiated energy from the laser diode array is extracted in the experimental setup; however, a much larger fraction can be extracted with an optimized setup.

Once the PCM is turned on and single-mode operation is obtained, the output becomes very stable with respect to the wavelength and the output power. The measured standard deviations of the detected power and the center wavelength are 1.26% and 0.01 nm (resolution limited), respectively, over a period of six hours of continuous operation at a drive current of two times the threshold current.

11.2 Grating Configuration

A new technique, using a phase conjugate mirror and a diffraction grating, to enhance the spatial and the temporal coherence of high-power laser diode arrays has been demonstrated. A fraction of the far-field radiation is directed to the grating and coupled to the phase conjugate mirror. For a drive current of $2 \cdot i_{th}$, single-mode operation is achieved. The spectral bandwidth is reduced to less than 0.03 nm, the coherence length is increased by a factor of 45 to at least 16 mm, and the far-field is narrowed down to 1.5 times the diffraction limit. The frequency of the output can be tuned over a wavelength range of 5 nm by tilting the grating. Even at almost maximum drive current ($3 \cdot i_{th}$) the coherence length is still increased by a factor of 28. More than 50% of the radiated energy from the array is extracted in the experimental setup, but a much larger fraction can be extracted with an optimized setup. The output beam of the configuration is very stable with respect

to the center frequency and the optical output power. During five hours of continuous operation the wavelength and the output power vary less than 0.01 nm and 0.56%, respectively.

11.3 Effects of the Material Dispersion

The scan rate (wavelength shift per unit time) in self-induced frequency scanning depends on the intensity of the beam inside the photorefractive crystal. The scan rate is found to be proportional to the intensity. Furthermore, the scan rate does not depend on the feedback level but only on the intensity (i.e. the response time of the crystal). These observations reveal that the self-induced frequency scanning is due to the photorefractive process in the conjugator.

It has been established that the orientation of the beam path in the crystal changes during self-induced frequency scanning. Moreover, it is shown that the self-induced frequency scanning of a laser diode array with feedback from a Cat conjugator is significantly altered by the presence of dispersion of prisms or by dispersive diffraction gratings placed in the external cavity in front of the crystal. It is demonstrated that these prisms or gratings can even suppress the self-induced frequency scanning and stabilize the output of the laser array. The experimental results show that the material frequency dispersion of $BaTiO_3$ is an important effect for the self-induced frequency scanning process.

Numerical simulations of the complex grating structure have been performed; the grating structure is generated when several longitudinal modes from a laser induce a Cat geometry in a barium titanate crystal. The results of the numerical analysis clearly show that the detuning curve (backreflection versus wavelength of the incident beam) of the generated grating structure is asymmetric with respect to the center wavelength of the laser that induced the grating structure. The asymmetric feedback to the laser, which is generated by diffraction in the grating structure, leads to self-induced frequency scanning of the laser. It is found that the material frequency dispersion of the barium titanate crystal causes the asymmetry and is the origin of the scanning process. The theoretical predictions are in good agreement with the experimental results.

11.4 Wavelength Selectivity of the Grating Structure

The detuning curve and the wavelength selectivity of the complex grating structure formed in a Cat conjugator have been measured. The results show that the wavelength selectivity of the grating structure of the Cat conjugator becomes larger (less selective) when the coherence length of the incident writing beam is decreased. For a coherence length that is much larger than the dimensions of the conjugator crystal, a wavelength selectivity as small as 0.026 nm (full width at half-maximum of the detuning curve) can be achieved. This lower limit depends on the size of the crystal; a larger crystal leads to a more selective grating structure. A simple model of the grating structure, which is capable of reproducing the measured detuning curves, has been presented. The model reveals that a long 2k-grating must be formed in the internal loop of the Cat conjugator in order to produce the small wavelength selectivity (0.026 nm) observed experimentally. Moreover, the shape of the detuning curve depends on the coherence length and is determined by the interference between light that is diffracted in a 2k-grating and light that travels one round trip in the internal loop in the conjugator. The results explain why the optical feedback generated by the dynamic gratings in the phase conjugator increases the coherence length of a multimode laser.

12 Future work

In this chapter we briefly discuss future experiments and ideas that would be natural to carry out in continuation of the present Ph.D. thesis. It does not represent a comprehensive review of all potential projects, but is limited to a few topics that are closely linked to the work contained in this thesis.

12.1 Improvement of the Self-Injection Locking Scheme

We believe that it is very likely that the performance of the off-axis phase conjugate self-injection locking scheme with a frequency selective element will be significantly better - and even at maximum drive current - if an antireflection coating ($< 1\%$) is applied to the output facet of the laser diode array. This is partly supported by the results obtained in Ref. [115].

12.2 Self-Injection Locking of Laser Diode Bars

Self-injection locking of a laser diode bar makes it possible to obtain a light source with very high output power (> 10 watt) and a near diffraction limited radiation pattern. A diffraction limited source that uses off-axis phase-conjugate self-injection locking has been reported.[17] It is therefore likely that the frequency selective phase-conjugate feedback scheme presented in this thesis will be capable of increasing both the spatial coherence and the temporal coherence of a laser diode bar.

12.3 Second Harmonic Generation

The diffraction limited radiation pattern and the single-mode spectrum from an improved laser diode array using phase conjugation opens the possibility of developing a high-power (> 100 mW) blue light source based on second harmonic generation. Since GaAlAs laser diode arrays can be fabricated with a lasing wavelength in the range of 750 nm to 880 nm, it may be possible to generate a blue light source with an desired wavelength in the range of 375 nm to 440 nm. Laser diode arrays can also be fabricated with a wavelength in the visible wavelength range of 630 nm to 690 nm and offers the potential of a UV light source.

The second harmonic may be generated through the use of the on-axis configuration with an etalon included in the external cavity. In this configuration the photorefractive crystal is used in a more unique way than just to improve the coherence properties of the laser diode array. A frequency doubling crystal is included in the external cavity. High-reflection coatings are applied to the surfaces of the doubling crystal and, as a result, an etalon is obtained. In such a scheme the etalon has two purposes. Firstly it acts as a frequency selective element so that the phase conjugation phase-locks the laser diode array and improves the coherence properties. Secondly, the etalon forms a resonant frequency doubling cavity. Since the phase conjugator automatically selects a frequency that matches the etalon, high conversion efficiency for the second harmonic generation is expected. The phase conjugator is dynamic and adjusts to any slow temperature change and, consequently, the phase conjugator has the potential of replacing a traditional electrical servo system.

References

[1] T. H. Maiman, "Stimulated optical radiation in ruby masers," Nature **187,** 493 (1960).

[2] G. P. Agrawal and N. K. Dutta, *Semiconductor Lasers*, 2nd ed. (Van Nostrand Reinhold, 1993), ISBN 0-442-01102-4.

[3] C. Lindsey, P. Derry, and A. Yariv, "Fundamental lateral mode oscillation via gain tailoring in broad area semiconductor lasers," Appl. Phys. Lett. **47,** 560 (1985).

[4] D. Botez and D. Scifres, *Diode Laser arrays* (Cambridege University Press, 1994), ISBN 0-521-41975-1.

[5] G. R. Hadley, "Index-guided arrays with a large index step," Opt. Lett. **14,** 308 (1989).

[6] S. O'Brien, D. F. Welch, R. A. Parke, D. Mehuys, K. Dzurko, R. J. Lang, R. Waarts, and D. Scifres, "Operating characteristics of a high-power monolithically integrated flared amplifier master oscillator power amplifier," IEEE J. Quan. Elec. **29,** 2052 (1993).

[7] D. J. Bossert, J. R. Marciante, and M. W. Wright, "Feedback effects in tappered broad-area semiconductor lasers and amplifiers," IEEE Photo. Tech. Lett. **7,** 470 (1995).

[8] S. Sternklar, S. Weiss, M. Segev, and B. Fischer, "Beam coupling and locking of lasers using photorefractive four-wave mixing," Opt. Lett. **11,** 528 (1986).

[9] M. Cronin-Golomb, B. Fischer, J. O. White, and A. Yariv, "Theory and applications of four-wave mixing in photorefractive media," IEEE J. Quan. Elec. **20,** 12 (1984).

[10] M. Cronin-Golomb, A. Yariv, and I. Ury, "Coherent coupling of diode lasers by phase conjugation," Appl. Phys. Lett. **48,** 1240 (1986).

[11] M. Segev, S. Weiss, and B. Fischer, "Coupling of diode laser arrays with photorefractive passive phase conjugate mirrors," Appl. Phys. Lett. **50,** 1397 (1987).

[12] S. Weiss, M. Segev, and B. Fischer, "Line narrowing and self-frequency scanning of laser diode arrays coupled to a photorefractive oscillator," IEEE J. Quan. Elec. **24,** 706 (1988).

[13] M. Segev, Y. Ophir, B. Fischer, and G. Eisenstein, "Line narrowing and self-frequency scanning of laser diode arrays coupled to a photorefractive oscillator," IEEE J. Quan. Elec. **24,** 706 (1988).

[14] S. MacCormack and R. W. Eason, "Near-diffraction-limited single-lobe emission from a high-power diode-laser array coupled to a photorefractive self-pumped phase-conjugator mirror," Opt. Lett. **16,** 705 (1991).

[15] S. MacCormack and J. Feinberg, "High-brightness output from a laser-diode array coupled to a phase-conjugating mirror," Opt. Lett. **18,** 211 (1993).

[16] S. MacCormack and J. Feinberg, "Injection locking a laser-diode array with a phase-conjugate beam," Opt. Lett. **19,** 120 (1994).

[17] S. MacCormack and J. Feinberg, "Self-locking of a laser diode bar using off-axis phase conjugation," In *CLEO*, **8,** 153 (Opt. Soc. of Am., Wash., 1994), paper CTuO1.

[18] M. Osinski and J. Buus, "The linewidth broadening factor in semiconductor lasers - An overview," IEEE J. Quan Elec. **23,** 9 (1987).

[19] G. Agrawal, "Fast-Fourier-transform based beam-propagation model for stripe-geometry semiconductors lasers: inclusion of axial effects," J. Appl. Phys. **56,** 3100 (1984).

[20] G. Agrawal, "Effect of index antiguiding on the far-field distribution of stribe-geometric lasers," J. Appl. Phys. **47,** 283 (1983).

[21] W. Streifer, R. D. Burnham, and D. R. Scifres, "An analytic study of (GaAl)As gain guided lasers at threshold," IEEE J. Quan. Elec. **18,** 856 (1982).

[22] A. Yariv, *Optical electronics*, fourth ed. (Saunders, 1991), ISBN 0-03-047444-2.

[23] A. Jakubowicz, "Material and fabrication-related limitations to high-power operation of GaAs/AlGaAs and InGaAs/AlGaAs laser diodes," Mat. Sci. Eng. B **44,** 359 (1997).

[24] J. Hendrix, G. Morthier, and R. Baets, "Influence of laser parameters and unpumped regions near the facets on the power level for catastrophic optical damage in short wavelength lasers," IEE Proc.- Optoelectron. **144,** 109 (1997).

[25] W. B. Joyce, "Carrier transport in double-heterostructure active layers," J. Appl. Phys. **53,** 7235 (1982).

[26] W. W. Chow and D. Depatie, "Filamentation in conventional double heterostructure and quantum well semiconductor lasers," IEEE J. Quan. Elec. **24,** 1297 (1988).

[27] D. Mehuys, R. J. lang, M. Mittelstein, J. Salzman, and A. Yariv, "Self-stabilized nonlinear lateral modes of broad area lasers," IEEE J. Quan. Elec. **23,** 1909 (1987).

[28] R. J. lang, A. G. Larsson, and J. G. Cody, "Lateral modes of broad area semiconductor lasers: theory and experiment," IEEE J. Quan. Elec. **27,** 312 (1991).

[29] J. K. Butler, D. E. Ackley, and D. Botez, "Coupled-mode analysis of phase-locked injection laser arrays," Appl. Phys. Lett. **44,** 293 (1984).

[30] E. Kapon, J. Katz, and A. Yariv, "Mode analysis of phase-locked arrays of semiconductor lasers," Opt. Lett. **10,** 125 (1984).

[31] J. R. Andrew, T. L. Paoli, W. Streifer, and R. D. Burnham, "Individual spatial modes of a phase-locked injection laser array observed through spectral selection and selection with an external mirror," J. Appl. Phys. **58,** 2770 (1985).

[32] G. Ronald, J. Hohimer, and A. Owyoung, "Free-running modes for gain-guided diode laser arrays," IEEE J. Quan. Elec. **23,** 765 (1987).

[33] J. M. Verdiell, H. Rajbenback, and J. P. Huignard, "Array modes of multiple-stripe diode lasers: A broad-area mode coupling approach," J. Appl. Phys. **66,** 1466 (1989).

[34] G. P. Agrawal, "Lateral-mode analysis of gain-guided and index-guided semiconductor-laser arrays," J. Appl. Phys. **58,** 2922 (1985).

[35] J. M. Verdiell and R. Frey, "A broad-area mode-coupling model for multiple-stripe semiconductor lasers," IEEE J. Quan. Elec. **26,** 270 (1990).

[36] J. D. Mehuys and A. Yariv, "Coupled-wave theory of multiple-stripe semiconductor injection lasers," Opt. Lett. **13,** 571 (1988).

[37] R. M. R. Pillai and E. M. Garmire, "Paraxial-misalignment insensitive external-cavity semiconductor-laser array emitting near-diffraction limited single-lobed beam," IEEE J. Quan. Elec. **32,** 996 (1996).

[38] J. R. Andrews, T. L. Paoli, and R. D. Burnham, "Diffraction effects in a diode arrays traveling-wave amplifier," Appl. Phys. Lett. **51,** 1676 (1987).

[39] E. Acosta, R. Gonzales, and C. Gomez-Reino, "Design of an anamorphic gradient-index lens to correct astigmatism of gaussian laser beams," Opt. Lett. **16,** 627 (1991).

[40] X. Tang, J. P. van der Ziel, and A. K. Chin, "Characterisation of the array modes of high-power gain-guided GaAs single-quantum-well laser arrays," IEEE J. Quan. Elec. **32,** 1417 (1996).

[41] A. E. Siegman, *Lasers* (Oxford University Press, 1986).

[42] G. H. M. van Tartwijk and D. Lenstra, "Semiconductor lasers with optical injection and feedback," Quan. Semiclass. **7,** 87 (1995).

[43] A. Ashkin, G. D. Boyd, J. M. Dziedzic, R. G. Smith, A. A. Ballman, J. J. Levinstein, and K. Nassau, "Optically-induced refractive index inhomogeneities in $LiNbO_3$ and $LiTaO_3$," Appl. Phys. Lett. **9,** 72 (1966).

[44] J. Feinberg, D. Heiman, A. R. Tanguay, and R. Hellwarth, "Photorefractive effects and light-induced charge migration in barium titanate," J. Appl. Phys. **51,** 1297 (1980).

[45] M. Gower, "Photoinduced voltages and frequency shifts in a self-pumped phase-conjugating $BaTiO_3$ crystal," Opt. Lett. **11,** 458 (1986).

[46] P. Gunter, "Holography, coherent light amplification and optical phase conjugation with photorefractive materials," Phys. Rep. **93,** 199 (1982).

[47] R. Rupp, R. Sommerfeldt, K. Ringhofer, and E. Kratzig, "Space charge field limitation in photorefractive LiNbO3:Fe crystals," Appl. Phys. B **51,** 364 (1990).

[48] J.B.Thaxter, "Electrical control of holographic storage in strontium-barium-niobat," Appl. Phys. Lett. **15,** 210 (1969).

[49] R. Mullen and R. Hellwarth, "Optical measurements of the photorefractive parameters of BSO," J. Appl. Phys. **58,** 40 (1985).

[50] J.P.Huignard and F. Micheron, "High-sensitivity read-write volume holographic storage in $Bi_{12}SiO_{20}$ and $Bi_{12}GeO_{20}$ crystals," Appl. Phys. Lett. **29,** 591 (1976).

[51] A. Ashkin, B. Tell, and J. Dziedzic, "Laser induced refractive index inhomogeneities and absorption saturation effects in CdS," IEEE J. Quan. Elec. **3,** 400 (1967).

[52] J. Fabre, J. M. C. Jonathan, and G. Roosen, "Photorefractive beam coupling in GaAs and InP generated by nanosecond light pulses," J. Opt. Soc. Am. B **5,** 1730 (1988).

[53] K. Hsu, C. M. Veber, and R. Roy, "Stochastic mode-locking theory for external-cavity semiconductorlasers," J. Opt. Soc. Am. B **8,** 262 (1991).

[54] M. Zgonik, K. Nakagawa, and P. Gunter, "Electro-optic and dielectric properties of photorefractive $BaTiO_3$ and $KNbO_3$," J. Opt. Am. B **12,** 1416 (1995).

[55] M. B. Klein and R. N. Schwartz, "Photorefractive effect in $BaTiO_3$: microscopic origins," J. Opt. Soc. Am. B **3,** 293 (1986).

[56] A. Mazur, U. van Stevendaaal, K. Buse, M. Weber, O. F. Schirmer, H. Hesse, and E. Kratzig, "Light-induced charge transport processes in photorefractive barium titanate crystals doped with iron," Appl. Phys. B **65,** 481 (1997).

[57] S. Ducharme and J. Feinberg, "Altering the photorefractive properties of $BaTiO_3$ by reduction and oxidation at 650° C," J. Opt. Soc. Am. B **3,** 283 (1986).

[58] G. C. Vally, "Simultaneous electron/hole transport in photorefractive materials," J. Appl. Phys. **59,** 3363 (1986).

[59] F. P. Strohkendl, J. M. C. Jonathan, and R. W. Hellwarth, "Hole-electron competition in photorefractive gratings," Opt. Lett. **11,** 312 (1986).

[60] D. Mahgerefteh and J. Feinberg, "Explanation of the apparent sublinear photoconductivity of photorefractive barium titanate," Phys. Rev. Lett. **64,** 2195 (1990).

[61] G. A. Brost and R. A. Motes, "Origin of the sublinear photorefractive response time in $BaTiO_3$," Opt. Lett. **15,** 1194 (1990).

[62] C. Kittel, *Introduction to solid state physics*, fourth ed. (Wiley and Sons, 1971), ISBN 0-471-49021-0.

[63] P. Gunter and J. P. Huignard, *Photorefractive materials and their applications I* (Springer-verlag, 1988), ISBN 3-540-18332-9.

[64] V. Grubsky, S. MacCormack, and J. Feinberg, "All-optical three-dimentional mapping of 180 degrees domains hidden in a $BaTiO_3$ crystal," Opt. Lett. **21,** 6 (1996).

[65] M. Zgonik, P. Bernasconi, M. Duelli, R. Schlesser, P. Gunter, M. H. Garrett, D. Rytz, Y. Zhu, and X. Wu, "Dielectric, elastic, piezoelectric, electro-optic, and elasto-optic tensors of $BaTiO_3$ crystals," Phys. Rev. B **50,** 5941 (1994).

[66] K. Buse, S. Riehemann, S. Loheide, H. Hesse, F. Mersch, and E. Kratzig, "Refractive indices of single domain $BaTiO_3$ for different wavelengths and temperatures," Phys. Stat. Sol. (a) 135 (1993).

[67] K. Buse, "Light-induced charge transport processes in photorefractive crystals II: Materials," Appl. Phys. B **64,** 391 (1997).

[68] D. Rytz, B. A. Wechsler, M. H. Garrett, C. C. Nelson, and R. N. Schwartz, "Photorefractive properties of $BaTiO_3$:Co," J. Opt. Soc. Am. B **12,** 2245 (1990).

[69] B. A. Wechsler, M. B. Klein, C. C. Nielson, and R. N. Schwartz, "Spectroscopic and photorefractive properties of infrared-sensitive rhodium-doped barium titanate," Opt. Lett. **19,** 536 (1994).

[70] N. Huot, J. M. C. Jonathan, G. Pauliat, D. Rytz, and G. Roosen, "Characterization of a photoreractive rhodium doped barium titanate at 1.06 μm," Opt. com. **135,** 133 (1997).

[71] A. Brignon, J. P. Huignard, M. H. Garrett, and I. Mnushkina, "Self-pumped phase conjugation in rhodium-doped $BaTiO_3$ with 1.06-μm nanosecond pulses," Opt. Lett. **22,** 215 (1997).

[72] U. van Stevendaaal, K. Buse, S. Kamper, H. Hesse, and E. Kratzig, "Light-induced charge transport processes in photorefractive barium titanate doped with rhodium and iron," Appl. Phys. B **63,** 315 (1996).

[73] H. Krose, R. Scharfschwerdt, O. Schirmer, and H. Hesse, "Light-induced charge transport in $BaTiO_3$ via three chage states of rhodium," Appl. Phys. B **61,** 1 (1995).

[74] N. Huot, J. M. C. Jonathan, and G. Roosen, "Validity of the three-charge-state model in photorefractive $BaTiO_3$:Rh at 1.06 μm in cw regime," Appl. Phys. B **65,** 489 (1997).

[75] N. Kukhtarev, V. B. Markov, S. G. Odulov, M. S. Soskin, and V. L. Vinetskii, "Holographic storage in electrooptic crystals. I. Steady state.," Ferroelectrices **22,** 949 (1979).

[76] G. C. Valley, "The secondary-center photorefractive model," Appl. Opt. **22,** 3160 (1983).

[77] K. Buse and E. Kratzig, "Three-valence charge-transport model for explanation of the photorefractive effect," Appl. Phys. B **61,** 27 (1995).

[78] P. Yeh, *Introduction to photorefractive nonlinear optics* (Wiley and Sons, 1993), ISBN 0-471-58692-7.

[79] A. Yariv and P. Yeh, *Optical waves in crystals* (Wiley and Sons, 1984), ISBN 0-471-09142-1.

[80] G. C. Valley and M. B. Klein, "Optimal properties of photorefractive materials for optical data processing," Opt. Eng. **22,** 704 (1983).

[81] J. Feinberg, "Self-pumped, continuous-wave phase conjugator using internal reflections," Opt. Lett. **7,** 486 (1982).

[82] Y. Fainman, E. Klancnik, and S. H. Lee, "Optimal coherent image amplification by two-wave coupling in photorefractive $BaTiO_3$," Opt. Eng. **25,** 228 (1986).

[83] B. Y. Zel'dovich, V. I. Popovichev, V. V. Ragul'skii, and F. S. Faizullo, "Connection between the wave fronts of the reflected and exciting light in stimulation Mandel'shtam-Brillouin scattering," Sov. Phys. JETP Lett. **15,** 109 (1972).

[84] D. A. Rockwell, "A review of phase-conjugate solid-state lasers," IEEE J. Quan. Elec. **24,** 1124 (1988).

[85] R. W. Hellwarth, "Generation of time reversed wave fronts by nonlinear refraction," J. Opt. Soc. Am. **67,** 1 (1977).

[86] A. Yariv and D. M. Pepper, "Amplified reflection , phase conjugation and oscillation in degenerate four-wave mixing," Opt. Lett. **1,** 16 (1977).

[87] J. P. Huignard, J. P. Herriau, P. Aubourg, and E. Spitz, "Phase-conjugate wavefront generation via real-time holography in $Bi_{12}SiO_{20}$ crystals," Opt. Lett. **4,** 21 (1979).

[88] J. O. White, M. Cronin-Golomb, B. Fischer, and A. Yariv, "Coherent oscillation by self-induced gratings in the photorefractive crystal $BaTiO_3$," Appl. Phys. Lett. **40,** 450 (1982).

[89] B. W. Liby and D. Statman, "Controling the linewidth of a semiconductor laser with photorefractive phase conjugate feedback," IEEE Trans. Quan. Elec. **32,** 835 (1996).

[90] R. A. Fisher, *Optical phase conjugation* (Academic Press, 1983), ISBN 0-12-257740-x.

[91] A. A. Zozulya, "Double phase-conjugate mirror is not an oscillator," Opt. Lett. **16,** 545 (1991).

[92] B. Fischer, S. Sternklar, and S. Weiss, "Photorefractive Oscillators," IEEE J. Quan. Elec. **25,** 550 (1989).

[93] V. T. Tikhonchuk and A. A. Zozulya, "Structure of light beams in self-pumped four-wave mixing geometries for phase conjugation and mutual conjugation," Prog. Quant. Electr. **15,** 231 (1991).

[94] B. Fischer, "Theory of self-frequency detuning of oscillations by wave mixing in photorefractive crystals," Opt. Lett. **11,** 236 (1986).

[95] R. Bylsma, A. Glass, D. Olson, and M. Cronin-Golomb, "Self-pumped phase conjugation in InP: Fe," Appl. Phys. Lett. **54,** 1968 (1989).

[96] K. R. MacDonald and J. Feinberg, "Theory of a self-pumped phase conjugator with two coupled interaction regions," J. Opt. Soc. Am **73,** 548 (1983).

[97] A. A. Zozulya, G. Montemezzani, and D. Z. Anderson, "Analysis of total-internal-reflection phase-conjugate mirror," Physical Review A **52,** 4167 (1995).

[98] G. Salomo, M. J. Miller, W. W. Clark, G. L. Wood, and E. J. Sharp, "Strontium barium niobate as a self-pumped phase-conjugator," Opt. Commun. **59,** 417 (1986).

[99] X. Yue, Z. Shao, X. Lui, Y. Song, and H. Chen, "Studies on the formation of self-pumped phase conjugation in a KNSBN crystal," Opt. Commun. **89,** 59 (1992).

[100] D. Rytz and D. Z. Shen, "self-pumped phase conjugator in potassium niobate ($KNbO_3$)," Appl. Phys. Lett. **54,** 2625 (1989).

[101] J. W. et al, "Photorefractive properties and self-pumped phase conjugation of tetragonal Fe-doped $KTa_{1-x}Nb_xO_3$ crystal," Appl. Phys. Lett. **61,** 2761 (1992).

[102] P. Lambelet, R. P. Salathe, M. H. Garrett, and D. Rytz, "Characterization of a photorefractive phase conjugator by optical low-coherence reflectometry," Appl. Phys. Lett. **64,** 1079 (1994).

[103] D. R. Hjelme and A. R. Mickelson, "On the theory of external cavity operated single-mode semiconductor lasers," IEEE J. Quan. elec. **23,** 1000 (1987).

[104] C. henry, "Theory of the linewidth of semiconductor lasers," IEEE J. Quan. Elec. **18,** 259 (1982).

[105] N. Schunk and K. Petermann, "Minimum Bit Rate of DPSK transmission for semiconductor laser with a long external cavity and strong linewidth reduction," J. Lightwave Technol. **5,** 1309 (1987).

[106] N. Schunk and K. Petermann, "Numerical analysis of the feedback regimes for a single-mode semiconductor laser with external feedback," IEEE J. Quan. Elec. **24,** 1242 (1988).

[107] L. N. Langley and K. A. Shore, "The effect of external optical feedback on timing jitter in modulated laser diodes," J. Lightwave Technol. **11,** 434 (1993).

[108] K.-S. Lee and C. Shu, "Stable and widely tuneable dual-wavelength continuous-wave operation of a semiconductor laser in a novel fabry-perot grating-lens external cavity," IEEE J. Quan. Elec. **33,** 1832 (1997).

[109] S. MacCormack and R. W. Eason, "Single-longitudinal-mode operation from a semiconductor laser array via feedback from a modified collimating objective," Appl. Opt. **29,** 2663 (1990).

[110] H. Hemmati, "Single longitudinal operation of semiconductor laser arrays with etalon feedback," Appl. Phys. Lett. **51,** 224 (1987).

[111] J. R. Leger, M. L. Scott, and W. B. Veldkamp, "Coherent addition of AlGaAs lasers using microlense and diffractive coupling," Appl. Phys. Lett. **52,** 1771 (1988).

[112] F. X. D'Amato, E. T. Siebert, and C. Roychoudhuri, "Coherent operation of an array of diode lasers using a spatial filter in a talbot cavity," Appl. Phys. Lett. **55,** 816 (1989).

[113] E. Hecht and A. Zajac, *Optics*, sixth ed. (Addison-Wesley Pub., 1974).

[114] A. C. F. den Boer, K. A. H. van Leeuween, H. C. W. Beijerinck, C. Fort, and F. S. Pavone, "Grating feedback in a 810 nm broad-area diode laser," Appl. Phys. B **63,** 117 (1996).

[115] Y. Li, M. B. S. Jr., and J. G. McInerney, "Widely, tunable, high-power external cavity semiconductor lasers," SPIE **1634,** 532 (1992).

[116] J. Dong, S. A. amd T. Ikeda, and K. Komori, "Single mode multiple-element laser array with grating filter," IEEE J. Quan. Elec. **29,** 2163 (1993).

[117] R. Lang and K. Kobayashi, "External optical feedback effects on semiconductor injection laser properties," IEEE J. Quan. Elec. **16,** 347 (1980).

[118] G. P. Agrawal, "Line narrowing in a single-mode injection laser due to external optical feedback," IEEE J. Quan. Elec. **20,** 468 (1984).

[119] L. Goldberg, H. F. Taylor, A. Dandridge, J. F. Weller, and R. O. Miles, "Spectral characteristics of semiconductor lasers with optical feedback," IEEE J. Quan. Elec. **4,** 555 (1982).

[120] A. Olsson and C. L. Tang, "Coherent optical interference effects in external-cavity semiconductor lasers," IEEE J. Quan. Elec. **17,** 1320 (1981).

[121] J. H. Osmundsen and N. Gade, "Influence of optical feedback on laser frequency spectrum and threshold conditions," IEEE J. Quan. Elec. **19,** 465 (1983).

[122] I. Ikushima and M. Maeda, "Lasing spectra of semiconductor lasers coupled to an optical fiber," IEEE J. Quan. Elec. **15,** 844 (1979).

[123] D. Lenstra, B. H. Verbeek, and A. J. D. Boef, "Coherence collapse in single-mode semiconductor lasers due to optical feedback," IEEE J. Quan. Elec. **21,** 674 (1985).

[124] E. Miltenyi, M. O. Ziegler, M. Hofmann, J. Sacher, W. Elsasser, and E. O. Gobel, "Long-term stable mode locking of a visible diode laser with phase-conjugate feedback," Opt. Lett. **20,** 734 (1995).

[125] G. Klose and A. Siahmakoun, "External mode locking with feedback from a self-pumped phase-conjugator $BaTiO_3$ crystal," Opt. Eng. **35,** 2988 (1996).

[126] R. W. Tkach and A. R. Chraplyvy, "Regimes of feedback effects in 1.5 μm distributed lasers," J. Lightwave Technol. **4,** 1655 (1986).

[127] P. Besnard, B. Meziane, and G. M. Stephan, "Feedback phenomena in a Semiconductor laser induced by distant reflectors," IEEE J. Quan. Elec. **29,** 1271 (1993).

[128] R. F. Broom, E. Mohn, C. Risch, and R. Salathe, "Microwave self-modulation of a diode laser couplied to an external cavity," IEEE J. Quan. Elec. **6,** 328 (1970).

[129] I. Ikushima and M. Maeda, "Self-coupled phenomena of semiconductor lasers caused by an optical fiber," IEEE J. Quan. Elec. **14,** 331 (1978).

[130] R. O. Miles, A. Dandridge, A. B. Tveten, H. F. Taylor, and T. G. Giallorenzi, "Feedback-induced line broadening in CW channel-substrate planar laser," Appl. Phys. Lett. **37,** 990 (1980).

[131] C. Henry and R. F. Kazarinov, "Instability of semiconductor lasers due to optical feedback from distant reflectors," IEEE J. Quan. Elec. **22,** 294 (1986).

[132] A. T. Ryan, G. P. Agrawal, G. R. Gray, and E. C. Gage, "Optical-feedback-induced chaos and its control in multimode semiconductor lasers," IEEE J. Quan. Elec. **30,** 668 (1994).

[133] H. Rong-Qing and T. Shang-Ping, "Improved rate equations for external cavity semiconductor lasers," IEEE J. Quan. Elec. **25,** 1580 (1989).

[134] K. Vanhala, K. Kyuma, A. Yariv, S.-K. Kwong, M. Cronin-Golomb, and K. Y. Lau, "Narrow linewidth, single frequency semiconductor laser with a phase conjugate external cavity mirror," Appl. Phys. Lett. **49,** 1563 (1986).

[135] S. Mailhot and N. McCarthy, "Influence of phase conjugate optical feedback on the emission properties of visible low-power diode laser," Can. J. Phys. **71,** 429 (1993).

[136] N. McCarthy and D. Gay, "Noise reduction in an argon laser with a phase-conjugating external cavity," Opt. Lett. **16,** 1004 (1991).

[137] W. B. Whitten and J. M. Ramsey, "Self-scanning of a dye laser due to feedback from a $BaTiO_3$ phase-conjugate reflector," Opt. Lett. **9,** 44 (1984).

[138] M. Cronin-Golomb and A. Yariv, "Self-induced frequency scanning and distributed Bragg reflection in semiconductor lasers with phase-conjugate feedback," Opt. Lett. **11,** 455 (1986).

[139] J. M. Ramsey and W. B. Whitten, "Phase-conjugate feedback into a continuous-wave ring dye laser," Opt. Lett. **10,** 362 (1985).

[140] J. Feinberg and G. D. Bacher, "Self-scanning of a continuous-wave dye laser having a phase-conjugating resonator cavity," Opt. Lett. **9,** 420 (1984).

[141] G. Agrawal and G. R. Gray, "Effect of phase-conjugate feedback on the noise characteristics of semiconductor lasers," Phys. Rev. A **46,** 46 (1992).

[142] G. R. Gray, D. Huang, and G. P. Agrawal, "Chaotic dynamics of semiconductor lasers with phase-conjugate feedback," Phys. Rev. A **49,** 2096 (1994).

[143] J. Revuelta, L. Pesquera, E. Hernandez-Garcia, and C. R. Mirasso, "Effect of phase-conjugate optical feedback on turn-on jitter in laser diodes," Opt. Lett. **20,** 2213 (1995).

[144] G. Agrawal and J. T. Klaus, "Effect of phase-conjugate feedback on semiconductor laser dynamics," Opt. Lett **16,** 1325 (1991).

[145] G. H. M. van Tartwijk, H. J. C. van der Linden, and D. Lenstra, "Theory of a diode laser with phase-conjugate feedback," Opt. Lett. **17,** 1590 (1992).

[146] L. N. Langley and K. Shore, "Intensity noise and linewidth characteristics of laser diodes with phase conjugate optical feedback," IEE Proc. Optoelectron. **141,** 103 (1994).

[147] A. Murakami, J. Ohtsubo, and Y. Liu, "Stability analysis of semiconductor laser with phase conjugate feedback," IEEE J. Quan. Elec. **33,** 1825 (1997).

[148] Y. Champagne, N. McCarthy, and R. Tremblay, "Optical phase-conjugate feedback effects on gain-guided diode laser charateristics," IEEE J. Quan. Elec. **25,** 595 (1989).

[149] P. Kurz, R. Nagar, and T. Mukai, "Highly efficient phase conjugation using spatial nondegenerate four-wave mixing in a broad-area laser diode," Appl. Phys. Lett. **68,** 1180 (1996).

[150] D. H. DeTienne, G. R. Gray, G. P. Agrawal, and D. Lenstra, "Semiconductor laser dynamics for feedback from a finite-penetration-depth phase-conjugate mirror," IEEE J. Quan. Elec. **33,** 838 (1997).

[151] W. A. van der Graff, L. Pesquera, and D. Lenstra, "Stability of diode laser with phase-conjugate feedback," Opt. Lett. **23,** 256 (1998).

[152] J. Feinberg, "Interferometer with a self-pumped phase-conjuagting mirror," Opt. Lett **8,** 569 (1983).

[153] B. W. Liby and D. Statman, "Phase delay in phase-conjugate external cavity laser," Opt. comm. **101,** 113 (1993).

[154] P. Kurz and T. Mukai, "Frequency stabilization of a semiconductor laser by external phase-conjugate feedback," Opt. Lett. **21,** 1369 (1996).

[155] M. Ohtsu, I. Koshishi, and Y. Teramachi, "A semiconductor laser as a stable phase conjugate mirror for linewidth reduction of another semiconductor," Jap. J. Appl. Phys. **29,** 2060 (1990).

[156] M. Cronin-Golomb, K. Y. Lau, and A. Yariv, "Infrared photorefractive passive phase conjugation with $BaTiO_3$: Demonstrations with GaAlAs and 1.09-μm Ar^+ lasers," Appl. Phys. Lett. **47,** 567 (1985).

[157] J. Feinberg, "Continuous-wave self-pumped phase conjugator with wide field of view," Opt. Lett. **8,** 480 (1983).

[158] L. Goldberg and M. K. Chun, "Injection locking characteristics of a 1 W broad stripe diode," Appl. Phys. Lett. **53,** 1900 (1988).

[159] G. L. Abbas, S. Yang, and V. W. S. Chan, "Injection locking of high-power broad-area diode lasers," Opt. Lett. **12,** 605 (1987).

[160] H. Tsuchida, "Tunable, narrow-linewidth output from an injection-locked high-power AlGaAs laser diode array," Opt. Lett. **19,** 1741 (1994).

[161] G. L. Abbas, S. Yang, V. W. S. Chan, and J. G. Fujimoto, "Injection behavior and modeling of 100 mW broad area diode lasers," IEEE J. Quan. Elec. **24,** 609 (1988).

[162] J. P. Hohimer, A. Owyoung, and G. R. Hadley, "Single-channel injection locking of a diode-laser array with a CW dye laser," Appl. Phys. Lett. **47,** 1244 (1985).

[163] N. Schunk and K. Petermann, "Noise analysis of injection-locked semiconductor injection lasers," IEEE J. Quan. Elec. **22,** 642 (1986).

[164] G. R. hadley, "Injection locking of diode lasers," IEEE J. Quan. Elec. **22,** 419 (1986).

[165] B. Tromborg, H. Olsen, X. Pan, and S. Saito, "Transmission line description of optical feedback and injection locking for fabry-perot and DFB lasers," IEEE J. Quan. Elec. **23,** 1875 (1987).

[166] P. Debernardi, "Locking characteristics of fabry-perot semiconductor laser oscillators with side-mode injection," Opt. Lett. **21,** 656 (1996).

[167] E.-K. Lee, H.-S. Pang, J.-D. Park, and H. Lee, "Bistability and chaos in an injection-locked semiconductor lasers," Phys. Rev. A **47,** 736 (1993).

[168] J. Sacher, D. Baums, P. Panknin, W. Elsasser, and E. O. Gobel, "Intensity instabilities of semiconductor lasers under current modulation, external light injection, and delayed feedback," Phys. Rev. A **45,** 1893 (1992).

[169] H. Li, T. L. Lucas, J. G. McInerney, M. W. Wright, and R. A. Morgan, "Injection locking dynamics of vertical cavity semiconductor lasers under conventional and phase conjugate injection," IEEE J. Quan. Elec. **32,** 227 (1996).

[170] M. M. Ibrahim and M. S. Ibrahim, "A comparison between rate-equantion and fabry-perot amplifier models of injection locked laser diodes," Opt. and Las. Tech. **28,** 39 (1996).

[171] L. Goldberg, H.F.Taylor, and J. F. Weller, "Injection locking of coupled-stripe diode laser arrays," Appl. Phys. Lett. **46,** 236 (1985).

[172] J.-P. weber and S. Wang, "Analysis of the far-field output angle scanning by injection locking of a diode laser array," Appl. Phys. Lett. **48,** 1719 (1986).

[173] M. K. Chun, L. Goldberg, and J. F. Weller, "Injection-beam parameter optimization of an injection-locked diode-laser array," Opt. Lett. **14,** 272 (1989).

[174] C. J. Chang-Hasnain, J. Berger, D. Scifres, W. Streier, and J. R. Whinnery, "high power with high efficiency in a narrow single-lobed beam from a diode laser array in an external cavity," Appl. Phys. Lett. **50,** 1465 (1987).

[175] R. Pillai and E. Garmire, "External-cavity semiconductor-laser array insensitive to paraxial misalignment," Opt. Lett. **20,** 2108 (1995).

[176] A. V. Chelnokov, J. M. Lourtioz, and P. Gavrilovic, "Ultrashort pulses in diffraction-limited beam from diode laser arrays with external cavity," Elec. Lett. **29,** 861 (1993).

[177] L. Goldberg and J. F. Weller, "Single lobe operation of a 40-element laser array in an external ring laser cavity," Appl. Phys. Lett. **51,** 871 (1987).

[178] C. Dam-Hansen, P. M. Johansen, and P. M. Petersen, "Temperature properties of laser-induced interference filters in lithium niobate," Opt. Commun. **118,** 607 (1995).

[179] F. C. Jahoda, P. G. Weber, and J. Feinberg, "Optical feedback, wavelength response, and interference effects of a self-pumped phase conjugation in $BaTiO_3$," Opt. Lett. **9,** 362 (1984).

[180] A. Shiratori and M. Obara, "Frequency-stable, narrow linewidth oscillation of red diode laser with phase-conjugate feedback using stimulated photorefractive backscattering," Appl. Phys. Lett. **69,** 1515 (1997).

[181] A. Shiratori and M. Obara, "Wavelength-stable, narrow-spectral-width oscillation of an AlGaInP diode laser coupled to a $BaTiO_3$:Co stimulated photorefractive backscattering phase conjugator," Appl. Phys. B **65,** 329 (1997).

[182] J. F. Canny, "A computational approach to edge dectection," III Trans. on Pat. Anal. and Mach. Intel. **8,** 679 (1986).

[183] C.-C. Sun, S. Yeh, M.-W. Chang, M.-W. Chang, and K. Y. Hsu, "Optimal incident conditions for a Cat-type self-pumped phase-conjugate mirror," Appl. Opt. **31,** 5769 (1992).

[184] A. A. Zozulya, M. Saffman, and D. Anderson, "Double phase-conjugate mirror: convection and diffraction," J. Opt. Soc. Am B **12,** 255 (1995).

[185] A. A. Zozulya, M. Saffman, and D. Z. Anderson, "Propagation of light beams in photorefractive media: fanning, self-bending, and formation of self-pumped four-wave-mixing phase conjugation geometries," Physical Review Letters **73,** 818 (1994).

[186] P. Xie, J. Dai, P. Wang, and H. Zhang, "Self-pumped phase conjugation in photorefractive crystal: Reflectivity and spatial fidelity," Phys. Rev. A **55,** 3092 (1997).

[187] R. S. Cudney, R. M. Pierce, G. D. Bacher, D. Mahgerefteh, and J. Feinberg, "Intensity dependence of the photogalvanic effect in barium titanate," J. Opt. Soc. Am. B **9,** 1704 (1992).

[188] W. H. Press, S. A. Teukolsky, W. T. Vetterling, and B. P. Flannery, *Numerical Recipes* (Cambridge, 1992), ISBN 0-521-43108.

[189] J. Yamanuchi, J. Shibayama, and H. Nakano, "Wide-angle propagating beam analysis based on the generalized Douglas scheme for variable coefficients," Opt. Lett. **20,** 7 (1995).

[190] L. Solymar, D. J. Webb, and A. Grunnet-Jepsen, *The Physics and Applications of photorefractive materials* (Clarendon Press, Oxford, 1996), ISBN 0-19-856501-1.

[191] M. del Pino, J. Limeres, and M. Carrascosa, "Time evolution of the photorefractive phase conjugation process in $BaTiO_3$," Opt. Comm. **131,** 211 (1996).

[192] H. Kogelnik, "Coupled wave theory for thick hologram gratings," Bell Syst. Tech. J. **48,** 2909 (1969).

[193] R. D. Vre and L. Hesselink, "Diffraction analysis of layered structures of photorefractive gratings," J. opt. Soc. Am. A **13,** 285 (1996).

[194] T. K. Gaylord and M. Moharam, "Analysis and applications of optical diffraction by gratings," Proceedings of the IEEE **73,** 894 (1985).

[195] Q.-C. He, "Theory of photorefractive phase conjugators with mutually incoherent beams," IEEE J. Quan. Elec. **24,** 2507 (1988).

[196] S.-C. D. L. Cruz, S. MacCormack, J. Feinberg, Q. B. He, H.-K. Liu, and P. Yeh, "Effect of beam coherence on mutually pumped phase conjugators," J. Opt. Soc. Am. B **12,** 1363 (1995).

[197] Q. B. He and P. Yeh, "Photofrefractive mutually pumped phase conjugation with partially coherent beams," Appl. Phys. B **60,** 47 (1995).

[198] X. Yi, C. Yang, P. Yeh, S. Lin, and K. Y. Hsu, "General solution of contradirectional two-wave mixing with partially coherent waves in photorefractive crystals," J. Opt. Soc. Am. B **14,** 1396 (1997).

[199] X. Yi, S. H. Lin, P. Yeh, and K. Y. Hsu, "Contradirectional two-wave mixing with partially coherent waves in photorefractive crystals," Opt. Lett. **21,** 1123 (1996).

[200] P. S. Brody and J. R. Goff, "Grating evolution and form in a single-crystal self-pumped barium titanate phase conjuagtor," SPIE **739,** 50 (1987).

[201] S. X. Duo, J. Zhang, M. G. Wang, H. Gao, and P. Ye, "Theoretical study on the effects of stimulated photorefractive backscattering in self-pumped phase conjugtors," J. Opt. Soc. Am B **12,** 1056 (1995).

[202] L. Zhang, J. Zhang, Z. Shao, X. Mu, H. Chen, and M. Jiang, "Origin of self-pumped phase conjugate waves in KNSBN crystals," Chin. Phys. Lett. **13,** 523 (1996).

[203] S. H. Lin, Y. W. Lian, P. Yeh, K. Y. HSU, and Z. Tong, "2k-gratings-assisted self-pumped phase conjugation: theoretical and experimental studies," J. Opt. Soc. Am. B **13,** 1772 (1996).

[204] A. V. Nowak, T. R. Moore, and R. A. Fisher, "Observations of internal beam production in barium titanate phase conjugators," J. opt. Soc. Am. B **5,** 1864 (1988).

[205] S. Dou, H. Hao, J. Zhang, Y. Lian, H. Wang, Y. Zhu, X. Wu, C. Yang, and P. Ye, "Studies on formation mechanisms of self-pumped phase conjugation in $BaTiO_3$:Ce crystals at wavelengths from 570 to 680 nm," J. Opt. Soc. Am. B **12,** 1048 (1995).

[206] A. T. Friberg, M. Kauranen, and R. Salomaa, "Dynamics of fabry-perot resonators with a phase-conjugate mirror," J. Opt. Soc. Am. B **3,** 1656 (1986).

[207] T. Brabec, F. Krausz, and A. J. Schmidt, "Longitudinal pumping of lasers with multistripe laser diodes," Appl. Opt. **30,** 1450 (1991).

A Components Used in the Experimental Setups

In this appendix most of the relevant components and instruments used in the experimental setups are listed.

Array I GaAlAs ten-stripe proton-implanted gain-guided laser array, with a 100 μm wide emitting junction. It is temperature controlled with a peltier element. The array has a threshold of 0.28 amp (= i_{th}) and a maximum output power of 0.5 watt at 0.9 amp ($3.2 \cdot i_{th}$). The reflectivity of the output facet is approximately $R_{out} = 0.04$. The center wavelength, λ_0, of the multimode spectrum at 25°C is 815 nm. The longitudinal mode spacing is $\Delta\lambda_{FP} = 0.11$ nm. Model SDL-2432-H1, serial number AK428. Manufacturer: SDL, San Jose, CA, USA.

Array II GaAlAs ten-stripe proton-implanted gain-guided laser array, with a 100 μm wide emitting junction. It is temperature controlled with a peltier element and has a maximum output power of 1 watt. The center wavelength, λ_0, of the multimode spectrum at 25°C is 800 nm. The longitudinal mode spacing is $\Delta\lambda_{FP}$ = 0.11 nm. Model SDL-2462-P1. Manufacturer: SDL, San Jose, CA, USA.

Single-mode laser diode Single-mode spectrum. The line width is less than 15 MHz. It is temperature controlled with a peltier element. The maximum output power is 100 mW. The wavelength at 25°C is 798 nm. Model SDL-5412-H. Manufacturerr: SDL, San Jose, CA, USA.

Grating Ruled grating with 1200 lines/mm and a blaze angle of 26.44° at 750 nm. The size is 25×25 $(\text{mm})^2$. Model: D43210. Manufacturer: Edmund Scientific, NJ, USA.

Collimation lens The effective focal length is 4.5 mm, diffraction limited performance. NA: 0.55. Model C230TM-B. Manufacturer: Thorlabs Inc., NJ, USA.

Etalon I Solid etalon. Thickness of 300 μm with a finesse of approximately 17. The free spectral range is 350 GHz (or 0.75 nm at 814 nm). The FWHM bandwidth of the etalon is 20 GHz (or 0.04 nm at 814 nm). Model: ES254-300U-3001-0815-0 with coatings. Manufacturer: VLOC optics, FL, USA.

Etalon II A free spectral range of 225 GHz and a finesse of 2.6. The FWHM bandwidth is 86 GHz (or 0.19 nm at 814 nm). Standard etalon from a Ti:sapphire ring laser (model: Coherent 899-01).

Positive cylindrical lens Plano-cylindrical glass lens with a focal length of +60 mm (60×20 $(\text{mm})^2$). Model: 01LCP005/076 AR coat. Manufacturer: Melles Griot, CA, USA.

Positive cylindrical lens Plano-cylindrical glass lens with a focal length of +150 mm (60×50 mm) Model: 01LCP013/076 AR coat. Manufacturer: Melles Griot, CA, USA.

Negative cylindical lens Plano-cylindrical glass lens with a focal length of -60 mm (60×21 mm). Model: 01LCN005/076 AR coat. Manufacturer: Melles Griot, CA, USA.

Convex singlet lens Symmetric-convex glass lens with a focal length of 76.2 mm (ϕ 50 mm). Model: 01LDX145/076 AR coat. Manufacturer: Melles Griot, CA, USA

Convex singlet lens Symmetric-convex glass lens with a focal length of 100 mm (ϕ 50 mm). Model: 01LDX171/076 AR coat. Manufacturer: Melles Griot, CA, USA.

Convex singlet lens Symmetric-convex glass lens with a focal length of 150 mm (ϕ 50 mm). Model: 01LDX205/076 AR coat. Manufactor: Melles Griot, CA, USA.

Achromat lens Focal length of 80 mm (ϕ 31.5 mm). Model: 322287. Manufacturer: Spindler & Hoyer, Gottingen, Germany.

Wave plate Zero-order half-wave wave plate at 810 nm with antireflection coating. Model: WZQ254-810-0-2005 Manufacturer: VLOC optics, FL, USA.

$BaTiO_3$ - Blue II Rhodium doped $BaTiO_3$ crystal with an 800 ppm concentration. The crystal is a 45°-cut crystal and measures $4.0\times5.2\times5.4$ mm^3 (a×a×c). Manufacturer: Deltronic Crystal, USA.

$BaTiO_3$ - Blue III Rhodium doped $BaTiO_3$ crystal with a 800 ppm concentration. The crystal has been cut along its crystallographic axes (orientation: 0°-cut) and measures $5.11\times5.53\times5.33$ mm^3 (a×a×c). Serial number: 6-26-2-c1. Manufacturer: Deltronic Crystal, USA.

$BaTiO_3$ - CROW Chromium-doped $BaTiO_3$ crystal. The crystal has been cut along its crystallographic axes (orientation: 0°-cut) and measures $5.8\times5.2\times2.9$ mm^3, with the c-axis along the longest dimension. The absorption at 800 nm is 1.01 cm^{-1}. The crystal is with Prof. J. Feinberg, the Physics Dept., University of Southern California, LA, USA.

Spectrum analyzer Tektronix 2753P. Frequency range: 0-1.8 GHz.

Fast photodiode Silicon photodiode. Frequency range: DC-1 GHz (3 db). Model: 1601. Manufacturer: New Focus, CA, USA.

B Personal Bibliography

The following publications have been prepared as a result of the work carried out during the present Ph.D study.

Refereed Articles

- M. Løbel, P. M. Petersen and P. M. Johansen, "Suppressing self-induced frequency scanning of a phase conjugate diode laser array using counterbalance dispersion", Appl. Phys. Lett., **72**, 1263 (1998).
- M. Løbel, P. M. Petersen and P. M. Johansen, "Single-mode operation of a laser diode array with frequency selective phase conjugate feedback", Opt. Lett., **23**, 825 (1998).
- M. Løbel, P. M. Petersen and P. M. Johansen, "Tunable single-mode operation of a high-power laser diode array using an external cavity with a grating and a photorefractive phase conjugate mirror", J. Opt. Soc. Am. B, **15**, 2000 (1998)
- M. Løbel, "Wavelength selectivity of the complex grating structure formed in a photorefractive phase conjugator", J. Appl. Phys., accepted for publication in Oct. issue (1998).
- M. Løbel, P. M. Petersen and P. M. Johansen, "Physical origin of laser frequency scanning induced by photorefractive phase conjugate feedback", J. Opt. Soc. Am. B, submitted February 1998.

Conference Presentations

- M. Løbel, P. M. Petersen and P. M. Johansen, "The influence of dispersion on the self-induced scanning of a broad area diode laser with phase conjugate feedback", In proceedings: Topical meeting on photorefractive materials, effects, and devices (PR97), (Chiba, 11-13 June, Japan), Opt. Soc. of Japan, paper TC2, p. 507 (1997).
- P. M. Petersen, M. Løbel and P. M. Johansen, "Single-mode operation of laser diode arrays", invited paper. CLEO/Europe 98, Glasgow, Scotland, United Kingdom, 13-18 Sep. (1998).

Patents

- M. Løbel and P. M. Petersen, "A method for enhancement of the coherence properties of laser systems using phase conjugate feedback and operated far above threshold ", Danish patent application No. 0665 (1997). PCT application submitted 1998.

C $BaTiO_3$ - Material Parameters

In Table 3 typical material parameters for $BaTiO_3$ are listed. Moreover, a few known parameters for the doped crystals used in the experiments have been included.

Parameter	Value	Unit	Note	Ref.
n_a	2.412	-	@ 633 nm	[66]
n_c	2.360	-	@ 633 nm	[66]
r_{42}^T	1300	10^{-12} m/V	unclamped	[65]
r_{33}^T	105	10^{-12} m/V	unclamped	[65]
r_{13}^T	8	10^{-12} m/V	unclamped	[65]
ϵ_c^T/ϵ_0	129	-	unclamped	[65]
ϵ_a^t/ϵ_0	4380	-	unclamped	[65]
N_D	$1{\cdot}10^{25}$	m^{-3}		[190]
N_A	$2{\cdot}10^{22}$	m^{-3}		[190, 186]
α_p	1.01	cm^{-1}	Cr:$BaTiO_3$ (CROW) @ 810 nm	
α_p	1.5	cm^{-1}	Rh:$BaTiO_3$ (Blue III) @ 813 nm	

Table 3. Typical material parameters for barium titanate crystals.

C.1 The Electro-Optic Tensor

The electro-optic effect is traditionally defined in terms of the change in the inpermeability tensor and is given by Eq. 21

$$\Delta\eta_{ij} = \sum_{k=1,2,3} r_{ijk}E_k. \tag{C.51}$$

The constants r_{ijk} are called the linear electro-optic coefficients, which are compponts of a tensor of rank 3. Although there are 27 components, the symmetry leads to the interchangeability of the first two indices i and j, i.e $r_{ijk} = r_{jik}$. This symmetry reduces the number of independent components to 18. As a result of the symmetry, it is convenient to introduce the contrated indices to abbreviate the notation, $r_{ijk} = r_{sk}$, where the relation between the ij and s is

ij	11	22	33	23,32	13,31	12,21
s	1	2	3	4	5	6

(C.52)

Using this notation the electro-optic coefficients are often written in terms of a 6×3 matrix. For $BaTiO_3$, which belongs to the tetragonal 4mm symmetry class, the matrix is given by[78]

$$r_{ijk} = r_{sk} \equiv \begin{bmatrix} 0 & 0 & r_{13} \\ 0 & 0 & r_{23} \\ 0 & 0 & r_{33} \\ 0 & r_{42} & 0 \\ r_{51} & 0 & 0 \\ 0 & 0 & 0 \end{bmatrix} = \begin{bmatrix} 0 & 0 & r_{13} \\ 0 & 0 & r_{13} \\ 0 & 0 & r_{33} \\ 0 & r_{42} & 0 \\ r_{42} & 0 & 0 \\ 0 & 0 & 0 \end{bmatrix}, \tag{C.53}$$

where $r_{51} = r_{42}$ and $r_{23} = r_{13}$. There are thus three independent components.

D Dispersion of Barium Titanate

The refractive index in $BaTiO_3$ depends on the optical frequency (dispersion). The refractive index can be expressed by the following Sellmeier formula

$$n_0(\lambda) = \sqrt{1 + \frac{A_{sell}\lambda^2}{\lambda^2 - a_{sell}^2}}. \tag{D.54}$$

The manufacturer (see Appendix A) of the Blue II and Blue III crystals, has provided the following coefficients for the Sellmeier formula

$$\begin{aligned} A_{sell} &= 4.0854 \\ a_{sell} &= 208.7 \text{ nm} \end{aligned}$$

We are interested in the dispersion at a given wavelength λ_0. By differentiating Eq. D.54 the following expression for the dispersion is obtained

$$\frac{\partial n_0}{\partial \lambda} = \frac{1}{2}\left(\sqrt{1 + \frac{A_{sell}\lambda^2}{\lambda^2 - a_{sell}^2}}\right)^{-1} \frac{2\lambda A_{sell}\left(\lambda^2 - a_{sell}^2\right) - 2\lambda^3 A_{sell}}{\left(\lambda^2 - a_{sell}^2\right)^2} \Big|_{\lambda=\lambda_0}. \tag{D.55}$$

For $\lambda_0 = 813$ nm we obtain $\partial n_0/\partial\lambda$ = -1.6·10^5 m^{-1}, and for $\lambda_0 = 514$ nm we obtain $\partial n_0/\partial\lambda$ = -7.7·10^5 m^{-1}. The simplified expression (the linear approximation) for the dispersion then becomes

$$n_0(\lambda) = n_0(\lambda_0) + (\lambda - \lambda_0)\frac{\partial n_0}{\partial \lambda}, \tag{D.56}$$

where λ_0 is the wavelength around which the dispersion has been linearized. The angle of refraction at the air crystal interface depends on the refractive index. The angle of refraction (θ_r) is determined by Snell's law:

$$\sin(\theta_i) = n_0(\lambda)\sin(\theta_r), \tag{D.57}$$

where θ_i is the angle of incidence at the crystal surface. The refractive index of air is taken to be unity. The dispersion of the crystal can now be expressed as a change in θ_r as the wavelength is changed a small fraction. This is known as the angular dispersion of the crystal ($\partial\theta_r/\partial\lambda$). By differentiating Eq. D.57 the following expression for the angular dispersion is obtained

$$\frac{\partial \theta_r}{\partial \lambda} = \frac{\partial \theta_r}{\partial n_0}\frac{\partial n_0}{\partial \lambda} = -\left(\sqrt{1 - \left(\frac{\sin(\theta_i)}{n_0(\lambda_0)}\right)^2}\right)^{-1} \frac{\sin(\theta_i)}{(n_0(\lambda_0))^2}\frac{\partial n_0}{\partial \lambda}, \tag{D.58}$$

where $\partial n_0/\partial\lambda$ is given by Eq. D.55. For an angle of incidence $\theta_i = 60^\circ$ and a wavelength of $\lambda_0 = 813$ nm, the angular dispersion becomes $\partial\theta_r/\partial\lambda = 2.8\cdot10^{-5}$ rad/nm. We have used $n_0(\lambda_0) = 2.32$.

Bibliographic Data Sheet **Risø–R–1038(EN)**

Title and author(s)

Improvement of the Coherence Characteristics of Laser Diode Arrays Using Photorefractive Phase Conjugation

Martin Bo Hjort Løbel

ISBN		ISSN
87-550-2373-8	87-550-2409-2 (internet)	0106-2840

Dept. or group	Date
Optics and Fluid Dynamics Department	May 1998

Groups own reg. number(s)	Project/contract No.

Pages	Tables	Illustrations	References
148	3	69	207

Abstract (Max. 2000 char.)

This thesis deals with new techniques for improvement of the coherence properties of laser diode arrays. A new configuration where a laser diode array is coupled to an external phase conjugate cavity is presented. The phase conjugator is a self-pumped photorefractive barium titanate crystal. The external cavity includes a frequency selective element and a spatial filter. Experimentally it is verified that the frequency selective element (an etalon or a diffraction grating), the spatial filter, and the conjugator cause the laser diode array to oscillate in one single spatial mode at one longitudinal mode. Therefore, the radiation becomes almost diffraction limited and the coherence length is improved significantly. It is found that the material dispersion in the barium titanate crystal plays a crucial role in the self-induced frequency scanning process that takes place when a multimode laser is coupled to such a conjugator. It is shown that a new concept - counterbalanced dispersion - that is based on dispersion in prisms or gratings can suppress the frequency scanning. A theoretical model of the grating structure in the barium titanate crystal is presented. From this model it is predicted that the dispersion causes the reflectivity of the conjugator to become asymmetric with respect to the wavelength. The asymmetry leads to the scanning phenomenon and, consequencely, we conclude that dispersion is the origin of the frequency scanning process. Moreover, it is found that the grating structure in the crystal is much more frequency selective than previously assumed. The wavelength selectivity depends on the coherence length of the laser beam that induces the dynamic gratings. This dependency leads to the self-narrowing effect and through this effect the coherence length of a multimode laser can be increased when the laser is coupled to a conjugator.

Descriptors

BARIUM TITANATE;COHERENCE;GRATING STRUCTURES;LASER DIODE ARRAYS; OPTICAL PHASE CONJUGATION;PHASE LOCKING; PHOTOREFRACTIVITY; SINGLE-MODE LASERS

Available on request from:
Information Service Department, Risø National Laboratory
(Afdelingen for Informationsservice, Forskningscenter Risø)
P.O. Box 49, DK–4000 Roskilde, Denmark
Phone (+45) 46 77 46 77, ext. 4004/4005 · Fax (+45) 46 77 40 13
E-mail: infserv@risoe.dk